NATIONAL AERONAUTICS AND SPACE ADMINISTRATION

The Deep Space Network
Progress Report 42-31

November and December 1975

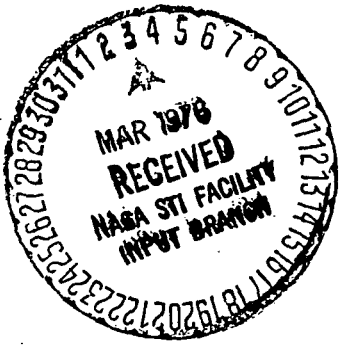

JET PROPULSION LABORATORY
CALIFORNIA INSTITUTE OF TECHNOLOGY
PASADENA, CALIFORNIA

February 15, 1976

NATIONAL AERONAUTICS AND SPACE ADMINISTRATION

The Deep Space Network
Progress Report 42-31

November and December 1975

JET PROPULSION LABORATORY
CALIFORNIA INSTITUTE OF TECHNOLOGY
PASADENA, CALIFORNIA

February 15, 1976

Preface

Beginning with Volume XX, the Deep Space Network Progress Report changed from the Technical Report 32- series to the Progress Report 42- series. The volume number continues the sequence of the preceding issues. Thus, Progress Report 42-20 is the twentieth volume of the Deep Space Network series, and is an uninterrupted follow-on to Technical Report 32-1526, Volume XIX.

This report presents DSN progress in flight project support, tracking and data acquisition (TDA) research and technology, network engineering, hardware and software implementation, and operations. Each issue presents material in some, but not all, of the following categories in the order indicated.

Description of the DSN

Mission Support
- Ongoing Planetary/Interplanetary Flight Projects
- Advanced Flight Projects

Radio Science

Special Projects

Supporting Research and Technology
- Tracking and Ground-Based Navigation
- Communications—Spacecraft/Ground
- Station Control and Operations Technology
- Network Control and Data Processing

Network and Facility Engineering and Implementation
- Network
- Network Operations Control Center
- Ground Communications
- Deep Space Stations

Operations
- Network Operations
- Network Operations Control Center
- Ground Communications
- Deep Space Stations

Program Planning
- TDA Planning
- Quality Assurance

In each issue, the part entitled "Description of the DSN" describes the functions and facilities of the DSN and may report the current configuration of one of the five DSN systems (Tracking, Telemetry, Command, Monitor & Control, and Test & Training).

The work described in this report series is either performed or managed by the Tracking and Data Acquisition organization of JPL for NASA.

Contents

Communications–Spacecraft/Ground

Station Control and Operations Technology

Network Control and Data Processing

NETWORK AND FACILITY ENGINEERING AND IMPLEMENTATION

Network

Deep Space Stations

OPERATIONS

Network Operations

Deep Space Stations

PROGRAM PLANNING

TDA Planning

DSN Functions and Facilities

N. A. Renzetti
Office of Tracking and Data Acquisition

The objectives, functions, and organization of the Deep Space Network are summarized. Deep space station, ground communication, and network operations control capabilities are described.

The Deep Space Network (DSN), established by the National Aeronautics and Space Administration (NASA) Office of Tracking and Data Acquisition (OTDA) under the system management and technical direction of the Jet Propulsion Laboratory (JPL), is designed for two-way communications with unmanned spacecraft traveling approximately 16,000 km (10,000 mi) from Earth to the farthest planets of our solar system. It has provided tracking and data acquisition support for the following NASA deep space exploration projects, for which JPL has been responsible for the project management, development of the spacecraft, and conduct of mission operations:

(1) Ranger.

(2) Surveyor.

(3) Mariner Venus 1962.

(4) Mariner Mars 1964.

(5) Mariner Venus 1967.

(6) Mariner Mars 1969.

(7) Mariner Mars 1971.

(8) Mariner Venus/Mercury 1973.

The DSN has also provided tracking and data acquisition support for the following projects:

(1) Lunar Orbiter, for which the Langley Research Center carried out the project management, spacecraft development, and mission operations functions.

(2) Pioneer, for which the Ames Research Center carried out the project management, spacecraft development, and mission operations functions.

(3) Apollo, for which the Lyndon B. Johnson Space Center was the project center and the Deep Space Network supplemented the Spaceflight Tracking and Data Network (STDN), which is managed by the Goddard Space Flight Center (GSFC).

(4) Helios, a joint United States/West Germany project.

(5) Viking, for which the Langley Research Center provides the project management and Lander spacecraft, and conducts mission operations, and for which JPL provides the Orbiter spacecraft.

The Deep Space Network is one of two NASA networks. The other, the Spaceflight Tracking and Data Network, is under the system management and technical direction of the Goddard Space Flight Center. Its function is to support manned and unmanned Earth-orbiting and lunar scientific and advanced technology satellites. Although the DSN was concerned with unmanned lunar spacecraft in its early years, its primary objective now and into the future is to continue its support of planetary and interplanetary flight projects.

A development objective has been to keep the network capability at the state of the art of telecommunications and data handling and to support as many flight projects as possible with a minimum of mission-dependent hardware and software. The DSN provides direct support to each flight project through that project's tracking and data systems. This management element is responsible for the design and operation of the hardware and software in the DSN which are required for the conduct of flight operations.

As of July 1972, NASA undertook a change in the interface between the network and the flight projects. Since January 1, 1964, the network, in addition to consisting of the Deep Space Stations and the Ground Communications Facility, had also included the Mission Control and Computing Facility and had provided the equipment in the mission support areas for the conduct of mission operations. The latter facilities were housed in a building at JPL known as the Space Flight Operations Facility (SFOF). The interface change was to accommodate a hardware interface between the network operations control functions and the mission control and computing functions. This resulted in the flight project's picking up the cognizance of the large general-purpose digital computers, which were used for network processing as well as mission data processing. It also assumed cognizance of all of the equipment in the flight operations facility for display and communications necessary for the conduct of mission operations. The network has already undertaken the development of hardware and computer software necessary to do its network operations control and monitor functions in separate computers. This activity became known as the Network Control System implementation. A characteristic of the new interface is that the network provides direct data flow to and from the stations via appropriate ground communications equipment to Mission Operations Centers, wherever they may be; namely, metric data, science and engineering telemetry, and such network monitor data as are useful to the flight project. It accepts command data from the flight project directly into the ground communications equipment for transmission to the station and thence to the spacecraft in a standardized format.

In carrying out its functions, the network activities can be divided into two general areas. The first includes those functions which are associated with the in-flight support and in tracking the spacecraft; its configuration can be characterized as follows:

(1) *DSN Tracking System.* Generates radio metric data; i.e., angles, one- and two-way doppler and range, and transmits raw data to mission control.

(2) *DSN Telemetry System.* Receives, decodes, records, and retransmits engineering and scientific data generated in the spacecraft to Mission Control.

(3) *DSN Command System.* Accepts coded signals from Mission Control via the Ground Communications Facility (GCF) and transmits them to the spacecraft in order to initiate spacecraft functions in flight.

The second category of activity supports testing, training, and network operations control functions and is configured as follows:

(1) *DSN Monitor and Control System.* Instruments, transmits, records, and displays those parameters of the DSN necessary to verify configuration and validate the network. Provides operational direction and configuration control of the network and primary interface with flight project mission control personnel.

(2) *DSN Test and Training System.* Generates and controls simulated data to support development, test, training, and fault isolation within the DSN. Participates in mission simulation with flight projects.

The capabilities needed to carry out the above functions have evolved in two technical areas:

(1) The Deep Space Stations that are distributed around Earth and which, prior to 1964, formed part of the Deep Space Instrumentation Facility. The technology involved in equipping these stations is strongly related to the state of the art of telecommunications and flight/ground design considerations and is almost completely multimission in character. Table 1 gives a description of the Deep Space Stations and the Deep Space Communications Complexes (DSCCs) they comprise.

(2) Ground communications. This technology supports the Earth-based point-to-point voice and data communications from the stations to the Network Operations Control Area at JPL, Pasadena, and to the Mission Operations Centers, wherever they may be. It is based largely on the capabilities of the common carriers throughout the world which are engineered into an integrated system by the Goddard Space Flight Center for support of all NASA programs. The term "Ground Communications Facility" is used for the sets of hardware and software needed to carry out the functions.

The Network Operations Control Center is the functional entity for centralized operational control of the network and interfaces with the users. It has two separable functional elements; namely, Network Operations Control and Network Data Processing.

The functions of the Network Operations Control Center are:

(1) Control and coordination of network support to meet commitments to network users.

(2) Utilization of the network data processing computing capability to generate all standards and limits required for network operations.

(3) Utilization of network data processing computing capability to analyze and validate the performance of all network systems.

The personnel who carry out the above functions are on the first floor of Building 230, wherein mission operations functions are carried out by certain flight projects. Network personnel are directed by an Operations Control Chief. The functions of the Network Data Processing are:

(1) Processing of data used by Network Operations Control for the control and analysis of the network.

(2) Display in Network Operations Control Area of data processed in Network Data Processing Area.

(3) Interface with communications circuits for input to and output from Network Data Processing Area.

(4) Data logging and production of the intermediate data records.

The personnel who carry out these functions are located in Building 202, which is approximately 200 m from Building 230. The equipment consists of minicomputers for real-time data system monitoring, two XDS Sigma 5's, display, magnetic tape recorders, and appropriate interface equipment with the ground data communications.

Table 1. Tracking and data acquisition stations of the DSN

DSCC	Location	DSS	DSS serial designation	Antenna		Year of initial operation
				Diameter, m (ft)	Type of mounting	
Goldstone	California	Pioneer	11	26(85)	Polar	1958
		Echo	12	26(85)	Polar	1962
		(Venus)[a]	13	26(85)	Az-El	1962
		Mars	14	64(210)	Az-El	1966
Tidbinbilla	Australia	Weemala	42	26(85)	Polar	1965
		Ballima	43	64(210)	Az-El	1973
—	Australia	Honeysuckle Creek	44	26(85)	X-Y	1973
Madrid	Spain	Robledo	61	26(85)	Polar	1965
		Cebreros	62	26(85)	Polar	1967
		Robledo	63	64(210)	Az-El	1973

[a]A maintenance facility. Besides the 26-m (85-ft) diam Az-El mounted antenna, DSS 13 has a 9-m (30-ft) diam Az-El mounted antenna that is used for interstation time correlation using lunar reflection techniques, for testing the design of new equipment, and for support of ground-based radio science.

Compatibility Test System for Use With the Mark III DSN Data Subsystems Implementation

A. I. Bryan
DSN Systems Engineering Office
G. H. Winn
DSN Facility Operations Office

This article reports on the Compatibility Test System (CTS) that will be used at the Compatibility Test Area, JPL, Pasadena (CTA 21), and the Spacecraft Compatibility/Monitor Station, Merritt Island, Florida (STDN MIL 71), to perform telecommunications compatibility tests with the Mariner Jupiter-Saturn 1977 and the Pioneer Venus 1978 spacecraft. The functional design of the new system utilizes capabilities provided by a Compatibility Test Assembly and the Mark III DSN Data Subsystems (MDS) configuration. A discussion of the Compatibility Test System implementation identifies the special-purpose equipment which comprises the Compatibility Test Assembly.

I. Introduction

Implementation of the Mark III Deep Space Network Data Subsystems (MDS) at the Compatibility Test Area, JPL, Pasadena (CTA 21), and the Spacecraft Compatibility/Monitor Station, Merritt Island, Florida (STDN MIL 71), necessitates a redesign of the Compatibility Test System (CTS) used to verify telecommunications compatibility between a spacecraft and the Deep Space Network (DSN). The new CTS, as designed by the DSN Systems Engineering Office, will be developed and implemented at CTA 21 to support the Mariner Jupiter-Saturn 1977 Spacecraft–DSN Compatibility Test Program, which starts during the second quarter of calendar year 1976. The test system will provide capabilities to satisfy both Mariner Jupiter-Saturn 1977 and Pioneer Venus 1978 Compatibility Test Program requirements.

II. Functional Design

The functional design of the Compatibility Test System is based on the following criteria:

(1) Implement a test capability for use at CTA 21 and MIL 71 to provide test monitor, control and simulation capabilities which will satisfy Mariner Jupiter-Saturn 1977 and Pioneer Venus 1978 Compatibility Test Program requirements.

(2) Provide a cost-effective implementation of the Compatibility Test System through utilization of the capabilities provided by the Mark III DSN Data Subsystems for test control and performance monitoring.

The Compatibility Test System hardware for Mariner Jupiter-Saturn and Pioneer Venus 1978 will consist of a Compatibility Test Assembly interfaced to a standard Mark III DSN Data Subsystems configuration at CTA 21 or MIL 71. The Compatibility Test Assembly contains special-purpose equipment that provides the capability to measure and analyze analog signals. Other compatibility test requirements will be met by utilization of the standard MDS capabilities for control, monitoring and simulation.

The functions of measurement, processing and reporting of analog signals will be performed by specialized applications software. Each applications program will perform as a high-priority task under the control of Operating System software. The standard Modular Computer Systems Corporation (MODCOMP) Operating System (MAX III) software will be extended to provide an analog input capability and a plotting capability to support the applications programs.

The Compatibility Test Assembly Controller will process analog information to perform two functions:

(1) Measure the phase stability of a spacecraft's transmitted carrier and telemetry subcarrier(s). Phase stability measurements are performed in real time by concurrently sampling the phase detector error signals of two ground receivers which are phase-locked with the spacecraft's downlink carrier. The root-mean-square (rms) voltage from either receiver indicates the phase noise of the receiver plus that of the spacecraft's transmitter. Cross-correlation of these two signals, displayed in the frequency and time domains, provides a measurement of the phase noise contributed by the spacecraft's transmitter. Subcarrier phase stability measurements utilize the same technique by sampling two subcarrier demodulators.

(2) Measure the relative power of the components of a spacecraft's transmitted radio-frequency signal and provide a frequency domain plot of the spectral components. Measurements of a spacecraft's transmitted spectrum components are performed by digitizing an analog recording of a spacecraft's transmitted RF signal. Time samples of the radio-frequency signal are transformed to the frequency domain by a Fast Fourier Transform algorithm. The resulting phase components of the frequency spectrum are processed to provide discrete spectral components of power. All power components are converted to relative values and referenced to the carrier. The resulting plot contains frequency and relative power values for each discrete spectral component.

The Compatibility Test System, by utilizing capabilities provided by the Mark III DSN Data Subsystems implementation, will also provide the following:

(1) Control and monitor of tests to determine the performance of a spacecraft's Command, Telemetry and Radio Metric Subsystems under simulated nominal and worst-case flight conditions. Test control and monitoring will be performed from a central input/output terminal.

(2) Spacecraft Radio Frequency Subsystem (RFS) tests utilize the control capabilities of the Block IV Receiver-Exciter and the special CTA 21/MIL 71 Microwave Subsystems. These subsystems provide capabilities to simulate doppler and to measure the acquisition characteristics and tracking performance of the spacecraft receiver.

III. CTS Implementation

Implementation of the Compatibility Test System requires an extension of the Mark III DSN Data Subsystems capabilities. This extension is provided by the Compatibility Test Assembly interfaced to the Communications Monitor Formatter (CMF) Assembly and special-purpose test software, which resides on the CMF Assembly Disk. The CMF redundant MODCOMP Model II-25 minicomputer is utilized as the Compatibility Test Assembly Controller.

Special-purpose equipment required to implement the Compatibility Test Assembly will be housed in one standard DSN 48-centimeter (19-inch) roll-around rack and will interface with the redundant CMF minicomputer through a single cable connected to an existing plug on the CMF Peripheral Controller Interface (PCI) Connector Panel. Only one set of Compatibility Test Assembly equipment will be procured for use at both CTA 21 and MIL 71. Upon completion of testing at JPL and prior to

initiation of testing in Florida, the Compatibility Test Assembly equipment will be shipped from CTA 21 to MIL 71.

It should be noted that when the Compatibility Test Assembly is interfaced to the CMF redundant minicomputer, it will in no way disturb the hardware integrity of the standard CMF Assembly. The Compatibility Test Assembly interface merely extends the input/output bus capabilities of the standard CMF Assembly configuration.

The new Compatibility Test Assembly consists of the following equipment:

(1) A twelve-bit Analog-to-Digital (A-D) Converter and Power Supply.

(2) A twelve-bit Digital-to-Analog (D-A) Converter and Power Supply.

(3) A Peripheral Controller Interface Assembly, which contains the A-D and D-A Interface Logic.

Standard MDS configuration equipment that will be used in conjunction with the Compatibility Test Assembly to provide the CTS capability consists of:

(1) The CMF redundant minicomputer.

(2) A General Electric TermiNet keyboard-printer as normally connected in the standard CMF Assembly configuration.

(3) A Varian high-speed printer-plotter as normally connected in the standard CMF Assembly configuration.

(4) The direct access storage device (Disk) that is part of the standard CMF Assembly configuration.

The block diagram in Figure 1 illustrates the hardware configuration of the Compatibility Test System functional capability.

The software packages to be used by the CTS will consist of:

(1) The standard DSN Operational Software Package used to process Telemetry, Command, Radio Metric and Monitor data.

(2) A software package consisting of a version of the standard MDS Operating System (MAX III) extended to handle the interface between the Compatibility Test Assembly and the CMF's MODCOMP minicomputer, and containing applications programs such as Phase Jitter Analysis and Downlink Spectrum Analysis. Applications programs will be prepared in Fortran IV (a standard software package on the MODCOMP II).

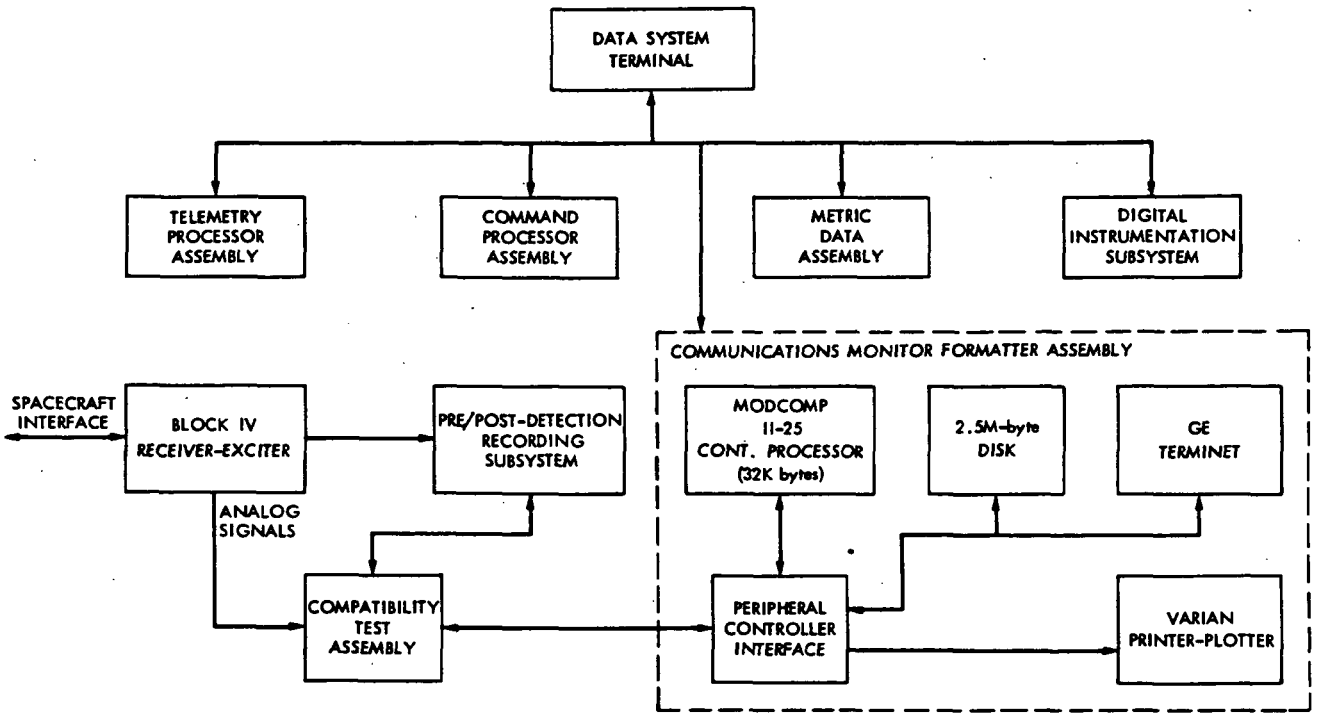

Fig. 1. Compatibility Test System configuration for CTA 21 and Mil 71

Viking Mission Support

D. J. Mudgway
DSN Systems Engineering Office
D. W. Johnston
DSN Operations Office

This article reports DSN activity in support of Viking 1 and 2 cruise operations, together with the implementation and new training directed toward completing the planetary configuration of the DSN for Viking support by 1 February 1976.

I. Background

As Viking 1 and 2 settle into the cruise phase of the mission, DSN Operations continues to support the Viking Flight Teams in providing tracking support from both 26-meter subnets, as well as the 64-meter subnet. At the same time, additions are being made to the Network, particularly at the 64-meter stations, to bring the cruise configuration up to meet the planetary requirements.

This situation leads to a demand for station time which far exceeds the resources available. The situation is further aggravated by additional requirements for operational tests to train the station crews and to qualify the added capabilities for flight support.

Some degree of resolution has resulted from the establishment of an integrated Viking scheduling committee, which coordinates all DSN demands for implementation testing and training with Project demands for flight support, sets priorities within this total body of work, and presents a total Viking support request to the scheduling office.

II. Planetary Testing and Training

A considerable number of Operational Verification Tests (OVTs) were carried out during this period. These are discussed below.

A. Operational Verification Tests

In the previous article, the DSN testing plan for planetary operations was outlined. At this time, the first testing phase is progressing smoothly and should be completed as forecast (reference *Progress Report 42-30*). The first phase testing at DSSs 11 and 14 (Goldstone, California) has been completed, and the program for DSSs 42 and 43 (Australia) and DSSs 61 and 63 (Spain) is proceeding as planned. Listed below are the tests completed at each facility and a brief summary of results.

DSS 14 64-meter planetary OVTs.

(1) OVT 1—90% successful, discovered more time required for pre-test calibrations.

(2) OVT 2—95% successful, low SNRs on one of six telemetry streams.

(3) OVT 3—90% successful, block decoder assembly down.

(4) OVT 4—100% successful.

DSS 11 and 14 combined planetary OVTs

(1) OVT 1—50% successful, problem with microwave link between DSSs 11 and 14.

(2) OVT 2—50% successful, delay in reconfigurations and validation of telemetry data rates.

(3) OVT 3—100% successful

(4) OVT 4—95% successful, SSA overheating problem.

DSS 43 64-meter planetary OVTs

(1) OVT 1—95% successful, minor operational problems.

(2) OVT 2—90% successful, no DODR recalls performed.

(3) OVT 3—65% successful, interference from real-time operations.

DSS 42 and 43 conjoint planetary OVTs

(1) OVT 1—100% successful.

(2) OVT 2—100% successful.

(3) OVT 3—100% successful.

DSS 63 64-meter planetary OVTs

(1) OVT 1—100% successful.

(2) OVT 2—70% successful, interface problem between Ground Communication Facility (GCF) and Network Operations Control Center (NOCC).

(3) OVT 3—90% successful, delay in data validation.

DSS 61 and 63 conjoint planetary OVTs

(1) OVT 1—80% successful, test start delayed, and equipment problems in the Network Analysis Team area.

(2) OVT 2—100% successful.

The above takes the DSN testing effort up to December 8. Phase one will be completed by early January. Phase two will begin the week of March 8, 1976. There will be four OVTs scheduled at each complex, consisting of two tests with the 64-meter stations by themselves, and two tests involving their 26-meter conjoint stations. This final OVT phase is scheduled to be completed during the week of April 8, 1976.

III. DSN Support of Additional Viking Testing

In addition to the above DSN tests, the support of System Integration Tests (SITs) and Ground Data System (GDS) Tests is progressing as forecast in the previous article. To date, DSSs 11 and 14 have participated in the following tests:

(1) Planetary SIT—100% successful. Interface problem between Ground Communication Facility and Viking Mission Computer Control Complex was resolved.

(2) GDS 5.1—Considered successful. No DSN problems encountered.

Following GDS test 5.1, the next GDS test will be 5.31 to be run December 15. This will involve DSSs 11 and 14 at Goldstone, California. The test results will be reported in the next article of this series.

In January, SIT and GDS testing will begin overseas at Australia and Spain. On January 8, a SIT test is scheduled for DSS 43 (Australia), with a retest, if necessary, on January 13. On January 15, a SIT is scheduled for DSS 63 (Spain), with a retest on January 22.

GDS 5.32 will be run in January, with the overseas portion beginning at DSSs 42 and 43 on January 15. On January 16, GDS 5.32 will be performed with DSSs 61 and 63. In February, GDS test 6.0 is scheduled. This will involve DSS 14 at Goldstone and DSS 43 in Australia. The remaining GDS test, 11.0, is scheduled for May, but no station has been designated at this time.

IV. Flight Operations Personnel Test and Training

As reported in the last article, the Flight Operations Personnel Test and Training follows GDS testing. These tests are scheduled to begin in mid-February. They should be completed by April. Details concerning these tests are not readily available at this time, and will be covered in future articles.

Pioneer Venus 1978 Mission Support

R. B. Miller
DSN Systems Engineering Office

The differential long baseline interferometry experiment for the purpose of measuring the wind velocities in the atmosphere of Venus as a part of the Pioneer Venus 1978 multiprobe mission is described.

I. Introduction

The Pioneer Venus multiprobe mission includes a differential long baseline interferometry experiment, which will attempt to measure the wind velocity in the atmosphere of Venus as four probes descend through the atmosphere. Basically, the experiment will be using interferometry techniques to measure the components of the wind velocity perpendicular to the line of sight (Earth–spacecraft direction) and established doppler techniques to measure the velocity components along the line of sight. As described in previous articles, the bus spacecraft is retarded by a trajectory correction after it releases the four probes, so that it will enter the Venusian atmosphere after all four probes have reached the surface of the planet. In this way, the bus serves as a reference signal, undisturbed by the Venusian atmosphere. A corrected difference is taken between the bus signal and each of the probe signals at a particular tracking station to eliminate ionospheric and interplanetary effects, and a second difference is taken between pairs of tracking stations which produces a measure of the rate of change of the angle subtended by the two stations and a probe.

Each pair of stations resolves only one component of the velocity. In order to resolve both components of the wind velocity perpendicular to the line of sight and to provide some measure of redundancy, four stations will be equipped to support this experiment. The two 64-meter DSN stations located at Goldstone, California, and Canberra, Australia, will be utilized, along with 12-meter Spaceflight Tracking and Data Network (STDN) stations located at Santiago, Chile, and Guam. The Principal Investigator for this experiment is Dr. Counselman and the Co-Investigator is Dr. Pettengill, both of the Massachusetts Institute of Technology. The Tracking and Data Acquisition Office of the Jet Propulsion Laboratory is responsible for seeing that all four ground stations are equipped for this experiment. The experimenters will be responsible for all nonreal-time processing of the data.

II. Basis of Differential Long Baseline Interferometry

The fundamental concept of interferometry and its application in the Pioneer Venus case are illustrated in Fig. 1. Pictured are two tracking stations located on the surface of Earth and two signal sources located near the planet Venus. For simplicity, consider that the two spacecraft and the two tracking stations are located on lines which are perpendicular to the Earth–Venus line of sight. Looking first at a single spacecraft, since the distance from Earth to Venus, r, is very much greater than the displacement of the spacecraft from the line-of-sight, y, then using similar triangles, the angles ϕ and θ are approximately equal. The difference in path length from the spacecraft to the two stations is shown as the distance δ; δ equals ϕd, where d is the distance separating the two stations. Similarly, y is equal to $r\theta$. Since ϕ is approximately equal to θ, then y is approximately equal to $(r/d)\delta$. δ represents the phase difference between the single spacecraft signal received simultaneously at the two tracking stations. As an indication of the potential power of the interferometry technique, if it were possible to measure δ to within 1 degree of phase at S-band, using the fact that 1 Hz at S-band is approximately 13 cm, an Earth–Venus distance of 50,000,000 km and a station separation of 8,000 km in the expression derived above, the displacement of the spacecraft could be resolved to within 3 meters at Venus. Unfortunately, there are several sources of error which would prevent making such a direct measurement. The two most significant effects are that the signal will have traveled through two completely different locations in Earth's ionosphere and, second, that in order to process the received signal, it is necessary to beat the signal against a local oscillator at each of the two stations. Differences in the local oscillators at the two stations would map directly into an error in the determination of δ. The differential technique is utilized to virtually eliminate both of these error sources.

Returning to Fig. 1, if a second spacecraft located in the vicinity of the spacecraft of interest is tracked simultaneously, then the same expression as derived above could be used to derive a differential expression:

$$y_1 - y_2 \cong \frac{r}{d}(\delta_1 - \delta_2)$$

Now, with a differential measurement, two important things happen. First, because the two spacecraft are located close to each other compared to the Venus–Earth distance, their signals will follow essentially the same ray path through Earth's ionosphere; therefore, differencing the signals will cancel out the ionospheric and atmospheric effects of Earth. Second, if the two signals are received through a single receiver at each of the stations, then at a particular station, both signals will have been beat against the same oscillator, and therefore, when they are differenced, the variations in the local oscillator will cancel out. This latter point is very important when considering the requirements on the ground equipment. In looking at the error sources of the experiment due to contributions from station equipment, because of this differential effect, only error sources which introduce a differential phase error between the two received signals have a significant effect on the experiment. Error sources which cause equal changes in the two received signals (such as local oscillator drift) have no first-order effect on the experiment.

In the above simplified discussion, one point which was ignored is the fact that δ in practice contains an unresolvable ambiguity. In practice, δ is many wavelengths long (one S-band wavelength is approximately 13 cm, where δ can be on the order of hundreds of kilometers) and should be better represented by the expression

$$\delta = n\lambda + \frac{p\lambda}{2\pi}$$

where λ is the signal wavelength, n is an unknown integer, and p is the fractional phase difference expressed in radians. p is defined as the fringe phase. Since it is not possible to determine n to sufficient accuracy, only the time variation of p is meaningful, and it is the time variation of p which is termed the fringe frequency in radio interferometry. However, in the Pioneer Venus case, that is exactly what is desired. Determining the time rate of change of p, we have the time rate of change of δ and therefore the derivative of y, which represents the velocity of the spacecraft perpendicular to the line-of-sight:

$$\frac{d(y_1 - y_2)}{dt} \cong \frac{r}{d}\frac{d(\delta_1 - \delta_2)}{dt} = \frac{r}{d}\frac{\lambda}{2\pi}\frac{dp}{dt}$$

where dp/dt, the fringe frequency, is the observable.

III. Differential Long Baseline Interferometry Requirements

The key requirements for the Pioneer Venus 1978 differential long baseline interferometry wind measurement experiment will be briefly described.

The objective of the experiment is to be able to measure the wind velocities as the probes fall through the atmosphere of Venus to about a 10-cm-per-second accuracy using a 100-second integration time for the signal-to-noise ratios expected at the DSN 64-meter antennas. It is fairly easy to show that this requirement translates into the need to be able to determine the phase difference between pairs of signals when averaged over 100 seconds to within 1 degree of phase at S-band. For the 9-meter STDN stations, which will have a significantly less favorable signal-to-noise ratio, it will clearly be necessary for the experimenters to integrate over much longer times in order to achieve the same accuracy, therefore sacrificing time resolution in the rate of change of the velocity. It is this 1 degree of relative phase error versus time over the bandwidth of interest requirement that will be the most difficult to meet, and the DSN and the STDN have not yet determined what can actually be achieved. Pre- and post-experiment calibration of the station equipment involved in the experiment will be necessary, as well as some form of calibration signals recorded along with the actual data. The experimenters are confident that a number of that order can be achieved based on similar experiments that were performed at lunar distances using ALSEP signals.

As was described in previous Progress Report articles, the total bandwidth which the five signals from the multiprobe mission might occupy (four probes plus the bus) is 1.7 MHz. It is therefore necessary to have receivers which can pass a 2-MHz bandwidth, and open-loop receivers will be modified for this purpose. Analog recording is felt to be incapable of meeting the differential phase requirement of this experiment, and therefore digital recordings will be made in real-time. Three-bit quantization is required, and this, together with the 2-MHz bandwidth, means that the recorders will have to be able to operate at at least 12 megabits per second. These recorders represent the most significant implementation for the Pioneer Venus mission.

The experiment also requires that the mean rate fractional accuracy of the sampling be three parts in 10^{12} and that the jitter on the samples be held to 10 nanoseconds root-mean-square. Additionally, the calibration tones which will be inserted in real-time should have an absolute accuracy of three parts in 10^{12}. This requirement will be met by hydrogen masers set with cesium standards at the DSN stations and cesium standards at the STDN stations.

IV. Ground Station Configuration

Four stations will be equipped for the Pioneer Venus 1978 differential long baseline interferometry wind measurement experiment. Figure 2 is a block diagram of the configuration which will be implemented at the DSN 64-meter Goldstone and Canberra stations and the STDN 9-meter Santiago and Guam stations. The five spacecraft signals will be detected by low-noise amplifiers, which at the STDN stations will be parametric amplifiers with a total system temperature of 100°, and at the DSN stations ruby masers with a total system temperature of less than 24°. Some form of yet-to-be-determined calibration reference frequencies will be inserted at this point in order to calibrate out drifts in the system. The five signals plus calibration tones will then pass through the open-loop receivers, which will pass a 2-MHz bandwidth. Signals will then go through an analog-to-digital converter and sampler and onto the 12-megabit-per-second digital recorders. The recorders will be redundant at each of the stations. The recorders will be able to record the 12-megabit-per-second rate at 76 cm (30 inches) per second, and therefore 80 minutes of recording will be possible between tape changes.

There are two principal remaining open areas in the differential long baseline interferometry wind measurement experiment. First is the determination by the DSN and the STDN of what is the actual differential phase error achievable by the ground equipment at a given signal-to-noise ratio. The second area concerns the details of both the pre- and post-experiment and real-time calibration. The complexity and sophistication of the required calibration will be dictated by the DSN and the STDN determined error contributions introduced by each of the elements in the ground station configuration.

Acknowledgment

The author is indebted to T. L. Grant of the NASA Ames Research Center for use of material from unpublished correspondence.

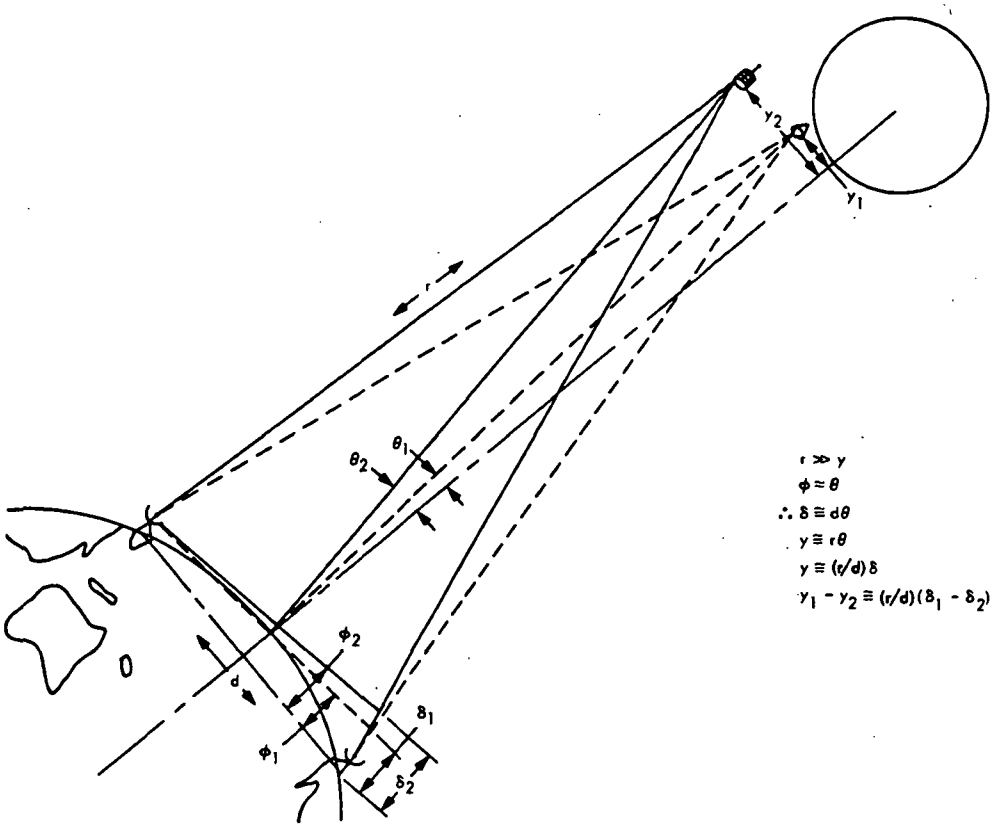

Fig. 1. Differential long baseline interferometry

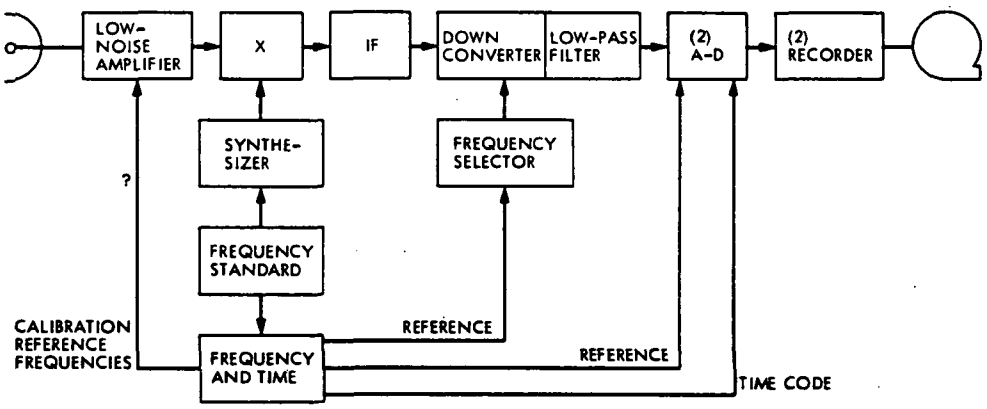

	LOW-NOISE AMPLIFIER	FREQUENCY STANDARD	ANTENNA
DSN STATIONS	24°	H-MASER	64-meter
STDN STATIONS	100°	CESIUM	9-meter

Fig. 2. Differential long baseline interferometry configuration for Pioneer Venus 1978 multiprobe wind measurement

Helios Mission Support

P. S. Goodwin
DSN Systems Engineering Office
W. G. Meeks, R. E. Morris, and S. E. Reed
Network Operations Office

Having observed its first year anniversary in orbit about the Sun, the Helios-1 spacecraft has performed satisfactorily. During its first year, valuable scientific data were obtained about the Sun and our solar system. As Helios 1 enters its second year of successful operation, preparations for the launch of Helios B are in their final stage.

I. Introduction

This is the seventh article in a series that discusses the Helios-1 flight support and Helios-B test and training activities by the Deep Space Network (DSN). The previous article (Ref. 1) reported the results of the Helios-1 second superior conjunction and second perihelion operations as well as Helios-B test results. This article covers Helios-1 cruise operations after the second perihelion through second aphelion. Also discussed are significant spacecraft anomalies, DSN tracking coverage, Helios DSN-STDN cross-support, and Helios-B test and training results. Helios-B launch is presently scheduled for 0534Z on January 15, 1976.

II. Mission Status and Operations

A. Helios-1 Second Aphelion Operations

One year of successful flight operations was completed by Helios 1 on 10 December 1975. The solar probe with its attendant scientific instruments has performed well, with the only exceptions being the initial problems encountered with Experiments 1 and 5 after launch (Ref. 2), and the recent Traveling-Wave Tube Amplifier-1 (TWTA-1) failure on 31 October 1974.

The failure of TWTA-1 manifested itself when an approximate 28-dB drop in the downlink signal level was observed during a spacecraft tracking pass over DSS 11 at Goldstone. The anomaly occurred at 1834 GMT, and to accelerate isolation, Goldstone DSS 12 support was requested by the DSN. Both stations verified identical downlink signal levels at −167 dBm. This level was below the telemetry threshold for 26-meter stations. The Helios Project declared a spacecraft emergency at 2040 GMT and requested 64-meter support for the impending Australian viewperiod. At 2121 GMT, the Project commanded the spacecraft from the failed high-power TWTA-1 mode (20 watts) to the 10-watt medium-power mode. This seemingly returned the probe back to a

normal operational mode. What had been thought of as normal operations was short-lived; a total TWTA-1 failure disrupted the DSS 43 downlink at 2253 GMT. The Project analyzed this failure, and the spacecraft was commanded to the low-power mode (0.5 watt) of operations at 2344 GMT. Once RF lock was achieved, the spacecraft was commanded to 16 bps, and normal operation in this mode was achieved.

With a satisfactory low-power downlink established, the Project continued to analyze the anomaly. The decision to switch to TWTA-2 medium-power mode was accomplished at 1610 GMT 1 November 1975. The spacecraft has operated normally since the switch to TWTA-2. Special DSN surveillance was provided by DSSs 11 and 63 until the spacecraft emergency was terminated during the DSS 11 track of the spacecraft on 1 November 1975 at 2130 GMT.

A Helios Project-sponsored TWTA Failure Analysis Review was conducted at JPL on 12–14 November 1975. The outcome of these meetings produced 14 action items plus 7 recommendations, directed to various Helios team members. The DSN was requested to continue to provide operational information on whether automatic gain control fluctuations are observable within the downlink after the switch to TWTA-2. The Failure Review also illustrated that further investigations will have to be conducted to reach a final conclusion about this TWTA failure.

B. Spaceflight Tracking and Data Network (STDN) Cross-Support

A DSN-STDN Helios Interface Agreement is now in preliminary form and will provide the necessary DSN-STDN Operations plans and interfaces which are required for Helios-1 and Helios-B STDN cross-support. The DSN-STDN cross-support configuration has also been defined, and 15 January 1976 is the designated target date to commence operations on a regular basis. Initially, only the Madrid STDN station will be available for support; the Goldstone STDN station, currently down for major rework, will become operational and provide Helios support after 1 March 1976.

There is one remaining interface problem concerning timing signal processing during tape recording playback. The problem has shown up as a time-tag offset between the Spacecraft Compatibility/Monitor Station, Merritt Island, Florida (STDN (MIL 71)) playback data records, produced from the Goldstone STDN tapes, and the Mission Control and Computing Center (MCCC) data records which were simultaneously recorded in real-time from DSS 12. The relative time-tag differences are a function of the Data Decoder Assembly (DDA) performance and the recorded bit rates. Indications are that the 1 pulse-per-second and 1000 pulse-per-second timing signals from the Time Code Translator to the DDA interface at STDN (MIL 71) are incorrect. A modified Time Code Translator has been shipped from JPL to STDN (MIL 71). When the timing problem is corrected, a test will be conducted to re-evaluate the STDN (MIL 71)-MCCC interface. The re-evaluation should be completed by the first week of January 1976.

C. Helios-B Test and Training

As we approach the launch of Helios B, DSN and Ground Data System testing is being successfully completed, and emphasis is shifting to Mission Operations System testing. Simulation System, Ground Data System, and DSN operational testing were completed during this reporting period. Only the DSN Configuration Verification Tests (CVTs) and the Mission Operations System tests remain before the final Operational Readiness Test and launch of the Helios-B spacecraft.

1. **Ground Data System Test.** One Ground Data System test was conducted on 5 December. This was a retest to validate a few items which failed to meet specifications during other U.S.-German Ground Data System tests. This test was successful, completing Ground Data System testing for Helios B.

2. **DSN Testing.** Network testing for initial acquisition with Australia Deep Space Stations 42 and 44 was completed by mid-November. Each station's operational crews participated in at least one Operational Verification Test; some in as many as three. Test scheduling conflicts with operational commitments, plus some doubt about the exact Helios-B launch date (the official date of 15 January 1976 being announced later), prevented the conduct of as many initial acquisition Operational Verification Tests with the crew selected to support launch activities as would have been desired. However, several Mission Operations System tests will exercise these procedures with the station launch support crew.

Step II maneuver Operational Verification Tests began with the first test at Goldstone DSS 12 on 7 November. As of this writing, six successful tests were conducted, four with DSS 12 and two with Goldstone DSS 11.

The plan for DSN support for the Helios-B Step II maneuver will differ slightly from that of Helios 1. This difference lies in the antenna polarization configuration prior to track. DSS 12 (prime) will configure for linear

horizontal polarization. DSS 11 will configure for linear vertical polarization. As the spacecraft's aspect angle is changed by attitude commands, the downlink signal polarization will go from linear horizontal to linear vertical. Thus the signal level received at DSS 12 will decrease while that at DSS 11 will increase. When the signal strength at DSS 11 surpasses that at DSS 12, the Project will transfer the uplink signal to DSS 11 for the remainder of the track. DSS 12 will reconfigure to linear vertical polarization for the remainder of the pass.

3. Mission Operations System Test and Training. Mission Operations System test and training activity continued at a predetermined pace throughout this reporting period. Three Inter-Team Training Tests, without DSN participation, were conducted in October. The DSN support began with two Combined Test and Training exercises in mid-November. Four Operational Demonstration Tests are scheduled from 25 November through 6 January 1976. These tests are designed to demonstrate the combined U.S.-German Networks ability to properly support all phases of the mission from launch to cruise. To date, all Mission Operations System testing has met objectives and has been considered successful.

The Operational Readiness Test is scheduled to take place on 12 January 1976. Launch for Helios B is now scheduled for 0534 GMT on 15 January 1976.

D. Actual Tracking Coverage Versus Scheduled Coverage

Helios-1 tracking coverage, along with Pioneer 10 and 11 tracking coverage, is now allocated on an equal priority basis for extended mission operations. This report covers a 56-day period for Helios-1 tracking coverage, from 17 October through 11 December 1975. Operations during this period consisted of normal cruise phase operations.

The total tracking coverage shared between the two Pioneers and Helios-1 spacecraft was 322 passes, equaling 2290 hours. The Helios allocation was approximately one-third of this total, or 99 passes and 699 hours of tracking coverage.

Due to Viking flight operations, the number of Helios-1 passes, the number of hours tracked, and the percentage of coverage supported during this period were all decreased from those of the last period. In conjunction with the other decreases, the duration of the average pass dropped from 7.6 hours to 7.0 hours. Inasmuch as the 26-meter subnet can support at a data rate of 2048 bps, its support increased 58 percent during this time frame; but the 64-meter network only supported Helios 1 for 183 hours, which was a drop of 71 percent from the last reporting period.

Helios-1 coverage should remain relatively stable at the level allocated during this period if the STDN support is provided as planned.

III. DSN System Performance for Helios

A. Command System

The command activity for Helios 1 continued to rise during this reporting period. The spacecraft's second perihelion occurring on 21 September 1975 (coverage lasting until 5 October) and the fact that this is the spacecraft's closest approach to Earth since launch phase have contributed to this increase in the spacecraft scientific data, and resulted in increased command activity. A total of 4669 spacecraft commands were processed through the Command System in the months of October and November. This is an increase of 1320 commands over the last period, and boosted the DSN cumulative command total to 23,301. Two Command System aborts were experienced in October; none in November. Both system aborts were attributed to operator error and involved no command equipment malfunctions. The Command System aborts cumulative total was increased to 5, with the overall abort total at 13 since spacecraft launch.

Command System downtime due to equipment problems during this reporting period was only 3.81 hours. There were an additional 1.95 hours lost due to high-speed data line outages. These figures show a significant decrease in downtime over the last period. Three transmitter failures were included in the 17 instances reported. Two of these occurred at Goldstone DSS 14 and one at Australia DSS 42.

B. Tracking System

The DSN Tracking System continued to provide very good support to the Helios Project during the second perihelion and aphelion. Several anomalies were detected during this period which required considerable support and analysis of the DSN Tracking System data.

What was later diagnosed as a Helios-1 spacecraft failure was noticed on 9 October. Ranging modulation on the downlink was just barely detectable, even at 64-meter stations operating with high power. At the time, it was believed that spacecraft ranging was lost forever. However, this was later determined to be associated with the spacecraft Traveling-Wave Tube Amplifier (TWTA-1)

failure of 31 October. Ranging returned after the switch to TWTA-2. To utilize Helios-1 spacecraft ranging, the modulator-exciter 1 must be configured to TWTA-2 by command from the Project. The first ranging in this manner was used on 9 November 1975. This operational procedure is being used and all spacecraft ranging commitments are being met.

The changeover from the special 2-MHz doppler bias for Helios-1 tracks to the standard 1-MHz bias occurred as scheduled on 11 October. Almost immediately, Australia DSS 43 and Spain DSS 63 began to show a very large doppler residual. The problem was traced in real-time to the Biased Doppler Detector Module of the Doppler Extractor. When the unit was tested at the Helios 1-MHz biased doppler frequency, a harmonic distortion showed up. Several replacement modules were tried. Some gave good doppler residuals while some did not. It was concluded that operation of the module so near its design specification is marginal and risky.

The Helios-B DSN Initial Acquisition Study, detailing DSN acquisition strategy at Australia DSS 42, was released on 10 November 1975. The report, prepared by the Network Operations Analyst for Tracking, was very comprehensive. Portions of the study will be published as part of the Helios-1 and Helios-B Network Operations Plan (Document 613-21), Revision B.

C. Telemetry System

Telemetry System analysis, as an on-going effort, was initiated during this reporting period as a result of the Traveling-Wave Tube Amplifier Failure Study Meeting. This action item was to analyze the Helios-1 AGC dropouts occurring after the switch to TWTA-2. The intent of the study which followed was to determine the presence of dropouts and to compare them with those dropouts previously found on TWTA-1. AGC strip-chart data were collected from several 26-meter stations which tracked Helios 1 from 14 to 22 November 1975. Examination of the data found that large cyclic variations in the AGC clouded any search of dropouts. Automatic Gain Control variations ranged from 2 dB to 5 dB in amplitude, with a period of approximately 20 seconds. This periodic variation seemed to have a secondary fluctuation (possibly AGC dropouts) having an amplitude of about 0.5 dB with an occasional 1 to 2 dB, and an occurrence frequency of approximately 30 per hour. Starting on 21 November, the periodic function decreased in amplitude, and by Pass 348 on 22 November (over DSS 11) the data showed that the periodic variation had gone. Remaining, however, was the secondary fluctuation which appeared to be AGC dropouts. (Figure 1 gives a picture of a typical strip-chart record.) The study is continuing.

There were only six Telemetry System Discrepancy Reports recorded during October, with an average mean-time-between-failures of 62 hours. The breakdown of November Discrepancy Reports is not yet available.

Helios-1 telecommunication link analysis for October and November is still in progress at this writing by the DSN Telemetry Analysis Group.

IV. Conclusions

Just prior to reaching its second aphelion, the Helios-1 spacecraft experienced its first major malfunction, a Traveling-Wave Tube Amplifier failure. Extra DSN tracking coverage and surveillance were given in support of this spacecraft emergency. Special recording and analysis of telemetry data were provided in support of the Helios Spacecraft Team's investigation of the anomaly.

A DSN-STDN Helios Interface Agreement was prepared during this reporting period which defines interfaces, configurations, and dates for STDN support of the Helios Project. Minor problems exist, but solutions are seen in the near future, and the plan has promise for providing future Helios telemetry coverage.

Helios-B launch preparations are progressing according to plan. Several test phases have been successfully completed during this reporting period. MOS testing will culminate with the Helios-B Operational Readiness Test scheduled for 12 January 1976. First opportunity for launch is 0534Z on 15 January 1976, and overall testing success has provided reassurance that all elements of the DSN are prepared for this opportunity.

With the launch of Helios B and increased activities of the Viking Project in preparation for the Mars encounter and landing, DSN coverage of Helios 1 is likely to decrease in favor of Helios B.

Acknowledgment

The authors wish to thank the following members of the Network Operations Analysis Group for their contribution of Periodic Network Performance Reports: R. Gillette, W. Tucker, R. Frampton, and B. Hoffman (Command); R. Allis and J. Hendricks (Telemetry); and A. Berman, R. Schlaifer, and L. Bright (Tracking).

References

1. Goodwin, P. S., et al., "Helios Mission Support," in *The Deep Space Network Progress Report 42-30*, pp. 65–69, Jet Propulsion Laboratory, Pasadena, California, Dec. 15, 1975.
2. Goodwin, P. S., "Helios Mission Support," in *The Deep Space Network Progress Report 42-26*, pp. 22–26, Jet Propulsion Laboratory, Pasadena, California, April 15, 1975.

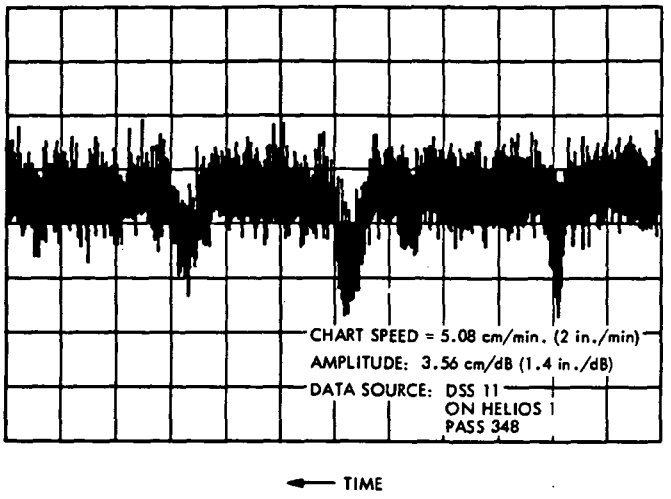

Fig. 1. Typical dropouts on Helios 1 downlink using TWT-2

Very Long Baseline Interferometry Covariance

J. W. Layland
Communications Systems Research Section

This article summarizes the methods and results of a covariance calculation for determination of DSN station location and clock parameters using very long baseline interferometry (VLBI) observation of Quasars. Errors of observation are assumed to arise from random (thermal) noise at the receiving antenna, and from errors in modeling the tropospheric delay. The critical error source is seen to be the troposphere: If errors in troposphere modeling are uncorrelated between observations, then 30–50 cm station-location determinations can be obtained with current modeling accuracies; if, however, these errors are correlated, then a factor-of-ten improvement in prediction of the tropospheric delay is needed to achieve this accuracy range.

I. Introduction

This article summarizes the methods and results of a covariance calculation for determination of DSN station location and clock parameters using VLBI observation of Quasars. A given observation set may currently include up to five stations and ten radio sources. Unknown parameters assumed to be simultaneously solved include the three-dimensional station location, two station clock parameters and the location of the Quasars. Both time delay and fringe frequency are observed. Errors of observation are assumed to arise from random (thermal) noise at the receiving antenna and from errors in modeling the tropospheric delay. The critical error source is seen to be the troposphere: If errors in troposphere modeling are uncorrelated between observations, then 30–50 cm station-location determinations can be obtained with current modeling accuracies; if, however, these errors are correlated, then a factor-of-ten improvement in prediction of the tropospheric delay is needed to achieve this accuracy range. Thermal noise, which is independent between observations, is comparatively insignificant relative to current troposphere errors if sufficient data are recorded for reliable detection of each Quasar (10^6 to 10^7 bits per observation).

II. Problem Model

The radio stars are located in space by their right ascension (RA) (α) and declination (dec) (δ). Tracking

stations are assumed to lie on the surface of a spherical Earth, and are hence also located by their α and δ coordinates and by a third coordinate, ρ, representing local variations from the mean Earth radius. (The geometry of the problem is described in Ref. 1.) Station clock offsets and clock rate offsets are assumed to be nominally zero but are treated as solved-for parameters in the covariance calculation. An observation is possible whenever any radio star is simultaneously in view of two or more of the tracking stations. A radio star is in view of a station whenever its elevation angle at that station is above some prespecified limit value. An observation set consists of a 24-hour interval during which the set of stars to be observed is rotated through the sky in steps of (typically) $\pi/100$ radians. At each step, any observation which is possible is added to the data set. No attempt is currently made to optimize the observing pattern or to eliminate conflicts in station usage. Some observations may occur simultaneously at three or more stations if their locations permit. The number of stations and their locations, and the number of stars and *their* locations are all variable data parameters. Most of the calculations to be described in the following have been performed using the three DSN stations at Goldstone, Calif., Canberra, Australia, and Madrid, Spain, for which no three-station observations are possible.

A VLBI observation results in noisy estimates of the time delay and doppler frequency difference between the observed Quasar noise signals at the two stations. Errors in the observation arise from thermal noise, from errors in modeling the propagation medium, and various other causes not to be considered here. Earth's troposphere consists of a thin shell over its surface. At Zenith elevation angle, this shell adds approximately 2 meters of additional delay to the path of a radio signal. As the elevation is lowered, the signal path travels through an increasingly longer segment of this tropospheric shell. If we let $\Delta\rho_z$ be the standard deviation of the error in modeling the tropospheric delay at zenith, and assume that this modeling error scales as the length of the in-troposphere signal path, then the standard deviation of the tropospheric delay model error at an elevation γ is

$$\Delta\rho_r = \Delta\rho_z/[A + \sin(\gamma)] \quad (1)$$

approximately, where $A \approx 0.02$. Furthermore, if we assume that any given observation is taken through a zone of troposphere which is reasonably layered and static, then the frequency error induced into the measurement results directly from Earth rotation, and changes in γ.

$$(d/dt)(\Delta\rho_r) = -\Delta\rho_z \cos\gamma \times (d/dt)(\gamma)/[A + \sin\gamma]^2 \quad (2)$$

The frequency error inferred in this way is clearly correlated with the delay error. Nothing in this formulation prevents us from assuming that different observations are taken through different zones of troposphere, and hence that the tropospheric modeling errors for each observation are independent. Current modeling capability is believed to be accurate to about 3% (Ref. 2), giving us

$$\Delta\rho_z \approx 2 \times 10^{-10} \text{ sec} \quad (3)$$

using only surface weather measurements at the tracking stations. It is expected that this figure can be reduced by a factor of 3–5 by using water vapor radiometer calibrations.

The effect of thermal noise depends upon the amount of data recorded and the time-and-frequency space spanned by the data-taking operation. Let us suppose that the spanned bandwidth of an observation is 20 MHz and the spanned time is 200 seconds. Suppose further that enough data are recorded to achieve a 6% resolution of the resultant ambiguity function; this can, for example, be achieved with 10^6 recorded bits from a 0.5 flux-unit ratio source observed by two 64-m antennas (Ref. 3). With this strategy, the standard deviation of the time delay measurement error is

$$\Delta\tau \approx 3 \times 10^{-9} \text{ sec} \quad (4)$$

Likewise, the frequency measurement error is $\Delta\nu_F = 3 \times 10^{-4}$ Hz. Assuming an S-band center frequency, and scaling by the Earth rotation rate for numerical convenience, we define

$$\Delta D \equiv \Delta\dot{\tau}/\omega_e \approx 2 \times 10^{-9} \text{ sec} \quad (5)$$

The three parameters $\Delta\rho_z$, $\Delta\tau$, and ΔD are variable data for the covariance calculations, with nominal values given by Eqs. (3)–(5). For any observation, the standard deviation of the error of observation is the rms of the thermal noise of the observation, and the tropospheric model error at each of the two stations. In the covariance calculation, all observations may be equally weighted, or weighted by the reciprocal of their variance. More sophisticated weightings dependent upon the errors projected into station locations could presumably improve the results.

Although the observed parameters are the Quasar noise signal time delay and doppler, the parameters of interest are the geometrical station and star locations. The time delay and doppler at a station, S_r, relative to a fictional

station at the Geo-Center, are defined in terms of the observing geometry by the two nonlinear equations:

$$\tau = Z_r \sin\delta + r_r \cos\delta \cos(\alpha_r - \alpha) + C_r + \dot{C}_r t_r \quad (6)$$

$$D = -r_r \cos\delta \sin(\alpha_r - \alpha) + \dot{C}_r \quad (7)$$

where (α, δ) are the Quasar RA and dec, (α_r, r_r, Z_r) the cylindrical coordinates of S_r at the time of observation, and C_r and $\dot{C}_r$ are the station clock offset and clock rate offset. Using R_e as the mean Earth radius, $Z_r = R_e(\rho_r \sin\delta_r)$ is the projection of the station position on Earth's spin axis, and $r_r = R_e \rho_r \cos\delta_r$ is its spin radius, or the projection on the equatorial plane, where $(\alpha_r, \delta_r, \rho_r)$ are the previously defined spherical coordinates of S_r. The observed time delay and doppler are of course the differences between the geocentric delays and dopplers at two observing stations.

The parameters of interest are derived from the observed parameters through a nonlinear least-squares estimation procedure. Details of such procedures in a radar context may be found in Ref. 4. The parameters to be solved for are station locations, rather than baselines, for ease in handling multiple baseline data. One real station, usually Goldstone, is used as reference for station coordinates, and one Quasar RA is also used as reference. The solution is assumed to be performed in a cylindrical coordinate system. The covariance of the errors resulting from the nonlinear least-squares estimation procedure is estimated by pretending that the problem is linear in the neighborhood of the solution point and applying the covariance result for a linear least-squares problem.

III. Summary of Calculations and Results

The first set of calculations, shown in Fig. 1, was intended to provide some direct comparison with the published results of Thomas and Fanselow (Ref. 5). These calculations do not include tropospheric errors. Two difficulties arise with this comparison. First, the coordinate systems used are not identical, so direct vector comparison is not convenient, although rss error-length comparison is. Second, the shape and size of the location error pattern has been observed to be a very strong function of the observation strategy. The observation set of Ref. 5 was at least partially optimized, whereas the observation set used here was wholly naive. The rss of the Madrid location error is shown in Fig. 1 for two observation sets for $\Delta\tau = 1 \times 10^{-9}$ second, and various ΔD. Other values of $\Delta\tau$ can be determined by appropriate scaling of both $\Delta\tau$ and ΔD. The poorer of the two observation sets shown consists of 118 observations of three stars located at (RA, dec) = (0., 0.8), (1., −0.05), (2.2, 0.1). The better observation set consists of 95 observations of these same three stars, plus 5 observations of a star located at (1.3, 1.5). The Madrid location error for both of these sets is noticeably poorer, with larger doppler errors than the Goldstone–Madrid rss baseline error as estimated from the results reported in Ref. 5. I believe at this time that this difference results wholly from the comparison difficulties cited above, principally the difference in observation strategy.

The remainder of the calculated errors to be presented include tropospheric effects, and most are computed at the nominal parameter values of Eqs. (3)–(5). For each calculated experiment, only the largest vector component of the station location error set is graphed; in most cases, this largest component is the Z-projection of the Canberra, Australia, station.

Figure 2 shows the one-sigma station location errors for a VLBI experiment involving the three DSN 64-meter stations and three radio stars at declinations of 0 and ±0.55 rn. The lower set of curves shows the expected resultant station location error for this particular experiment set. The upper set of curves shows the station location error scaled by the square root of the number of observations, which itself varies with elevation angle. This serves as a figure-of-merit for the observation pattern, and also indicates crudely what the deterioration in results would be if the errors of observation were correlated rather than independent. The improvement in results by weighting of the input data is also clear from this figure.

Some very low-elevation observations result in dramatic reduction of the location error indicated in Fig. 2. Upon inspection, it appears that these critical observations are the very few observations possible on the improbably long Madrid–Canberra baseline. With the exception of these observations, the best elevation limit would appear to be in the neighborhood of 10 to 12 degrees, and perhaps such a limit is appropriate on baselines with better visibility, with observations made at 3 to 4 degrees on the Madrid–Canberra baseline only.

Figure 3 is another look at the Canberra declination error for a VLBI experiment involving the three DSN 64-meter stations and three radio stars at declinations of 0 and ±0.35 rn. This smaller declination spread allows observations to be made on the Canberra–Madrid baseline at slightly higher elevations, which is, in turn, reflected in a different signature for location error vs. elevation. The

decreased spread in declination of the stars results in some decrease in the attainable station location resolution.

Looking at Fig. 2, there is some temptation to believe that the observations at or near the horizon are the most important to reducing the station location errors. Accordingly, a covariance calculation was performed which limited the elevation angle of at least one station of the pair to a band within 10 degrees of the selected horizon. This is shown in Fig. 4 for the same data as in Fig. 2. At best, only a slight benefit has accrued from this strategy at the higher horizon limit values, and a sizeable loss has accrued for low horizon limits.

Figure 5 shows the Canberra Z error obtained when the observations are perturbed by the tropospheric modeling error only. As in Fig. 2, the stars are located at 0 and ±0.55 rn. This approximates the situation obtained when a very large amount of data is recorded for each observation. The dependence upon the very low-elevation observations is enhanced in this figure.

There is at least an academic interest in knowing what improvements can be achieved by using additional tracking stations. This has been investigated for specific additions, with the results shown in Figs. 6 and 7. The stars observed are at declinations of 0 and ±0.55 rn. Figure 6 shows the Canberra Z error calculated for an experiment using the DSN plus the Spaceflight Tracking and Data Network (STDN) station in Hawaii. Figure 7 shows the Canberra Z error for a 4-station VLBI experiment including the former DSN station at Johannesburg, South Africa. Roughly speaking, the addition of a properly placed station to the DSN results in a sizeable improvement in the largest station location error component and a reduced need for low-elevation observations.

Figure 8 shows the effect of varying the thermal noise contribution to a VLBI experiment involving the three DSN stations and four radio stars at declinations of -0.5, 0, 0.17 and 0.8 radians. The noise contribution is indicated as number of bits recorded per station, although such variation can also result from varying source strengths. The point corresponding to the noise parameters of Eqs. (4) and (5), of 10^6 bits per observation, is shown for reference. Even if we assume optimistically that troposphere modeling errors are independent, we can operate with the total bit count in the neighborhood of 10^6 bits per observation, or 2×10^8 bits per total experiment—which fits on one computer tape—with little loss in resolution. If the assumption of independent troposphere errors is false, the thermal noise is still more strongly dominated by tropospheric effects; then, however, the desired 50-cm accuracy becomes unachievable. The truth should lie somewhere between these curves.

IV. Conclusions

Only a few conclusions arise naturally from the results presented here:

(1) Tropospheric modeling errors represent a dominant error source, which masks thermal receiver noise as long as enough data is recorded for detection.

(2) Independence between samples for the errors in the troposphere model is crucial to the delivery of meaningful results. If it is not achieved, then at least an order-of-magnitude improvement in model accuracy will be required.

(3) Observations on the Madrid–Canberra baseline are important when only the DSN stations are utilized.

V. Future Work

Several specific actions seem required to complete the analysis presented here:

(1) Add the capability to do directed observations as well as clock-driven observation sets.

(2) Add terms for ionospheric and other error sources.

(3) Experiment further with observations and weighting strategies.

These actions will be accomplished as time permits.

References

1. Williams, J. G., "Very Long Baseline Interferometry," JPL SPS 37-62, Vol. II, pp. 49–55, March 1970.

2. Madrid, G. A., et al., *Tracking System Analytical Calibration Activities for the MM'71 Mission*, JPL TR 32-1587, March 1974.

3. Hurd, W. J., "DSN Clock Synchronization by Maximum Likelihood VLBI," JPL TR 32-1526, Vol. X, DSN-PR, pp. 82–95, August 15, 1972.

4. Shapiro, I. I., *The Prediction of Ballistic Missile Trajectories from Radar Observations*, McGraw-Hill Book Co., New York, 1957.

5. Thomas, J. B., and Fanselow, J. L., *A Preliminary Covariance Analysis for the 14-63 Baseline*, IOM 3391.5-409, May 2, 1975 (JPL internal document).

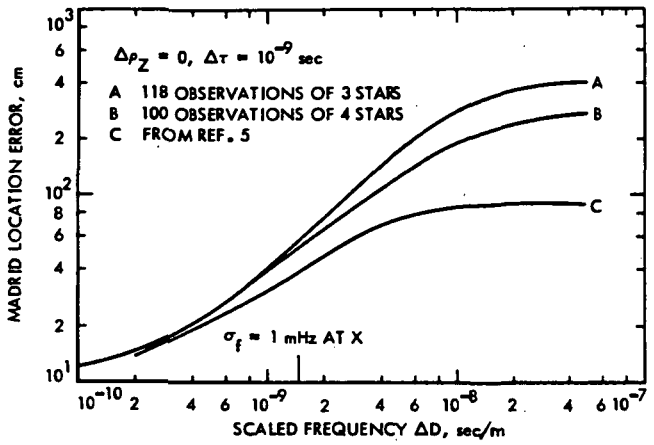

Fig. 1. Madrid location error vs. frequency error for fixed delay error, no troposphere

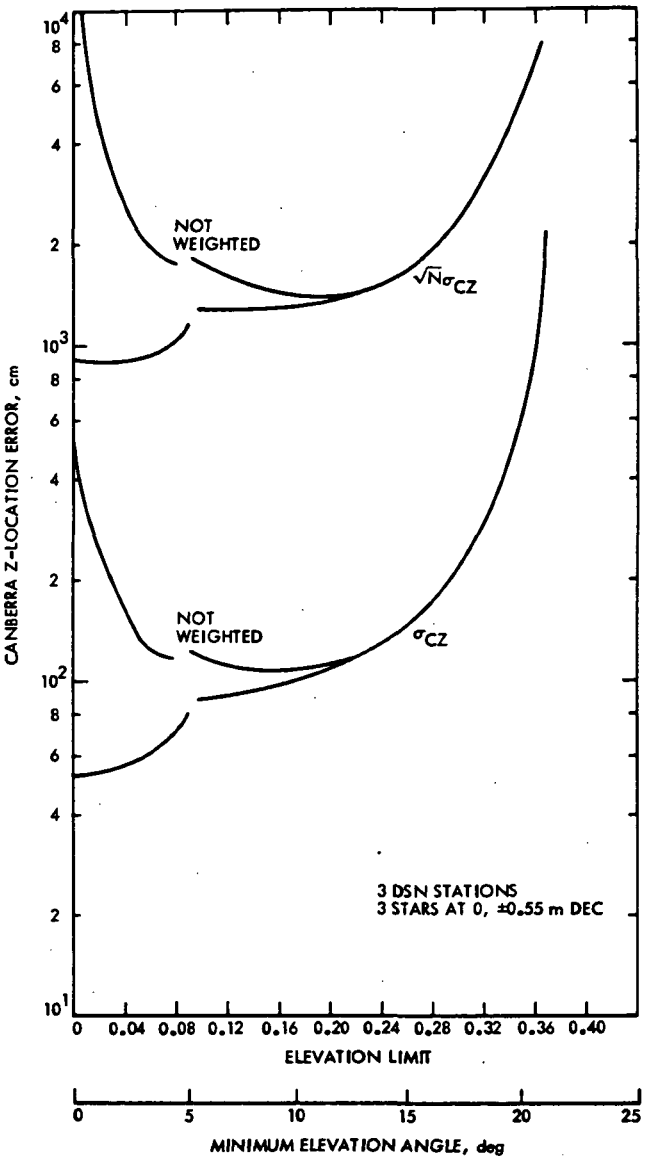

Fig. 2. Canberra location error vs. horizon with 3 DSN stations and 3 stars at 0 and ±0.55 m

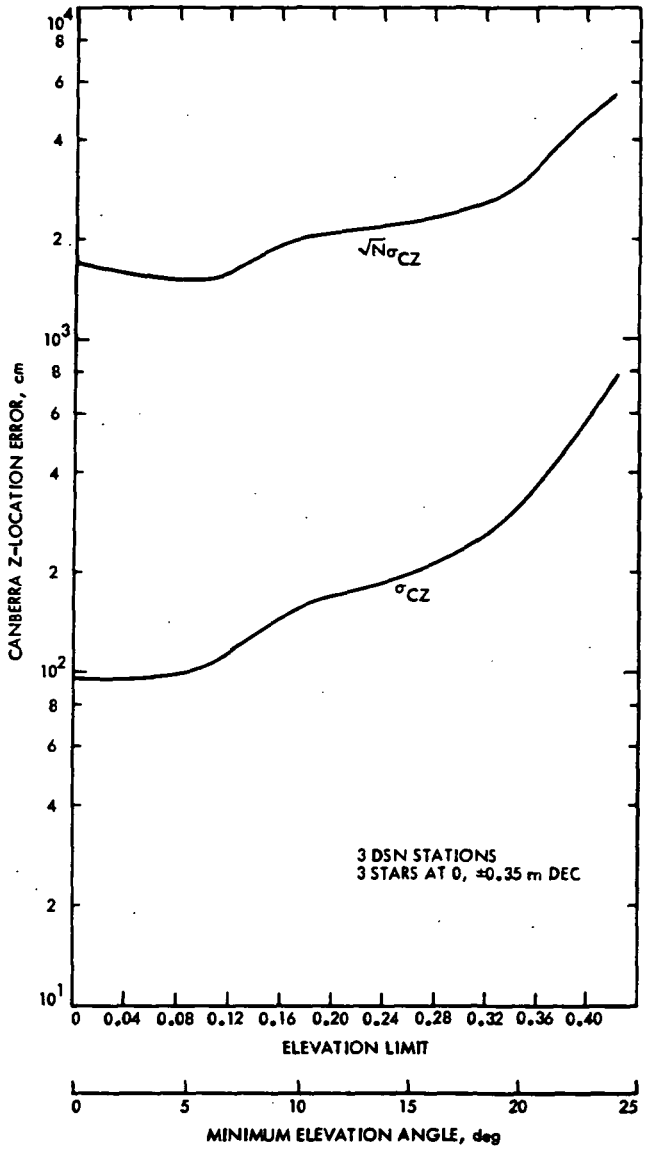

Fig. 3. Canberra location error vs. horizon with 3 DSN stations and 3 stars at 0 and ±0.35 m

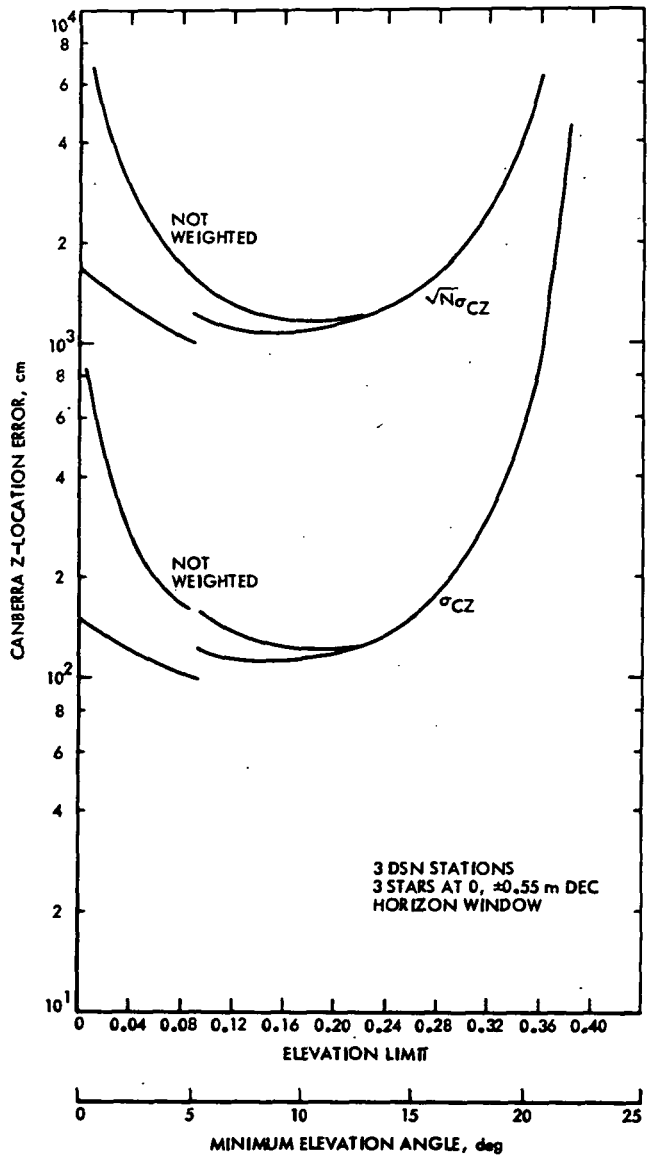

Fig. 4. Canberra location error with horizon window for 3 DSN stations and 3 stars

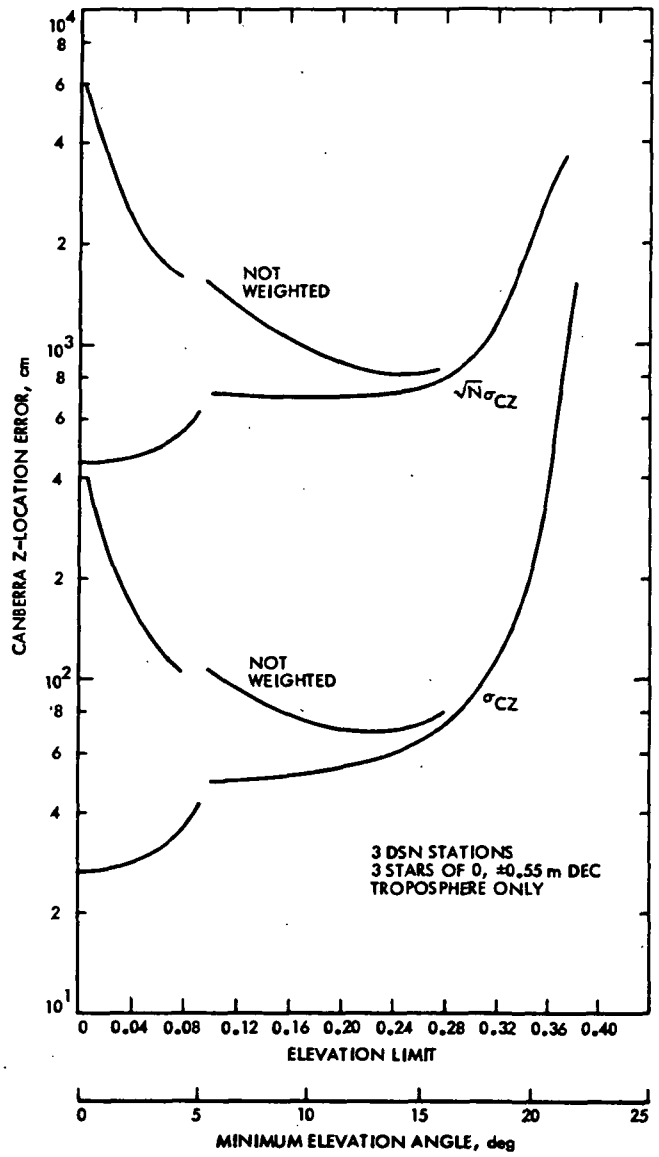

Fig. 5. Canberra location error vs. horizon for 3 DSN stations, 3 stars, troposphere noise only

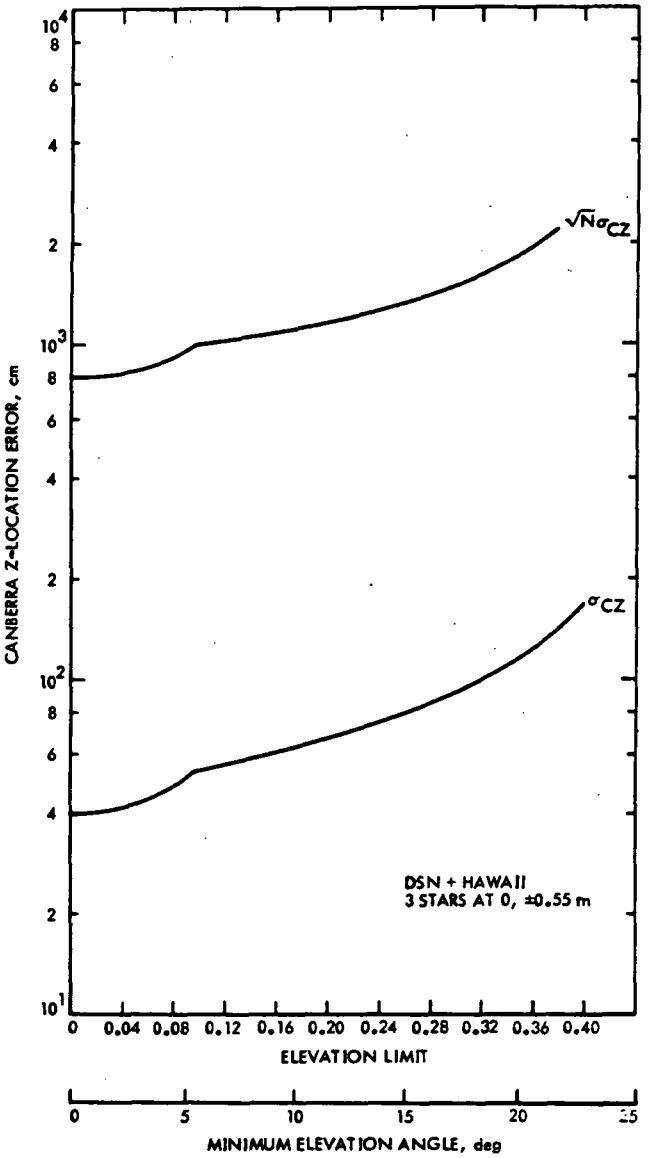

Fig. 6. Canberra location error for DSN plus Hawaii and 3 stars

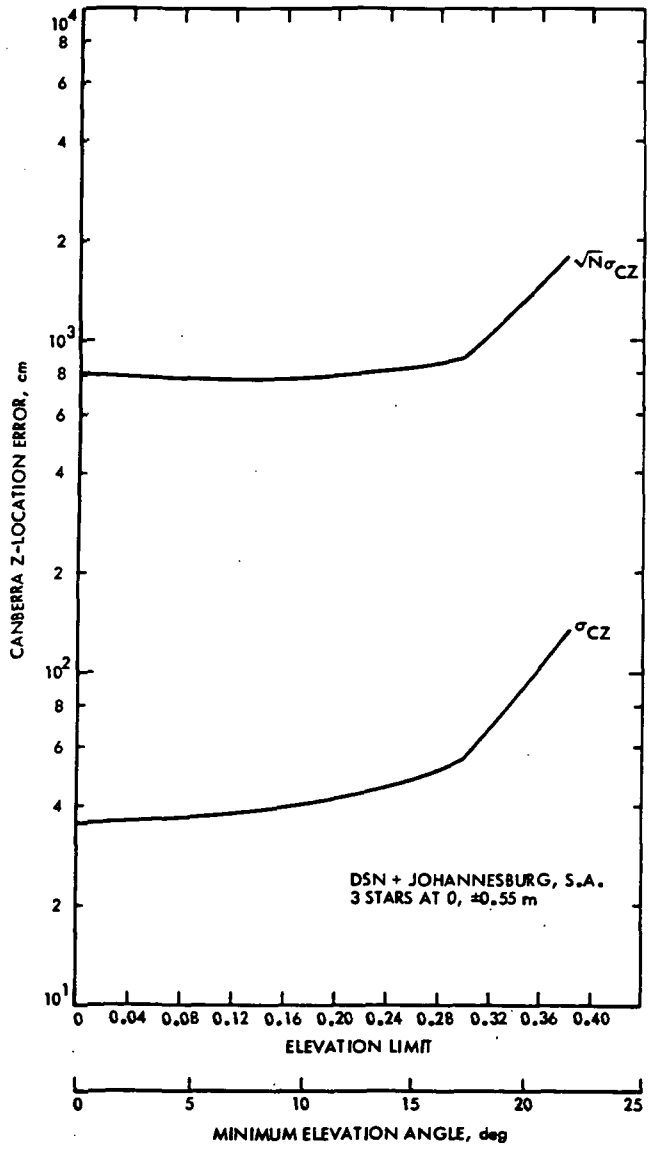

Fig. 7. Canberra location error for DSN plus Johannesburg, South Africa, and 3 stars

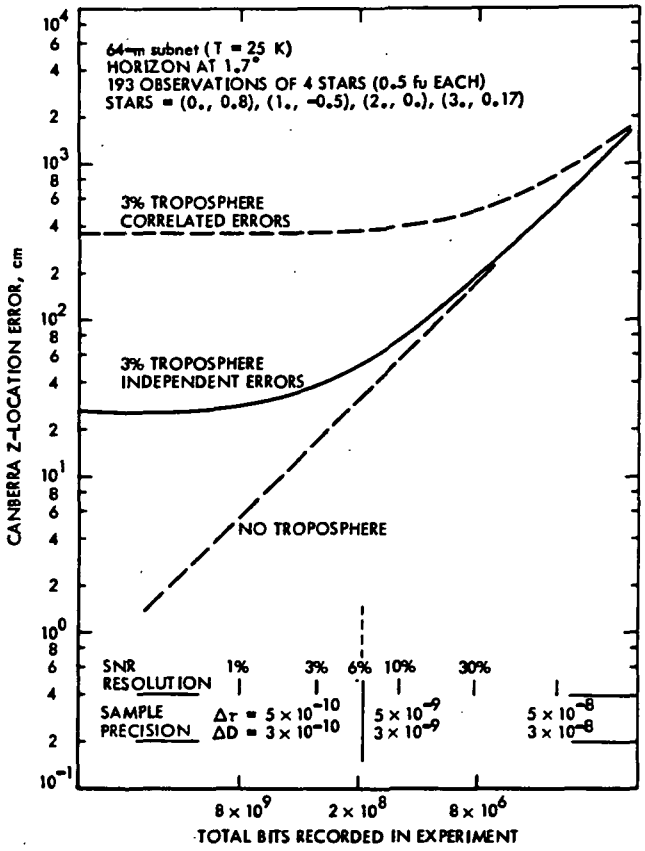

Fig. 8. Canberra location error vs. SNR for 3 DSN stations and 4 stars

Binary Sequential Ranging With Sine Waves

W. L. Martin and J. W. Layland
Communications Systems Research Section

Current ranging systems of the Deep Space Network estimate the range to a spacecraft by measuring the phase of a square-wave range code after its round-trip from station to spacecraft and back. Distortion of this waveform, in the form of phase-shifts of the harmonics of the square wave, can seriously degrade ranging accuracy. In this report, we show that such degradation can be largely eliminated by zonal filtering the range code to only its sine-wave fundamental at no net cost in ranging signal power or accuracy.

I. Introduction

Current ranging systems of the Deep Space Network estimate the distance from the DSN Tracking Stations to a spacecraft by transmitting to the spacecraft a square-wave range code of approximately 2 μs period, and then measuring the phase of this square wave as it is returned from the spacecraft relative to a time-delayed and doppler-shifted copy of transmitted code (Ref. 1). The ambiguity inherent in the periodicity of this square wave is resolved by using lower frequency codes which are coherent with it. There is currently some interest in increasing the precision to which this measurement is performed, or at least in ensuring that the degree of precision of which the system is theoretically capable is achieved in practice. This article proposes a minor change to existing-type ranging systems which can help to achieve that goal.

Figure 1 is an overall functional block diagram of the ranging operation. The delay through the station alone is measured via the zero-delay or calibration subsystem. The delay through the spacecraft transponder is separately measured prior to flight. The net delay through the transmission medium, from which is inferred the true range, is estimated as the delay value remaining when the station and spacecraft delays are subtracted from the overall measured delay. We are in all cases not measuring the delay per se, but are instead measuring the phase of the square-wave range code. The exact relationship between the measured phase of any nonsinusoidal waveform and its "delay" can be somewhat fuzzy. This fuzziness results if waveform dispersion occurs anywhere along the signal path. We can combat it by using only a sine wave for the highest frequency code component, or by performing all measurements using only the sine wave fundamental of this component. In the following, we review some of the ramifications of this possible change to the binary coded sequential ranging systems.

II. Additive Noise Effects

Let us presume that we wish to use only the fundamental sine wave component of a range code for delay measurement. The first thing to determine is what effect

this will have on the measurement errors due to noise. The signal received, $r(t)$, is assumed to be an ideal square wave, of power s, and delay-shift θ, plus a White noise component $n(t)$ with one-sided spectral density N_0. The reference signal is an ideal unit-amplitude (unit-energy) square wave, and correlation detection is employed at two reference phases to estimate θ. The two correlations obtained are

$$X = \int_0^t SQ_T(\eta) \cdot r(\eta) d\eta$$
$$Y = \int_0^t SQ_T\left(\eta - \frac{T}{2}\right) \cdot r(\eta) d\eta \tag{1}$$

In Eq. 1, t is the measuring integration time and T is the bit period of the code. The expected value of X and Y has peak value $\sqrt{s} \cdot t$ and depends upon θ as shown in Fig. 2. The variance of both X and Y is $N_0 \cdot \frac{t}{2}$. The estimated delay, $\hat{\theta}$ is given by

$$\hat{\theta} = \frac{Y}{|X| + |Y|} \cdot \frac{T}{2} \tag{2}$$

whenever X is positive. Following Goldstein (Ref. 1) we use

$$\sigma_\theta^2 \approx \left(\frac{\partial \theta}{\partial \hat{x}}\right)^2 \sigma_x^2 + \left(\frac{\partial \theta}{\partial \hat{y}}\right)^2 \sigma_y^2 \tag{3}$$

which implies

$$\sigma_\theta^2 \approx \frac{N_0}{2} t \left(\frac{T}{2\sqrt{st}}\right)^2 \left\{\left(1 - \frac{|Y|}{|X| + |Y|}\right)^2 + \left(\frac{-Y \operatorname{sgn} X}{|X| + |Y|}\right)^2\right\}$$
$$\sigma_\theta^2 \leq \frac{N_0 T^2}{8 s t}$$
$$\sigma_\theta^2 \geq \frac{N_0 T^2}{16 s t} \tag{4}$$

The estimator variance is at its maximum when either X or Y is zero, and at its minimum when $|X| = |Y|$. Equation 4 will be our reference against which the variance of the estimated phase of a modified range code will be measured.

As an alternate technique, let us use unit-energy sinusoids for the reference signals. The two correlations obtained are

$$X' = \int_0^t \sqrt{2} \sin\left(\frac{\pi}{T}\eta\right) r(\eta) d\eta$$
$$Y' = \int_0^t \sqrt{2} \cos\left(\frac{\pi}{T}\eta\right) r(\eta) d\eta \tag{5}$$

As before, the variance of both X' and Y' is $N_0 \cdot t/2$. The mean values of X' and Y' will be determined by expanding the received square-wave range code in its Fourier series form.

$$r(\eta) = n(\eta) + \sqrt{s} \cdot \frac{4}{\pi} \cdot \sum_{i \text{ odd}} \frac{1}{i} \sin\left[i \cdot \frac{\pi}{T} \cdot (\eta + \theta)\right] \tag{6}$$

The two correlations are then approximately given by

$$X' = \sqrt{2s} \cdot t \cdot \frac{2}{\pi} \cdot \cos\left(\frac{\pi}{T} \cdot \theta\right) + n_x$$
$$Y' = \sqrt{2s} \cdot t \cdot \frac{2}{\pi} \cdot \sin\left(\frac{\pi}{T} \cdot \theta\right) + n_y \tag{7}$$

The estimate of θ is now given by

$$\theta = \frac{T}{\pi} \arctan(Y,X)$$

Using the same technique as before in Eq. 2-4, we find

$$\sigma_\theta^2 = \frac{N_0}{2} \cdot t \cdot \left(\frac{T}{\pi}\right)^2 \Big/ \left[\left(\sqrt{2s}\, t \cdot \frac{2}{\pi}\right)^2 (\sin^2\theta + \cos^2\theta)\right]$$
$$\sigma_\theta^2 = \frac{N_0 T^2}{16 s t} \tag{8}$$

This surprising result indicates that by using only the fundamental component of the received range code, we achieve the same performance with respect to additive noise that we could achieve with the entire square wave, and we achieve such performance irrespective of the actual delay between the received and reference code waveforms. Clearly the harmonics of the square-wave range code are of no benefit to us for conventional ranging operation. They can in fact be detrimental as we shall see shortly.

III. Harmonic Phase-Shift Effects

To understand the effects that harmonic phase shifts, or waveform dispersion, have upon the ranging operation, we need to refer to the overall system diagram of Fig. 1. The calibration-subsystem in the station is wideband and as close to delay-free as possible. As a result, when range measurement is performed in-station to calibrate station equipment delays, it is almost entirely the station equipment, the receiver, the exciter, modulator, and transmitter, and the ranging subsystem itself that establishes the details of the range code waveform, and its harmonic structure. The spacecraft transponder, on the other hand, has a limited bandwidth that passes only the fundamental and its third harmonic; in current transponders, the third harmonic is somewhat attenuated, although not phase-shifted.

The range to the spacecraft is measured as follows: first, the station delay is measured, with all station equipment in the configuration which will be used with the spacecraft measurement. Next, the delay is measured through the Earth-to-spacecraft link and the spacecraft transponder, and then the station delay and the previously measured spacecraft delay are subtracted from this value. (See Ref. 2 for more detail.) For error-accounting, the calibration subsystem is directly in the range-measurement path. We envision two cases: first, where the station equipment generates and processes a perfect square wave range code, and second, where some station equipment has changed in such a way that the harmonics of the range code are phase-shifted and/or attenuated relative to the fundamental. For both cases, the spacecraft transponder passes first and third harmonics of the range code with no relative phase shift, although with some, say 3 dB, attenuation of the third harmonic. Additive noise will be ignored.

The range code received at the ranging subsystem via the station's receiver may be represented as

$$r(t) = \frac{4}{\pi}\left\{\sin\left(\frac{\pi}{T}t\right) + \frac{\alpha_3}{3}\sin\left(3\frac{\pi}{T}\cdot t + \theta_3\right) + \frac{\alpha_5}{5}\sin\left(5\frac{\pi}{T}\cdot t + \theta_5\right) + \cdots\right\} \tag{9}$$

where we denote by α_k/k, the gain, and θ_k, the phase shift of the kth harmonic relative to the first. The two correlation values used to compute the delay value are

$$\bar{X}(\tau) = C\cdot\left\{\cos\left(\frac{\pi}{T}\tau\right) + \sum_{\substack{k=3\\ odd}}^{\infty}\frac{\alpha_k}{k^2}\cos\left(k\cdot\frac{\pi}{T}\cdot\tau + \theta_k\right)\right\}$$

$$Y(\eta) = X(\eta - T/2) \tag{10}$$

During most of its operation, the local code reference of the ranging subsystem is constrained to track so that $X(\tau) = Y(\tau)$, and the real delay measurement is contained within the physical shifts accumulated by the local coder. This forces

$$0 \equiv X(\tau) - X(\tau - T/2)$$

$$0 \equiv \left\{\cos\left(\frac{\pi}{T}\cdot\tau\right) - \cos\left(\frac{\pi}{T}\cdot\tau - \frac{\pi}{2}\right)\right\} + \sum_{\substack{k=3\\ odd}}^{\infty}\frac{\alpha_k}{k^2}\left\{\cos\left(k\cdot\frac{\pi}{T}\cdot\tau + \theta_k\right) - \cos\left(k\cdot\frac{\pi}{T}\cdot\tau + \theta_k - \frac{\pi}{2}\right)\right\} \tag{11}$$

The true tracking point is at $\tau = T/4$. If we define η as the offset from the true tracking point, i.e., $\eta = \tau - T/4$, change variables in Eq. (11), and manipulate it with trigonometric identities, the tracking point is defined by:

$$0 \equiv \sin\left(\frac{\pi}{4}\right)\cdot\sin\left(\frac{\pi}{T}\eta\right) + \sum_{k=3,odd}^{\infty}\frac{\alpha_k}{k_2}\sin\left(k\frac{\pi}{4}\right)\cdot\sin\left(k\cdot\frac{\pi}{T}\eta + \theta_k\right) \tag{12}$$

or

$$0 \equiv \sin\left(\frac{\pi}{4}\right)\cdot\sin\left(\frac{\pi}{T}\eta\right) + \sum_{k=3,odd}^{\infty}\frac{\alpha_k}{k^2}\sin\left(k\frac{\pi}{4}\right)\cdot\left\{\sin\left(k\cdot\frac{\pi}{T}\eta\right)\cdot\cos(\theta_k) + \cos\left(k\cdot\frac{\pi}{T}\eta\right)\cdot\sin(\theta_k)\right\}$$

Denoting by $\lceil x\rceil$, the greatest integer less than x, we can represent $\sin\left(k\frac{\pi}{4}\right) = \sin\left(\frac{\pi}{4}\right)\cdot(-1)^{\lceil k/4\rceil}$ for all odd k. Let us also assume that η is small; that for any offset which is of genuine interest with respect to ranging, we can approximate

$$\sin\left(k\cdot\frac{\pi}{T}\cdot\eta\right) \approx k\cdot\frac{\pi}{T}\eta$$

$$\cos\left(k\cdot\frac{\pi}{T}\cdot\eta\right) \approx 1 \tag{13}$$

Then the offset from the true tracking position is given by

$$\eta \approx -\frac{T}{\pi}\frac{\sum \frac{\alpha_k}{k^2}(-1)^{\lceil k/4 \rceil}\sin\theta_k}{1+\sum \frac{\alpha_k}{k}(-1)^{\lceil k/4 \rceil}\cos\theta_k} \qquad (14)$$

Note that there are two obvious conditions which can make $\eta = 0$: if either $\theta_k = 0$, for all k, or if $\alpha_k = 0$, for all $k \geq 3$. In both cases, the delay measured by the ranging system is the delay suffered by the range code fundamental and there is no fuzziness in the meaning of that delay. The second case corresponds to performing the range measurement with the code fundamental only.

The details of the error in the ranging operation can now be determined. If the station equipment generates and processes a perfect square wave, then there is no error caused by the code harmonics in measuring station delays, and $\eta = 0$. Similarly, even though the transponder filters out harmonics so that $\alpha_k \simeq 0$ for $k \geq 5$, and $\alpha_3 < 1$, we still have $\theta_3 = 0$ so that $\eta = 0$ in measuring delays through the spacecraft also. If we have also a calibration of the spacecraft delays using a perfect square wave, the net error in measuring range to that spacecraft is nil.

In an alternate scenario, let us assume that some harmonic distortion arises somewhere within the complex equipment of the tracking station. The delay measured for the ground system then suffers an error which is well described by Eq. (14). Let β_3 be the gain factor of the spacecraft alone at the third harmonic of the high frequency range code, and use $\beta_k = 0$ for $k \geq 5$ to indicate that the transponder does not pass the fifth and higher harmonics. Assume that the spacecraft adds no phase shift to the third harmonic, and let α_k, θ_k as before denote station equipment amplitude and phase characteristics. Then the delays measured through the spacecraft are in error by

$$\eta_{s/c} = -\frac{T}{\pi}\frac{\frac{1}{9}\alpha_3\beta_3\sin\theta_3}{1+\frac{1}{3}\alpha_3\beta_3\cos\theta_3} \qquad (15)$$

And if we assume that the spacecraft delay itself was calibrated with a reference station without distortion, the net error in measuring spacecraft range is $\eta_{s/c} - \eta$, or

$$RE = \frac{T}{\pi}\left\{\frac{\sum \frac{\alpha_k}{k^2}(-1)^{\lceil k/4 \rceil}\sin\theta_k}{1+\sum \frac{\alpha_k}{k}(-1)^{\lceil k/4 \rceil}\cos\theta_k} - \frac{\frac{1}{9}\alpha_3\beta_3\sin\theta_3}{1+\frac{1}{3}\alpha_3\beta_3\cos\theta_3}\right\} \qquad (16)$$

For a concrete example, consider a station system which has $\alpha_3 = \alpha_5 = 1$, $\alpha_k = 0$ for $k \geq 7$, and has $\theta_3 = 10$ deg, $\theta_5 = -30$ deg, and a spacecraft for which $\beta_3 = 1/2$. Here, the resultant range error is

$$RE = \frac{T}{\pi} \times \left\{\frac{\frac{1}{9}\sin 10\,\text{deg} + \frac{1}{25}\sin 30\,\text{deg}}{1+\frac{1}{3}\cos 10\,\text{deg} - \frac{1}{5}\cos 30\,\text{deg}} - \frac{\frac{1}{18}\sin 10\,\text{deg}}{1+\frac{1}{6}\cos 10\,\text{deg}}\right\} \qquad (17)$$

$$RE = .008 * T$$

In current ranging systems, where T is approximately one microsecond, this resultant error is eight nanoseconds, or approximately 2-1/2 meters. Larger errors than this are quite plausible, considering the amount of equipment in the ranging signal path!

IV. Ameliorating the Waveform Dispersion Effects

There are a number of alternative things which can be done in response to the magnitude of the effects evidenced in Eq. (16). First of all, if the overall error budget is of the order of 10 to 20 meters, it can simply be ignored, as reasonable care with the equipment can restrain RE well below this value. If, however, we are asking how accurate the spacecraft range can be measured, then more care must be used. As a second approach, we could design and control the parameters of all tracking stations of the Network so that phase-shifts imposed upon the harmonics of range code by the station equipment are held within

prespecified tolerances. The actual phase-shift tolerances allowable may be determined from Eq. (16) once the allowable range-error is established. A third alternative is to make the calibration subsystem itself mimic the transfer characteristics of the spacecraft transponder. In this way, the harmonic structure of the range code arriving at the ranging subsystem via either the spacecraft or the calibration subsystem is identical, and the range error equation analogous to Eq. (16) is likewise ideally zero. Considering component tolerances, and in particular, variations between spacecraft transponders, there would in fact be some slight residual range error resulting.

The fourth alternative is that one which is being promulgated by this report, namely the use of the fundamental sine wave component only of the range code. This can be accomplished by inserting an appropriate filter anywhere on the signal path within the station equipment that is common to both the spacecraft and calibration measurements, or by use of a sine-wave reference waveform as was analyzed in part II. Use of the sine-wave reference seems impractical from the standpoint of available equipment. Appropriate filtering of the received signal on the path from the receiver to the ranging subsystem can achieve the identical result. Filtering at the receive-end of the signal path will remove all coherent harmonics of the range code, not only those generated intentionally as part of the square-wave range code, but also those which arise from nonlinearities along the signal path. Filtering could also be applied to the uplink range code between the ranging subsystem and the modulator. If the average uplink modulation index is maintained, and no peak deviation limit is imposed, the ranging signal power is in fact slightly increased. Filtering of the uplink, however, does not eliminate the desirability of further filtering of the downlink, since nonlinearities in the ranging path beyond the uplink filter can still inject harmonics at strange phase-angles. The filter (or filters) are directly in the group-delay path of the ranging measurement and their delay stability is critical to range accuracy, even though the exact delay value is not.

For the experiments to be described, the filter was inserted in the 10-MHz signal line from the receiver as shown in Fig. 3. This point is preferable to others since it is the last opportunity to remove distortion prior to correlation and therefore serves to offset any degradation occurring elsewhere in the system. In principle, a correlator using a pure sine-wave reference would be superior. However, because the present systems are all mechanized using digital techniques the external filter was selected as the most practical approach.

The characteristics of the filter needed to be uniform across the band pass with a linear phase-frequency slope so as to ensure maximum group delay stability. However, once the band edge was reached, a rapid attenuation was desired to eliminate unwanted harmonics. It was decided to design for a cutoff frequency of ± 1 MHz and a rejection of at least 60 dB in the stop band beyond ± 1.5 MHz where the offending harmonics are located.

A schematic diagram of the filter is shown in Figure 4 (component values will be found in Table 1). An elliptic function design was selected as providing the best band-pass relative to band-stop characteristics. While ripples exist both within and without the band pass, their magnitude is sufficiently small that the performance of the filter should not be affected. Moreover, the steep attenuation characteristic obtainable with this design makes its use in this application attractive.

The basic design consists of a low-pass filter, 1 MHz in bandwidth which has been translated to 10 MHz by resonating elements. Because certain, identifiable, components determine the attenuation characteristics while others control center frequency and symmetry, it is important to select these critical components carefully.

For example, L1 to L4 and C5 to C11 comprise the basic low-pass filter and therefore determine the band-pass/band-stop characteristics as well as the transition between. Because the placement of poles and zeros is critical to this design, it is important that actual component values be selected to accurately reflect the computed numbers. The procedure followed with inductors was to adjust the number of turns with the aid of an inductance bridge until the closest possible value was obtained. Using this method, inductances within one percent of the calculated values could be realized. With the capacitors, up to three were connected in parallel to bring the capacitance to within one percent of the computed value.

Because of the high performance requirements and the critical characteristics of this filter noted earlier, it was necessary to utilize high Q circuit components. Glass capacitors were used throughout and the torroidal inductors were wound with the largest size wire which could reasonably be fitted on the ferrite cores. Measured Q's for the finished inductors were in excess of 100.

After collecting the components comprising the low-pass portion of the filter, it was necessary to translate the entire spectrum to a 10-MHz center frequency for use

with the ranging system. This was accomplished with C1 to C4 and L5 to L11. Since the only purpose of these components is to adjust the center frequency, conformance with calculated values is less important. The procedure followed was to pick an element within the low-pass filter and adjust the translating component so that the pair was resonant at 10 MHz. Thus C1 was trimmed until L1 and C1 were a series tuned circuit at 10 MHz. Likewise, turns were changed on L8 until it formed a parallel tuned circuit with C8. In general, each of the 11 tuned circuits (Ln, Cn) comprising the filter was adjusted individually.

The element pairs were then assembled into a specially made copper module as shown in Figure 5. Because of the high attenuation required, it was deemed advisable to separate the various sections into four compartments to minimize leakage. An effort was made to place the components in the center of the cell to reduce stray capacitance; the module itself served as circuit ground.

Following assembly, tests were made to determine the bandwidth of the filter, and group delay and phase delay characteristics. Figure 6 is a photograph of the amplitude response as measured with a General Radio model 1711 Sweep Generator and associated Model 1714 Display Unit. A sweep speed of 500 kHz per centimeter was used so as to provide maximum resolution in the frequency band from 8 through 12 MHz.

The response appears to be reasonably symmetrical about the 10-MHz center frequency particularly at ± 500 kHz where the first range code sidebands are located. Beyond approximately ± 900 kHz the filter begins to reduce the signal rapidly. At ± 1.5 MHz where the third range code harmonic is situated, the attenuation exceeds 60 dB. While there is a slight asymmetry on the high frequency side of the curve, between about 1.2 and 1.4 MHz, it is considered unimportant since the design goal had been met at the ± 1.5 MHz frequencies.

Figure 7 shows the phase delay over the same band of frequencies. Because of the measurement technique, the figure appears to have a sawtooth pattern. In fact, the heavier lines, sloping down to the right, should be treated as a single continuous, unsegmented line. Ideally, the phase change should be linear with varying frequency. Practically, this is difficult to obtain in a multipole filter such as this one. In this case, the phase-frequency relationship is reasonably linear over a range sufficient to contain the first range code sidebands. Since the code spectrum is discrete, nonlinearities occurring beyond 10 MHz ± 500 kHz should not materially affect the group delay.

Filter group delay appears in Figure 8. Note that the filter has an insertion delay of approximately 600 nanoseconds at 10 MHz. This increases to about 700 nanoseconds for the lower range code sideband (9.5 MHz) and to about 900 nanoseconds for the upper sideband (10.5 MHz). The average sideband delay compares well with the 808 nanosecond delay actually measured by the ranging system.

At this point the intrinsic problem with filters is obvious. Where large attenuations and steep transitions are required, a design meeting these conditions will also include a rather substantial group delay. With large delays come the concomitant problems with stability which may introduce errors considerably in excess of those sought to be eliminated. The underlying problem, of course, is one of trying to resolve a phase comparison to approximately 0.1 percent. Clearly, this defect could be substantially reduced by widening the bandwidths and raising the code frequency. However, since the intent here was merely to investigate the feasibility of a filter as a solution to the harmonic phase shift problem, little attention was devoted to stabilizing the unit for field operations.

V. Ranging Test Results

To test the effectiveness of the filter as well as the hypothesis that much of the ranging inaccuracy is caused by nonuniform phase shifts in the higher order range code harmonics, the system was connected as shown in Figure 3. First, the system delay was measured using a zero delay device. Second, a Mariner Venus-Mercury transponder was substituted for the zero delay device and the total delay remeasured. The difference between this and the prior measurement represents the transponder delay. Thereafter, the phase modulator in the ground exciter system was changed and the entire procedure repeated. In principle, the transponder delay should remain unchanged. However, because of the way in which the modulator and spacecraft ranging channel act upon the higher order range code harmonics, the transponder delay undergoes an apparent change. Installation of the filter served to remove the range code harmonics so that correlation is only with the code fundamental.

Results of these tests are shown in Figure 9. Transponder delays were measured at 1-dB and 9-dB carrier suppression. Two ground system modulators were employed. Number 2002 exhibited fairly normal operating characteristics. However, number 2034, while allegedly meeting Network test specifications, had been observed to exhibit unusual behavior such as low sensitivity.

It can be seen from the figure that the transponder delay varies greatly as the modulation index is changed on number 2034. This distortion is substantially greater at low modulation levels than it is at high levels. Note that with the filter installed, the difference is reduced to less than one-third of its former value at small modulation angles. As the carrier suppression is increased to 9 dB the differences have disappeared within the uncertainty of the measurement as indicated by the brackets. However, while making a dramatic improvement, the effect is still present. Since it seems unlikely that any higher order harmonics are passing through the filter, the explanation must lie elsewhere. At this juncture it is uncertain why divergence exists and further tests will be necessary to develop a better understanding of the causal relationships.

VI. Summary and Future Plans

Our preliminary analysis, described herein, has confirmed the existence of a real, or at least a potential, limitation to ranging accuracy resulting from phase shifts of the higher harmonics of the square-wave range code. Experimental and analytical evidence has been developed which shows that this limitation can be largely eliminated by filtering the range code to its fundamental component only at the receiver.

Additional testing should be performed to more exactly quantify the improvement to be obtained in this manner. Also, since that filter is now itself a critical component of the station's group delay path, the stability of that filter under temperature and other environmental variables must be determined.

Acknowledgment

Experimental results reported herein were obtained with the able and gracious assistance of Mr. D. L. Brunn, and the staff of the Telecommunications Development Laboratory.

References

1. Goldstein, R. M., "Ranging with Sequential Components," JPL SPS-37-52, Vol. II, pp. 48-49, July 31, 1968.

2. Otoshi, T. Y. and Batelaan, P. D., "S/X Band Experiment: Zero Delay Device," JPL *DSN Progress Report* 32-1526, Vol. XIV, pp. 73-80, April 15, 1973.

Table 1. Filter components

Component designation	Computed value	Measured value	Measured Q
L1	5.11 μH	4.95 μH	185
L2	4.17 μH	4.27 μH	195
L3	5.09 μH	4.90 μH	195
L4	4.75 μH	4.60 μH	195
L5	0.792 μH	0.790 μH	185
L6	0.259 μH	0.262 μH	185
L7	0.395 μH	0.400 μH	175
L8	0.157 μH	0.157 μH	140
L9	0.115 μH	0.116 μH	130
L10	0.137 μH	0.136 μH	130
L11	0.127 μH	0.126 μH	140
C1	50 pF	50 pF	
C2	60.7 pF	61 pF	
C3	49.7 pF	50 pF	
C4	53 pF	53 pF	
C5	320 pF	320 pF	
C6	977 pF	980 pF	
C7	641 pF	640 pF	
C8	1612 pF	1612 pF	
C9	2198 pF	2200 pF	
C10	1849 pF	1847 pF	
C11	1989 pF	1980 pF	

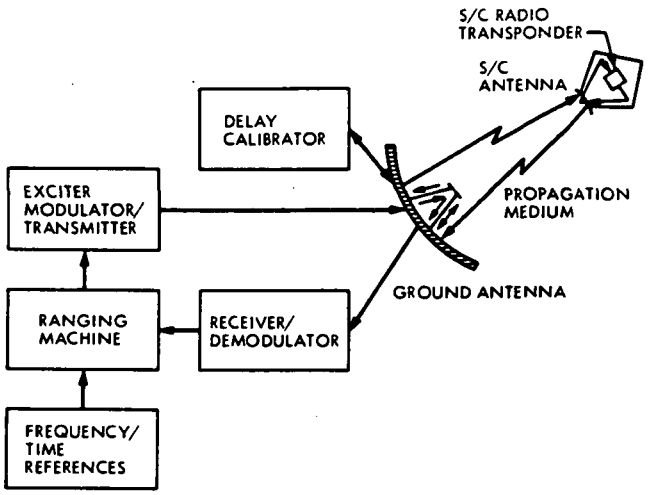

Fig. 1. System block diagram

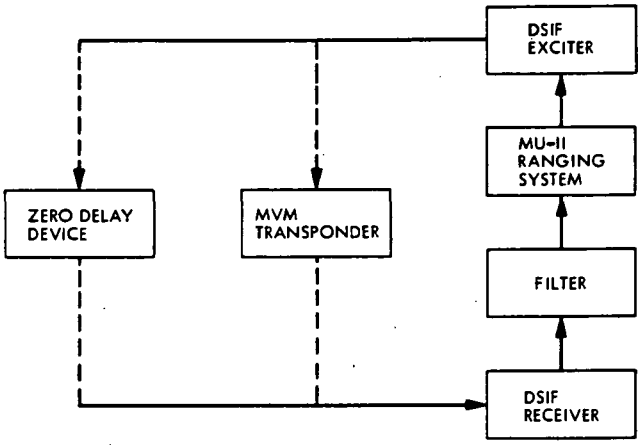

Fig. 3. Filter test configuration

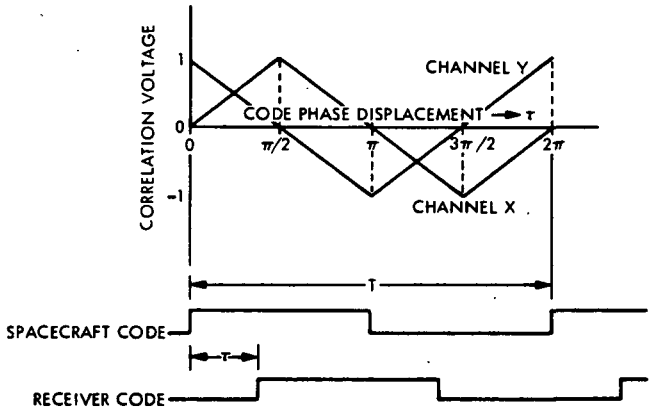

Fig. 2. Ranging correlation values for square-wave reference

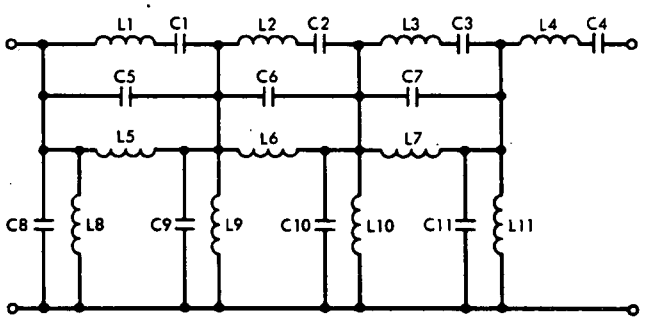

Fig. 4. Ranging code filter schematic

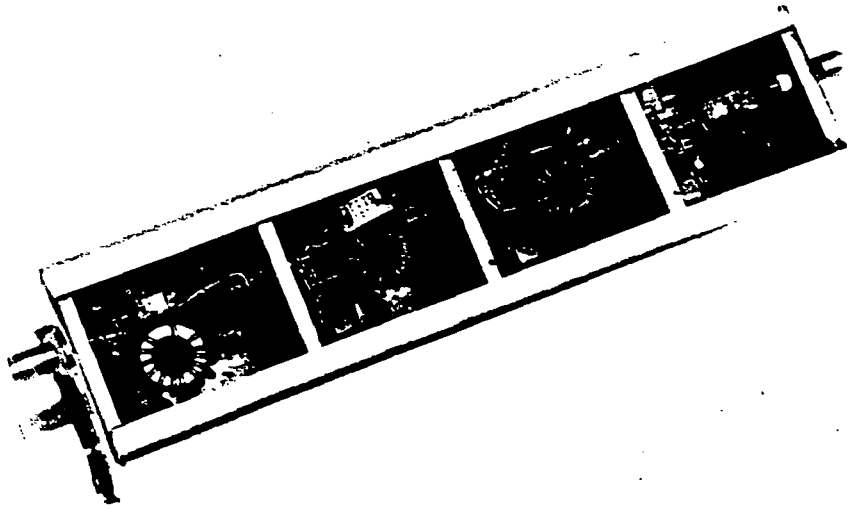

Fig. 5. Ranging code filter module

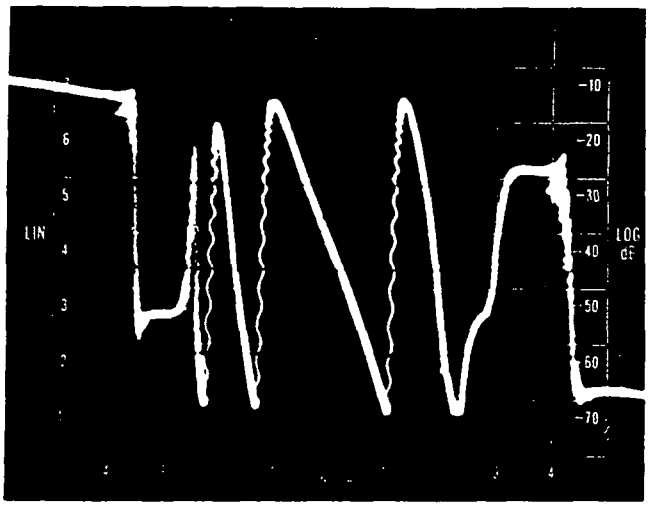

SWEEP SPEED. HORIZ. 500 KHz per cm
VERT. 50 deg per cm
CENTER FREQUENCY 10 MHz

Fig. 6. Filter amplitude response

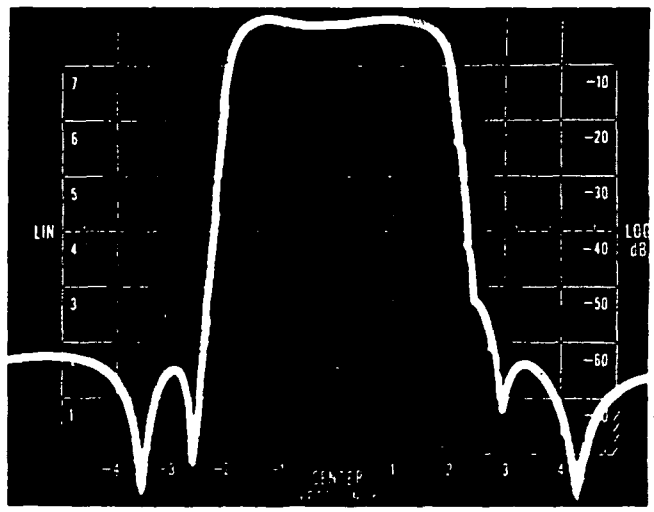

SWEEP SPEED: HORIZ. 500 kHz per cm
VERT. 10 dB per cm
CENTER FREQUENCY 10 MHz

Fig. 7. Filter phase delay

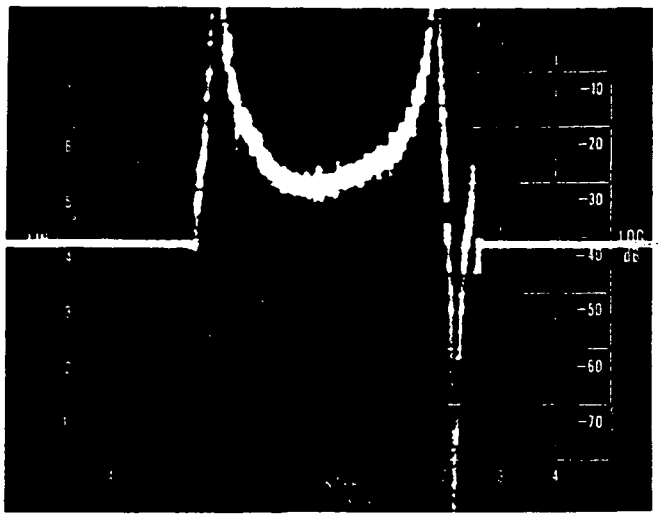

SWEEP SPEED. HORIZ. 500 KHz per cm
VERT. 500 ns per cm
CENTER FREQUENCY 10 MHz

Fig. 8. Filter group delay

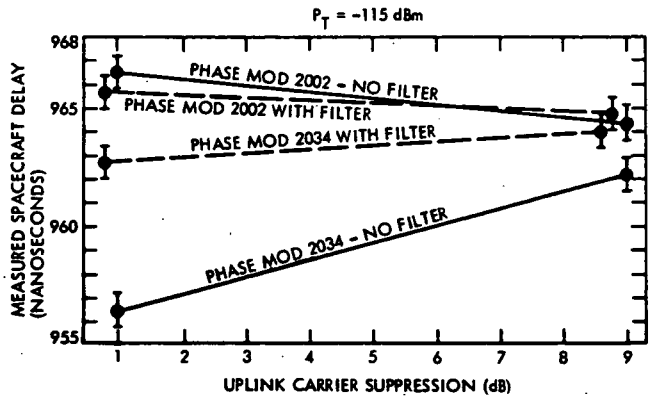

Fig. 9. Filter insertion results

Multipath Tests on 64-m Antennas Using the Viking Orbiter-1 and -2 Spacecraft as Far-Field Illuminators

T. Y. Otoshi
Communications Elements Research Section

D. L. Brunn
R. F. Systems Development Section

Far-field multipath tests were performed on the 64-m antennas at Goldstone, DSS 14, and Madrid, DSS 63, by use of the transponders on the Viking Orbiter-1 and -2 spacecraft. At the time of the tests, Viking Orbiter-1 and -2 spacecraft were in their interplanetary orbits to Mars and were respectively about 21.9 million and 13.9 million km from Earth. The test results showed that the effects of multipath in the far-field of the 64-m antenna were to cause less than a 5-ns peak-to-peak variation on two-way range and 0.1-dB peak-to-peak variations on received signal level. The multipath signal level was calculated to be approximately 40 dB weaker than the primary signal in the far-field main beam direction.

I. Introduction

In a previous article (Ref. 1), it was shown that multipath effects on 64-m antennas could be the cause of the 15-m range residual observed between DSS 43 and DSS 63 during Mariner 10 Mercury Encounter 1 on March 29, 1974. To support this conclusion, however, it was necessary to prove that on the 64-m antenna, the multipath error occurs only in ground station delay calibrations and does not occur in a far-field range measurement to a spacecraft. There was, therefore, considerable interest in performing tests to show that multipath effects in the far-field were negligibly small.

In practice it is difficult to perform a far-field ranging test on the 64-m antenna because, in order to be in the far-field of the 64-m antenna at S-band, the transponder must be located at least 62.8 km (39 mi) away and 5.6 km (3.5 mi) high for a minimum elevation angle of 5 degrees. Due to the non-availability of suitable collimation towers, radiosonde balloons, or satellites for ranging tests, it was necessary to use a spacecraft located in the far-field. A

spacecraft that is sufficiently far from Earth will appear like a point source that radiates constant power. Since the ground station tracking antenna can accurately follow any movement of the spacecraft (due to the spacecraft orbit and Earth's rotation), the test conditions are nearly equivalent to those which would be created by a stationary far-field collimation tower in the sky.

The first known far-field test of a large antenna using a spacecraft was reported by Levy et al. (Ref. 2) in 1967. In this test the Surveyor spacecraft on the moon was used as the far-field illuminator. One of the interesting test results obtained was the focus curve shown in Fig. 1. The focus curve shows the relationship of far-field gain changes as a function of subreflector position relative to nominal. It was shown by Potter (Ref. 3) that the ripples observed on the focus curve in Fig. 1 were caused by a multipath component originating from a reflection from the horn aperture. This test result, although restricted to signal level data, presented the first known evidence that a small multipath effect existed in the far-field of the 64-m antenna.

In July 1975, a series of far-field multipath tests was performed on the 64-m antenna at DSS 14 using the ranging transponder on the Helios spacecraft as the far-field illuminator. However, due to the long interplanetary media of about 2 AU and because Helios was only 7 degrees from the Sun as seen from Earth, the differenced range versus integrated doppler (DRVID) and signal level data were excessively noisy. Therefore, no conclusions could be made on far-field multipath effects.

A unique opportunity to perform far-field tests with a spacecraft under ideal conditions came about two months after the launching of the Viking Orbiter (VO) -1 and -2 spacecraft. It is the purpose of this article to present the far-field results obtained with the Viking spacecraft as well as to compare the experimental data with theoretical data.

II. Theoretical Results

As was shown by Potter (Ref. 3), the focus curve for a Cassegrain antenna has a parabolic shape for defocusing losses of less than 1 dB. The approximate expression for the focus curve is

$$G_{dB}(x) \approx (G_0)_{dB} - A_2(x - x_0)^2 \qquad (1)$$

where

$G_{dB}(x)$ = antenna gain, dB

$(G_0)_{dB}$ = antenna gain at maximum, dB

A_2 = constant

x = focus position

x_0 = focus position for maximum gain

Figure 2 shows the focus curve of the 64-m tricone system at 2.295 GHz. This curve as based on Eq. (1) has a value for A_2 of 0.02126 dB/cm^2 (0.13716 dB/in.^{2}) for the 64-m tricone configuration (see Potter, Ref. 3). If multipath effects are present in the far-field, they will introduce ripples in the focus curve similar to that shown in Fig. 1.

Although there is a similar focus curve for the uplink frequency of 2.113 GHz, the spacecraft radio system removes the uplink signal level variations and transmits back a constant coherent downlink signal back to Earth. Therefore, in a far-field multipath test, one only needs to consider defocusing losses on the downlink signal at approximately 2.295 GHz.

To the authors' knowledge, no published information is available concerning the far-field group delay and phase delay changes resulting from the defocusing of the subreflector on a Cassegrain antenna. A defocused subreflector computer program written by Sorensen (Ref. 4) was modified by Rusch to yield far-field data for a defocused Cassegrain antenna. The phase versus frequency and phase versus subreflector position data were used to compute far-field group and phase delay changes, respectively. Figure 3 shows the group delay change[1] due to defocusing of a symmetrical Cassegrain antenna in the absence of multipath. The primary feed was assumed to have an E- and H-plane power pattern of (43.63) (20 $\log_{10}$ cos γ), which is nearly equivalent to the main lobe power pattern for the Potter horn described in Refs. 5 and 6. The angle γ is the angle from boresight of the primary feed. Although the present 64-m antenna has a corrugated feedhorn and a tricone configuration, it is not expected that the delay change curve for the present configuration would differ significantly from that shown in Fig. 3. For comparison purposes, the dashed curve shows the total (uplink plus downlink) delay change relationship for a single ray traveling only along the axis of the subreflector. It can be seen that the total change in the far-field due to contributions from the entire aperture is slightly less than the delay change for the single on-axis ray.

From the Sorensen/Rusch Program, it was found that the phase delay change was equal to the group delay

[1]The Sorensen/Rusch Program results showed that the phase delay change was the same as group delay change as a function of subreflector position. Therefore, Fig. 3 applies to either phase or group delay changes.

change. Since, by definition, DRVID is group delay change minus phase delay change (Ref. 7), the far-field DRVID data should show no change as a function of subreflector position. However, if there is a multipath effect in the far-field, the group delay changes will be much larger than phase delay changes and a cyclical variation on DRVID data will be observed due to subreflector movement.

III. Experimental Results

A. VO-2 Tests at DSS 14

On October 23, 1975, a far-field test was performed with the VO-2 spacecraft at DSS 14. At the time of the test the VO-2 spacecraft was approximately 13.9 million km from Earth. A strong received signal level of −136 dBm and a good ranging power-to-noise ratio of 33 dB were prevalent at DSS 14 during the far-field ranging tests. Other favorable conditions for this test were the short round-trip light time (RTLT) of 93 seconds and the absence of any solar and ionospheric effects introduced into the DRVID data. A short RTLT was desirable for the far-field multipath test because a short RTLT is equivalent to a short interplanetary medium. A shorter interplanetary medium generally has less electron content than a longer one, and, therefore, the DRVID data will be less likely to change due to electron density changes. No ionospheric or solar effects were introduced because the tests at DSS 14 were done during night-time hours.

The far-field multipath test consisted of ranging to the spacecraft and recording DRVID and received signal level data as a function of subreflector positions. For this test, the subreflector was moved in 1.27-cm (0.5-in.) increments over a total distance of 15.24 cm (6 in.). The test began and ended with the subreflector at the nominal setting so that one could observe and remove the long-term drift in the test data.

The experimental test results may be seen in Figs. 4–7. Figure 4 shows the results of taking 4 hours of DRVID data while moving the subreflector and 2 hours of data while keeping the subreflector stationary for comparison purposes. The drift in the DRVID data during the 4-hour multipath test was about 10 ns. After removing this drift by fitting a second-order curve to the experimental data, the residual differences at each subreflector position were then averaged. A least squares fit of the multipath equation was then made to the averaged DRVID points by use of the Multipath Computer Program described in Ref. 1. The resulting plot shown in Fig. 5 shows relatively good correlation between calculated and experimental values. The peak-to-peak change in range delay was about 3 ns. The Multipath Program calculated the multipath signal to be −45 dB relative to the primary signal in the far-field. This relative multipath signal strength will produce a ripple of 0.1 dB in the downlink received signal level focus curve.

Figure 6 shows the downlink received signal level data obtained during the far-field multipath tests. A comparison of experimental and theoretical results may be seen in Fig. 7. The experimental points were obtained from averaging the received signal level values at each subreflector setting and normalizing them to the received signal level value at the 0 in. position.[2] A least squares parabolic curve was then fitted to the experimental data points. For comparison purposes, the peak of the tricone theoretical curve (Fig. 2) was aligned with the peak of the experimental curve. It can be seen that excellent agreement was obtained between theory and experiment. The deviations of the data about the experimental curve are consistent with the deviations caused by a multipath signal being −45 dB with respect to the principal wave.

For purposes of comparison, the results of pre-cals done with the zero delay device at DSS 14 are shown in Fig. 8. It can be seen that the peak-to-peak variations are 40 ns and 3 dB for range delay and received signal level, respectively. One explanation as to why a small multipath effect occurs in the far-field measurements but a large effect occurs in zero delay calibrations is the following: The primary waves impinging on the paraboloidal dish surface add up in phase in the far-field. Although the multipath wave signal strengths at a localized area can be as strong as −15 dB relative to that of the primary wave, the multipath waves are not the same in phase or amplitude over the entire dish surface. Therefore, when the multipath components combine in the far-field, they do not necessarily add in phase. Since cancellations can occur, it is not unreasonable that the net far-field multipath signal level can be −45 dB relative to the primary wave in the main beam.

B. VO-1 Tests at DSS 63

On October 26, 1975, a far-field multipath test was also performed at DSS 63. This test was similar to the DSS 14 test but differed in that the VO-1 spacecraft was used instead of VO-2. The RTLT was 146 seconds, which indicates that the VO-1 spacecraft was approximately 21.9

[2]The subreflector position on the equipment is indicated in inches rather than in centimeters. In order for data to be meaningful and be useful to the user and also to avoid double conversions, the units should be kept in inches as reported.

million km from Earth. VO-1 was farther from Earth than VO-2 was; therefore, the received signal level was weaker. The ranging power-to-noise ratio was 22 dB as compared to 33 dB obtained with VO-2. In order to eliminate ionospheric and solar effects, the test at DSS 63 also was done during night-time hours.

Although far-field data had already been successfully obtained at DSS 14 with the VO-2 spacecraft, the test was performed at DSS 63 because the DSS 63 64-m antenna was known to have the largest multipath effect (Ref. 1) and also had a cone missing. These differences in ground station configurations could cause far-field multipath effects to differ.

Figure 9 shows the DRVID data during the 3-hour period that the subreflector was being moved. It may be seen that there was virtually no drift in the DRVID data during the test. Because this was an abbreviated test, DRVID stability data with the subreflector stationary were not obtained during the same VO-1 pass. However, examination of DRVID stability data at DSS 63 for a VO-2 pass three days later showed that the DRVID drift between 0000 GMT and 0700 GMT was only 10 ns. Therefore, it can be reasonably assumed that the drift during the DSS 63 VO-1 test was also small.

Figure 10 shows a comparison of the averaged experimental DRVID data at each subreflector setting and a best fit theoretical curve which is based on the multipath equations (Ref. 1). Although there is only partial agreement between theory and experiment, the peak-to-peak variation of range delay is only about 5 ns. The multipath signal was calculated to be 39 dB weaker than the primary signal in the far-field.

Figure 11 shows the experimental received signal levels during the multipath test. In Fig. 12, which shows the normalized plot, each data point is the result of averaging data at each subreflector position. A comparison of a least squares parabolic curve (fitted to the experimental data points) and the theoretical curve for the tricone configuration may be seen in Fig. 12. It can be seen that the agreement between the experimental parabolic curve and the theoretical curve is reasonably good. Although the agreement between theory and experiment is not as good as that obtained in the DSS 14 VO-2 tests, it should be pointed out that at DSS 63, the 64-m antenna has a cone missing. In addition, the received signal level with VO-1 was 10 dB lower than that on the VO-2 tests, and therefore, the data were noisier.

IV. Conclusions

Good experimental results were obtained from the far-field multipath tests on the 64-m antennas at DSS 14 and DSS 63 and the two Viking spacecraft. The far-field multipath effects were found to be small. The variations due to subreflector movement were typically less than 5 ns peak-to-peak on total range delay and less than 0.1-dB cyclic variation on received signal level.

The excellent results obtained from Viking spacecraft can be attributed to a good ranging power-to-noise ratio (>20 dB), a short RTLT (<3 min), and the absence of solar or ionospheric effects.

Acknowledgments

Technical discussions and background information provided by D. Bathker of the Communications Elements Research Section were helpful. The computer program enabling computations of group delay change as a function of subreflector position was furnished by Dr. W. V. T. Rusch, JPL Consultant and Professor of Electrical Engineering at the University of Southern California. Harvey Marks of Informatics assisted with the Viking tests at DSS 14.

References

1. Otoshi, T. Y., "S-Band Zero-Delay Device Multipath Tests on the 64-m Antenna at DSS 43, DSS 63, and DSS 14," in *The Deep Space Network Progress Report 42-29*, pp. 20–30, Jet Propulsion Laboratory, Pasadena, CA, Oct. 15, 1975.

2. Levy, G. S., et al., "Lunar Range Radiation Patterns of a 210-Foot Antenna at S-Band," *IEEE Transactions on Antennas and Propagation*, Vol. AP-15, No. 2, pp. 311–313, March 1967.

3. Potter, P. D., "Network Engineering and Implementation: S- and X-Band Feed Systems," in *The Deep Space Network Progress Report*, Technical Report 32-1526, Vol. X, pp. 135–140, Jet Propulsion Laboratory, Pasadena, CA, Aug. 15, 1972.

4. Sorensen, O., "Application of the Geometrical Theory of Diffraction to Cassegrain Subreflector with Laterally Defocused Feeds," Masters' Thesis, Lab. Electromagnetic Theory, Tech. University Denmark, Lyngby, Fall 1973.

5. Potter, P. D., "A New Horn Antenna with Suppressed Sidelobes and Equal Beamwidths," *Microwave J.*, Vol. 6, No. 6, pp. 71–78, June 1963.

6. Otoshi, T. Y., and Stelzried, C. T., "Improved RF Calibration Techniques: Cosmic Background Noise Temperature Measurements at 13 cm," in *The Deep Space Network*, Space Programs Summary 37-57, Vol. II, pp. 90–100 (for horn pattern data at S-band, see Fig. 59, pp. 96–97), Jet Propulsion Laboratory, Pasadena, CA, May 31, 1969.

7. MacDoran, P. F., "A First-Principles Derivation of the Differenced Range Versus Integrated Doppler (DRVID) Charged-Particle Calibrations Method," in *The Deep Space Network*, Space Programs Summary 37-62, Vol. II, pp. 28–34, Jet Propulsion Laboratory, Pasadena, CA, Mar. 31, 1970.

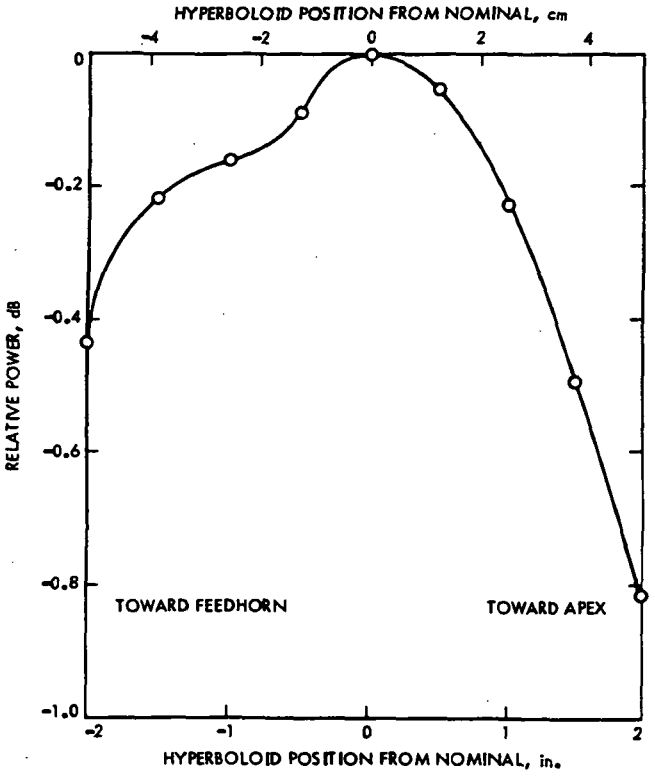

Fig. 1. 64-m antenna Surveyor focus curve (from Ref. 2)

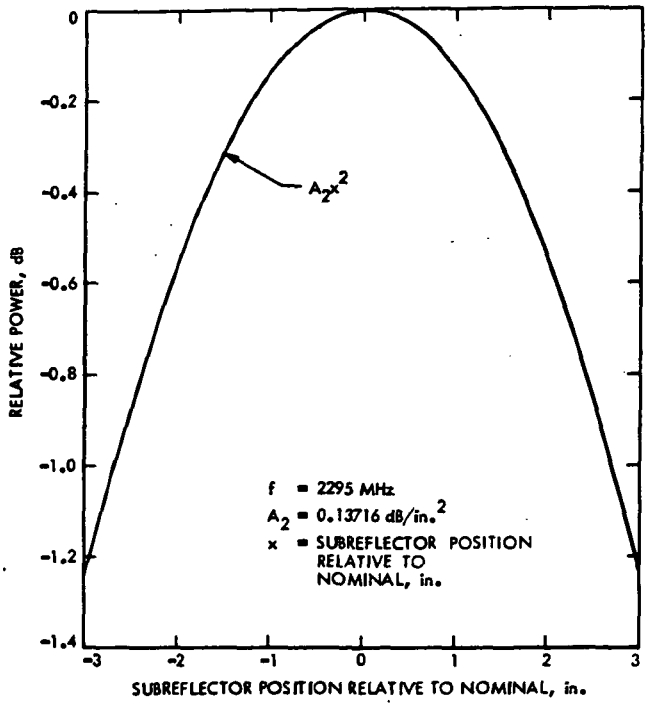

Fig. 2. Far-field focus curve from 64-m Cassegrain antenna tricone configuration in the absence of multipath

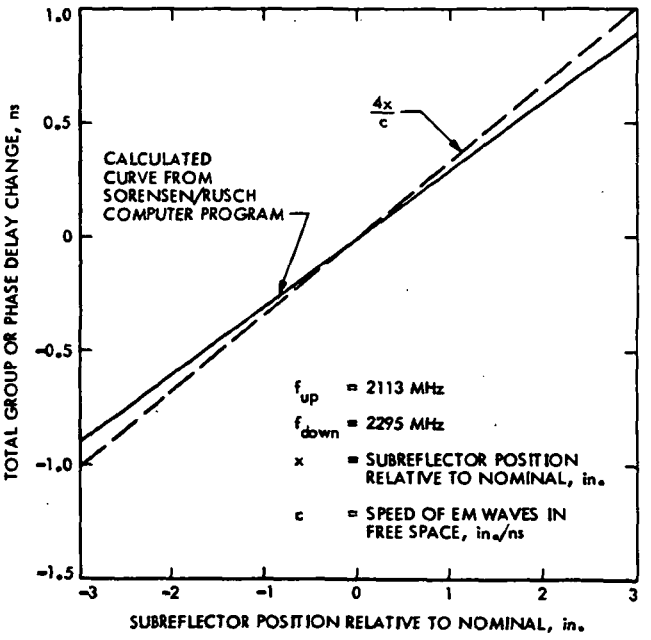

Fig. 3. Total uplink plus downlink phase or group delay change in the far-field of a defocused 64-m Cassegrain antenna in the absence of multipath

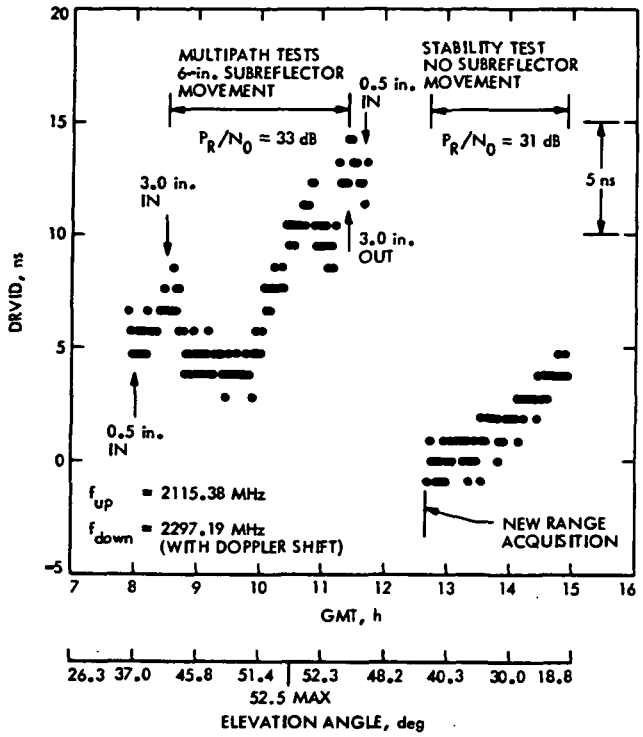

Fig. 4. Original DRVID data from DSS 14 VO-2 spacecraft multipath test on 1975 GMT Day 296. Polarization is RCP.

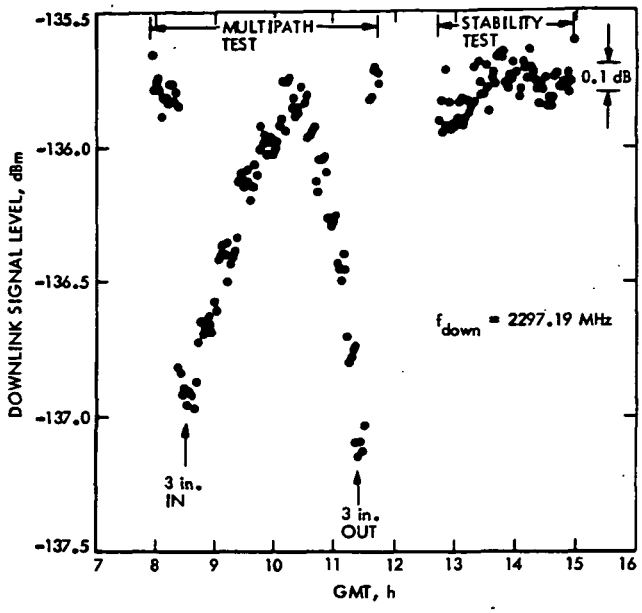

Fig. 6. Received signal level during DSS 14 VO-2 multipath test on 1975 GMT Day 296. Polarization is RCP.

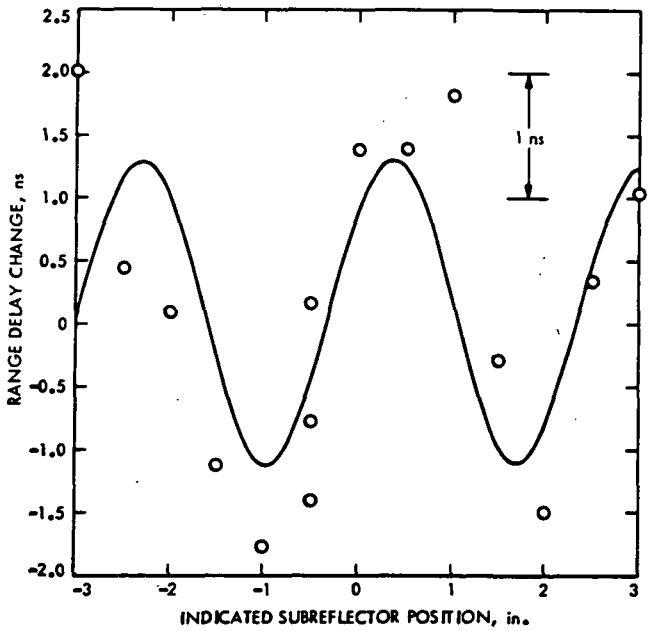

Fig. 5. Reduced DRVID data from DSS 14 VO-2 spacecraft multipath test on 1975 GMT Day 296

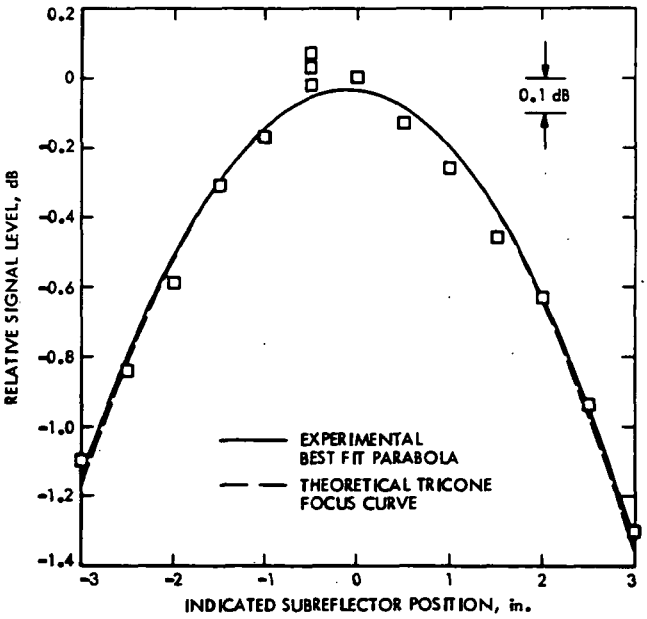

Fig. 7. Theoretical and experimental results for relative received signal level on DSS 14 VO-2 multipath test on 1975 GMT Day 296

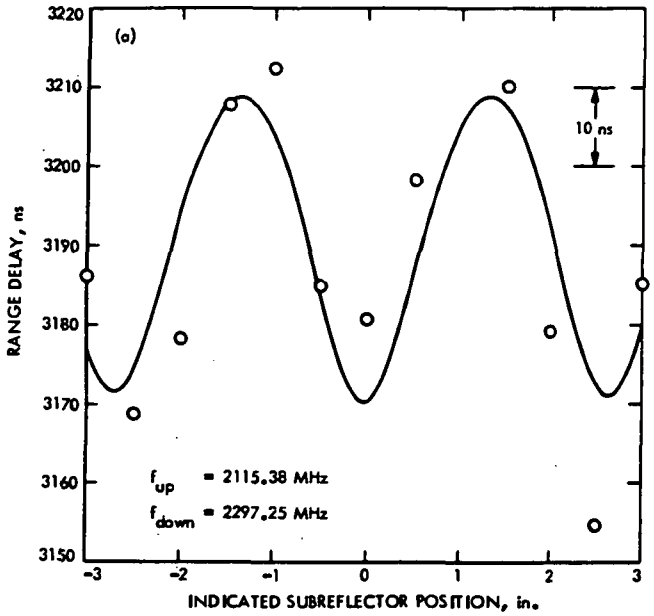

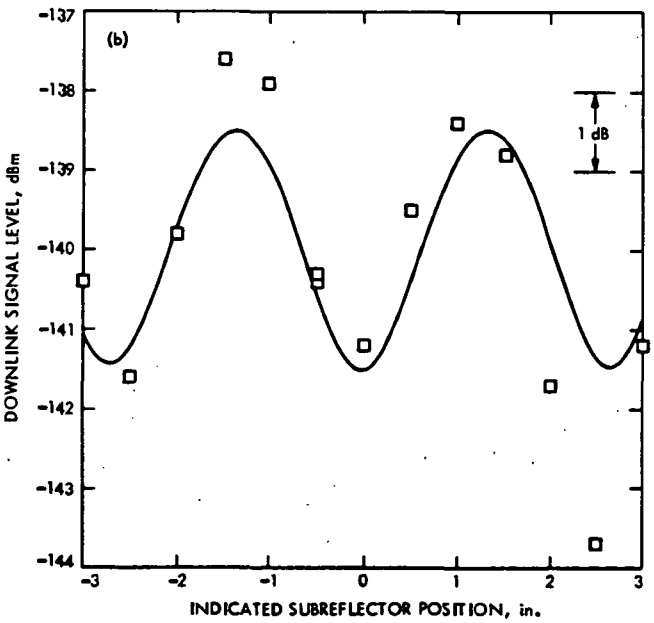

Fig. 8. Theoretical and experimental results for multipath tests on DSS 14 VO-2 Pass 44 pre-cal on 1975 GMT Day 296. Polarization is RCP.

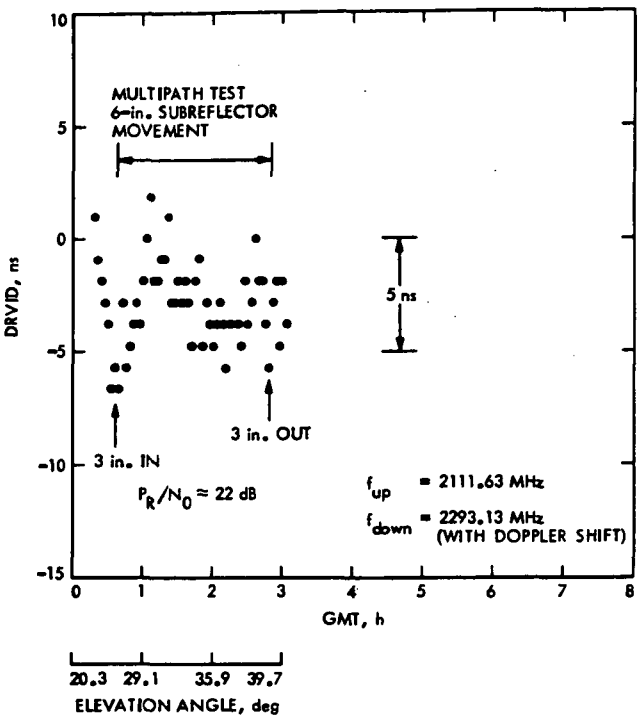

Fig. 9. Original DRVID data from DSS 63 VO-1 spacecraft multipath test on 1975 GMT Day 299. Polarization is RCP.

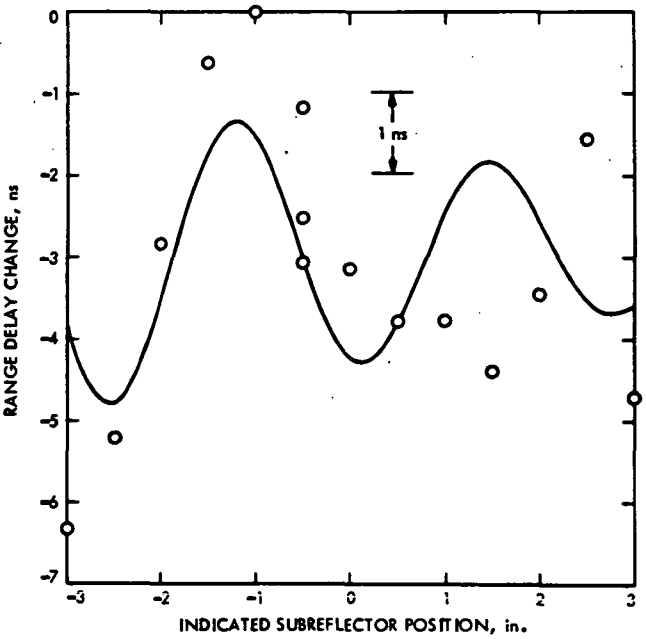

Fig. 10. Reduced DRVID data from DSS 63 VO-1 spacecraft multipath test on 1975 GMT Day 299

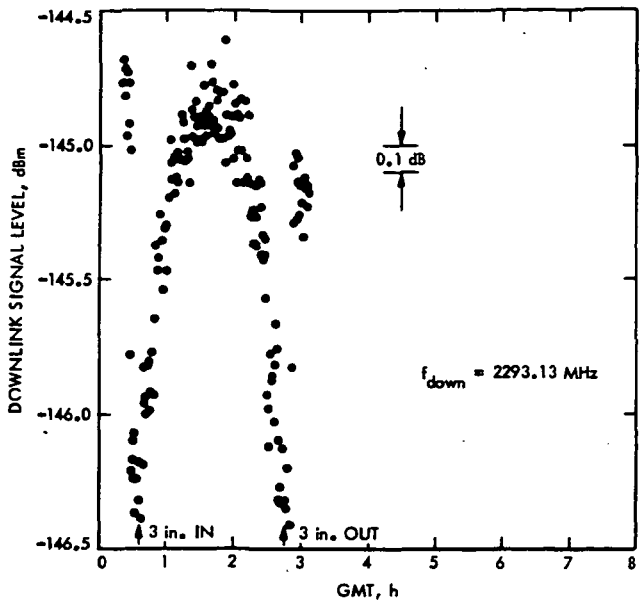

Fig. 11. Received signal level during DSS 63 VO-1 multipath test on 1975 GMT Day 299. Polarization is RCP.

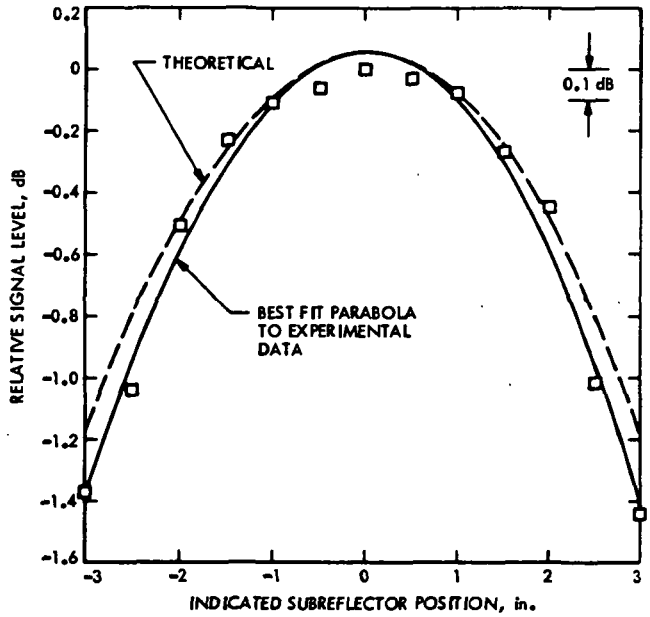

Fig. 12. Theoretical and experimental results for relative received signal level on DSS 63 VO-1 multipath test on 1975 GMT Day 299

Design of a Superconducting Cavity Stabilized Maser Oscillator

W. Higa
Communications Elements Research Section

The pioneering works of W. H. Hartwig (Ref. 1), S. R. Stein and J. Turneaure (Ref. 2), J. J. Jimenez and A. Septier (Ref. 3), and others (Ref. 4) have shown the possibility of using a superconducting cavity to stabilize a microwave oscillator. The achievement of cavity Qs of the order of 10^{10} has made possible the realization of frequency standards with performance which could surpass that of the hydrogen maser.

The present study explores the possibility of integrating a superconducting cavity with a traveling wave maser to obtain a frequency standard with very high spectral purity.

I. Introduction

There are two basic methods for using a high Q resonator to stabilize a microwave oscillator. In one method, a voltage controlled oscillator (VCO) is used in a FM detector loop, as shown in Fig. 1, to stabilize the oscillator frequency. The second method, shown in Fig. 2, utilizes the high Q resonator as a transmission filter and stabilizes a microwave oscillator to the cavity/frequency. Both methods have been used by the investigators mentioned in Refs. 1–4.

The motivation for the present program was the long experience with traveling wave masers (TWMs) and closed-cycle refrigerators (CCRs), which technologies appeared to blend in very naturally with the requirements for a good superconducting cavity stabilized maser oscillator (SCSMO).

In the present article, a discussion is presented of the microwave electronics problems related to the SCSMO. In future articles, the cryogenics problems will be discussed and the statistical properties of the output signal from a SCSMO will be described.

II. Design of a SCSMO

The low-noise performance of a TWM would appear to make it a good device for integrating with a superconducting cavity to achieve a stable oscillator.[1] In such an application the TWM would operate at high signal levels

[1] S. R. Stein is investigating the use of parametric amplifiers for reasons similar to ours (Ref. 5).

and in partial gain saturation in order to provide amplitude stabilization. Thus, it is apparent that the application of the TWM here is completely different from the usual linear-unsaturated mode in a receiving system.

In the usual electron tube or semiconductor oscillator, the mechanism for amplitude stabilization is contained in the Van der Pol equation (Ref. 6), which introduces damping terms proportional to the square of an exciting voltage or current. Whereas the Van der Pol equation was derived through phenomenological arguments to explain experimental observations in electronic oscillators, the same saturation effects were already inherent in the equations for the solid state maser as originally proposed by Bloembergen (Ref. 7). Subsequently, it was observed that power saturation in a maser was necessarily accompanied by a rise in the spin temperature of the amplifying medium, and that the spin temperature determined the noise performance of a maser.

Siegman (Ref. 8) has postulated an equation to account for saturation in a TWM; however, for present purposes a graphical approach will be adequate. Figure 3 shows a typical response for a TWM as a function of distance along an amplifying structure of great length; typical operating points a and b for an amplifier of length L cm are shown. The small signal gain G of the TWM is given by the slope for small values of x, while the oscillator gain G_o is given by P_b/P_a and is, of course, less than G. The response shown in Fig. 3 is for fixed conditions on certain parameters, such as pump power, operating temperature, and the static magnetic field. Variations in these parameters will cause corresponding power fluctuations in the oscillator output. Moreover, to the extent that these variations also cause frequency and phase fluctuations, they will need to be examined in greater detail in a later study.

An important observation can, however, be made at this point: the low-noise performance of a TWM can be realized in an oscillator provided the input section of the maser operates in the linear-unsaturated mode. The signal-to-noise ratio then can be made sufficiently high by the time the signal suffers amplitude saturation, toward the end of the TWM, that the spectral purity is not degraded. In other words, the high spin temperature (which implies high noise temperature) toward the end of the structure, due to saturation, will not degrade a properly designed SCSMO.

The microwave design problem is then to provide the proper coupling coefficients to the superconducting cavity so as to achieve the desired gain G_o while maximizing the loaded Q.

Figure 4 shows the equivalent circuit for the SCSMO. The transmission cavity has been analyzed in great detail by Montgomery, Dicke and Purcell (Ref. 9) and only the results need to be given here.

The transmission loss through the cavity at resonance is given by

$$T(\omega_0) = (4\beta_1\beta_2)/(1 + \beta_1 + \beta_2)$$

and the loaded Q is given by

$$Q_L = Q_u/(1 + \beta_1 + \beta_2)$$

In the above equations,

$T(\omega_0)$ = transmission loss at resonance

β_1 = coupling coefficient at input

β_2 = coupling coefficient at output

Q_L = loaded Q of cavity

Q_u = unloaded Q of cavity

An X-band TWM can easily have a gain in excess of 40 dB; hence, an oscillator gain of 30 dB is reasonable. Thus the transmission loss through the cavity should be around 10^{-3}. Assuming the input coupling can be made equal to the output coupling,

$$\beta_1 = \beta_2 = \beta$$

one has, finally,

$$T(\omega_0) = 4\beta^2/(1 + 2\beta)$$

and

$$Q_L = Q_u/(1 + 2\beta)$$

Using the numbers quoted above,

$$Q_L \approx (1/1.03)Q_u$$

Thus, the high gain in a TWM makes possible a loaded Q which approaches the unloaded Q.

One of the advantages of the servoed oscillator shown in Fig. 1 is that the time constant of the loop may be made sufficiently long to smooth out the noise in the system. With the SCSMO the noise is negligible, and the cavity performs a smoothing of any phase instabilities which may be inherent in the TWM. For Qs of the order of 10^{10} and

oscillations at a frequency of 10^{10} Hz, the time constant of the cavity is around 1 second. The transit time through a TWM is something less than a microsecond, and the superconducting cavity thus averages a signal which makes over a million round trips through the TWM. Small phase fluctuations through the TWM are nullified, and a highly monochromatic signal should be realizable.

Turneaure and Stein (Ref. 2) have shown that the Q of a superconducting cavity can increase by as much as an order of magnitude per Kelvin in the region of 4 to 1.5 K. It is essential, therefore, to operate the cavity at around 1.5 K; the TWM may be operated at 4.2 K. It is apparent then that the difficult problem to be solved for a continuously operating SCSMO is that of cryogenic refrigeration. Not only is it necessary to maintain the cavity at around 1.5 K with high temperature stability but the cavity also needs to be kept free of any mechanical motion. These problems will be discussed in a future study.

III. Conclusions

The superconducting cavity appears to be compatible with a traveling wave maser. The real advantage of the superconducting cavity stabilized maser oscillator is that the cavity can be integrated with the TWM in such a way that rigid microwave connections can be made. Second-order perturbations resulting from fluctuations in transmission line joints are thus eliminated. However, the more serious problem is that of the mechanical (dimensional) stability of the cavity itself.

A special closed-cycle refrigerator needs to be developed for the SCSMO, and it will be discussed in the next report.

References

1. W. H. Hartwig, "Superconducting Resonators and Devices," *Proc. IEEE*, Vol. 61, pp. 58–70, Jan. 1973.
2. S. R. Stein and J. P. Turneaure, "The Development of the Superconducting Cavity Stabilized Oscillator," *Proc. 27th Annual Symposium on Frequency Control*, 1973, pp. 414–420.
3. J. J. Jimenez and A. Septier, "S- and X-Band Superconducting Cavity Stabilized Oscillators," *Proc. 27th Annual Symposium on Frequency Control*, 1973, pp. 406–413.
4. Excellent bibliographies are presented in Refs. 1–3.
5. S. R. Stein, "Application of Superconductivity to Precision Oscillators," *Proc. of the 29th Annual Symposium on Frequency Control*, 1975, pp. 321–327.
6. B. Van der Pol, "The Nonlinear Theory of Electric Oscillations," *Proc. I.R.E.*, Vol. 22, pp. 1051–1086, Sept. 1934.
7. N. Bloembergen, "Proposal for a New Type Solid State Maser," *Phys. Rev.*, 104, p. 324, 1956.
8. A. E. Siegman, *Microwave Solid State Masers*, McGraw Hill, N. Y., 1964.
9. C. G. Montgomery, R. H. Dicke, E. M. Purcell, *Principles of Microwave Circuits*, (Radiation Laboratory Series) McGraw Hill, 1948.

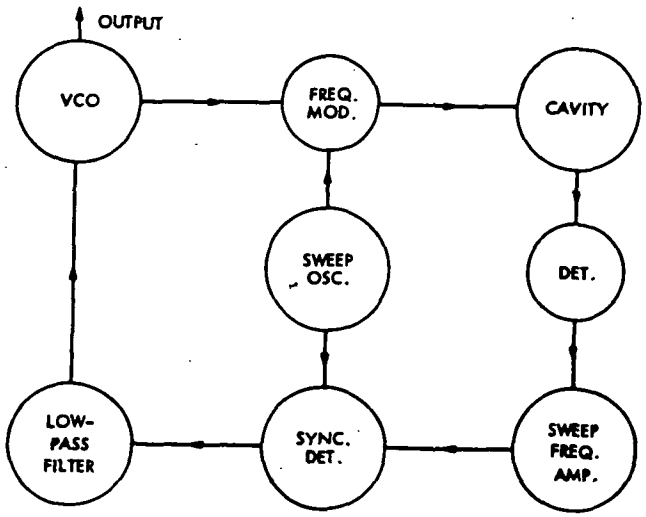

Fig. 1. Frequency modulation servoed oscillator. (The superconducting cavity is used as a frequency discriminator.)

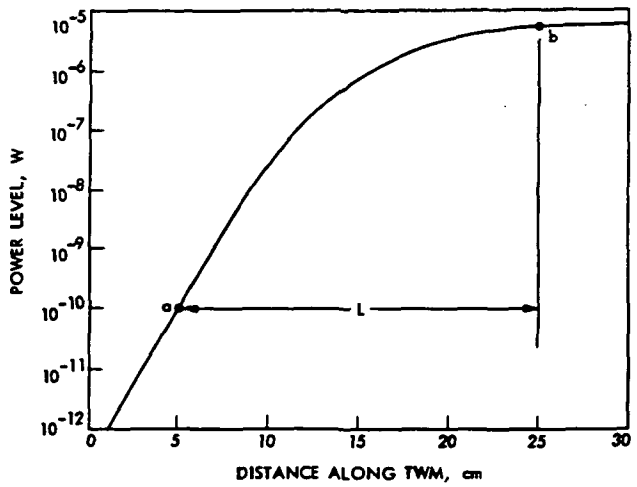

Fig. 3. Typical power saturation curve for a TWM (see text)

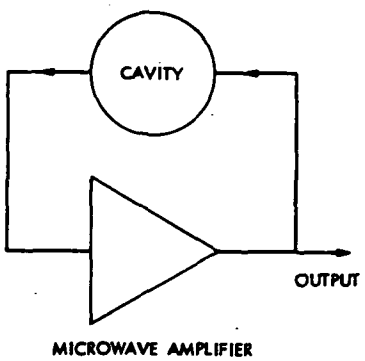

Fig. 2. Regenerative microwave oscillator (The cavity is used as a transmission filter.)

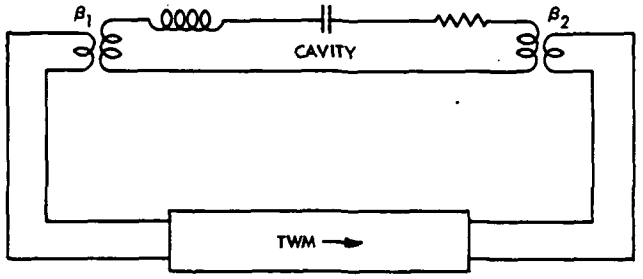

Fig. 4. Equivalent circuit for a SCSMO (A small part of output signal would be used as the stable oscillator output.)

QVLBI Doppler Demonstrations Conducted During Pioneer 11 Encounter and Solar Conjunctions

C. C. Chao
Tracking and Orbit Determination Section

During the Jupiter encounter of Pioneer 11 in December 1974, a limited amount of simultaneous two-way and three-way doppler was obtained. It was demonstrated in this study that, based on a very short arc (two weeks) of differenced doppler (quasi very long baseline interferometry or QVLBI doppler), the B-plane predictions were as good as 200 km at E-1 day and 400 km at E-3 days.

During the two solar conjunctions of Pioneer 10 and 11, which occurred in March 1975, several passes of QVLBI doppler were obtained and analyzed. The data quality of QVLBI doppler was found to be two to three times better than the conventional two-way doppler when the Sun-Earth-probe angle was less than 5 degrees.

I. Introduction

Studies in Ref. 1 have shown that using differenced two-way and three-way (QVLBI) doppler data rather than the conventional two-way doppler data may significantly improve the accuracy with which the trajectory of a spacecraft can be determined in the presence of process noise. Process noise describes the effect of unmodeled spacecraft accelerations due to attitude control gas leaks and solar radiation pressure anomalies, etc. This data type has been successfully demonstrated using the radio metric data of Pioneer 10 (Ref. 2) and that of Mariner 10 (Ref. 3). The results of the Pioneer 10 demonstration indicate an order of magnitude improvement at Jupiter *B*-plane in the presence of large unmodeled accelerations (10^{-8} km/sec^2) due to the four massive Galilean satellites. The results of the later demonstration conducted with Mariner 10 conclusively showed that this new data type can reduce the effects of moderate unmodeled spacecraft accelerations (10^{-10} km/sec^2) by an order of magnitude and reduce the effects of the solar corona by a factor of five when the Sun-Earth-probe (SEP) angle is less than 5 degrees.

Unmodeled spacecraft accelerations and solar plasma effects will be two major difficulties in navigation of future space missions such as Mariner Jupiter–Saturn and the Saturn flyby of Pioneer 11. The latter effect is even more important because solar conjunction will occur during many of the critical periods of planet encounter of Mariner Jupiter–Saturn and Pioneer 11 missions. The order of magnitude increase in data noise due to the solar corona makes the orbit determination (OD) extremely difficult. During the solar conjunction of Mariner 10, the doppler data noise became so large (1.1 Hz) that neither the S-band-X-band (S-X) dual-frequency technique nor the sequential estimation method was able to calibrate or remove this effect. Therefore, the OD strategy relied heavily on the solutions based on QVLBI doppler data. By comparing short arc solutions with that from conventional data, a factor of 4 improvement in *B*-plane uncertainties was found (Ref. 3).

During the Pioneer 11 encounter of Jupiter, one month of simultaneous two-way and three-way doppler data were received. The two-way doppler data during this period were relatively clean, and the accelerations due to Galilean satellites had been correctly modeled. Therefore, we do not expect significant improvement in data quality from the QVLBI doppler data. Consequently, the Pioneer encounter demonstration emphasized the orbit determination capability of this new data type.

Later in the spring of 1975, both Pioneer 10 and Pioneer 11 were in solar conjunction, and a few passes of two-way and three-way doppler were obtained. Because of very limited data coverage, data quality improvement was demonstrated with no attempt at studying the OD improvement.

II. Pioneer Encounter

Similarly to previous demonstrations (Refs. 2,3), the results of orbit determination based on this new data type will be compared with those from conventional data types. In the meantime, both of them will be compared with the true values determined from both pre- and post-encounter data. The simultaneous two-way and three-way doppler data coverage was little less than a month during encounter, with 18 days before and 10 days after the closest approach of Jupiter. Figure 1 shows the data distribution of two-way and three-way simultaneous doppler for that period. On most of the days, the coverage was less than 2 hours, which is relatively poor compared with the continuous coverage of conventional two-way doppler data.

During this period, the conventional doppler data was relatively quiet. Consequently, we do not anticipate significant improvement in data quality from the new data type as we did in previous demonstrations. Instead, we emphasize the actual capability for navigation of this two-way and three-way differenced doppler. Besides, the ephemerides of the four massive Galilean satellites, which were turned off in the previous Pioneer 10 demonstration (Ref. 2), were included in the orbit determination program this time.

Three different data types are included in this analysis: the conventional two-way doppler (F2), the two-way and three-way differenced (QVLBI) doppler (F3C) and the ramped range (ETR). The selected data arc starts from 30 days before Jupiter encounter, with conventional doppler loosely weighted (Table 1). Six ramped range data were evenly distributed in this interval, and they are weighted at 10 km. Three cases of OD solutions at three different data arcs were obtained. In the first case, six state parameters and two parameters for the constant frequency bias for the DSS 14–43 baseline (A1001) and the DSS 43–63 baseline (A1002) were estimated. In the second case, two more parameters for the relative frequency drift (A2001, A2002) were added to the estimated list. The third case is the state only solution without QVLBI doppler and with two-way doppler weighted normally at 0.045 Hz and ramped range (10 km). Table 2 shows all the estimated and considered parameters, together with a priori and nominal values used in the OD analysis. Those a priori values are standard values used by the Pioneer 10–11 navigation team.

The three data arcs give solutions at 5, 3 and 1 days before encounter. The *B*-plane values shown in Fig. 2 indicate an excellent agreement in the **B** · **T** component between that predicted by QVLBI doppler (solid and empty triangles) and the post-encounter best estimate (less than 60 km). The **B** · **R** component, which is the out-of-plane component and usually is difficult to predict, has a spread of 1000 km in the solutions from QVLBI data. This is not surprising because at E–5 days, the QVLBI doppler only sparsely covered an arc of about 10 days. At E–3 days, the **B** · **R** prediction missed the best estimate by less than 400 km. The best prediction from QVLBI data was good to 200 km, which is at E–1 day with only a 16-day arc of QVLBI doppler. The predictions based on continuous two-way doppler (case 3) at E–5, E–3 and E–1 day agree with the best estimate within 120 km. It is estimated that the QVLBI doppler data coverage actually obtained during this time span (E–30 days to E–1 day) is less than 15 percent of the possible QVLBI doppler covered during the same time interval (based on 7-hour

two-way and three-way overlap per 24 hours). Had we had all the possible two-way and three-way data during that time span, considerable improvement in *B*-plane accuracy would have been expected.

The difference between the solid and empty triangles (Fig. 2) tends to indicate the effect due to the drift between frequency standards (new Rb maser 5065A). The estimated values for frequency biases are shown in Fig. 3. The bias between DSS 14 and DSS 43 was as large as 33.9 mHz, which is consistent with the estimated value from the Mariner 10 QVLBI doppler demonstration (Ref. 3). The slope of the frequency drift between DSS 14 and DSS 43 for this period is unusually small at 0.1 mHz per month. The slope between DSS 43 and DSS 63 is also small during this interval. It is seen from Fig. 3 that the estimated values of bias (case 1 solution) differed from the values when slopes were estimated at the same time (case 2 solutions). This is true particularly for the E–5 day solution. It may be responsible for the large error in *B*-plane predictions. When both bias and slope are estimated from a short arc of data, the two parameters are highly correlated and thus degrade the uncertainty of estimated biases. By comparing results (covariance) of case 1 and case 2, the bias may be determined from 2 weeks of QVLBI data within a few tenths of a mHz if slopes are not estimated and station location has no error, while in case 2, when slopes are estimated, the uncertainty of estimated bias becomes as large as 20 mHz. The above fact strongly suggests that better frequency standards such as H-masers with long-term drift less than one tenth of a mHz or better are highly desirable for QVLBI doppler tracking. If we had H-masers as frequency standards, with the constant bias properly removed either by estimating in the Orbit Determination Program or other independent methods such as VLBI or SITT[1], the *B*-plane solution would be improved significantly.

Figure 4 shows the sensitivity of *B*-plane components to various parameters for the three different data arcs. It is as expected that the QVLBI data type is much less sensitive to errors in the mass and ephemerides of Jupiter than the conventional data type. QVLBI doppler is more sensitive to errors in station location and frequency standards.

As a research effort, only the simultaneous two-way and three-way doppler data (without differencing) from E–18 days to E+10 days were used together with the six ramped range data to estimate the dynamic constants of the Jupiter system. It was hoped that the common error sources would be implicitly removed from the simultaneous data. Those estimated values for the mass of Jupiter, J2, and J4 and the masses of the four Galilean satellites have good agreement with earlier determinations (Ref. 4) and are shown in Table 3.

III. Solar Conjunctions of Pioneer 10–11

The two Pioneer 10–11 spacecraft had solar conjunctions in late March and early April 1975. Since the celestial longitude is approximately the same for both spacecraft, the minimum Sun-Earth-probe angle occurs approximately at the same time—March 24 for Pioneer 11 and April 4 for Pioneer 10. This minimum angle reaches a little less than 2 degrees for both spacecraft.

A total of 4 passes of QVLBI doppler were obtained in late March during the solar conjunction of Pioneer 11. A summary of these data is shown in Table 4. Unfortunately, one pass of three-way doppler received at DSS 44 was bad, and another pass of three-way doppler at DSS 42 on March 23, when the 2-degree minimum angle occurred, was questionable because the three-way data were found to be 60 percent more noisy than those of the two-way doppler received at the same time at DSS 14. According to earlier observations (Ref. 3), it is unlikely that the 60 percent increase in data noise is due to the gradient in the solar corona. A possible explanation for the noise in the three-way data is that during that time, the 26-meter antenna of DSS 42 was at only 9 dB, which was very marginal to receive useful doppler data. Two good passes of QVLBI doppler were received on March 29 and 31. On March 29, the SEP angle was about 4 degrees and the data noise of both two-way and three-way doppler was around 0.026 Hz (60-second count time). After differencing the simultaneous doppler, the data noise became 0.0098 Hz, a factor of 3 improvement (Fig. 5). Two days later, the SEP angle was about 5 degrees, and the data noise was improved from 0.0177 Hz to 0.0089 Hz after differencing (Fig. 6).

During the Pioneer 10 solar conjunction, two passes of QVLBI doppler were received on March 22 and March 30. On March 22, the SEP angle was about 10 degrees and the data noise of two-way doppler received at DSS 12 was 0.0134 Hz (see Table 5). There is no noticeable improvement in the differenced data, which have a data noise of 0.0132 Hz. This is about the normal data noise of two-way doppler at 60-second count time. Comparison with the two-way doppler data noise (0.0144) during the Pioneer 11 conjunction, when the SEP angle was 15 degrees, seems to indicate that solar corona effects become less important

[1]SITT is the Simultaneous Interference Tracking Technique which, as has been demonstrated, can estimate the relative frequency offset good to a few parts of a mHz.

when the SEP angle is greater than 15 degrees. The effect due to the ionosphere was not calibrated because, near local noon, it is estimated to be less than 0.002 Hz. The most interesting pass in this analysis is the one received on March 30 with two-way at DSS 14 and three-way at DSS 43. The SEP angle was at 4 degrees, and the noise seen in two-way doppler residuals was an order of magnitude higher than that found during Pioneer 11 conjunction (SEP = 4 deg). This increase strongly suggests active solar activities, particularly during the first 15 minutes of this one-hour pass, as shown in Fig. 7. After differencing, the noise is still as large as 0.28 Hz in the first 15 minutes and 0.092 Hz in the remaining 35 minutes (Table 5). The noise in the differenced doppler implies large spatial gradient and/or smaller-scale (less than the DSS 14–43 distance of 7000 km) inhomogeneities in the solar plasma. This particular pass of data may be useful in studying solar activities.

It is also interesting to see the integrated doppler residuals due to solar plasma. Figure 8 shows the equivalent range residuals after integrating the two-way and differenced doppler residuals as shown in Fig. 7. It clearly indicates that the 30-meter variation in integrated two-way doppler residuals was improved to less than 5 meters after differencing. The linear drift in the differenced range residuals seems to reveal the frequency offset between the two station standards. The factor of 3 improvement in doppler quality and the improvement in range quality of nearly an order of magnitude during solar conjunction have demonstrated the importance of this differenced data type.

A summary of per pass (1σ) data noise is shown against SEP angle in Fig. 9. The improvement in the differenced doppler data noise is not as good as that of the Mariner 10 solar conjunction, which had a factor of 5 or better improvement. This difference is not well understood. A possible explanation is that the Pioneer 10 and 11 spacecraft were 8 and 5 AU, respectively, away and thus the signal-to-noise ratio was low compared to Mariner 10 data. Consequently, this tended to cause cycle slipping in the two-way or three-way doppler, which would degrade the differenced doppler.

IV. Conclusion

The results of this study have demonstrated the navigational capability based on a short arc of QVLBI doppler during Jupiter encounter and the improved data quality of this data type during solar conjunction. With only two weeks of QVLBI doppler at 3 days before encounter, the prediction at Jupiter *B*-plane was good to 400 km. This differenced doppler has improved the data noise during solar conjunction by a factor of 2 to 3. During a time of active solar activities, the integrated doppler (range) noise was reduced by nearly an order of magnitude after differencing.

Acknowledgement

The author would like to thank Anton Lubeley for his assistance in data processing.

References

1. Ondrasik, V. J., and Rourke, K. H., "Applications of Quasi-VLBI Tracking Data Types to the Zero Declination and Process Noise Problems," paper presented at AAS/AIAA Astrodynamics Specialties Conference, AAS No. 71-339, August 17, 1971.

2. O'Reilly, B. B., and Chao, C. C., "An Evaluation of QVLBI OD Analysis of Pioneer 10 Encounter Data in the Presence of Unmodeled Satellite Accelerations," The Deep Space Network Progress Report 42-22, May-June 1974, Jet Propulsion Laboratory, Pasadena, California.

3. Chao, C. C., and Ondrasik, V. J., "The QVLBI Doppler Demonstration Conducted with Mariner 10," JPL Deep Space Network Progress Report 42-47, March-April 1975.

4. Anderson, J. D., Null, G. W., and Wong, S. K., "Gravity Results from Pioneer 10 Doppler Data," *Journal of Geophysical Research*, Vol. 79, No. 25, Sept. 1974.

Table 1. Data summary during Pioneer II encounter

Station ID	Data type	Time of earliest point	Time of latest point	Total points
DSN-43	F2—S	03 NOV 74 10:10:32.00	12 DEC 74 12:55:32.00	919
DSN-63	F2—S	03 NOV 74 17:35:32.00	12 DEC 74 22:30:32.00	831
DSN-14	F2—S	06 NOV 74 02:09:32.00	13 DEC 74 00:59:32.00	588
DSN-14	ETR—S	07 NOV 74 02:30:30.00	01 DEC 74 03:20:30.00	3
DSN-43	ETR—S	13 NOV 74 08:55:30.00	10 DEC 74 07:05:30.00	3
DSN-63	F3C—S	15 NOV 74 14:37:32.00	12 DEC 74 12:59:02.00	71
DSN-14	F3C—S	15 NOV 74 22:47:32.00	12 DEC 74 21:13:32.00	135
DSN-43	F3C—S	18 NOV 74 04:45:32.00	13 DEC 74 03:38:32.00	152

QVLBI: Data	Weight
F3C	0.005 Hz
ETR	10 km
F2	0.5 Hz

Table 2. Estimated and consider parameters and the a priori values

Name	DX	Sigma	A priori sig.	New value	Previous	Nominal
			Estimated parameters			
X	−0.20963859+003	0.12816+005	0.10000+005	−0.2616640180689983+008	−0.26166192+008	−0.26166166+008
Y	0.94837902+003	0.52173+005	0.10000+005	0.2884050131638451+008	0.28839553+008	0.28839064+008
Z	−0.29388873+004	0.16898+006	0.10000+005	0.1040944516061885+008	0.10412384+008	0.10413440+008
DX	0.39066160−004	0.33225−002	0.10000+001	0.6129445346992491+001	0.61294063+001	0.61294066+001
DY	−0.22425842−003	0.13698−001	0.10000+001	−0.6547890364795064+001	−0.65476661+001	−0.65476163+001
DZ	0.62536468−003	0.43661−001	0.10000+001	−0.2471630467680742+001	−0.24722558+001	−0.24723309+001
A1001	0.13401015−010	0.30045−010	0.10000−010	0.1340101533576107−010	0.00000000	0.00000000
A1002	−0.62326979−011	0.23034−009	0.10000−010	−0.6232697922876701−011	0.00000000	0.00000000
A2001	0.10147428−020	0.31975−019	0.31623−017	0.1014742772031248−020	0.00000000	0.00000000
A2002	0.48452651−020	0.15498−018	0.31623−017	0.4845265095899446−020	0.00000000	0.00000000
			Consider parameters			
GM5	Mass of Jupiter		0.25000+004			0.12671303+009
J502	J2 of Jupiter		0.44159−003			0.14730637−001
J504	J4 of Jupiter		0.60000−003			−0.59322944−003
501GM	Masses of the four satellites		0.75000+002			0.59369039+004
502GM			0.75000+002			0.32476577+004
503GM			0.10000+003			0.98766103+004
504GM			0.21500+003			0.71323529+004
LO14	Station longitude		0.10000−003			0.24311052+003
LO43			0.10000−003			0.14898130+003
LO63			0.10000−003			0.35575202+003
CU14	Spin axis distance		0.10000−001			0.52039962+004
CU43			0.10000−001			0.52052508+004
CU63			0.10000−001			0.48624504+004
DMW5	Set III ephemerides of Jupiter		0.70520−006			0.44149977−006
DP5			0.53292−006			0.16706886−006
DQ5			0.52240−006			0.26149561−006
EDW5			0.26653−006			−0.58308401−007
DA5			0.28634−007			−0.15887297−007
DE5			0.26127−006			−0.24894730−006

Table 3. Summary of estimated values of the dynamic constants of the Jupiter system

	Sampson (1921)	de Sitter (1931)	Pioneer 10, Anderson, et al.	Pioneer 11, simultaneous 2-way and 3-way doppler
GM_5			$126{,}713{,}600 \pm 2500$	$126{,}714{,}027 \pm 4000$
J_2			$(1.4720 \pm 0.0040) \times 10^{-2}$	$(1.4754 \pm 0.0022) \times 10^{-2}$
J_4			$(-6.5 \pm 1.5) \times 10^{-4}$	$(-5.97 \pm 3.66) \times 10^{-4}$
GM_{Io}[a]	4.497	3.81 ± 0.40	4.696 ± 0.06	4.606 ± 0.03
GM_{Europa}	2.530	2.48 ± 0.07	2.565 ± 0.06	2.519 ± 0.13
$GM_{Ganymede}$	7.988	8.17 ± 0.13	7.845 ± 0.08	7.878 ± 0.48
$GM_{Callisto}$	4.504	5.09 ± 0.53	5.603 ± 0.17	5.637 ± 0.11

[a]The satellite masses are in units of the mass of Jupiter $\times 10^{-5}$.

Table 4. Data summary of Pioneer 11 solar conjunction

	3-way doppler			2-way doppler			Differenced doppler	
Date	DSS	No. of data	Data noise, Hz	DSS	No. of data	Data noise, Hz	No. of data	Data noise, Hz
3/1	44	24	Bad	12	28	0.014	0	
3/23	42	149	0.16	14	145	0.10	145	0.16
3/29	11	14	0.025	61	106	0.026	14	0.0098
3/31	11	58	0.017	61	56	0.018	56	0.0089

Table 5. Data summary of Pioneer 10 solar conjunction

	2-way doppler			Differenced doppler		
Date	DSS	No. of data	Data noise, Hz	DSS	No. of data	Data noise, Hz
3/22	12	36	0.0134	44	36	0.0132
3/30	14	13	0.48	43	13	0.286
	14	35	0.212	43	35	0.092

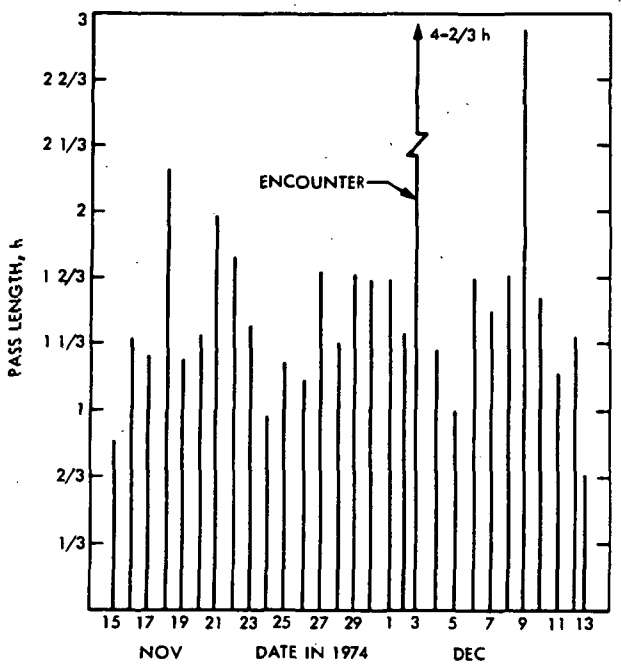

Fig. 1. QVLBI doppler data distribution

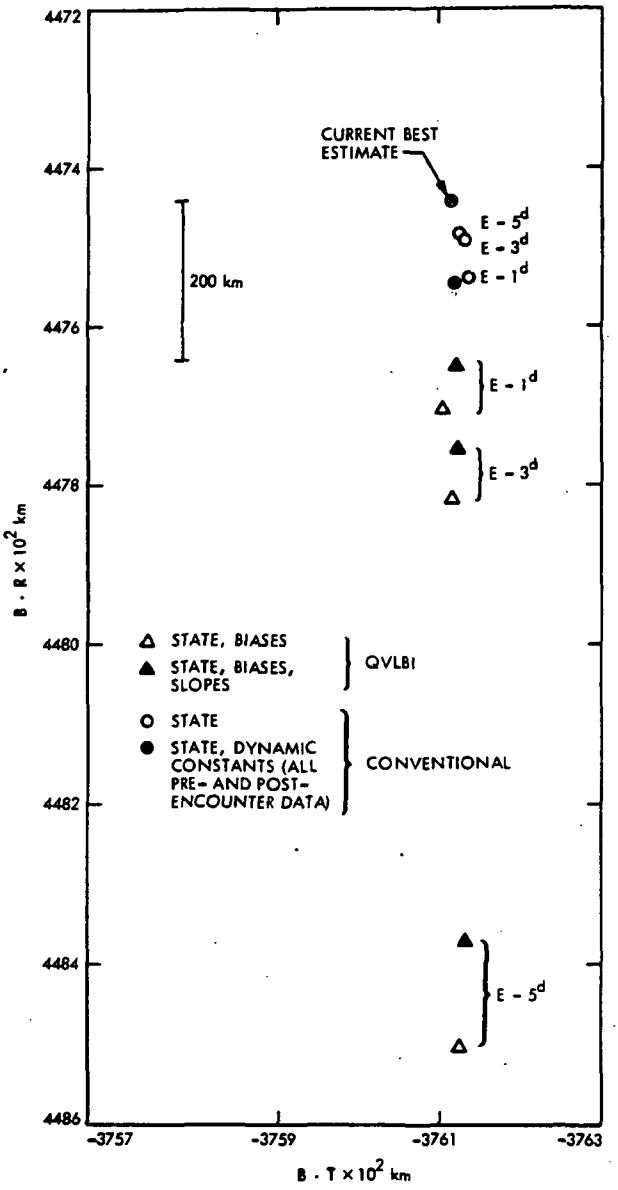

Fig. 2. Jupiter B-plane predictions

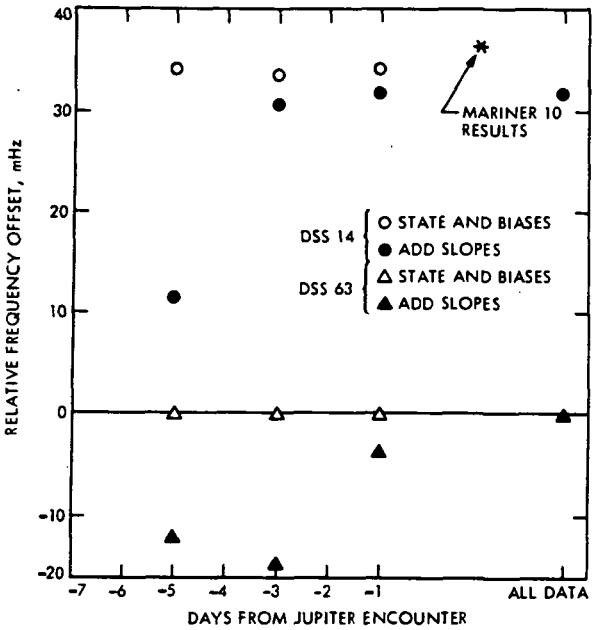

Fig. 3. Estimated values of frequency offset (all relative to DSS 43)

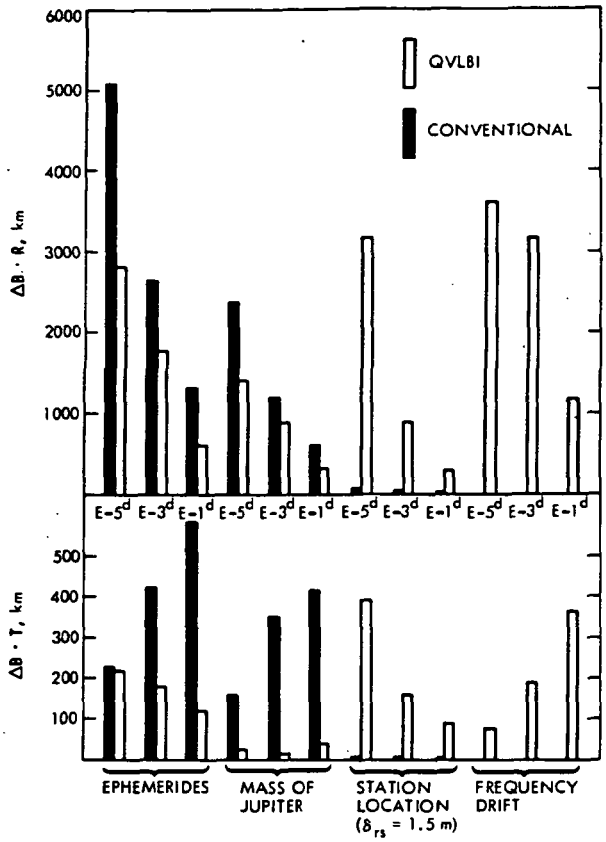

Fig. 4. Sensitivity at *B*-plane due to various error sources

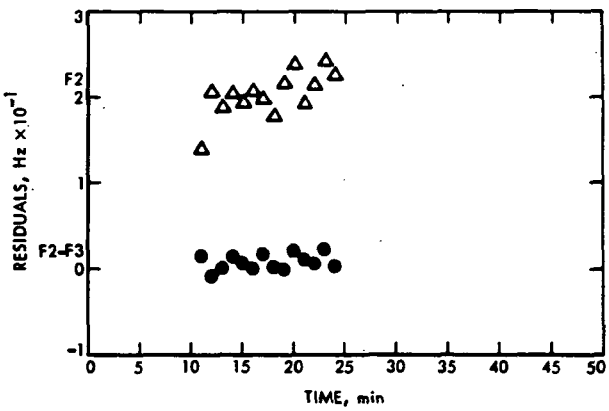

Fig. 5. Residuals of 2-way and differenced doppler on March 29 (Pioneer 11), when SEP = 4 deg

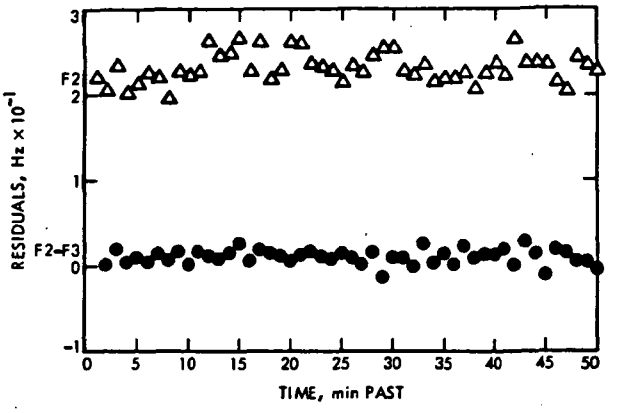

Fig. 6. Residuals of 2-way and differenced doppler on March 31 (Pioneer 11), when SEP = 5 deg

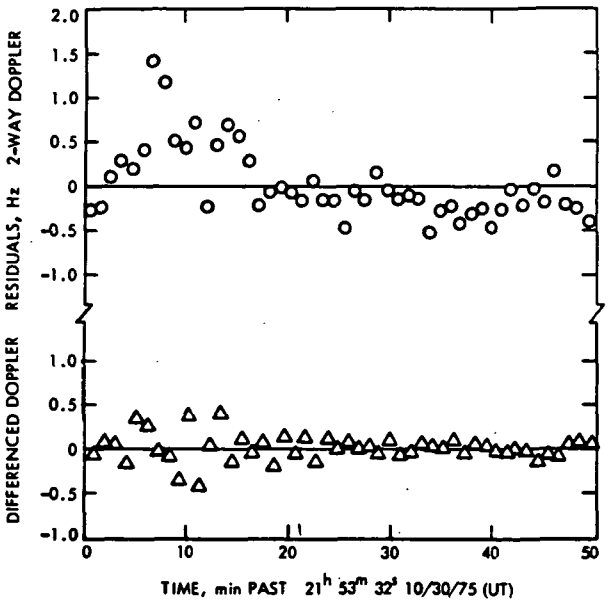

Fig. 7. Residuals of 2-way and differenced doppler during Pioneer 10 solar conjunction (SEP = 4 deg)

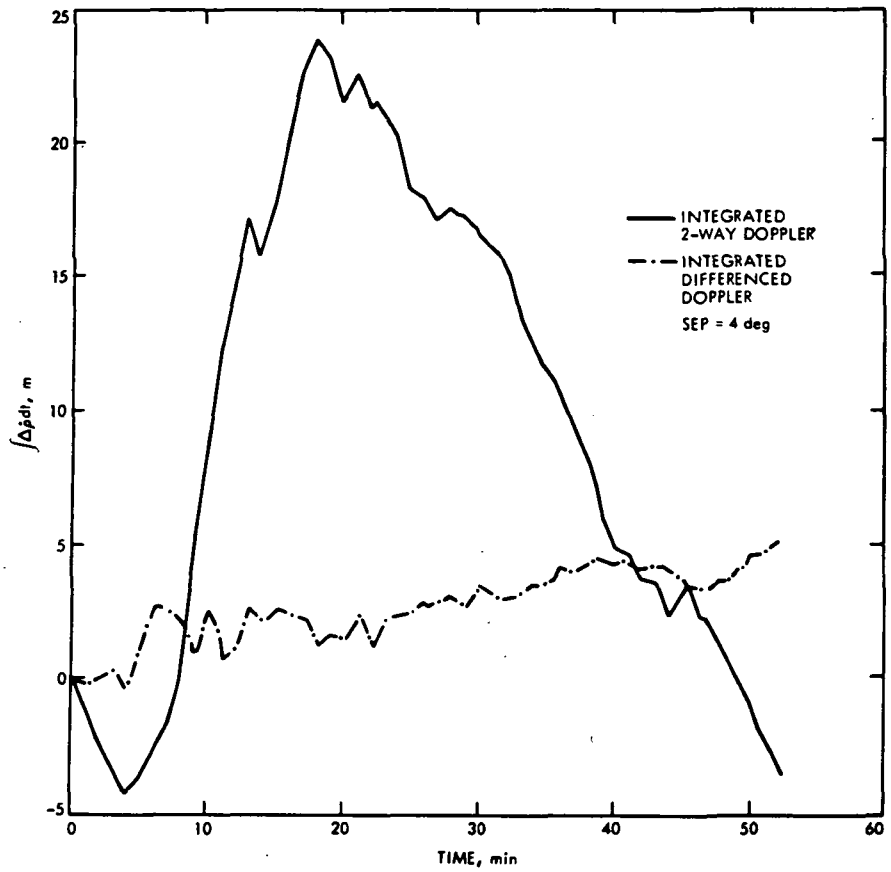

Fig. 8. Integrated doppler residuals during Pioneer 10 solar conjunction

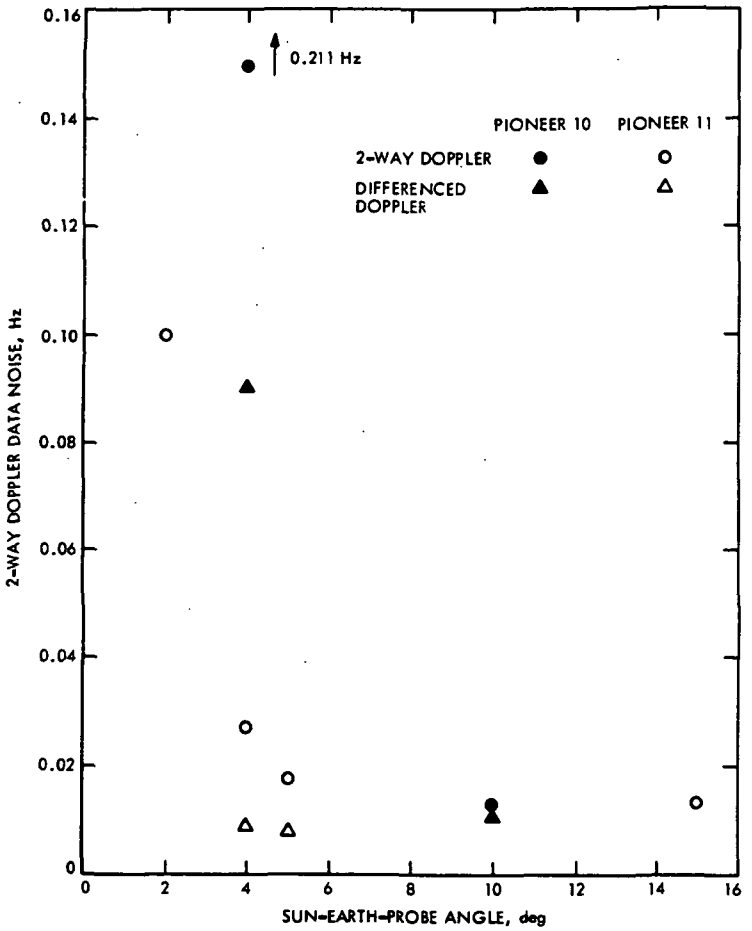

Fig. 9. Per pass 2-way and differenced doppler data noise vs. Sun–Earth–probe angle

Threshold Analysis for VLBI Delay and Doppler

J. W. Layland
Communications Systems Research Section

This article considers the problem of estimating the delay difference and doppler frequency difference for the arrival of a white noise signal from a distant Quasar at two widely separated receiving stations on Earth. The nonlinear Barankin bound is reviewed as it applies to the very long baseline interferometry (VLBI) problem, and used to evaluate the signal-to-noise ratio threshold for VLBI Estimates. We conclude by comparing the performance of several sampling strategies for VLBI data.

I. Introduction

This article considers the problem of estimating the delay difference and doppler frequency difference for the arrival of a white noise signal from a distant Quasar at two widely separated receiving stations on Earth. At both receiving stations, the signal is corrupted by additive white Gaussian noise, and further, by filtering, and perhaps other processing. This additive noise is statistically independent of the signal, and the noises at the two stations are independent of each other. Our parameter estimator is that parameter transformation which maximizes the cross correlation between the corrupted signals received at the two stations. If the signal-to-noise ratio (SNR) in this estimator is sufficiently high, the maximizing parameters are well-defined, and the calculation of estimator variance is quasi-linear. As the estimator SNR decreases, the problem becomes distinctly nonlinear, and bounds or approximations are required. The SNR at which the nonlinear effects become important is called the threshold of the system.

The bounds derived by Barankin (Ref. 1) for estimation error under a wide variety of conditions apply here. These bounds include the quasi-linear Cramer-Rao bound as a special case. Swerling (Ref. 2) has applied the Barankin bounds to the variance of the estimate of time delay and doppler shift for a radar signal, and McAulay and Seidman (Ref. 3) have applied it to a threshold analysis for pulse-position modulation. The VLBI problem can be transformed in a systematic way to the problem of estimating the parameters of a "known" wideband Gaussian signal in wideband Gaussian noise, so that much of this above-cited work can be directly applied.

II. The Barankin Bound

For the approximate application of the Barankin bound to the VLBI problem, it is convenient to follow the notation and arguments of Swerling (Ref. 2). A more rigorous and exact formulation could be built from the formulations used by Barankin (Ref. 1) or Kiefer (Ref. 4).

Let $\{F(t,\xi)\}$ be a family of real-valued functions of time t and defining parameter vector ξ. We wish to estimate some of the components of ξ by observing functions $Z(t)$ over $T_1 \leq t \leq T_2$ where

$$Z(t) = F(t,\xi) + x(t) \tag{1}$$

and where $x(t)$ is a real-valued Gaussian random process with zero-mean and covariance function $\psi_x(s,t)$. Given appropriate conditions, $x(t)$ can be expanded in the Karhunen-Loueve Series

$$x(t) = \sum_{i=1}^{\infty} \frac{x_i}{\sqrt{\chi_i}} \phi_i(t) \tag{2}$$

where the x_i are independent, zero-mean, unit-variance Gaussian random variables, and χ_i, $\phi_i(t)$ are the eigenvalues and orthonormal eigenfunctions of the integral equations

$$\phi(s) = \chi \int_{T_1}^{T_2} \psi_x(s,t)\,\phi(t)\,dt \tag{3}$$

We further suppose that for all ξ, we can express

$$F(t,\xi) = \sum_{i=1}^{\infty} \beta_i(\xi) \cdot \phi_i(t) \tag{4}$$

over the observation interval, where

$$\beta_i(\xi) = \int_{T_1}^{T_2} F(t,\xi)\,\phi_i(t)\,dt \tag{5}$$

Barankin's result for the greatest lower bound to the variance of any estimator for ξ is

$$\sigma^2 \geq \frac{\left[\sum_{k=1}^{K} (\xi_k' - \xi_0) \cdot a_k\right]^2}{\sum_{k=1}^{K}\sum_{l=1}^{K} G(\xi_k', \xi_l'' | \xi_0) \cdot a_k a_l} \tag{6}$$

where ξ_0 is the true parameter value, K is any finite integer, the ξ_k' are alternate parameter values, and the a_k are arbitrary real numbers. In the above notation, the function $G(\cdot,\cdot|\cdot)$ is defined by

$$G(\xi', \xi'' | \xi_0) = \exp\left\{\sum_{i=1}^{\infty} \chi_i \left[\beta_i(\xi') - \beta_i(\xi_0)\right]\left[\beta_i(\xi'') - \beta_i(\xi_0)\right]\right\} \tag{7}$$

This bound may be made arbitrarily tight by appropriate choices of K and $\{a_k, \xi_k'\}$.

The Cramer-Rao bound can be derived from Eq. (6) by taking a limit as two of the ξ_k' smoothly approach each other at ξ_0, and their corresponding a_k grow equally and oppositely to infinity. The resulting zeroth-index derivative term can be included in the bound (6) as (Ref. 3)

$$\sigma^2 \geq \frac{\left[a_0 + \sum_{k=1}^{\infty} a_k(\xi_k' - \xi_0)\right]^2}{\sum_{k=0}^{\infty}\sum_{l=0}^{\infty} a_k a_l d_{k,l}} \tag{8}$$

where

$$d_{00} = \frac{\partial}{\partial \xi'} \frac{\partial}{\partial \xi''} G(\xi', \xi'' | \xi_0)\big|_{\xi' = \xi'' = \xi_0}$$

$$d_{0k} = d_{k0} = \frac{\partial}{\partial \xi'} G(\xi', \xi_k'' | \xi_0)\big|_{\xi' = \xi_0, k \in [1,K]}$$

$$d_{k,l} = G(\xi_k', \xi'' | \xi_0)\big|_{k,l \in [1,K]} \tag{9}$$

Equation 8 is the Cramer-Rao Bound if $a_i = 0$, for all $i > 0$. Continuing to follow Ref. 3, let A denote the column vector of the a_i, and N denote the column vector of the n_i defined by $n_0 = 1$, $n_i = \xi_i' - \xi_0$ for $i \in [1, K]$. If D denotes the matrix of $\{d_{kl} | k, l \in 0, K\}$, then the bound may be rewritten as

$$\sigma^2 \geq A^t N N^t A / A^t D A \tag{10}$$

The right-hand-side of Eq. (10) is maximized by letting $A = \lambda D^{-1} N$, for any λ, so that the greatest lower bound on the variance is

$$\sigma^2 \geq N^t D^{-1} N \tag{11}$$

We will apply this form of the Barankin Bound to the VLBI estimation problem.

III. Very Long Baseline Interferometry Detection and Parameter Estimation

Figure 1 shows an overview of the features of the VLBI problem. The white noise signal from the radio star is received at the two stations with some relative delay and doppler offset which can be related to Earth's rotational

position and velocity. Local ambient noise, usually much stronger than the radio-star signal, is added at each receiver, and the resultant is filtered, translated by a local oscillator to a manageable frequency and bandwidth, and then sampled, hard-clipped, and recorded. The recorded signals are then brought together at leisure, modified by an a priori estimate of the relative delay and doppler, and cross-correlated. Refined estimates of the delay and doppler are extracted from this cross-correlation.

The input to the cross-correlator from station 1 may be denoted as $x_{j+k} = \text{Sign}\{S(j+k, \hat{f}) + n_1(j+k, \hat{f})\}$, and the input from station 2 may be denoted $y_j = \text{Sign}\{S^*(j+d, f_0) + n_2(j, f_0)\}$. Here $S^*(\cdot,\cdot)$ is the naturally delayed and doppler-shifted version of $S(\cdot,\cdot)$, and k and $\hat{f}$ are our a priori estimates of this delay and doppler, respectively. Because of their origins as white noise, and subsequent filtering, $S(\cdot,\cdot)$ and $n_1(\cdot,\cdot)$ have identical autocorrelation functions, as do $S^*(\cdot,\cdot)$, and $n_2(\cdot,\cdot)$.The cross-correlation

$$Z(k,f) = \sum_j x_{j+k} \cdot y_j \tag{12}$$

is evaluated as a function of k and f near its maximum. The final estimate of the actual delay and doppler is made much finer than the integral steps in k.

Let us denote by T_{n1} and T_{n2} the noise temperatures of the environment at stations 1 and 2, respectively, and by T_{s1} and T_{s2} the increment to these noise temperatures caused by the radio-star "signal" at the two stations. T_{s1} and T_{s2} may differ as a result of differing antenna collecting areas, efficiencies, etc. Denote as r_j and m_j the signal and noise terms respectively in x_j, and as r'_j and m'_j the signal and noise terms in y_j. By definition of the hard limiting, the average values of $(r_j + m_j)^2 = (x_j)^2 = 1$ and $(r'_j + m'_j)^2 = (y_j)^2 = 1$. Furthermore, $E_r\{(E_m\{r_j + m_j\})^2\} = (2/\pi)(T_{s1}/T_{n1})$, and $E_r\{(E_m\{r'_j + m'_j\})^2\} = (2/\pi)(T_{s2}/T_{n2})$, where E_α denotes expected value over the distribution of the random variable α, and where we assume $T_{si} \ll T_{ni}$.

Because the number of samples in the summation (12) is large, $Z(\cdot,\cdot)$ will be approximately Gaussian (by the central limit theorem), and its distribution specified by its first two moments. The first moment is

$$\begin{aligned}\overline{Z(k,f)} &= \sum_j \overline{x_{j+k} \cdot y_j} \\ &= \sum_j \overline{r_{j+k} \cdot r'_j} \\ &= N \cdot \frac{2}{\pi} \sqrt{\frac{T_{s1}}{T_{n1}} \cdot \frac{T_{s2}}{T_{n2}}} \cdot \phi(k-d, \hat{f} - f_0)\end{aligned} \tag{13}$$

where N is the number of samples, and $\phi(\cdot,\cdot)$ is the normalized autocorrelation (ambiguity) function for the filtered signal process.

The second moment is

$$\overline{Z(k,f) \cdot Z(\ell,g)} = \sum_j \sum_i \overline{[r_{j+k} + m_{j+k}][r'_j + m'_j][r_{i+\ell} + m_{i+\ell}][r'_i + m'_i]} \tag{14}$$

If we expand the right hand side of Eq. (14), and drop those terms with zero expected values,

$$\begin{aligned}\overline{Z(k,f) \cdot Z(\ell,g)} = \sum_j \sum_i \{ &\overline{r_{j+k} \cdot r_{i+\ell} \cdot r'_j \cdot r'_i} \\ &+ \overline{m_{j+k} \cdot m_{i+\ell}} \cdot \overline{r'_j \cdot r'_i} \\ &+ \overline{r_{j+k} \cdot r_{i+\ell}} \cdot \overline{m'_j \cdot m'_i} \\ &+ \overline{m_{j+k} \cdot m_{i+\ell}} \cdot \overline{m'_j \cdot m'_i} \}\end{aligned} \tag{15}$$

In order to get the most information possible on a per-sample basis, the sampling is performed at a rate such that $\overline{x_j x_k} \approx 0$ and $\overline{y_j y_k} \approx 0$ for $j \neq k$. Hence at the sample points

$$\begin{aligned}\overline{m_{j+k} \cdot m_{i+\ell}} &= \beta \cdot \overline{r_{j+k} \cdot r_{i+\ell}} \\ \overline{m'_j \cdot m'_i} &= \beta' \cdot \overline{r'_j \cdot r'_i}\end{aligned} \tag{16}$$

For some constants β, β' and any particular i, j, k, ℓ. We will assume that Eq. (16) holds at interpolated values also. With this assumption, Eq. (15) may be rewritten in a statistically-equivalent but simpler form:

$$\begin{aligned}\overline{Z(k,f)\, Z(\ell,g)} = \sum_j \sum_i \Big\{ &\overline{r_{j+k} \cdot r_{i+\ell} \cdot r'_j \cdot r'_i} \\ &+ \overline{m_{j+k} \cdot m_{i+\ell}} \cdot \overline{r'_j \cdot r'_i} \cdot \left(1 + \frac{\beta'}{\beta} + \beta'\right) \Big\}\end{aligned} \tag{17}$$

Equations (13) and (17) are representative of the detection of a known Gaussian signal, $\{r_i\}$ embedded in Gaussian noise. The constants β, and β' are

$$\begin{aligned}\beta &= 1 \Big/ \left(\frac{2}{\pi} \frac{T_{S1}}{T_{N1}}\right) - 1 \\ \beta' &= 1 \Big/ \left(\frac{2}{\pi} \frac{T_{S2}}{T_{N2}}\right) - 1\end{aligned} \tag{18}$$

On a per-sample basis, the noise-to-signal ratio for this

detection problem is

$$NSR_j = \beta + \beta' + \beta \cdot \beta'$$

$$= \frac{1}{\left(\frac{2}{\pi}\right)^2 \frac{T_{s1}}{T_{N1}} \cdot \frac{T_{s2}}{T_{N2}}} - 1 \tag{19}$$

It is convenient to consider the detection problem as if the interfering noise samples have unit variance. If it is so normalized, each of the "signal" samples has energy given by $E_s = 1/NSR_j$, or

$$E_s = \frac{\left(\frac{2}{\pi}\right)^2 T_{s1} \cdot T_{s2}}{T_{N1} \cdot T_{N2} - \left(\frac{2}{\pi}\right)^2 T_{s1} \cdot T_{s2}} \tag{20}$$

With the VLBI parameter estimation problem thus transformed to one of parameter estimation for a known signal in noise, the formulation of the Barankin bound (Eq. 8) is directly applicable. Since the sequence of samples of the signal and noise processes at both stations are virtually independent from sample-to-sample, we take as the orthonormal basis for the signal set, the sequence of sample functions themselves. We normalize so that the interfering noise samples have unit variance, and hence so $\chi_j = 1$, for all sample indices j. The signal projections $\beta_j(\cdot)$ are a scaled version of the r_j. The number of samples, N from which the estimates of delay and doppler are made, is large, so that central limit theorem applies, and

$$\sum_j \chi_j \beta_j(\xi) \cdot \beta_j(\xi') \simeq N \cdot E\{\beta_j(\xi) \cdot \beta(\xi')\} \tag{21}$$

Or using the normalized autocorrelation function $\phi(\cdot,\cdot)$:

$$\sum_{j=1}^{N} \chi_j \beta_j(\xi) \cdot \beta_j(\xi') \simeq N \frac{\left(\frac{2}{\pi}\right)^2 T_{s1} \cdot T_{s2}}{T_{N1} T_{N2} - \left(\frac{2}{\pi}\right)^2 T_{s1} \cdot T_{s2}} \phi(\xi - \xi') \tag{22}$$

Note that here ξ denotes a vector parameter which can include delay or doppler offsets, or both.

The $G(\cdot,\cdot|\cdot)$ function for VLBI (Eq. 7) is defined by

$$G(\xi', \xi'' | \xi^0) = \exp\{R \cdot [\phi(\xi' - \xi'') - \phi(\xi' - \xi^0) - \phi(\xi'' - \xi^0) + \phi(\xi^0 - \xi^0)]\} \tag{23}$$

where

$$R = N \cdot \frac{\left(\frac{2}{\pi}\right)^2 T_{s1} \cdot T_{s2}}{T_{N1} \cdot T_{N2} - \left(\frac{2}{\pi}\right)^2 T_{s1} \cdot T_{s2}}$$

The D matrix of Eqs. (9) to (11) is defined from Eq. (23) as

$$D = \{d_{kl} | k, l = 0, \cdots, K\}$$

$$d_{k,l} = \exp\{R[\phi(0) - \phi(\xi_k'' - \xi_0) - \phi(\xi'' - \xi_0) + \phi(\xi_k'' - \xi'')]$$

for $k, l \epsilon [1, K]$ indices of alternate ξ.

$$d_{k,0} = d_{0,k} = R \cdot \frac{\partial}{\partial \xi'} [\phi(\xi' - \xi_k'') - \phi(\xi' - \xi_0)]|_{\xi' = \xi_0} \quad \text{for } k \epsilon [1, K]$$

$$d_{00} = R \cdot \frac{\partial}{\partial \xi'} \frac{\partial}{\partial \xi''} \phi(\xi' - \xi'')|_{\xi' = \xi'' = \xi_0} \tag{24}$$

Furthermore, we note that ξ_0 is presumed to be the global maximum of $\phi(\cdot)$ so that the second term of d_{0k} is trivially equal to zero. If we restrict the set of alternate ξ_k'' to local maxima of $\phi(\cdot)$, the first term of d_{0k}, and hence d_{0k} itself, is zero for all k. With this restriction on D, the Barankin bound for σ^2 becomes

$$\sigma^2 \geq \frac{1}{d_{0,0}} + N_1' D_1^{-1} N_1 \tag{25}$$

where the subscripts 1 in the second term of Eq. (25) are meant to imply that the zero-index row and column have been dropped. The first term of Eq. (25) is the Cramer-Rao Bound; the second is the nonlinear threshold term.

IV. A Very Long Baseline Interferometry Example

The wideband quasar noise signal is processed at the two receiving stations into a form which is suitable for recording. This processing corresponds to constraints on available equipment bandwidths, recording rates, data storage capacities, etc. The basic constraint is the bandwidth of the low-noise Maser amplifier, which we will hypothesize to be 40 MHz centered at 2 or 8 GHz for present systems. This is still too wide for any but the fastest recorders, and is further reduced by filtering several narrow channels from the passband which span the full bandwidth available (bandwidth synthesis); or by sampling the full bandwidth into a buffer memory, and

then recording at a slower rate once that buffer is filled (burst mode). Both sampling modes have side-lobes in the delay-estimator which arise at roughly the reciprocal of the spanned bandwidth (10^{-6} sec). There are also side-lobes in the frequency estimator at roughly the reciprocal of the recording or sampling interval (10^{-2} Hz). Burst sampling will generate additional sidelobes spaced a few Hz away from the true frequency, but these should be able to be removed by a priori knowledge, as should some of the more widely spaced side lobes in time-delay.

Bandwidth synthesis systems which have been proposed utilize two channels at the extremes of the available bandwidth, plus a third channel placed somewhere between to reduce the sidelobe amplitudes. The exact sidelobe structure is sensitive both to the position of this third channel, and to the bandwidth of the channels. For an overall spanned bandwidth of 40 MHz, a reasonably tolerable side-lobe structure is achieved if the third channel is located 5 MHz from the passband center. While this position is perhaps not optimum, it offers near optimum side-lobe suppression which is far better than that provided at many alternative positions, such as at, e.g., 6 MHz. Figure 2 shows the effect of varying the individual channel widths for a 40-MHz spanned bandwidth with the third channel located at 5 MHz. The function plotted is the aggregate autocorrelation function for the three recorded channels, which results with optimum use of all available information. The recording bandwidths are 6 MHz, 4 MHz and 2 MHz for Figs. 2a, 2b, and 2c, respectively. The corresponding Barankin lower bound to delay estimate error is shown in Fig. 3, lines B, C, and D, respectively. As could be anticipated from the sidelobe structure of Fig. 2, the threshold performance degrades seriously as the individual channel bandwidth is narrowed, and would continue to degrade if the recording bandwidth were reduced further. At Estimator signal-to-noise ratios well above threshold, the delay estimate error depends only minimally upon the individual channel bandwidths.

Figure 3 also shows the Barankin lower bound to the delay estimate error achieved by a full bandwidth 40-MHz Burst Mode System (line A). The autocorrelation function is the familiar $\sin(x)/x$. Threshold performance of the burst mode sampling is better by about 2 to 3 dB than that for bandwidth synthesis with 6-MHz channels, and better by about 10 dB than that for bandwidth synthesis with 2-MHz channels. At high SNRs, however, the delay estimate error is 2 dB worse for burst mode than for bandwidth synthesis.

The doppler estimator error has not been calculated per se, but its shape can be inferred as follows: The recording of data is approximately uniform in time over some fixed interval. Accordingly the transform of this interval is the $\sin(x)/x$ function and the doppler estimate error is identical to line A of Fig. 3 with the abscissa relabeled as appropriate: for example, if the recorded sample occupied 40 sec, then $\sigma_\tau = 10^{-6}$ sec on Fig. 3, line A is comparable to $\sigma_f = 10^{-3}$ Hz.

V. System Implications

One can draw a variety of conclusions from Figure 3, depending upon where and how he looks. Above threshold, for example, a three-fold improvement in delay estimate error requires roughly a 10-dB increase in estimator SNR, or a hundred-fold increase in the number of samples processed. This is a potentially expensive way to gain accuracy. This improvement in accuracy could perhaps be better achieved by other means, such as increasing the spanned bandwidth, if possible, and operating the system at some nominal margin above its threshold. We would like furthermore to be able to operate with a performance curve like Fig. 3A or Fig. 3B with a threshold as low as possible to minimize the amount of data needed to ensure above-threshold operation. Line 3B corresponds to a recording channel bandwidth of 15 percent of the spanned bandwidth, and for spanned bandwidths which are significantly larger than the 40 MHz considered here, it suggests that the use of a combined burst/bandwidth synthesis recording is desirable. For example, it does not appear reasonable to burst-sample a 200-MHz spanned bandwidth with present-day equipment, but 15 percent bandwidth channels, each 30 MHz wide, could be easily burst-sampled and recorded. Such operation would lead to a performance curve of the type of line B, Fig. 3, but with the delay-estimate error in the above-threshold region reduced five-fold by the increased spanned bandwidth.

References

1. Barankin, E. W., "Locally Best Unbiased Estimates," *Ann. Math. Stat.*, Vol. 20, pp. 477–501, 1949.

2. Swerling, P., "Parameter Estimation for Waveforms in Additive Gaussian Noise," *J. SIAM*, Vol. 7, pp. 154–166, 1959.

3. McAulay, R. J. and Seidman, L. P., "A Useful Form of the Barankin Lower Bound and Its Application to PPM Threshold Analysis," *IEEE Transactions on Information Theory*, Vol. IT-15, No. 2, pp. 273–279, March 1969.

4. Kiefer, J., "On Minimum Variance Estimators," *Ann. Math Stat.*, Vol. 23, pp. 627–629, 1952.

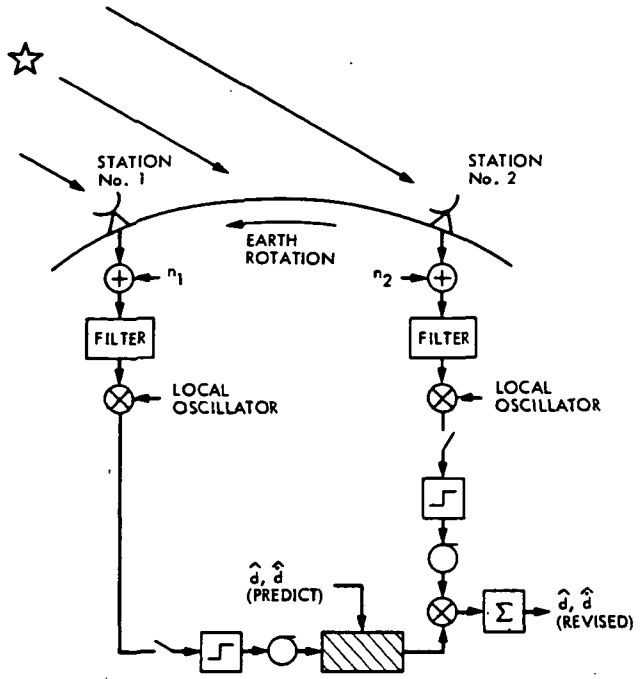

Fig. 1. Overview of VLBI receiving/processing functions

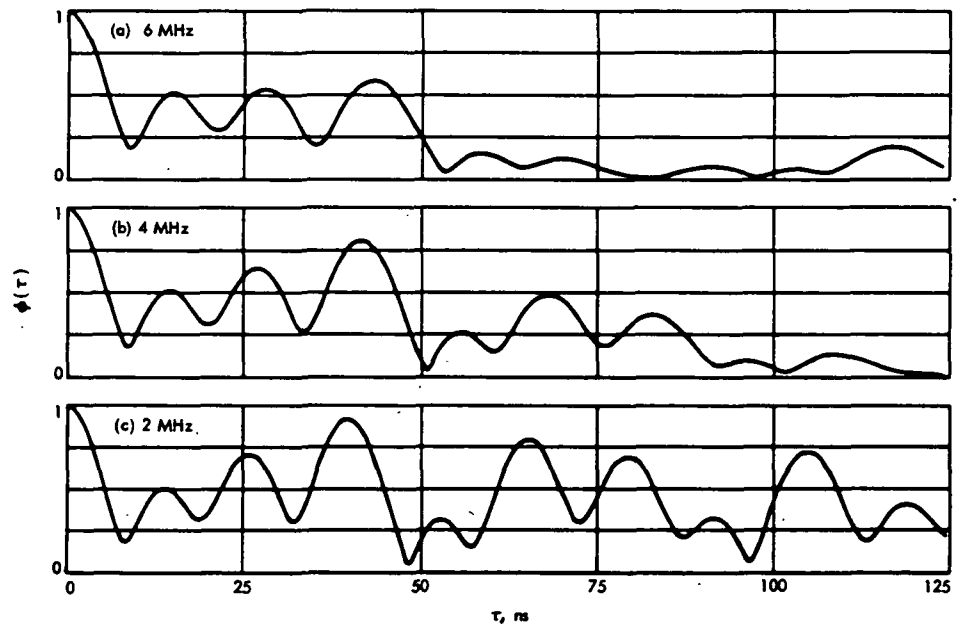

Fig. 2. Aggregate autocorrelation functions for 3-channel bandwidth synthesis with: (a) 6 MHz channels, (b) 4 MHz channels, (c) 2 MHz channels

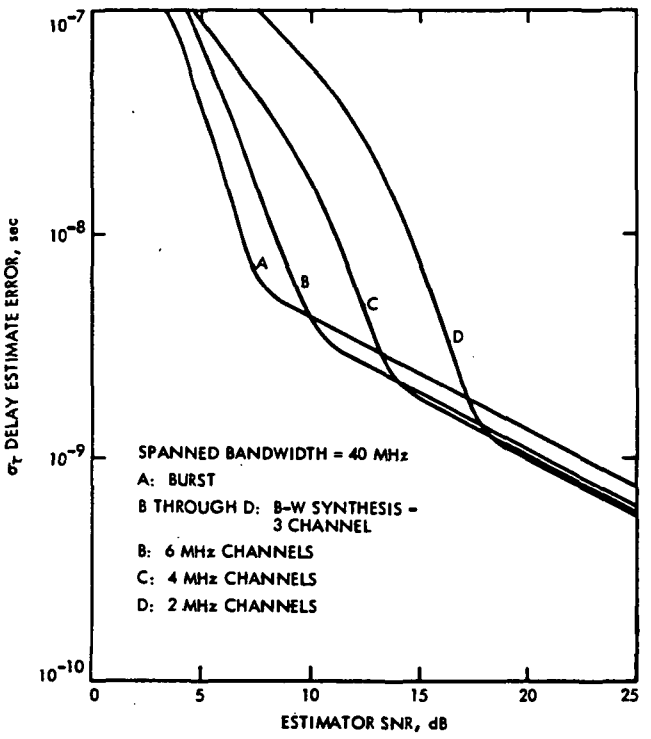

Fig. 3. Delay estimate error vs. estimator SNR in dB

Analysis of Command Detector Signal-to-Noise Ratio Estimator

R. G. Lipes
Communications Systems Research Section

We have investigated a specific technique for making $(SNR)^{1/2}$ estimates by using in-phase channel output averages to estimate signal and quadrature channel output averages to estimate noise. We have produced bounds to determine the accuracy of this technique when fluctuations of one standard deviation occur. Our results show the estimate is relatively independent of actual input signal-to-noise ratio (SNR) and can be improved only by increasing the number of samples in the averages.

I. Introduction

The present design of a command detector being developed for NASA calls for a signal-to-noise ratio (SNR) estimate that will be used for monitoring operations of the detector. Naturally, we wish to know for a given SNR and number of samples how good the estimate will be. The samples are derived from in-phase and quadrature outputs that are effectively data and error integrators. As is to be expected, the command detector circuitry must be as simple as possible. For this reason the absolute value of the in-phase and quadrature outputs rather than their squares will be sampled. Furthermore, since samples of the absolute value of the output provide an estimate of the square root of the SNR rather than the SNR itself, in this report we will be concerned with the relationship between SNR, number of samples, and the estimated square root of SNR. We will use the ratio of the mean plus standard deviation of the estimate to actual $(SNR)^{1/2}$ as a measure of the accuracy of the estimate. This ratio will be determined as a function of number of samples.

In Section II, we will model the probability distribution of the in-phase and quadrature outputs and develop an estimate for the square root of SNR. In Section III we will give bounds for the mean and variance of this estimate that converge to the exact values as the number of samples becomes large. Because these asymptotically tight bounds are easily calculated, they are presented rather than the exact values whose integral representations required numerical integration for evaluation. Finally, in Section IV we will discuss results and conclusions.

II. Probability Distribution of Samples and Development of Estimate

A. Data Integrator Output

The output of the in-phase or data channel is integrated for one symbol time T. The absolute value of the resulting integration becomes a single sample so that the ith sample X_i can be expressed as

$$X_i = \left| \int_{t_i}^{t_i+T} [d(t) + n_I(t)]\, dt \right| \tag{1}$$

where $d(t)$ is the data assumed to be $\pm A$ over one symbol time, and $n_I(t)$ is the noise of the in-phase channel assumed to be white Gaussian. Thus,

$$X_i = \left| \pm AT + \int_{t_i}^{t_i+T} n_I(t)\, dt \right| \tag{2}$$

The random variable

$$Z_{I,i} \equiv \int_{t_i}^{t_i+T} n_I(t)\, dt$$

is zero mean Gaussian with variance

$$\sigma^2 = \int_{t_i}^{t_i+T} dt \int_{t_i}^{t_i+T} ds\, \overline{n_I(t)\, n_I(s)} = \frac{N_0 T}{2} \tag{3}$$

where $N_0/2$ is the power spectral density of $n_I(t)$. Since the noise is assumed white Gaussian and the samples X_i are taken from non-overlapping intervals, they are independent and identically distributed. From Eqs. (2) and (3) we have for the probability density

$$P_X(\alpha) = \begin{cases} \dfrac{1}{(2\pi\sigma^2)^{1/2}} \left\{ \exp\left[-\dfrac{1}{2\sigma^2}(\alpha - AT)^2 \right] \right. \\ \left. + \exp\left[-\dfrac{1}{2\sigma^2}(\alpha + AT)^2 \right] \right\}, & \alpha \geq 0 \\ 0, & \alpha < 0 \end{cases} \tag{4}$$

where $\sigma^2 = N_0 T/2$.

B. Error Integrator Output

The output of the quadrature or error channel is also integrated for one symbol time and the absolute value taken to form a single sample Y_i:

$$Y_i = \left| \int_{t_i}^{t_i+T} n_Q(t)\, dt \right| \tag{5}$$

where $n_Q(t)$ is the noise of the quadrature channel also assumed to be white Gaussian with power spectral density $N_0/2$. Because the samples Y_i are taken from non-overlapping intervals, they are independent and identically distributed. Their probability density is obtained from Eq. (4) with $AT = 0$:

$$P_Y(\alpha) = \begin{cases} \dfrac{2}{(2\pi\sigma^2)^{1/2}} \exp\left[-\dfrac{\alpha^2}{2\sigma^2} \right], & \alpha \geq 0 \\ 0, & \alpha < 0 \end{cases} \tag{6}$$

C. Development of Estimate

The output of the in-phase channel before the absolute value is taken is

$$\int_{t_i}^{t_i+T} [d(t) + n_I(t)]dt = \pm AT + Z_{I,i} \tag{7}$$

The square of the mean of this output is $(AT)^2$ while its variance (Eq. 3) is $\sigma^2 = N_0 T/2$. Conventionally, the input SNR is defined as the bit signal energy divided by the one-sided noise spectral density or

$$\frac{A^2 T}{N_0} = \frac{1}{2} \frac{(AT)^2}{(N_0 T/2)}$$

Thus the signal-to-noise ratio estimator of the command detector will estimate the quantity

$$(\mathrm{SNR})^{1/2} \equiv \left[\frac{(AT)^2}{2(N_0 T/2)} \right]^{1/2} = \frac{AT}{\sigma} \frac{1}{2^{1/2}} \tag{8}$$

In Appendix A we show that the mean of the sample X_i (Eq. 1) is given by

$$\overline{X_i} = AT\left[1 + 2\epsilon\left(\frac{AT}{\sigma} \right) \right] \tag{9}$$

where the function $\epsilon(AT/\sigma)$ is defined by Eq. (A-4) of Appendix A. This function is sufficiently complicated so that forming an unbiased estimate of AT using only the $\{X_i\}$ is not feasible. Nevertheless, for input SNRs greater than 3 dB (the design point input SNR for the command detector is 10.5 dB), $|\epsilon| \leq 0.0042$. Consequently we can neglect ϵ and employ M samples of the $\{X_i\}$ to form our estimate ν of AT:

$$\nu \equiv \frac{1}{M} \sum_{i=1}^{M} X_i \tag{10}$$

From Appendix A by setting $AT = 0$, we find the mean of Y_i:

$$\overline{Y}_i = \left(\frac{2}{\pi}\right)^{1/2}\sigma = \left(\frac{2}{\pi}\right)^{1/2}\left(\frac{N_0 T}{2}\right)^{1/2} \tag{11}$$

Thus, an unbiased estimate of σ would be

$$\Delta \equiv \frac{1}{M}\left(\frac{\pi}{2}\right)^{1/2}\sum_{i=1}^{M} Y_i$$

However, σ is in the denominator of Eq. (8), so Δ^{-1} will not provide an unbiased estimate of σ^{-1}. As we show in Appendix B as $M \to \infty$, $\overline{\Delta^{-1}} \to \sigma^{-1}$ so we will use Δ^{-1} as an estimate of σ^{-1} even though it is not unbiased. Our estimate W of $(\mathrm{SNR})^{1/2}$ is, therefore,

$$W \equiv \frac{\nu\Delta^{-1}}{2^{1/2}} = \left(\frac{1}{M}\sum_{i=1}^{M} X_i\right)\left(\frac{1}{M}\left(\frac{\pi}{2}\right)^{1/2}\sum_{i=1}^{M} Y_i\right)^{-1}\frac{1}{2^{1/2}} \tag{12}$$

where we note that $\{X_i\}$ and $\{Y_i\}$ are statistically independent.

III. Expressions for the Mean and Variance of Estimate

The mean and variance of our estimate W are given by

$$\overline{W} = \overline{\nu}\,\overline{\Delta^{-1}}\,\frac{1}{2^{1/2}} \tag{13a}$$

$$2\sigma_W^2 = \overline{\nu^2}\,\overline{\Delta^{-2}} - (\overline{\nu})^2(\overline{\Delta^{-1}})^2 = \sigma_\nu^2\sigma_{\Delta^{-1}}^2 + \sigma_\nu^2(\overline{\Delta^{-1}})^2 + (\overline{\nu})^2\sigma_{\Delta^{-1}}^2 \tag{13b}$$

The mean of ν is $\overline{X}_i$ and is given by Eq. (9), while the variance is $1/M$ times the variance of X_i; so from Appendix A:

$$\sigma_\nu^2 = \frac{1}{M}\sigma^2\left\{1 - 4\left(\frac{AT}{\sigma}\right)^2\left[\epsilon^2\left(\frac{AT}{\sigma}\right) + \epsilon\left(\frac{AT}{\sigma}\right)\right]\right\} \tag{14}$$

In Appendix B we derive integral representations for the mean and variance of Δ^{-1}, but here we will display only easily calculated bounds for these quantities that are obtained from the integral representations:

$$\frac{1}{\sigma}\frac{M}{M+1} + \frac{1}{\sigma}\frac{4M}{(M-1)(M+3)}\left(\frac{2}{\pi}\right)^{(M+1)/2} < \overline{\Delta^{-1}} \le \frac{1}{\sigma}\frac{M}{M+1} + \frac{1}{\sigma}\frac{4M}{(M-1)(M+3)}\frac{2}{\pi} \tag{15a}$$

$$\sigma_{\Delta^{-1}}^2 \le \frac{1}{\sigma^2}\left\{\frac{64M(M+1)}{(M^2-4)(M+4)}\frac{1}{\pi^2} + \frac{8M}{(M+1)(M+4)}\frac{1}{\pi} - \frac{M^2}{(M+1)^2(M+2)}\right\}$$
$$- \frac{1}{\sigma^2}\left\{\frac{8M^2}{(M^2-1)(M+3)}\left(\frac{2}{\pi}\right)^{(M+1)/2} + \left[\frac{4M}{(M-1)(M+3)}\right]^2\left(\frac{2}{\pi}\right)^{M+1}\right\} \tag{15b}$$

where the derivation requires $M > 3$. Since $(1/2)\,(AT/\sigma)^2$ is the actual SNR, we have the following bounds on our estimate W using Eqs. (9), (13), (14), and (15),

$$(\mathrm{SNR})^{1/2}\left[\frac{M}{M+1} + \frac{4M}{(M-1)(M+3)}\left(\frac{2}{\pi}\right)^{(M+1)/2}\right][1+2\epsilon] < \overline{W} \le (\mathrm{SNR})^{1/2}\left[\frac{M}{M+1} + \frac{4M}{(M-1)(M+3)}\left(\frac{2}{\pi}\right)\right][1+2\epsilon] \tag{16a}$$

$$\sigma_W^2 \le \left\{\frac{64M(M+1)}{(M^2-4)(M+4)}\frac{1}{\pi^2} + \frac{8M}{(M+1)(M+4)}\frac{1}{\pi} - \frac{M^2}{(M+1)^2(M+2)} - \frac{8M^2}{(M^2-1)(M+3)}\left(\frac{2}{\pi}\right)^{(M+1)/2}\right.$$
$$\left. + \left[\frac{4M}{(M-1)(M+3)}\right]^2\left(\frac{2}{\pi}\right)^{M+1}\right\}\left\{\frac{1}{2M}[1 - 8(\mathrm{SNR})(\epsilon^2+\epsilon)] + (\mathrm{SNR})[1+2\epsilon]^2\right\}$$
$$+ \left[\frac{M}{M+1} + \frac{4M}{(M-1)(M+3)}\left(\frac{2}{\pi}\right)\right]^2[1 - 8(\mathrm{SNR})(\epsilon^2+\epsilon)]\frac{1}{2M} \tag{16b}$$

where $\epsilon = \epsilon([2(\mathrm{SNR})]^{1/2})$ is the function defined by Eq. (A-4) of Appendix A.

IV. Discussion of Results and Conclusions

We can measure the accuracy of the estimate by considering the ratio

$$\frac{\overline{W}_{ub} + \sigma_W}{(\mathrm{SNR})^{1/2}} \tag{17}$$

where $\overline{W}_{ub}$ is the upper bound on the mean $\overline{W}$ of Eq. (16a) and σ_W is the upper bound on the standard deviation of Eq. (16b). This ratio should be close to unity if our estimate is good and measures roughly how closely the estimate approximates $(\mathrm{SNR})^{1/2}$ when statistical fluctuations of one standard deviation occur. We have plotted this ratio in Fig. 1 as a function of M, the number of samples, for input SNRs (as defined by Eq. 8) of 0, 5.25, and 10.5 dB. The design point input SNR for the command detector is 10.5 dB so the 0 dB curve represents performance of the estimate when the input SNR is 10.5 dB below design.

From Fig. 1 we notice immediately two features of the estimate. First, the accuracy of the estimate is quite insensitive to actual input SNR: the ratios are within 0.15 dB of each other for $M \geq 16$ for input SNRs differing by 10.5 dB. Furthermore, increasing input SNR above 8 dB has virtually no effect on the estimate. Second, the accuracy is extremely dependent on the number of samples: an estimation accurate to within 1.5 dB requires about 45 samples while one good to within 0.5 dB requires more than 500 samples. The number of samples M must be increased to improve the estimate, and since the standard deviation of the estimate decreases as $M^{-1/2}$ for M large, an extremely large number of samples is required for very accurate estimates. Figure 1 gives quantitative support to these concluding remarks.

Finally, we should note that previous analyses (Refs. 1–7) have arrived at essentially the same conclusions. The estimate in this work is for $\mathrm{SNR}^{1/2}$ and is obtained from averages of absolute values of in-phase and quadrature channels. In the previous works the estimates were for SNR and were obtained from averages of squares of the relevant channel outputs. Intuitively, we might expect this work to agree qualitatively with the other analyses, but, in fact, it agrees quantitatively as well. For given input SNR and number of samples, averages of either absolute values or squares provide estimates of approximately the same accuracy (Ref. 7).

References

1. Gilchriest, C. E., "Signal to Noise Monitoring," in Space Programs Summary 37-27, Vol. IV, Jet Propulsion Laboratory, Pasadena, California, June 1976, pp. 169–184.
2. Boyd, D. W., "Signal to Noise Ratio Monitoring: Calculation of an Important Probability Density Function," in Space Programs Summary 37-37, Vol. IV, Jet Propulsion Laboratory, Pasadena, California, February 1966, pp. 259–261.
3. Boyd, D. W., "Signal to Noise Ratio Monitoring: Error Analysis of the Signal to Noise Ratio Estimator," in Space Programs Summary 37-39, Vol. IV, Jet Propulsion Laboratory, Pasadena, California, June 1966, pp. 172–179.
4. Layland, J. W., "On S/N Estimation," in Space Programs Summary 37-48, Vol. III, Jet Propulsion Laboratory, Pasadena, California, December 1967, pp. 209–212.
5. Layland, J. W., Burow, N. A., and Vaisnys, A., "MMTS: Bit Sync Loop Lock Detector," in *The Deep Space Network*, SPS 37-52, Vol. II, Jet Propulsion Laboratory, Pasadena, California, July 1968, pp. 121–124.
6. Anderson, T. O., and Hurd, W. J., "Symbol Synchronizer for Low Signal to Noise Ratio Coded Systems," in *The Deep Space Network*, SPS 37-53, Vol. II, Jet Propulsion Laboratory, Pasadena, California, September 1968, pp. 51–63.
7. Lesh, J. R., "Accuracy of Signal to Noise Estimator," in *The Deep Space Network*, Tech. Rept. 32-1526, Vol. X, pp. 217–234, Jet Propulsion Laboratory, Pasadena, Calif., Aug. 1972.
8. Abramowitz, M., and Stegun, I., *Handbook of Mathematical Functions*, National Bureau of Standards, p. 299.

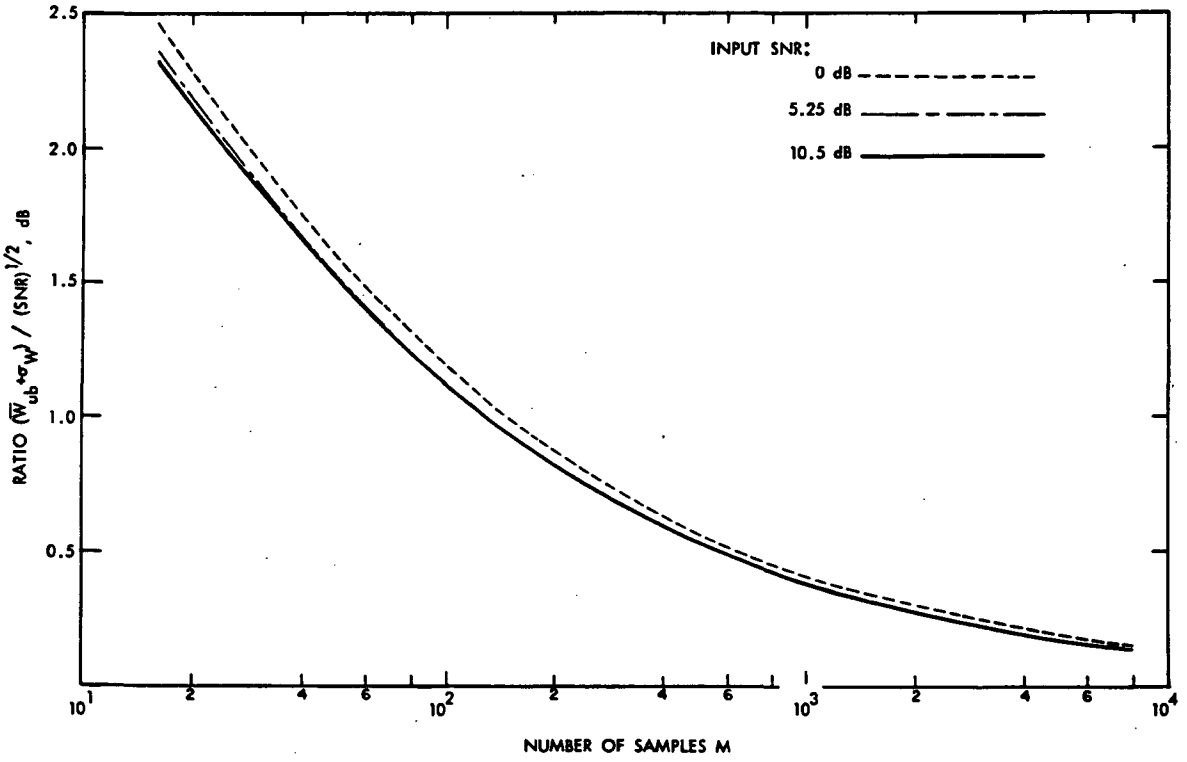

Fig. 1. Plots of ratio of upper bound of estimate W_{ub} plus one standard deviation σ_W to actual $SNR^{1/2}$ as a function of number of samples M. The three plots are for input SNRs of 0, 5.25, and 10.5 dB defined by Eq. (8) of the text.

Appendix A

In this appendix we will derive the mean and variance for a random variable X whose probability density is given by

$$P_X(\alpha) = \begin{cases} \frac{1}{(2\pi\sigma^2)^{1/2}}\left\{\exp\left[-\frac{1}{2\sigma^2}(\alpha - AT)^2\right] \right. \\ \left. + \exp\left[-\frac{1}{2\sigma^2}(\alpha + AT)^2\right]\right\}, & \alpha \geq 0 \\ 0, & \alpha < 0 \end{cases} \tag{A-1}$$

I. Mean of X

The mean of X is given by

$$\begin{aligned} \overline{X} &= \int_{-\infty}^{\infty} \alpha P_X(\alpha)\, d\alpha \\ &= \int_{-AT/\sigma}^{\infty} (\sigma u + AT) \exp\left[-\frac{1}{2}u^2\right]\frac{du}{(2\pi)^{1/2}} \\ &\quad + \int_{AT/\sigma}^{\infty} (\sigma u - AT) \exp\left[-\frac{1}{2}u^2\right]\frac{du}{(2\pi)^{1/2}} \\ &= \left(\frac{2}{\pi}\right)^{1/2}\sigma \exp\left[-\frac{1}{2}\left(\frac{AT}{\sigma}\right)^2\right] \\ &\quad + AT\left[Q\left(-\frac{AT}{\sigma}\right) - Q\left(\frac{AT}{\sigma}\right)\right] \end{aligned} \tag{A-2}$$

where we use the function

$$Q(x) = \int_x^{\infty} \exp\left[-\frac{1}{2}u^2\right]\frac{du}{(2\pi)^{1/2}}$$

Since $Q(-x) = 1 - Q(x)$, we have

$$\overline{X} = AT\left[1 + 2\epsilon\left(\frac{AT}{\sigma}\right)\right] \tag{A-3}$$

where the function $\epsilon(y)$ is defined by

$$\epsilon(y) = \exp\left[-\frac{1}{2}y^2\right]\frac{1}{y}\frac{1}{(2\pi)^{1/2}} - Q(y) \tag{A-4}$$

and vanishes as $\exp[-y^2/2](1/y^3)$ as y becomes large.

II. Variance of X

The second moment of X is

$$\begin{aligned} \overline{X^2} &= \int_0^{\infty} \alpha^2 \exp\left[-\frac{1}{2}\left(\frac{\alpha - AT}{\sigma}\right)^2\right]\frac{d\alpha}{(2\pi\sigma^2)^{1/2}} \\ &\quad + \int_0^{\infty} \alpha^2 \exp\left[-\frac{1}{2}\left(\frac{\alpha + AT}{\sigma}\right)^2\right]\frac{d\alpha}{(2\pi\sigma^2)^{1/2}} \end{aligned} \tag{A-5}$$

If we substitute $\beta = -\alpha$ in the second integral, we have

$$\overline{X^2} = \int_{-\infty}^{\infty} \alpha^2 \exp\left[-\frac{1}{2}\left(\frac{\alpha - AT}{\sigma}\right)^2\right]\frac{d\alpha}{(2\pi\sigma^2)^{1/2}} = \sigma^2 + (AT)^2 \tag{A-6}$$

which is the second moment of a Gaussian random variable with mean AT and variance σ^2. The variance of X is

$$\sigma_X^2 = \overline{X^2} - (\overline{X})^2 = \sigma^2\left\{1 - 4\left(\frac{AT}{\sigma}\right)^2\left[\epsilon^2\left(\frac{AT}{\sigma}\right) + \epsilon\left(\frac{AT}{\sigma}\right)\right]\right\} \tag{A-7}$$

where $\epsilon(AT/\sigma)$ is given by Eq. (A-4).

Appendix B

In this appendix we wish to give integral representations and bounds for the mean and variance of Δ^{-1}, where

$$\Delta = \frac{1}{M}\left(\frac{\pi}{2}\right)^{1/2} \sum_{i=1}^{M} Y_i$$

I. Integral Representations

We will give a representation for $\overline{\Delta^{-L}}$, where $M > L + 1$, which insures convergence of the integral. From the probability density for Y_i (Eq. 6 of the text), we have

$$\overline{\Delta_M^{-L}} = \int \cdots \int d\alpha_1 \cdots d\alpha_M \exp\left[-\frac{\alpha_1^2 + \cdots + \alpha_M^2}{2\sigma^2}\right] \times \left(\frac{2}{\pi\sigma^2}\right)^{M/2} \left[\frac{1}{M}\left(\frac{\pi}{2}\right)^{1/2} \sum_{i=1}^{M} \alpha_i\right]^{-L} \tag{B-1}$$

where the subscript M indicates M samples. We will utilize the following identity to obtain a representation for $[\alpha_1 + \cdots + \alpha_M]^{-L}$:

$$[c + \alpha_1 + \cdots + \alpha_M]^{-1} = \int_0^\infty d\beta \exp\{-\beta[c + \alpha_1 + \cdots + \alpha_M]\} \tag{B-2}$$

Differentiating L times with respect to c and setting $c = 0$ gives

$$[\alpha_1 + \cdots + \alpha_M]^{-L} = \frac{1}{(L-1)!}\int_0^\infty \beta^{L-1} \exp\{-\beta[\alpha_1 + \cdots + \alpha_M]\} \tag{B-3}$$

Substituting (B-3) into (B-1) and interchanging the order of integration gives

$$\begin{aligned}\overline{\Delta_M^{-L}} &= \left(\frac{2}{\pi}\right)^{L/2} \frac{M^L}{(L-1)!} \int_0^\infty \beta^{L-1} \left[\int_0^\infty d\alpha \exp\left[-\frac{1}{2\sigma^2}(\alpha^2 + 2\sigma^2\beta\alpha)\right]\left(\frac{2}{\pi\sigma^2}\right)^{1/2}\right]^M d\beta \\ &= \left[\left(\frac{2}{\pi}\right)^{1/2} \frac{M}{\sigma}\right]^L \frac{1}{(L-1)!} \int_0^\infty x^{L-1} \left[2\,Q(x) \exp\left(\frac{1}{2}x^2\right)\right]^M dx \end{aligned} \tag{B-4}$$

where

$$Q(x) \equiv \int_x^\infty \exp\left[-\frac{y^2}{2}\right] \frac{dy}{(2\pi)^{1/2}}$$

The mean and variance of Δ^{-1} are obtained from (B-4) using $L = 1,2$.

II. Bounds for Mean and Variance

The bounds we will obtain depend upon the inequality of Ref. (8), which for our application states:

$$\left(\frac{2}{\pi}\right)^{1/2} [x + (x^2 + 4)^{1/2}]^{-1} < Q(x) \exp\left[\frac{1}{2}x^2\right] \leq \left(\frac{2}{\pi}\right)^{1/2} [x + (x^2 + 8/\pi)^{1/2}]^{-1} \tag{B-5}$$

Applying this to (B-4) gives

$$\begin{aligned}&\frac{1}{(L-1)!}\left(\frac{M}{\sigma}\right)^L 2^M \left(\frac{2}{\pi}\right)^{(M+L)/2} \int_0^\infty x^{L-1} [x + (x^2 + 4)^{1/2}]^{-M} dx < \overline{\Delta_M^{-L}} \leq \frac{1}{(L-1)!} \\ &\times \left(\frac{M}{\sigma}\right)^L 2^M \left(\frac{2}{\pi}\right)^{(M+L)/2} \int_0^\infty x^{L-1} [x + (x^2 + 8/\pi)^{1/2}]^{-M} dx \end{aligned} \tag{B-6}$$

C-2

A. Bound for the Mean

Consider (B-6) when $L = 2$. The integrals involved can be done by letting $x = a \sinh(t)$, so

$$\int_0^\infty x\,[x + (x^2 + a^2)^{1/2}]^{-M}\,dx = \frac{1}{M^2 - 4}\,\frac{1}{a^{M-2}} \tag{B-7}$$

Thus, (B-6) becomes

$$\frac{1}{\sigma^2}\,\frac{4M^2}{M^2 - 4}\left(\frac{2}{\pi}\right)^{(M+2)/2} < \overline{\Delta_M^{-2}} \leq \frac{1}{\sigma^2}\,\frac{4M^2}{M^2 - 4}\left(\frac{2}{\pi}\right)^2 \tag{B-8}$$

We can obtain the bound on $\overline{\Delta_M^{-1}}$ by relating $\overline{\Delta_M^{-1}}$ to $\overline{\Delta_M^{-2}}$ Consider (B-4) for $L = 2$ and integrate by parts with $u = (Q(x))^M$ and $dv = \exp[-(1/2)x^2M]\,x\,dx$:

$$\begin{aligned}\overline{\Delta_M^{-2}} &= \left[\frac{M}{\sigma}\left(\frac{2}{\pi}\right)^{1/2}\right]^2 2^M \left\{\left[Q^M(x)\exp\left[\frac{1}{2}x^2M\right]\frac{1}{M}\right]_0^\infty \right.\\ &\left. + \int_0^\infty Q^{M-1}(x)\exp\left[\frac{1}{2}x^2(M-1)\right]\frac{dx}{(2\pi)^{1/2}}\right\}\\ &= -\frac{M}{\sigma^2}\,\frac{2}{\pi} + \frac{M^2}{M-1}\,\frac{1}{\sigma}\,\frac{2}{\pi}\,\overline{\Delta_{M-1}^{-1}}\end{aligned} \tag{B-9}$$

Using (B-9) with inequality (B-8), we find:

$$\frac{1}{\sigma}\,\frac{M}{M+1} + \frac{1}{\sigma}\,\frac{4M}{(M-1)(M+3)}\left(\frac{2}{\pi}\right)^{(M+1)/2} < \overline{\Delta_M^{-1}} \leq \frac{1}{\sigma}\,\frac{M}{M+1} + \frac{1}{\sigma}\,\frac{4M}{(M-1)(M+3)}\,\frac{2}{\pi} \tag{B-10}$$

B. Bound for the Variance

Consider (B-6) when $L = 3$. Again letting $x = a \sinh(t)$ simplifies the integrals giving:

$$\int_0^\infty x^2\,[x + (x^2 + a^2)^{1/2}]^{-M}\,dx = \frac{2M}{(M^2 - 1)(M^2 - 9)}\,\frac{1}{a^{M-3}} \tag{B-11}$$

So, (B-6) becomes

$$\frac{1}{\sigma^3}\,\frac{8M^4}{(M^2-1)(M^2-9)}\left(\frac{2}{\pi}\right)^{(M+3)/2} < \overline{\Delta_M^{-3}} \leq \frac{1}{\sigma^3}\,\frac{8M^4}{(M^2-1)(M^2-9)}\left(\frac{2}{\pi}\right)^3 \tag{B-12}$$

We can relate $\overline{\Delta_M^{-3}}$ to $\overline{\Delta_M^{-2}}$, $\overline{\Delta_M^{-1}}$ by using $L = 3$ in (B-4) and integrating by parts with $u = x(Q(x))^M$ and $dv = \exp[(1/2)x^2M]\,x\,dx$:

$$\begin{aligned}\overline{\Delta_M^{-3}} &= \frac{1}{2}\left(\frac{M}{\sigma}\left(\frac{2}{\pi}\right)^{1/2}\right)^3 2^M \left\{\left[xQ^M(x)\exp\left[\frac{1}{2}x^2M\right]\frac{1}{M}\right]_0^\infty \right.\\ &\left. - \frac{1}{M}\int_0^\infty \frac{d}{dx}\left[xQ^M(x)\right]\exp\left[\frac{1}{2}x^2M\right]dx\right\}\\ &= \frac{1}{2}\left(\frac{M}{\sigma}\left(\frac{2}{\pi}\right)^{1/2}\right)^3 2^M \left\{\frac{1}{(2\pi)^{1/2}}\int_0^\infty \left[Q(x)\exp\left(\frac{1}{2}x^2\right)\right]^{M-1} x\,dx \right.\\ &\left. - \frac{1}{M}\int_0^\infty \left[Q(x)\exp\left(\frac{1}{2}x^2\right)\right]^M dx\right\}\\ &= \frac{1}{\pi\sigma}\,\frac{M^3}{(M-1)^2}\,\overline{\Delta_{M-1}^{-2}} - \frac{1}{\pi}\,\frac{M}{\sigma^2}\,\overline{\Delta_M^{-1}}\end{aligned} \tag{B-13}$$

Using (B-13) with inequality (B-12) we find a bound for the variance $\sigma^2_{\Delta^{-1}}(M-1) \equiv \overline{\Delta_{M-1}^{-2}} - (\overline{\Delta_{M-1}^{-1}})^2$

$$\sigma^2_{\Delta^{-1}}(M-1) \leq \frac{1}{\sigma^2\pi^2}\,\frac{64M(M-1)}{(M+1)(M^2-9)} + \frac{1}{\sigma}\left(\frac{M-1}{M}\right)^2 \overline{\Delta_M^{-1}} - (\overline{\Delta_{M-1}^{-1}})^2 \tag{B-14}$$

Using bound (B-10) for $\overline{\Delta_M^{-1}}$, $\overline{\Delta_{M-1}^{-1}}$, we finally obtain

$$\begin{aligned}\sigma^2_{\Delta^{-1}}(M) \leq \frac{1}{\sigma^2}&\left\{\frac{64M(M+1)}{(M^2-4)(M+4)}\,\frac{1}{\pi^2} + \frac{8M}{(M+1)(M+4)}\,\frac{1}{\pi} - \frac{M^2}{(M+1)^2(M+2)}\right\}\\ &- \frac{1}{\sigma^2}\left\{\frac{8M^2}{(M^2-1)(M+3)}\left(\frac{2}{\pi}\right)^{(M+1)/2} + \left[\frac{4M}{(M-1)(M+3)}\right]^2\left(\frac{2}{\pi}\right)^{M+1}\right.\end{aligned} \tag{B-15}$$

High-Power Transmitter High-Voltage Power Supply Ripple

E. J. Finnegan
R. F. Systems Development Section

This article reports the results of decreasing the high-voltage power supply ripple by redesigning the low-pass filter.

I. Introduction

During a routine checkout of the high-power transmitter at DSS 14 located at Goldstone, California, it was noticed that the digital fast klystron body detector, a body overcurrent sensing device, continuously tripped the transmitter high-voltage off. Investigation showed that the ripple voltage of the high-voltage power supply had increased sufficiently to cause the body peak currents to activate the fast body detector.

II. Investigation

Measurements were made of the ripple voltage at the output of the dc filter (Fig. 1). It was found that the ripple voltage was very high, approximately 300 volts; the high-voltage specification is .1 percent of the high voltage. This high ripple voltage indicated further problems in the filter choke (inductor) or capacitor. The capacitor was checked and found to be in good condition. The inductor was then checked and found to have changed its inductance from 1 henry to .1 henry. It was theorized that the gap in the iron of the inductor had changed resulting in a change in inductance. However, the high-voltage insulation isolating the inductor coil from the iron core had not broken down. It was tested to 80 kV with a high-potential tester. The spare inductor was installed and the ripple voltages checked again including the inductor input and output. It was found that the input ripple was alarmingly high. The three phase full wave output of the transformer-rectifier should be 4.2 percent instead of the 75 percent found. This indicated strongly that the filter system was resonating. DSS 63 and DSS 43 were then checked and they were found to be operating in the same condition; the ripple voltage was 30,000 volts while running the klystron at 35,000 volts. The filter in its old configuration was a choke (inductor) input filter. It was then changed to a pi configuration. Tests were run to determine the optimum value of the input capacitor to be used and .2μF was the determined value.

III. Conclusion

A temporary Engineering Change Order was written in order to change the filter to a pi configuration using a .15μF capacitor on the input that was immediately

available. In the future this will be changed to the .2μF capacitor. Results of the new filter are shown in the enclosed photos. Figure 2a shows the ripple voltage without any capacity at the input to the filter which is 15,000 volts (original configuration). The dc voltage is 20,000 volts. Figure 2b shows the input of the filter at 20 kV dc with a .15μF capacitor at the input pi configuration. As can be seen, the ripple voltage is reduced to less than 1,000 volts peak-to-peak.

Figure 3a shows the ripple voltage at the output of the filter (choke input). The ripple voltage is greater than 50 volts peak-to-peak at 20 kV dc. Figure 3b shows the ripple voltage at the output of the new filter, pi configuration. As can be seen, the ripple is reduced to less than 20 volts peak-to-peak.

Figure 4 shows the ripple at the klystron operating level of 60 kV. The ripple at this point is approximately 30 volts peak-to-peak. The input ripple to the filter was 3,800 volts; this is within specs for the filter and the output ripple is within specs for the transmitter.

This will reduce the modulation on the klystron output in the future, thus transmitting a purer spectrum.

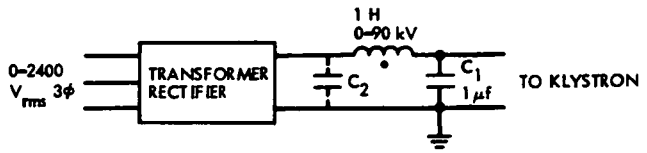

Fig. 1. High-voltage power supply and filter configuration

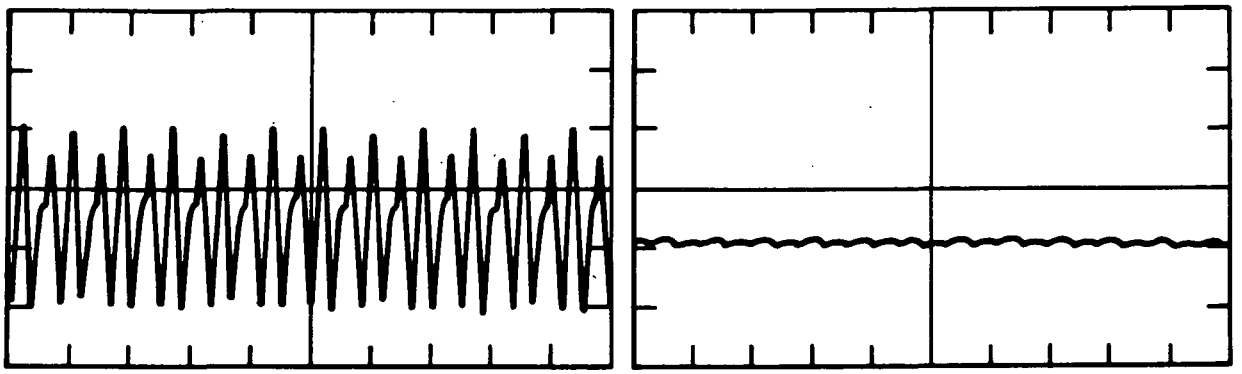

'A' NO CAPACITY

VERT = 5000 V/cm
V_{dc} = 20 kV
HOR = 1 ms/cm

'B'

0.15 μf CAPACITOR ON INPUT

Fig. 2. High-voltage power supply ripple (input)

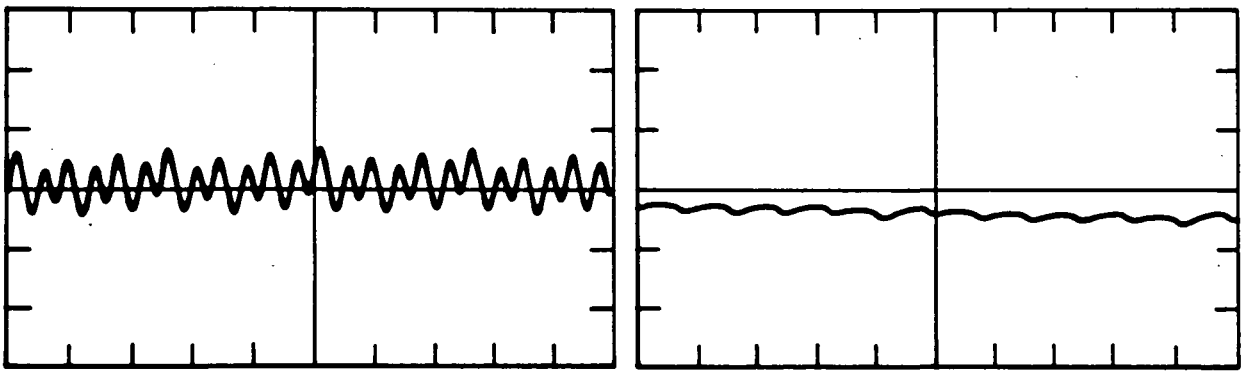

'A' NO CAPACITOR

VERT = 50 V/cm
V_{dc} = 20 kV
HOR = 1 ms/cm

'B'

0.15 μf CAPACITOR ON INPUT

Fig. 3. High-voltage power supply ripple (output)

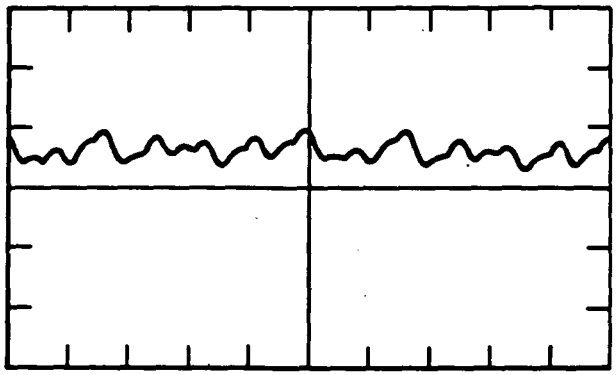

V_{dc} = 60 kV
VERT = 50 V/cm
HOR = 0.5 ms/cm

Fig. 4. High-voltage power supply ripple, output of filter

Venus Station Automation: Communications Link

A. Zygielbaum
Communications Systems Research Section

A highly error-resistant communications system has been developed in support of the demonstration of the remote automatic control of the Venus Station (DSS 13). This article describes in general the computer communications software used to connect the JPL control terminal to the Venus Station, and describes in some detail the software used to drive the teletype line which is part of the link.

I. Introduction

Remote automatic control of the Venus Station (DSS 13) has recently been demonstrated (Ref. 1). During this demonstration, data from several pulsars were acquired by a Sigma 5 computer at JPL. The system configuration at the Venus Station is an outgrowth of that used in a demonstration of local automatic control of that station (Ref. 2). The system configuration at JPL is similar to that used previously to monitor the performance of the Mu-I ranging system at DSS 14 (Ref. 3). This article describes in general the computer communications software used to connect the JPL control terminal and Venus Station, and describes in some detail the highly error-resistant software used to drive the teletype (TTY) line which is part of the link.

At the Venus Station, an XDS 930 is used as the main control computer. It is connected to two XDS 910 computers by high-speed links known as D/R units (Refs. 2 and 4). Currently, the only available data path from the Venus XDS 930 to JPL is via a 10 character-per-second teletype line. Using standard XDS teletype buffers, the 930 is connected to an XDS 920 at JPL, which, in turn, is connected to a Sigma 5 computer via another D/R link. The software which drives this link has been previously described (Ref. 5).

II. Definition of Task

The primary task was to implement a simple to use, reliable communications link between the Venus XDS 930 computer and a Xerox Sigma 5 computer at JPL. The topology of the path between these machines in shown in Fig. 1. To facilitate user programming, identical Fortran-callable user interfaces were defined for both ends of the link. Extensive error checking and retransmission capability were required for reliability.

Three software design and development efforts were embodied in the primary task. A teletype handler was needed to link the XDS 930 at the Venus Station and the XDS 920 at JPL. To extend the connection, a "switcher" program had to be written for the XDS 920 to interface the teletype handler and the D/R software controlling the link to the Sigma 5. Finally, Fortran-callable subroutines were required for the Sigma 5 to drive the D/R software, and provide a user interface identical to that in the Venus XDS 930.

III. User Interface

The teletype handler appears as the collection of Fortran-callable subroutines shown in Table 1. Identical software is used at each end of the link. As a result, both the Venus XDS 930 user and the XDS 920 "switcher" utilize the same subroutine calls to access the teletype lines. These same calls are made available in the Sigma 5 by the transparent combination of the XDS 920 switcher and the Sigma 5 interface package.

Two logical full duplex channels are provided by the communications link. Messages conveyed by the link are blocked to facilitate retransmission. The user can assign a transmission priority of 1 to 15 (1 is highest) to either channel. The channel with the highest priority can preempt the other channel. If they are given equal priorities, data blocks on the channels are interleaved so that the traffic on both channels appears to be transmitted simultaneously.

Sending a message is equivalent to transferring a core image from one end of the link to the other. The respective users must supply the buffers from which these data are taken and into which these data are placed. At either end, two transmit flags control transmission on both channels while two receive flags control reception.

To supply a buffer and begin transmission, the SNDMSG(LOC,CHN,PRY,RTRY,CHCNT) subroutine is used. The parameters are: LOC, the first location of the buffer; CHN, the channel number (1 or 2); PRY, the channel priority; RTRY, the number of times any particular block of the message is retransmitted before a line error is declared; and CHCNT, the number of 4-bit bytes in the buffer. A buffer is designated for reception with the SETRX (CHN,LOC,CNT) subroutine. Once again, LOC and CHN are the first location in the buffer and the channel number, respectively. The size of the buffer is given as CNT computer words to prevent data overflows.

It would be unacceptable to transmit a message if a receive buffer had not been provided (i.e., if SETRX had not been executed at the receiver). Coordination of the two sides of the link for transmission is provided by transmit flags. The mechanism for coordinating flags at both ends of the link will be discussed later.

These flags are accessed by the subroutine TXSTAT (CHN,FLG), where CHN is the channel number and FLG is a dummy variable into which the flag value is placed. The transmit flag normally has the value 1, indicating that a receive buffer for that channel is available at the remote end of the link and that the channel is free. A value of 0 implies that SNDMSG has been executed and, therefore, the channel is busy. If the transmission is successful, the flag remains busy, 0, until a new receive buffer is supplied via SETRX. When the receiving user supplies the buffer, the transmit flag again becomes 1. If the transmission is unsuccessful, that is, if a particular block has been retransmitted RTRY times, then the flag is set to -1. No action is required by the receiver user as the receiving buffer is still considered empty.

Data reception is coordinated through receive flags. A receive flag is accessed by the subroutine RXSTAT (CHN,FLG). Again, CHN is the channel number and FLG becomes equal to the receive flag. Once a receive buffer has been supplied, the receive flag remains 1 until a message has been succesfully received. Note that there is no indication to the receiving user that a message receipt is in progress or that an unsuccessful transmission was attempted. If a correct message is received, the receive flag is set to 0. It will not be reset to 1 until SETRX is called to supply a new buffer.

A utility subroutine MSGCNT(CHN,CNT) is provided to indicate the number of 4-bit bytes received in a message. This subroutine will return the count as the dummy variable CNT for channel CHN provided that the receive flag is 0, that is, if a message has just come in. If the flag has any other state, MSGCNT will return -1.

Sample receiver and transmitter programs are shown in Fig. 2. The transmit routine first executes a busy wait until the channel is free. Upon exiting this loop, it starts the transmission of the buffer IRRAY. Coincidentally, the receiver waits for a message to come in. Upon receipt, MSGCNT is used to determine the incoming byte count. Execution of SETRX supplies a new receive buffer and, consequently, frees the channel.

System initialization is facilitated through the TINIT subroutine. This subroutine may be called by either user

at any time. Its effect is to initialize all flags and to terminate all traffic activities. At both ends of the link, the transmit flags are set to 0 and the receive flags are set to −1. This receive flag state alerts the remote user to the fact that the link has been reinitialized and indicates that new receive buffers must be supplied as well as any interrupted transmissions restarted. When SETRX is called, the transmit flag at the opposite side of the link will be set to 2, initialization complete. Concurrently, the local receive flag will become 1, i.e., no message. A typical intialization sequence is shown in Fig. 3. The CALL TXSTAT checks for initialization complete. RXSTAT is called to detect and protect against a simultaneous initialization from the other end.

IV. The Teletype Link

Characteristics of the teletype circuit influenced the software design. Preliminary experiments indicated that a particular teletype circuit including the computer buffers, microwave, land lines, and associated equipment has a per character error rate of 10^{-3}. Two error checking schemes are used to ensure reliable communication. First, information to be transmitted is divided into four-bit bytes and encoded into the first four bits of the teletype character. The fifth bit of the teletype character is character parity. Second, data are divided into blocks of 120 characters, and the characters within a block are bit-wise exclusive-ored to form a checksum parity character, or longitudinal parity check. If an error is detected, the block is retransmitted. A block size of 120 characters was selected as small enough to minimize the probability of retransmission and yet large enough to prevent channel saturation by overhead bookkeeping characters.

Two types of teletype characters are designated, data characters and utility characters. Constrained to be of even parity, data characters contain text and block overhead information. Odd parity characters are used as utility signals called "interhandlers" to control the interlocked transmission of blocks and synchronize the initialization of the system. The use of distinguishing parity permits the interleaving of interhandlers and text with no ill effect.

The interhandlers consist of two odd parity characters transmitted consecutively twice. The five-bit characters are each denoted by two octal digits. Table 2 relates these numbers to teletype characters. For instance, the interhandler which notifies the remote teletype program to initialize is 37/01/37/01. Any combination of 37 and 01 occurring within 4 characters will cause the interhandler to be recognized (e.g., the message 47/01/37/02 is valid). Since the interhandlers are selected to be of at least distance 2, this technique yields simple error correction. The interhandlers are summarized in Table 3.

Interhandlers are given odd parity to permit them to be inserted into the text of a message. This prevents delay of up to one block time (13.7 seconds) in the transmission of an interhandler. If an odd parity character is received, its validity as an interhandler character is checked. If it is valid, it is accepted. If it is not valid and message receipt is in progress, an error flag is set to indicate that a character with improper parity was received. If a message is not in progress, the character is ignored.

Whenever data or link parameters are transmitted, they are encoded into four-bit bytes. The data bits become the four most significant bits of a five-bit teletype character, with the remaining bit used to set even parity.

Data are sent in blocks of 120 characters (480 bits). The format of a block is shown in Fig. 4. The start-of-block interhandler alerts the receiver to imminent data. Following immediately, a header information sub-block includes a message number, channel number, block number, and block character count. The message number for each channel is set to 0 during initialization and incremented by one for each message of a channel. It is transmitted as one character, hence it is modulo 16. The channel number identifies whether the block is assigned to channel 1 or 2. To order the message, a block number is initialized as the number of blocks in a message. It is allowed 2 characters (8 bits). As each block of a message is sent, the block number is decremented by one. The final block of a message, therefore, has a block number equal to one. Used in conjunction with the message number, the block number helps keep track of the sequence of blocks and messages as an error detection tool. The character count is 8 bits (two characters) containing the number of characters in the block. "Text" contains the data to be transmitted. End of text is marked by the interhandler 10/25. It is followed by a checksum derived from a character-by-character bit-wise exclusive-or of the text and header information sub-block. Finally, the end of block is designated by 10/34/10/34.

After a block is sent, the transmitter awaits a reply from the receiver before continuing. This reply or handshake is used to synchronize the link and control retransmission. As a block is received, an error flag is set (1) if any particular text or header sub-block character has odd parity, (2) if the count of received characters and the block character count disagree, (3) if the derived checksum parity and transmitted checksum parity disagree, (4) if the block

number is out of sequence, (5) if the message number is changed prior to receipt of block number one, or (6) if the end of block is received prior to the end of text interhandler. If the error flag has not been set, the receiver replies to the transmitter with the block-received-OK interhandler; otherwise, block-not-okay is sent. At the transmitter, in the former case, the message is continued or if complete, the transmitter channel remains busy but inactive until the receiver signals that a new receive buffer is available. In the latter case, a parameter set by the user for that channel, designated RTRY, is decremented. If it remains >0, the block is retransmitted. IF RTRY is 0, the user is notified that the channel is in error and the channel is freed.

V. The XDS 920 Switcher

With the teletype link from the Venus Station XDS 930 to the XDS 920 at JPL established, the next step is the path between the XDS 920 and the Xerox Sigma 5. These machines are, fortunately, already interconnected via the D/R high-speed link. Software to support the D/R unit is available and utilized. As this software will be described in a cursory fashion here, the reader is again referred to the article by Layland (Ref. 5) for more detail.

A program to interface between the D/R software and the teletype software described earlier resides in the XDS 920. This program, in combination with the Sigma 5 software, discussed in the next section, appears transparent to the user. Hence, the Sigma 5 user believes he is communicating directly with the teletype handlers. The main tasks, then, for the XDS 920 "switcher" program are to route and reformat message traffic through the D/R link and to extend the teletype transmit and receive flags to the Sigma 5.

Communication with the Sigma 5 is maintained via the aforementioned D/R link software. This software is capable of transferring blocks of 126 8-bit bytes at rates approaching 25 kilobytes per second. Seven logical bidirectional channels are provided. Five of these were used in this implementation. D/R channels 1 and 3 are assigned to teletype channels 1 and 2, respectively, of the teletype handler for traffic from JPL to Goldstone. D/R channels 2 and 4 were assigned to teletype channels 1 and 2, respectively, for Goldstone to JPL traffic. D/R channel 5 was used for "signals" to coordinate and control the XDS 920/Sigma 5 link.

As far as the user is concerned, the teletype handlers can transfer memory blocks of arbitrary size. On the other hand, the D/R unit software is limited to transferring blocks of 126 8-bit bytes. Therefore, the switcher and Sigma 5 software must cooperate by disassembling messages into D/R unit blocks for transmission and by reassembling these blocks into core images upon reception. To maintain compatibility with the teletype link, the Sigma 5 software must be informed of the receive 4-bit character count for the entire message. This is done by inserting the character count into the first two bytes, i.e., 16 bits of each D/R block. Although this information is unnecessarily repeated, the time penalty is negligible. In the opposite direction, the switcher makes use of the SNDMSG subroutine to transmit traffic to Goldstone. The subroutine must be supplied with channel priority, number of retrys and the four-bit character count. This information is supplied by the Sigma 5 user and sent to the switcher program as the first four bytes of each D/R block.

It should be noted that the teletype channel priority scheme is not reflected in the D/R link. This is simply because of the high speed of that link. Whenever a full message is ready to be transmitted from the switcher to the Sigma 5, or vice versa, it is sent on a first-come first-serve basis without regard to priority.

The signals used to coordinate and control the message traffic over the D/R link are given in Table 4. These signals allow the Sigma 5 applications program to direct the teletype subroutines in the XDS 920 and interrogate their status much as if the teletype were directly under its control and not separated by two additional interface programs. The sequence of events in handling this link is identical to that discussed earlier.

VI. The Sigma 5 End

An overriding requirement in the communications link design was that both ends of the link appear identical to the user. The purpose of the Sigma 5 program is to establish an interface between the Fortran-callable subroutines and the D/R link software. This interface provides compatibility with the teletype routines, splits arbitrary-length outgoing data messages into D/R blocks, and concatenates incoming D/R blocks into arbitrary-length messages.

The environment of the Sigma 5 led to an immediate problem. The communications software is a subprogram of the user's program. The D/R link's software is a subroutine of the communications software. While the D/R software is interrupt-driven and therefore runs in real time, the communication subprograms run only when called by the user program. The communications software

must, however, chop messages into D/R blocks and "feed" them to the D/R subprograms. In the inverse, the communications software must concatenate D/R blocks into messages. To keep the link running, therefore, either repeated calls to some "keep running" subroutine or some "busy-wait" is required. The former alternative would violate the premise that both ends of the link be identical. The latter could cause possibly hazardous delays to the user program.

To avoid this problem, the interface subroutines are constructed around a FIFO list, the task list. Whenever some subroutine has a pending operation, it places a particular number in the list and executes a return to the calling program. The internal subroutine STACKPUT(N) is used for this operation. To keep the system running, the subroutines TXSTAT and RXSTAT contain calls to STACKGET. STACKGET removes, in turn, the topmost item in the list and transfers control to the designated subroutine. When the subroutine execution is complete, control is returned to STACKGET. This process is repeated until the task list is emptied. Control then returns, as appropriate, to TXSTAT or RXSTAT. Since TXSTAT and RXSTAT are routinely called by a user program, and in fact are usually part of some testing loop, the use of the task list provides satisfactory operation which is transparent to the user.

The communications link is normally operated from the timesharing terminal on the Sigma 5. Because of the design of the link, some time is spent in busy-waiting on the status of the transmit or receive flags. During these periods, it was deemed inappropriate to delay concurrent background or batch processing jobs. On the other hand, TXSTAT and RXSTAT must be repetitively called, as just described, to keep the system going. A subroutine, "ENDSLICE," was added to the link software to allow the user program to return the unused portion of a time-share time slice to the operating system. ENDSLICE will return the slice only if the link is not actively receiving or transmitting, that is, only if repeated calls to TXSTAT or RXSTAT are not necessary.

VII. Conclusion

The communications system has now successfully operated for an elapsed period approaching 100 hours. It is therefore considered "operational" and will continue to be used in the station automation experiment as long as teletype is the primary digital data link with the Venus Deep Space Station.

References

1. Moyd, K., "Remote Automatic Control of DSS 13," in *The Deep Space Network Progress Report 42-30*, Jet Propulsion Laboratory, Pasadena, California.

2. Moyd, K., "Automatic Control of DSS 13," in *The Deep Space Network Progress Report 42-29*, Jet Propulsion Laboratory, Pasadena, California, December 15, 1975.

3. Erickson, D. E., and Layland, J. W., "An Experiment in Remote Monitoring of Mu-Ranging Operation at Mariner Mars 1971 Superior Conjunction," Jet Propulsion Laboratory DSN Progress Report TR 32-1526, Vol. XV, pp. 156–166, Pasadena, California, June 15, 1973.

4. Lushbaugh, W. A., "A Driver/Receiver Unit for an Intercomputer Communications Link," Jet Propulsion Laboratory DSN Progress Report TR 32-1526, Vol. XV, pp. 109-115, Pasadena, California, June 15, 1973.

5. Layland, J. W., "Software for Multicomputer Communications," Jet Propulsion Laboratory DSN Progress Report 42-26, pp. 145–154, Pasadena, California, April 15, 1975.

Table 1. Summary of subroutines

SNDMSG(LOC,CHN,PRY,RTRY,CNT)

Causes a data block to be transmitted.

LOC —Location of the first word of data
CHN —Channel 1 or 2
PRY —Priority 1 to 15
RTRY—Number of block retransmissions
CNT —Number of 4-bit bytes of data

TXSTAT(CHN,FLG)

Returns transmit status of channel CHN as one of the following values for FLG:

2—Channel initialized
1—Message received, channel free
0—Channel busy
−1—Message not received (error), channel free

RXSTAT(CHN,FLG)

Returns receive status for channel CHN as one of the following values for FLG:

−1—No buffer
0—Message in
1—No message in

SETRX(CHN,LOC,CNT)

Assigns a receive buffer starting at LOC, CNT words in size, to channel CHN.

TINIT

Initializes the link.

ENDSLICE *** Sigma 5 ONLY ***

Releases unused time slices to the operating system.

MSGCNT(CHN,CNT)

If the receive flag for CHN is 0, CNT will be assigned a value equal to the number of 4-bit bytes just received. If the flag is not 0, then CNT will become −1.

Table 2. Teletype characters

Letters character	Octal code	Figures character	Octal code
Letters	37	Figures	33
A	03	0	26
B	31	1	27
C	16	2	23
D	11	3	01
E	01	4	12
F	15	5	20
G	32	6	25
H	24	7	07
I	06	8	06
J	13	9	30
K	17	–	03
L	22	?	31
M	34	:	
N	14	$	11
O	30	!	15
P	26	&	32
Q	27	#	24
R	12	'	13
S	05	(	17
T	20	)	22
U	07	.	34
V	36	,	14
W	23	;	36
X	35	/	35
Y	25	"	21
Z	21	Blank	00
Bell	05	Space	04
Line feed[a]	02	Carriage return	10

[a]Figures character.

Table 3. Teletype link interhandlers

Interhandler	Teletype characters
Order initialize	37/01/37/01
Initialization complete	37/31/37/31
Block received OK	37/26/37/26
Block received in error	37/23/37/23
Start of block	10/02/10/02
End of text	10/25
End of block	37/34/37/34
Channel 1 buffer available	37/15/37/15
Channel 2 buffer available	37/13/37/13

Table 4. D/R link signals

Signal	Number
Order initialize	0
Initialization complete	1
Channel 1 free	2
Channel 2 free	3
Start message channel 1	4
Start message channel 2	5
End message channel 1	6
End message channel 2	7
Bad teletype data channel 1[a]	8
Bad teletype data channel 2[a]	9

[a]920 to Sigma only.

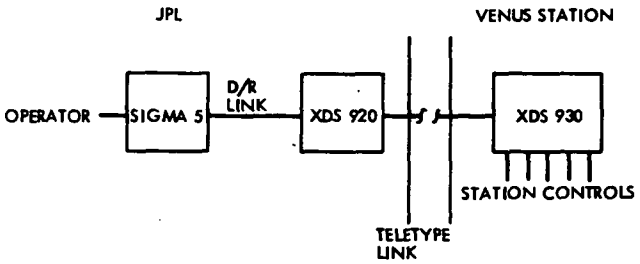

Fig. 1. Communications system

```
TRANSMITTER
        .
        .
1       CALL TXSTAT (1, IFLG)
        IF (IFLG) 3, 1, 2
2       CALL SNDMSG (IRRAY (1), 1, 1, 2, 200)
        .
        .
        .
3       TYPE 4
4       FORMAT ($TRANSMISSION ERROR$)
        .
        .
        .

RECEIVER
        .
        .
1       CALL RXSTAT (1, IFLG)
        IF (IFLG) *, 2, 1
2       CALL MSGCNT (1, CNT)
        CALL SETRX (1, IRRAY (1), 2000)
```

* THIS INITIALIZATION STATE IS DISCUSSED ELSEWHERE

Fig. 2. Sample message transfer programs

```
        CALL TINIT
3       CALL SETRX (1, LOC1, CNT1)
        CALL SETRX (2, LOC2, CNT2)
1       CALL TXSTAT (1, FLG)
        IF (FLG-2) 1, 2, 1
2       CALL RXSTAT (1, FLG)
        IF (FLG) 3, 4, 4
4       CONTINUE
```

Fig. 3. Initialization sequence

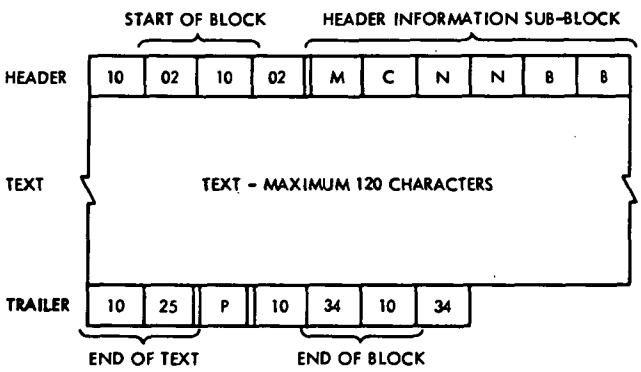

M = MESSAGE NUMBER
C = CHANNEL NUMBER
N = 2-DIGIT BLOCK NUMBER
B = 2-DIGIT CHARACTER COUNT
P = LONGITUDINAL PARITY

Fig. 4. Block format

Implementation of Wideband Digital Recording Equipment in the DSN

K. R. Kimball
DSN Data Systems Development Section

The DSN is implementing wideband digital recording equipment for mission support in the 1978–1981 time era. This article describes the development status of this equipment and the factors which were of major importance in the design approach. Design of equipment is discussed to the functional block diagram level.

I. Introduction

Beginning in late 1977, wideband digital recording equipment will be implemented at the 64-meter Deep Space Stations (DSS). This equipment is necessary for support of flight project data acquisition and spacecraft navigation requirements. Specifically, a 12-megabit/sec recording capability is required in support of the Pioneer Venus probe entry wind experiment in December 1978; the capability to record 24 Mbits/sec is required for the DSN to use very long baseline interferometry (VLBI) techniques for determination of Earth platform parameters (UT-1 and polar motion) to the accuracy necessary for spacecraft navigation in the 1978–1981 time era.

Efforts toward implementing such a capability began in late 1974. Magnetic tape recording was adopted as the most acceptable means to accomplish digital recording at the required rates; multi-track recording on 2.5-cm (1-inch) wide magnetic tape, using an instrumentation-type tape transport, is the general approach used by the recording industry to achieve such data rates.

II. System Design Factors and Influences

A. Capability Available From Commercial Sources

A key aspect of the implementation approach adopted by the DSN for wideband digital recording is to commercially procure *from a single contractor* that portion of the recording equipment which is to perform the primary functions of recording and reproducing user-supplied digital data at the rates and error tolerances required by the DSN. This approach places the responsibility for engineering those interfaces which are most critical to wideband digital recording in a single organization, and simplifies the specifications for the equipment being procured.

One of the first activities in the design effort was to become familiar with the capability that the recording

industry had achieved in wideband digital recording. The following summarizes the key observations made during this effort:

(1) Several industry sources claimed digital recording capability in excess of 50 Mbits/sec.

(2) There were (and are) no standards within the industry for wideband digital recording (i.e., formats, densities, track widths, track spacing, encoding system, etc.)

(3) Although advertised as such, no truly "off-the-shelf" product line was offered by any industry source; this was in part due to the fact that users of such equipment had had widely varying requirements.

(4) Most systems were still undergoing design changes and improvements.

(5) There existed a large variance in the prices for equipment which ostensibly performed equivalent functions; in general the pricing of the equipment appeared high relative to the amount of electronics provided.

(6) The specifications of system bit error rates were vague; specifically, techniques for distinguishing equipment errors from those errors resulting from tape imperfections were not well defined.

Following the industry survey, a JPL specification for 25-Mbit/sec recording equipment was generated. The technical requirements of this specification were written to be generally consistent with the level of capability observed during the industry survey; i.e., it was expected that several sources would be capable of supplying recording equipment in accordance with the JPL specification.

B. Supporting Research and Technology Activities

A second major influence on the implementation design approach was the related effort conducted by JPL's Communications Systems Research Section. In July 1974, a purchase order was issued by this section for the procurement of an off-the-shelf 80-Mbps record/reproduce system. The selected manufacturer encountered several difficulties in producing a system which met the required specifications. The specific technical outgrowths of this procurement which had an impact on the specification and selection of the DSN equipment were as follows:

(1) A conservative design approach would preclude the use of tape track widths less than 25 mils for digital recording.

(2) The procedures and techniques for testing bit error rates must be carefully specified to ensure that a truly *parallel* bit error rate is measured, and to eliminate the effects of tape flaws.

(3) The minimization of electrical and mechanical adjustments is vital if the system is to be operationally acceptable.

C. Related Efforts Within NASA

Similar requirements for wideband digital recording exist within NASA for several planned and proposed applications. The rate requirements for these applications fall in the range of 15 to 120 Mbits/sec. Cognizance of these related efforts is under NASA's Goddard Space Flight Center (GSFC).

In March 1975, a JPL–GSFC wideband recorder technology working sub-group was established (as part of a larger VLBI working group); the primary objectives of this sub-group were to:

(1) Exchange information as to development status and design approach.

(2) Assess the degree to which format and interface standards could be adopted to permit inter-network experiments.

(3) Assess the degree of operational risk associated with the relatively new level of technology present in wideband digital recording systems.

The first meeting of the working group was very productive in terms of information exchange, and there were several areas of agreement as to desirable interface and format characteristics. Although JPL had by this time selected a system contractor and the design of the equipment was well underway, several aspects of the detailed design were influenced by the results of this meeting. It is believed that the DSN equipment as currently designed could be readily compatible with any potential "NASA-standard" system.

D. Operational and Reliability Considerations

The most common reservations generally expressed about recording equipment center around operability, maintainability, and reliability. In an attempt to be responsive to these concerns, the following design goals were established and have been of major importance in the system design:

(1) An automated pre-pass performance verification of the recording equipment should be provided.

(2) Some degree of real-time read-after-write data monitoring capability should be provided.

(3) Tape-changing should be the only real-time operator function; the functions of starting, stopping, and rewinding tape should be automated.

(4) A hard-copy log of all recording activity should be provided.

(5) The capability should be provided to receive control information from a remote operator, and to report system status to station monitoring equipment.

(6) The recorder transport should accommodate 41-cm (16-inch) reels for extended recording time.

(7) DSN Hi-Rel hardware should be used wherever appropriate.

(8) The recording system MTBF should be >500 hr.

(9) Modular design should be provided to facilitate troubleshooting and repair.

(10) Mechanical and electrical adjustments should be minimized.

E. Cost Considerations

The effort to minimize costs while providing capability consistent with requirements has had an impact upon the design in two significant respects. The first was the procurement of the commercial recording equipment in two distinct configurations. One configuration is intended for use at DSSs, where data recording is the primary function, and the other is destined for use at a central playback facility. The "record" configuration has full 25-Mbit/sec recording capability but limited reproduce capability; the "reproduce" configuration has complete playback capability but only that record capability required for system performance checks. An estimated 20-percent reduction in price of the commercial recording equipment was achieved by procuring units without the full record/reproduce function.

Equipment costs were also minimized by implementing only 20 channels of electronics in recording equipment which is designed to accommodate 28 channels; the digital recording rates required for the DSN application can be comfortably accommodated on 20 recorded tracks. Although all systems are equipped with 28-track read/write heads and 28 channels of head drivers and reproduce amplifiers, those channel electronics which exhibit greater complexity and cost (record and reproduce amplifiers, encoders, and decoders) have been limited to the 20-channel configuration.

III. Detailed Design Description

A. Commercial Wideband Digital Recording Equipment

As outlined above, two configurations of recording equipment are being procured from a systems contractor. A functional block diagram of the record configuration is shown in Fig. 1. The input to the recording equipment consists of 20 synchronous channels of digital data and a common data clock. The nominal data rates per channel for the DSN configuration are shown in Table 1.

Each input channel is recorded on a separate track after being reformatted by the encode/sync-insertion logic. The reformatting process consists of merging additional data bits (on a non-replacement basis) with the input data for each channel. For every 200 user input bits received on a given channel, an additional 43 bits are generated and merged to create a 243-bit data frame. The frame content is shown in Fig. 2. As a result of the reformatting process, the actual bit rate of information recorded on each track is 21.5 percent higher than the original input bit rate. The primary functions of the reformatting are (1) to provide a means for removing skew between tracks during playback, (2) to limit the low-frequency content of the recorded serial bit stream, and (3) to provide a means for error detection during reproduction.

A limited read-after-write capability also exists in the record configuration. Two reproduce–decoder channels are provided; one of these channels is hardwired to a specific track, while the other can be switched via a multiplexer to any of the 20 recorded tracks. This multiplexing capability allows real-time monitoring of data quality on a track-selective basis. The functions of the decoder channels are (1) to eliminate data skew between recorded channels, (2) to remove the previously merged "overhead" bits and reproduce the data as it originally appeared at the user input, (3) to produce an error output signal which will indicate the bit error rate of the respective channel, and (4) to provide a signal which indicates the synchronization status of each decoder channel.

A block diagram of the reproduce configuration, intended for use at a central playback facility, is shown in Fig. 3. The individual elements of this configuration are equivalent in function to those of the record configuration. A full complement of reproduce amplifiers and decoders is provided for playback of 20 data tracks. The decoders and deskew electronics produce 20 synchronous channels of digital data. The content and phase relationship of these data is identical to that supplied by the user during the record process; the fact that overhead bits were added and

subsequently deleted during the record-reproduce process is transparent to the user.

An externally supplied data clock controls the data output frequency within a ±2-percent range of the nominal playback rates. Data can be reproduced at the originally recorded rate or at any of the nominal rates below the original rate.

B. Equipment Configuration at DSN Sites

A functional block diagram of the planned equipment configuration at DSN sites is shown in Fig. 4. The basic functional elements of the system are:

(1) Analog-to-digital (A-D) converters and data formatter

(2) Wideband recording equipment (2 units)

(3) Recording monitor unit

(4) Recording controller and log printer

The primary functions and characteristics of these elements are outlined below.

The A-D converters and data formatter will perform the following functions:

(1) Digitize up to 6 analog inputs; single-bit quantization is planned for very long baseline interferometry (VLBI) applications, while 3-bit quantization of a single input will be provided for the Pioneer Venus wind experiment.

(2) Derive A-D sampling clocks from the DSN hydrogen maser frequency reference; sampling rates up to 25 MHz can be provided with less than 3 nanoseconds sampling jitter.

(3) Provide a utility input port which will allow any external digital data stream to be recorded.

(4) Distribute the digitized data onto 18 parallel data lines for input to the recording equipment.

(5) Generate two redundant channels of digital housekeeping data for input to the recording equipment. Housekeeping tracks will include data time tag, system configuration data, and auxiliary data received from the recording controller.

(6) Provide a data generator which will serve as a data source for stand-alone performance evaluation of the equipment.

The functional characteristics of the "commercial recording equipment" shown in Fig. 4 were discussed in detail in Section IIIA. This equipment (transport and electronics) will be controlled and monitored via a remote control interface connection to the recording controller.

The function at the recording monitor unit is to accumulate, display, and transmit to the controller data which reflects the status and condition of the recording process. Specific functional tasks performed are:

(1) Selection of the multiplexed channel monitored during the read-after-write process.

(2) Accumulation and display of statistics on the selected channel, and input of these statistics to the controller for verification of proper values.

(3) Monitoring of the housekeeping tracks and extraction of the time tag information for display and verification of proper content by the controller.

(4) Reflection of the status and activity of the tape transports.

It is planned for the recording controller, in conjunction with the log printer, to perform the following functions:

(1) Stop, start, and sequence transports and rewind tapes when appropriate.

(2) Monitor real-time data quality.

(3) Receive auxiliary data (e.g., weather, radiometer, antenna position, etc.) through a DSN standard interface port and reformat these data for inclusion on the recorded housekeeping data tracks.

(4) Detect system alarm conditions and transmit alarm status via the standard interface port.

(5) Provide a hard-copy log of recording activity and performance characteristics.

(6) Provide an automated pre-pass performance verification test.

IV. Installation Schedule

The current implementation schedule calls for installation and integration testing to be completed as indicated below:

DSS 14: 1 January 1978

DSS 43: 1 February 1978

Santiago (STDN station): 1 January 1978

Guam (STDN station): 1 February 1978

DSS 63: 1 March 1979

The equipment installed at Santiago and Guam is being loaned to the Spaceflight Tracking and Data Network (STDN) for support of the Pioneer Venus entry probe wind experiment and will be returned to the DSN in January 1979.

V. Potential for Expanded Recording Capability

An attempt has been made throughout the design process to provide a recording system which is general-purpose in nature, and to allow for future expansion or modification of recording capability. Some of the potential requirements for which such equipment could be used are:

(1) Recording of digitized pre-detection telemetry data.

(2) Recording of radio science data.

(3) Post-detection recording of multi-megabit telemetry data streams.

Increases in recorded data rate capacity could be accommodated by any of the following means:

(1) Recording data at a tape speed of 305 cm/sec (120 inches/sec), yielding an aggregate 55.6-Mbit/sec capacity; recording time per reel, however, is reduced to 20 minutes at this tape speed.

(2) Recording data at a tape speed of 610 cm/sec (240 inches/sec), yielding an 111-Mbit/sec capability. The operational feasibility of this tape speed is questionable, as reel changes are required at 10-minute intervals (assuming continuous recording on 41-cm (16-in.) reels). A second drawback is that the recording systems being supplied to the DSN will have no reproduce capability at 610 cm/sec. Data recorded at 610 cm/sec must be played back at 305 cm/sec.

(3) Increasing the number of recorded tracks from 20 to 28. This would result in a 40% increase in capability at any tape speed.

(4) Increasing on-tape bit density from the current 11 kbits/cm (28 kbits/inch) to 13 kbits/cm (33 kbits/inch).

All of the above are technically feasible, and there exists a potential system rate capability in the 150-Mbit/sec range. However, any future consideration of increasing the data rate capacity of the system must be heavily dependent on (1) the experience gained with the equipment in its present configuration, (2) operational considerations, and (3) equipment costs.

Table 1. Nominal DSN recording rates

Tape speed, cm/sec (in./s)	Input bit rate (per track), Mbits/sec	Aggregate bit rate (20 tracks), Mbits/sec
305 (120)	2.78	55.6
152 (60)	1.39	27.8
76 (30)	0.694	13.9
38 (15)	0.347	6.94

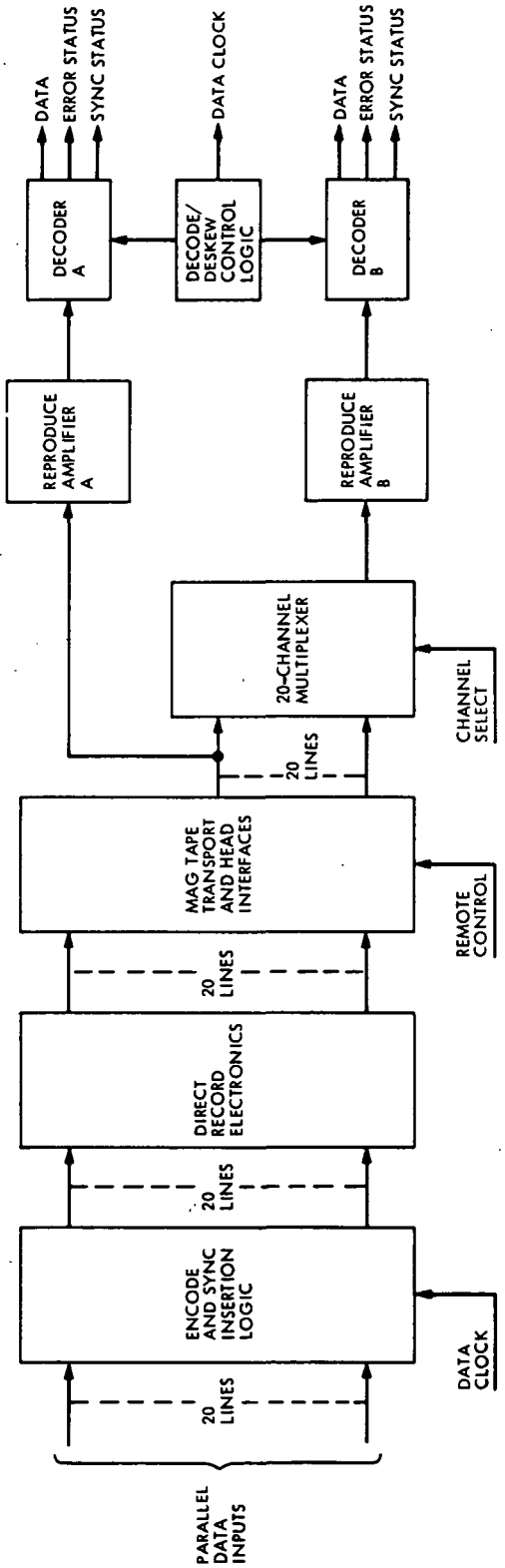

Fig. 1. Functional block diagram of commercial "record" configuration

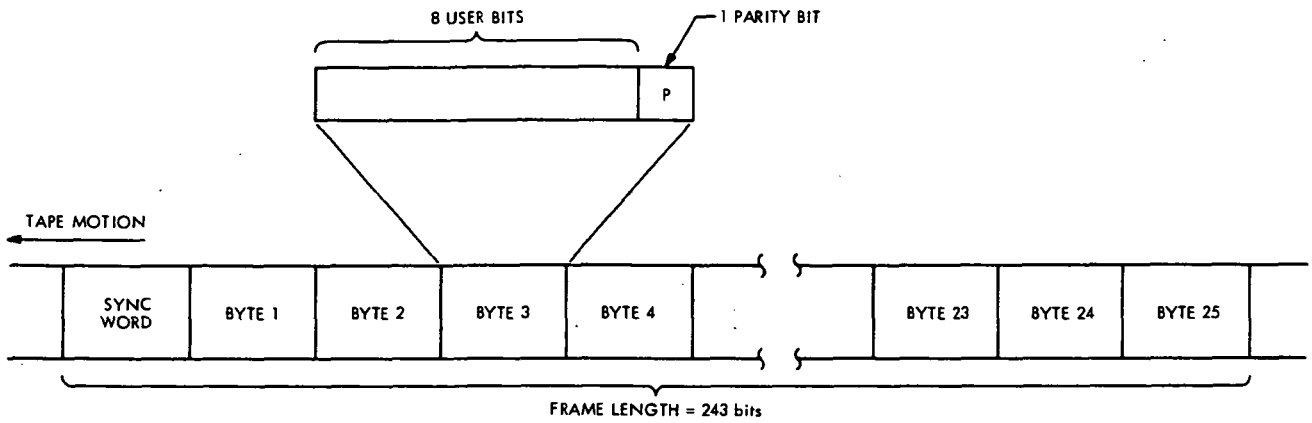

FRAME CONTENT = 200 USER DATA INPUT BITS + 25 PARITY BITS + 18 SYNC BITS = 243 TOTAL
SYNC WORDS = 746500_8 AND 031277_8 (ALTERNATING COMPLEMENTS)
PARITY = ODD, CODING = NRZ-MARK
OVERHEAD = 21.5%

Fig. 2. Recorded data format (typical for all tracks)

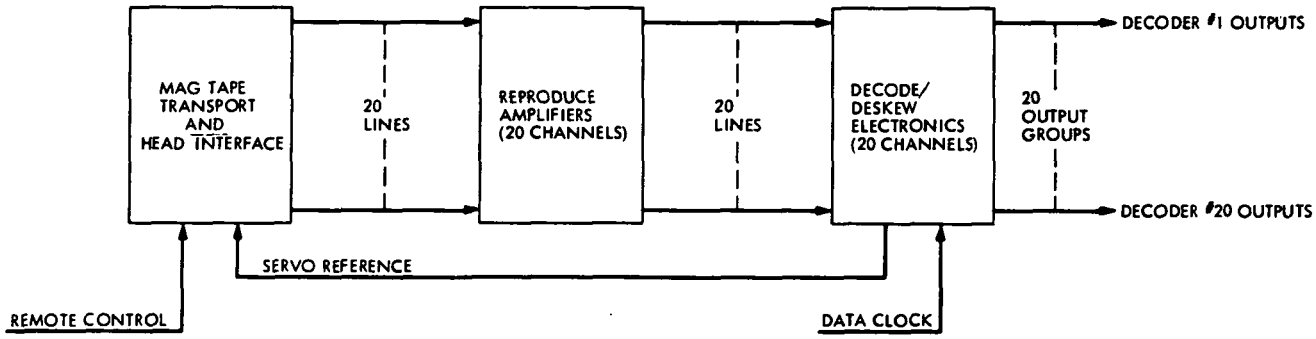

Fig. 3. Functional block diagram of commercial "reproduce" configuration

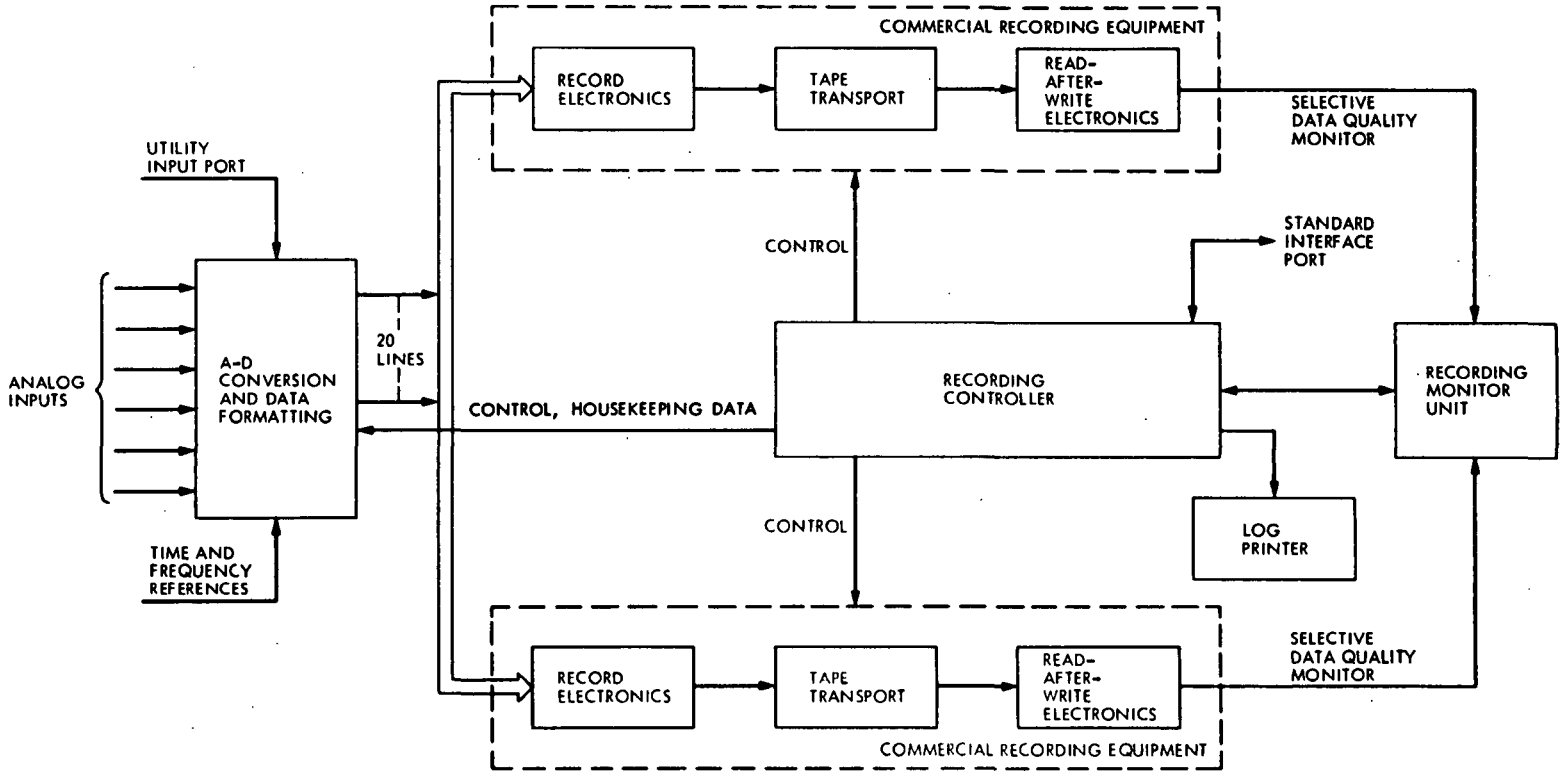

Fig. 4. Functional block diagram of equipment configuration at DSS

S-Band-X-Band Directional Coupler

R. Lay
R. F. Systems Development Section

In support of an effort to reduce microwave noise bursts at the DSN tracking stations, an S-band-X-band directional coupler has been fabricated. The goal was to develop a directional coupler that has a coupling of about 30 dB using two different rectangular waveguide sizes.

I. Introduction

The DSN tracking stations have experienced occasional problems with excessive microwave noise bursts appearing in the low-noise receivers during high-power diplexing at S-band. Locating the source of such noise bursts has often proved to be quite difficult. The S-band-X-band directional coupler, shown in Figure 1, has been investigated as a possible aid in locating the source of the noise bursts.

It is assumed that the electrical breakdown that generates the noise burst has a broad band spectrum. The directional coupler couples the X-band component of the noise burst through WR 112 waveguide to a test receiver while, in effect, completely isolating the test receiver from the high-level S-band being transmitted in WR 430 waveguide. By inserting the directional coupler at various locations in the waveguide system, it should be possible to isolate the source of noise bursts to a particular component.

II. Design Considerations

With reference to Figure 2, the directional coupler consists of two unequal size rectangular waveguides coupled together by means of a series of small coupling apertures on the broad walls between the two guides. The coupling theory is based on the diffraction of electromagnetic radiation by an aperture, where its size is small compared with the wave length. An incident wave in port 1 couples power into ports 3 and 4.

By proper adjustment of the aperture position d, the radiation in the direction of port 4 can be minimized and that in the direction of port 3 enhanced. The amplitude equations of the excited fields in the secondary waveguide are given in both References 1 and 2 in terms of its exciting and excited fields. In the case of a circular aperture, they are proportional to the cube of the radius. With the aid of a computer program the four amplitude equations have been solved for the proper aperture position d in order to obtain the maximum radiation into port 3 using a single-hole coupler model. The aperture position d = 3.1750 cm (1.25 inches) was chosen, and a circular aperture of radius r_0 = 0.436563 cm (0.171873 inches). Since the single-hole coupler model has a narrow bandwidth, many apertures were used in order to obtain better directivity over a larger bandwidth. There is a drawback in couplers using different sizes of coupling apertures because the ratio of the coupling coefficients is not constant over the frequency band. Thus, equal size

apertures were used, and equal spacing between the apertures was used for simplicity. Fifteen circular apertures were used, and the spacing between them, D = 1.9320 cm (0.80 inches) was chosen.

III. Tests

A waveguide coupler test sample has been fabricated. Low-power tests indicate that both good coupling and directivity were found over several bands of frequencies. Using a waveguide taper from X-band to S-band, it was possible to propagate an X-band signal inside the WR 430 waveguide of the coupler. With reference to Figure 2, the output of the excited waveguide (WR 112) was plotted on the X-Y plotter over a bandwidth as shown in Figure 3. Port 4 monitors the forward direction of the radiated power from port 1 and port 3 monitors the reverse direction of the radiated power from port 1. The directivity is obtained by subtracting one from the other.

With the test equipment available, a desirable frequency range would be the 8407-8417 MHz, which would afford about 30-dB coupling and 22-dB directivity over the 10-MHz bandwidth (Figure 3).

References

1. Montgomery, Dicke, and Purcell, "Principles of Microwave Circuits," *Radiation Laboratory Series*, pp. 177-179.
2. R. E. Collin, *Foundations for Microwave Engineering*,, McGraw-Hill Book Company, New York, 1966 pp. 190-197, pp. 270-282.

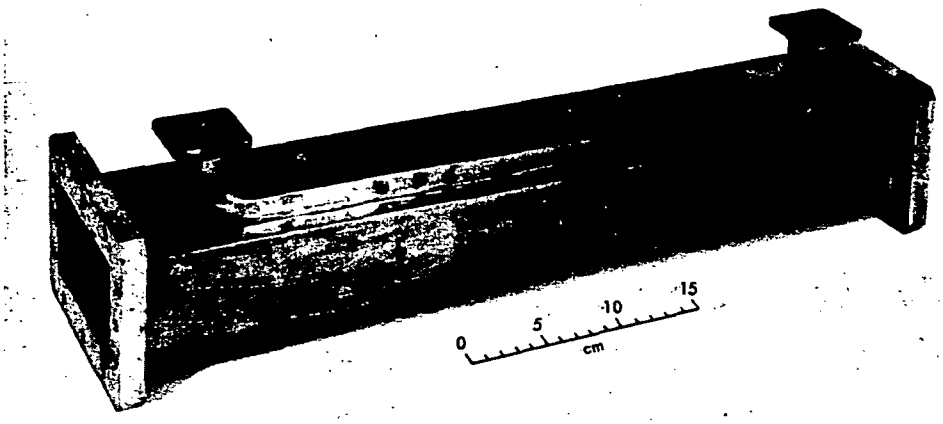

Fig. 1. S-band-X-band directional coupler

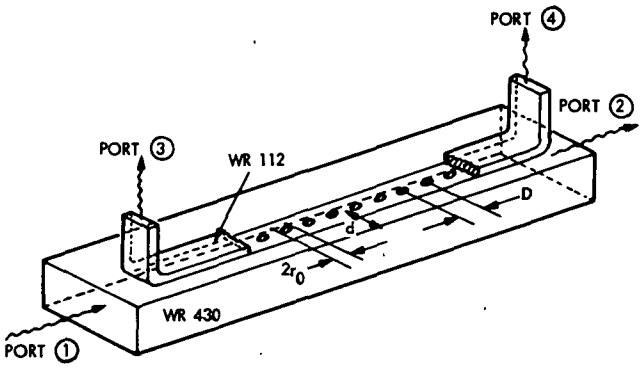

Fig. 2. Mechanical parameters

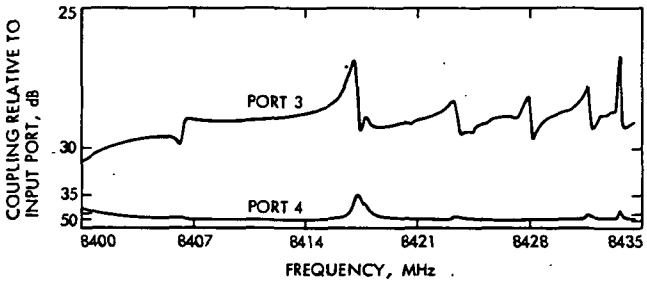

Fig. 3. Coupler performance

Heat Transfer Criteria of a Tubular Solar Collector – The Effect of Reversing the Flow Pattern on Collector Performance

F. L. Lansing
DSN Engineering Section

A new evacuated tubular solar collector has been selected for further investigation for the application of Goldstone energy conservation projects. This article presents briefly the exact heat transfer analysis of this two-pass-flow collector in an effort to determine the difference in performance characteristics with two different flow patterns. The results from this analysis are not only the determination of the collected heat rate and the temperature profiles at each cross section but also the prediction of the maximum attainable fluid temperature at zero flow rate in both cases.

I. Introduction

Part of the updated technology in energy conservation measures, using solar-assisted equipment, is the development of a new evacuated tubular two-pass-flow solar collector. This is a prospective candidate collector with a relatively higher thermal performance than the flat-plate type. The collector has been selected by the DSN Engineering Section for further theoretical and practical investigation for application in Goldstone energy conservation projects.

Limited laboratory measurements were the only data available for the performance of this collector. The latest attempt (Ref. 1) at NASA Lewis Research Center using a solar simulator and an analogous one-pass-flow tubular collector was found insufficient to provide the relevant performance characteristics of the actual two-pass-flow tubular collector. The common analysis procedure (Ref. 2) of assuming an overall, one-directional heat loss to the surroundings in a flat-plate collector expression is no longer adequate for exact performance analysis with two different kinds of flow patterns. This suggested the need for exact heat transfer and flow analyses as an essential step in the determination of performance characteristics over wide ranges of irradiancies, fluid flow rates, inlet fluid temperatures and ambient conditions. This article presents the steps and results of these analyses.

II. Collector Description and Flow Patterns

The tubular collector, as shown schematically in Figs. 1a and 2a, is composed of three all-glass concentric tubes, namely, a feeder tube, an absorber tube and a cover tube. The annulus space between the absorber and cover tubes is evacuated to such a low pressure ($\sim 10^{-4}$ torr) that convection and conduction losses are negligible. The absorber tube surface is coated with a selective material which minimizes outward long-wave radiation losses. In flow pattern (1), as shown in Fig. 1, the fluid, normally water, starts from the inlet section of the feeder tube and absorbs some of the useful solar energy along its path, thus raising its temperature. At the closed end of the collector, the fluid reverses its direction and passes in the annulus spacing between the feeder and absorber tubes. The temperature distribution along one streamline is as shown in Fig. 1b.

In flow pattern (2), as shown in Fig. 2, the fluid path is reversed from the above. It starts from one end of the collector through the annulus spacing, turns around at the closed end, and then leaves from the other end from the feeder tube. Both flow patterns (1) and (2) alternate, in each collector module, as shown in Fig. 3.

For more irradiancy augmentation, the set of collectors is mounted, with lateral spaces separating them from each other with a highly reflective back reflector, as shown in Fig. 4. This increases the overall irradiancy (Refs. 1 and 2) by as much as 64 percent at normal solar incidence.

III. Analysis

For a segment of the collector of length dx at steady-state conditions, the heat flux is divided as shown in Fig. 5, where

dQ_1 = the total irradiation on the cover tube from all sides (including irradiancies from the back reflector and reflections from adjacent collectors).

dQ_2 = the energy absorbed by the absorber tube (including absorption from multiple reflections within the evacuated space).

dQ_3 = the total outward reflection loss from all sides of the cover tube.

dQ_4 = the energy absorbed by the cover tube (including absorption from multiple reflections within the evacuated space).

dQ_5 = the long-wave radiation exchange between the cover and absorber tubes. (This is absorbed by the cover, thus raising its temperature.)

dQ_6 = the heat transfer to fluid (2) in the annulus pass from the absorber tube surface.

dQ_7 = the augmented radiation and convection loss between the cover tube and ambient air and sky.

dQ_8 = the heat transfer to fluid (1) in the feeder tube.

dQ_9 = the sensible heat gain to fluid (2) in the annulus pass.

For both flow patterns, at steady state, the heat balance of the absorber tube alone can be expressed as

$$dQ_2 - dQ_5 - dQ_6 = 0 \tag{1}$$

and the heat balance of the cover tube alone can be written as

$$dQ_4 + dQ_5 - dQ_7 = 0 \tag{2}$$

By eliminating the cover tube temperature, $T_3(x)$, and the absorber tube temperature, $T_8(x)$, from the heat balance equations for fluids (1) and (2), the problem is reduced to the solution of the two simultaneous differential equations, as follows:

$$\left.\begin{aligned} \frac{dT_1(x)}{dx} + K_1T_1(x) &= K_1T_2(x) \\ -\frac{dT_2(x)}{dx} + K_3T_2(x) &= K_1T_1(x) + K_4 \end{aligned}\right\} \text{for flow pattern (1)} \tag{3}$$

and

$$\left.\begin{aligned} -\frac{dT_1(x)}{dx} + K_1T_1(x) &= K_1T_2(x) \\ \frac{dT_2(x)}{dx} + K_3T_2(x) &= K_1T_1(x) + K_4 \end{aligned}\right\} \text{for flow pattern (2)} \tag{4}$$

where K_1, K_2, K_3, and K_4 are constants determined from the steady-state thermal analysis, and $T_1(x)$, $T_2(x)$ are the fluid temperatures in passes (1) and (2), respectively, at a distance x from the inlet section.

IV. Boundary Conditions

(1) $T_1(x) = T_2(x)$ at $x = L$ for both flow patterns (1) and (2)

(2) $T_1(x) = T_1(0)$ at $x = 0$ for flow pattern (1)

(3) $T_2(x) = \overline{T}_2(0)$ at $x = 0$ for flow pattern (2)

The temperature distribution $T_1(x)$, $T_2(x)$ of the fluid for pattern (1) or $\overline{T}_1(x)$, $\overline{T}_2(x)$ for pattern (2) can now be determined.

For flow pattern (1), and at the inlet section ($x = 0$), the temperature of the fluid leaving the collector $T_2(0)$ is given by

$$T_2(0) = T_1(0) + \left\{\left[T_1(0) - \frac{K_4}{K_3 - K_1}\right]\frac{s_1}{K_1} \times \left[\frac{1 - \exp[(s_1 - s_2)L]}{1 - \frac{s_1}{s_2}\exp[(s_1 - s_2)L]}\right]\right\} \quad (5)$$

where s_1 and s_2 are the roots of the quadratic auxiliary equation:

$$s_{1,2}^2 - (K_3 - K_1)s_{1,2} - K_1(K_3 - K_1) = 0 \quad (6)$$

For flow pattern (2) and at the inlet section ($x = 0$), the temperature of the fluid leaving the collector $\overline{T}_1(0)$ is given by

$$\overline{T}_1(0) = \overline{T}_2(0) - \left\{\left[\overline{T}_2(0) - \frac{K_4}{(K_3 - K_1)}\right]\frac{\overline{s}_1}{K_1} \times \left[\frac{1 - \exp[(\overline{s}_1 - \overline{s}_2)L]}{(1 - \frac{\overline{s}_1}{\overline{s}_2}\exp[(\overline{s}_1 - \overline{s}_2)L] + \frac{\overline{s}_1}{K_1}(\exp[(\overline{s}_1 - \overline{s}_2)L] - 1)}\right]\right\} \quad (7)$$

where $\overline{s}_1$ and $\overline{s}_2$ are the roots of the quadratic auxiliary equation:

$$\overline{s}_{1,2}^2 + (K_3 - K_1)\overline{s}_{1,2} - K_1(K_3 - K_1) = 0 \quad (8)$$

From Eqs. (6) and (8), it can be proved that the roots $\overline{s}_1$ and $\overline{s}_2$ are related to the roots s_1, s_2 by

$$\left.\begin{aligned} \overline{s}_1 &= -s_1 \\ \overline{s}_2 &= -s_2 \\ K_1(s_1 s_2) + (s_1 + s_2) &= 0 \end{aligned}\right\} \quad (9)$$

Substituting Eq. (9) in Eq. (7) will show that the expressions, Eq. (5) and Eq. (7), for the leaving fluid temperature in both fluid patterns are identical.

The results from this analysis are the determination of the collected heat rate and also the temperature distribution of the fluid as it flows in each pass in addition to the absorber and cover temperatures.

V. Maximum Fluid Temperature for Zero Flow Rate

The constants K_1, K_2, K_3, K_4, s_1, s_2, $\overline{s}_1$, and $\overline{s}_2$ are found to approach an infinity value as the mass flow rate approaches zero. However, their quotients have finite values independent of the fluid rate. Accordingly, it is always possible to find finite values for the ratios s_1/s_2, $\overline{s}_1/\overline{s}_2$, $K_4/(K_3 - K_1)$, $\overline{s}_1/K_1$, and s_1/K_1. Using L'Hopital's rule for indefinite quantities, the maximum fluid temperature, $T_2(0)$, for both flow patterns will be the limiting value, from Eq. (5) or Eq. (7), as the mass flow rate approaches zero. This is given by

$$[T_2(0)]_{max} = T_1(0) + \left[T_1(0) - \frac{K_4}{K_3 - K_1}\right]\frac{s_2}{K_1} \quad (10)$$

VI. Numerical Example

The following numerical example will show the difference in performance between the two flow patterns of the tubular solar collector. The data were arbitrarily abstracted to be as close as possible to actual running conditions. However, the conclusions may be generalized at any other relevant conditions.

Irradiation with normal incidence to back reflector

Inlet water temperature $T_1(0)$ in pattern (1) or $T_2(0)$ in pattern (2)	70°C
Ambient temperature T_0	30°C

Sky temperature	4°C
Irradiation intensity	0.75 kW/m²
Tube length	1.067 m
Feeder tube diameter	0.029 m
Absorber tube diameter	0.041 m
Cover tube diameter	0.51 m
Glass refraction index	1.526
Cover tube transmissivity	0.91
Cover tube emissivity	0.90
Absorber tube absorptivity	0.85
Absorber tube emissivity	0.10
Mass flow rate	5 kg/hr
Area of back reflector/ single collector	0.10645 m²
Distance between two consecutive cover tubes	0.05 m
Distance between cover tubes and back reflector	0.05 m
Wind speed	11 km/hr
Water specific heat	11.634×10^{-4} kWh/kg K

A. Collector Efficiency

The relevant constants K_1, K_2, K_3, and K_4 were calculated and given as

$$K_1 = 0.88532\ \text{m}^{-1} \qquad K_3 = 0.90242\ \text{m}^{-1}$$

$$K_2 = 2.50333\ \text{m}^{-1} \qquad K_4 = 13.44064\ \text{K/m}$$

The roots of Eq. (6) were given by

$$s_1 = +0.13189\ \text{m}^{-1} \qquad s_2 = -0.11479\ \text{m}^{-1}$$

and those of Eq. (8) were given by

$$\overline{s_1} = -0.13189\ \text{m}^{-1} \qquad \overline{s_2} = +0.11479\ \text{m}^{-1}$$

Substituting in Eqs. (5) and (7), the leaving temperature $T_2(0)$ in flow pattern (1) or $\overline{T}_1(0)$ in flow pattern (2) was found to be the same in both cases and equal to 350.96 K (77.96°C).

The instantaneous collector efficiency, based on the irradiation on the back reflector, was then calculated as

$$\text{collector efficiency} = \frac{(77.96 - 70) \times 5 \times 11.634 \times 10^{-4}}{0.75 \times 0.10645} = 58\%$$

for both flow patterns.

B. Temperature Distribution

For this example, the absolute temperature of the fluid in the feeder tube $T_1(x)$, the fluid in the annulus spacing $T_2(x)$, the absorber surface temperature $T_s(x)$ and the cover surface temperature $T_3(x)$ were given by

flow pattern (1)

$$T_1(x) = 786.026 - 177.572 \exp(0.13189x) - 265.454 \exp(-0.11479x)\ \text{K}$$

$$T_2(x) = 786.026 - 204.025 \exp(0.13189x) - 231.036 \exp(-0.11479x)\ \text{K}$$

$$T_s(x) = 5.369 + 0.993\, T_2(x)\ \text{K}$$

$$T_3(x) = 290.47 + 0.026\, T_s(x)\ \text{K}$$

flow pattern (2)

$$\overline{T}_1(x) = 786.026 - 231.036 \exp(-0.13189x) - 204.025 \exp(0.11479x)\ \text{K}$$

$$\overline{T}_2(x) = 786.026 - 265.454 \exp(-0.13189x) - 177.572 \exp(0.11479x)\ \text{K}$$

$$\overline{T}_s(x) = 5.369 + 0.993\, T_2(x)\ \text{K}$$

$$\overline{T}_3(x) = 290.47 + 0.026\, T_s(x)\ \text{K}$$

The temperature profile was plotted in Fig. 6 for each flow pattern. It is obvious that in the case of flow pattern (2), the fluid in the annulus spacing at the closed end ($x = L$) will reach a higher temperature than that in flow pattern (1). This is due to the augmenting heat transfer from solar irradiancy and from the relatively hotter fluid in the feeder tube.

C. Maximum Temperature for Zero Flow Rate

Since the running conditions in this example were initially characterized by a slow flow rate (5 kg/hr), it was reasonable to assume, without great loss of accuracy, that

the convective and radiative heat transfer coefficients do not change appreciably by further decrease of the flow rate. Accordingly, the ratio s_2/K_1 approaches -0.12965 and $K_4/(K_3 - K_1)$ approaches 786.026 K as the mass flow rate approaches zero. The limit of the temperature difference $[T_2(0) - T_1(0)]$ from Eq. (10) approaches 57.44°C as the mass flow rate approaches zero. This means that it is possible for the previous operating conditions and both flow patterns to reach a leaving fluid temperature of 127.44°C by one collector with an extremely slow flow rate.

VII. Performance Comparison

The results of the above steady-state analysis can be summarized as follows:

(1) The working fluid with different flow patterns (1) and (2) in the tubular solar collector yields the same value of temperature difference only across the open end of the collector. This result is a useful tool in simplifying the collector module performance by adopting *one* analytical expression for both flow patterns between inlet and leaving fluid temperatures.

(2) The design of selective coating and its durability should take into consideration the larger thermal gradient and the higher absorber tube temperature in flow pattern (2) compared with that in flow pattern (1). The relatively faster degradation of the coating of flow pattern (2) compared with that of flow pattern (1) will affect the maintenance costs.

Having established an analytic expression for collector performance enables the study of future topics. Examples of these topics are the effects of introducing different types of working fluids or setting different collector dimensions.

References

1. Simon, F., *Solar Collector Performance Evaluation with the NASA-Lewis Solar Simulator — Results for an All-Glass-Evacuated Tubular Selectivity Coated Collector with a Diffuse Reflector*, NASA Technical Memorandum NASA TM X-71695, 1975.

2. Beekly, D. C., and Mather, G. R., "Analysis and Experimental Tests of High Performance Tubular Solar Collector," Presented at Int. Solar Energy Society Meeting, UCLA, August 1975.

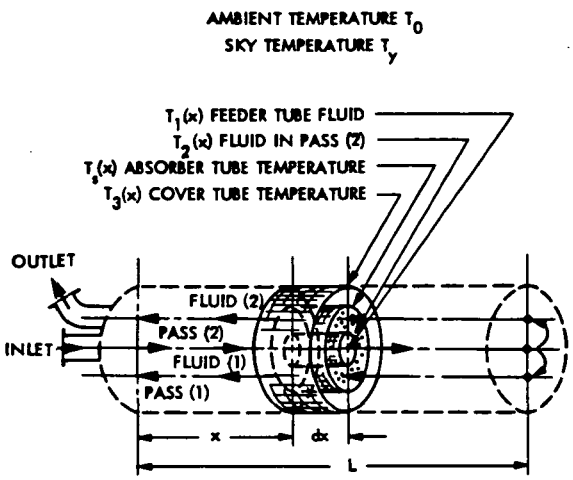

Fig. 1a. Collector configuration (flow pattern 1)

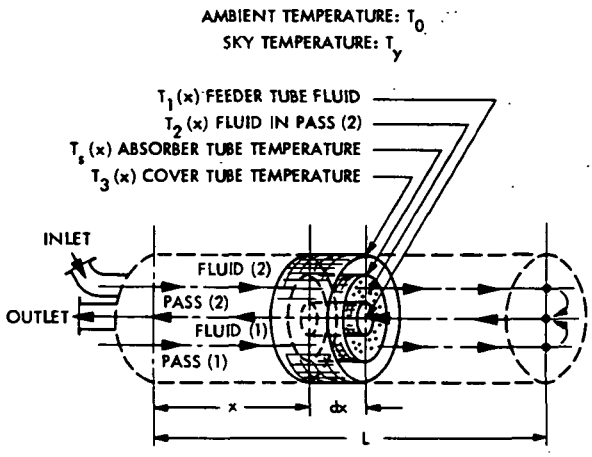

Fig. 2a. Collector configuration (flow pattern 2)

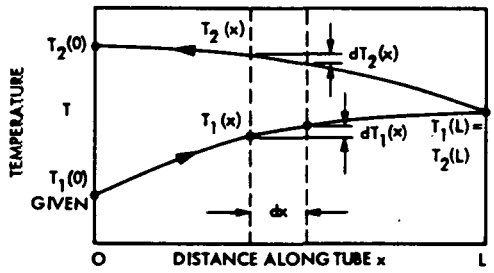

Fig. 1b. Temperature distribution along one collector (flow pattern 1)

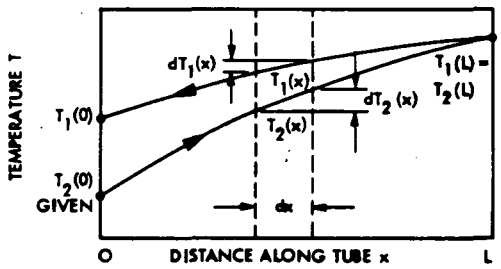

Fig. 2b. Temperature distribution along one collector (flow pattern 2)

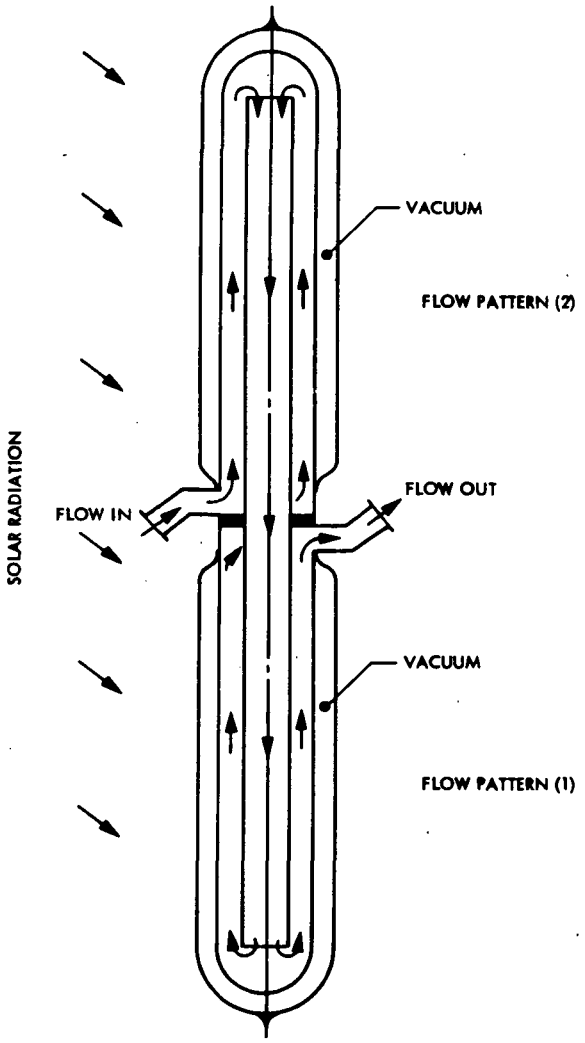

Fig. 3. Two collector tubes in series

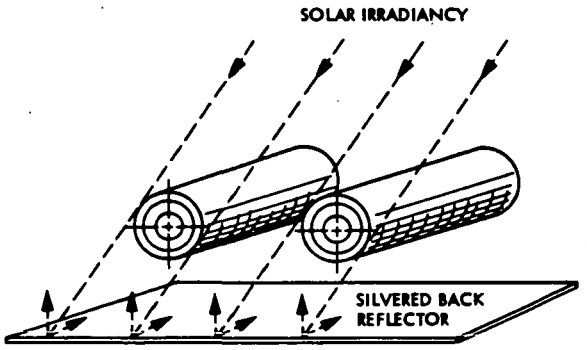

Fig. 4. Arrangement of two collectors with a flat back reflector

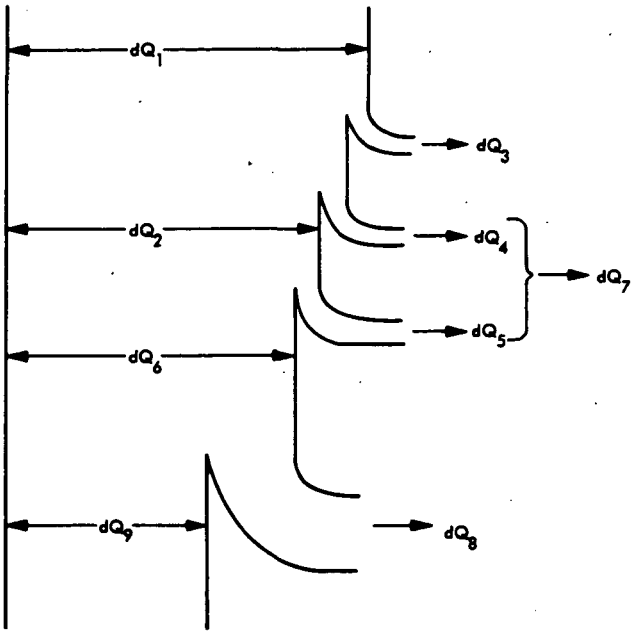

Fig. 5. Sankey diagram for the two-pass-flow collector

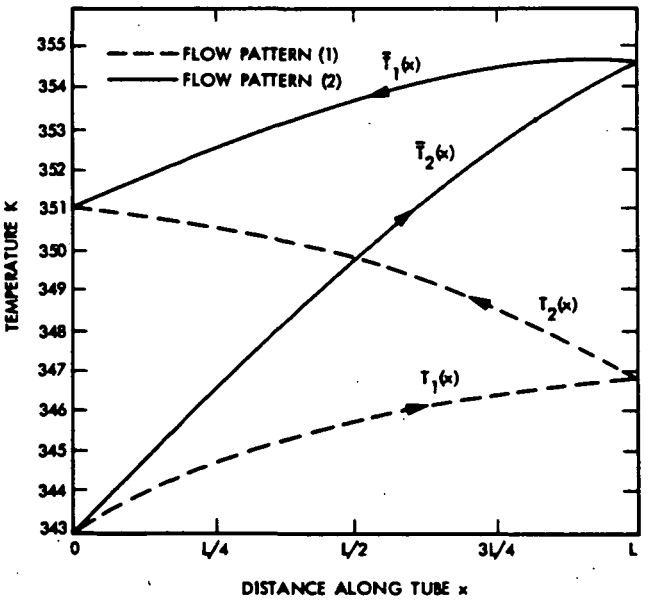

Fig. 6. Temperature distribution along a streamline with a flow pattern (1) and (2)

Tracking Operations During the Viking 2 Launch Phase

J. A. Wackley
Network Operations Office

Viking 2 launch phase operational procedures, and in particular the DSN initial acquisition procedures, were very intensively considered and conservatively designed to accommodate even the most unfavorable of launch possibilities. These procedures were successfully implemented and strongly contributed to the highly successful launch of Viking 2.

I. Introduction

The Viking 2 spacecraft was launched from the Air Force Eastern Test Range (AFETR) at 18:38:59.96 Greenwich Mean Time (GMT) on 9 September, 1975, at a launch azimuth of 96.507 degrees. Like its sister spacecraft, Viking 1, the mission of Viking 2 is to study the planet Mars via direct measurements in its atmosphere, on its surface, and in orbit around it. After being placed in a parking orbit by the combination Titan III-E/Centaur D-1T launch vehicle, Viking 2 was injected into a trans-Mars, heliocentric transfer orbit over southern Africa. The resulting near-Earth portion of the orbit was such that, within the Deep Space Network (DSN), the Australian complex of tracking stations was first to view the spacecraft. The Deep Space Station (DSS) selected to perform the initial acquisition was DSS 42, with DSS 44 serving as a backup.

In the following sections, the prelaunch tracking operations planning will be reviewed and an analysis of the subsequent launch phase tracking operations at DSS 42 and DSS 44 will be presented.

II. Review of the Viking Acquisition Strategy

Since Viking 2 was similar to Viking 1 in both the trajectory it was to follow and in the characteristics of its radio frequency subsystem, it was not necessary to make any major revisions to the acquisition plan used during the Viking 1 launch (described in detail in Reference 1). The main points of this plan were:

(1) Antenna to be driven in computer mode until after confirmation of two-way. In order to accomplish this, tracking predictions based within two seconds of the actual liftoff time were needed by the stations. Thus, with this necessity in mind, the new Polynomial Coefficient Tape-Network Operations Control Center Prediction software (PCT-PREDIK) prediction generation system was carefully exercised

in prelaunch testing and an elaborate PCT generation plan was developed (see Reference 1). By the day of launch, the throughput time of the system had been reduced from approximately 41 minutes to less than 30 minutes.

(2) Uplink acquisition to commence at approximately rise plus three minutes in order to collect as much two-way doppler data as possible before the interruption in data to be caused by the uplink transfer to DSS 44.

(3) Uplink acquisition sweep to encompass $XA \pm 110$ Hz by use of the voltage-controlled oscillator (VCO). The extent of the sweep was chosen based upon the combination of the trajectory uncertainties and the spacecraft receiver uncertainties provided by the Orbiter Performance Analysis Group (OPAG) these being (at VCO level):

3σ *XA* TRAJECTORY ~ .05 Hz

3σ *XA* S/C RECEIVER ~ 15 Hz

3σ *XA* S/C "RANDOM WALK" ~ 7.5 Hz

3σ *XA* S/C VCO TEMPERATURE ~ 5.6°C

and

$\partial XA/\partial T \sim 9$ Hz/°C

which when combined give a total 3σ uncertainty of approximately 53 Hz. Thus the sweep was designed to encompass approximately twice the 3σ values about the *XA*. Figure 1 details the *XA* frequency versus time.

(4) Uplink tuning rate to be 3 Hz/sec (VCO). This rate was considered to be close to the limit of the accurate manual tuning capability and when received at the spacecraft would result in an effective tuning rate of about 280 Hz/sec, approximately the geometric mean of the allowable tuning rates.

Additionally, the open window launch trajectory for 9 September resulted in maximum angular and frequency rates of:

$d/dt\,\{HA\} \cong .06$ degree/second

$d/dt\,\{D2\} \cong 119$ Hz/second (S-band)

$d/dt\,\{XA\} \cong .6$ Hz/second (VCO)

where

HA = Local (station) hour angle

D2 = Two-way doppler frequency

XA = Spacecraft receiver best lock with doppler accounted for

While these rates are higher than those encountered during the Viking 1 launch, they are much lower than those encountered in previous parking orbit ascent trajectories. Figure 2 is a stereographic illustration of the launch pass over DSS 42. The Elevation Angle versus time is shown in Figure 3, which also serves as a time line for the important tracking events at DSS 42.

III. Postflight Analysis of the Viking 2 Launch Phase

A. Tracking Predictions

1. The PCT-PREDIK Prediction Generation System. The PCT-PREDIK System functioned smoothly and efficiently during the Viking 2 launch phase. Because the Viking Flight Path Analysis Group (FPAG) was able to deliver the first PCT at launch minus two hours 30 minutes, Stations 42 and 44 had more than enough time to generate a drive tape well before launch using predicts set B09D. During the launch countdown, changes made to the predicted frequency were small enough (XMTREF was changed by 3 Hz) that it was decided not to generate the planned frequency update predicts (predicts set B09F).

As was the case in the Viking 1 launch, the remaining throughput time problems and concerns were allayed when launch occurred within a fraction of a second of the expected time. This left only one predicts set to be generated between launch and spacecraft rise; this set updated the frequencies and gave the stations text predicts with a GMT time field (all previous text predicts had been generated in time from launch (TFL)).

2. Prediction accuracy. During the early portion of the DSS 42 launch pass, the radiometric data, when differenced with the preflight nominal predicts set B09E by the Network Operations Control Center (NOCC) pseudoresidual program yielded the following residuals:

$\Delta HA \sim -.07$ degree

$\Delta D2 \sim -29$ Hz (S-band)

$\Delta XA \sim 14$ Hz (VCO)

These can be compared to the 3σ uncertainties supplied by the Viking project:

$\Delta HA \sim .002$ degree

$\Delta D2 \sim 10$ Hz (S-band)

$\Delta XA \sim 55$ Hz (VCO; total frequency/trajectory uncertainty)

The residuals, in general, exceeded the 3σ uncertainties (which must be considered miniscule when compared to

previous mission trajectory uncertainties). The hour angle residual had no impact on the acquisition of the downlink and caused no degradation of received signal level even though it substantially exceeded the 3σ uncertainty. Additionally, the magnitude of this angle residual is nearly equal to the hour angle residual of the Viking 1 launch which places it among the smallest early launch pass angle residuals yet achieved.

The two way doppler residuals shown in Figure 4 started quite large (approximately –300 Hz), but gradually decreased to approximately –29 Hz (or three times the expected 3σ value) as the apparent motion of the spacecraft approached sidereal rate.

The difference between the measured and predicted best lock frequencies, ΔXA, fell well within the total trajectory/frequency 3σ uncertainty. Though larger than the ΔXA for the Viking 1 launch ($\Delta XA \sim -0.3$ Hz) the magnitude of this ΔXA fell easily within the boundaries of the prescribed uplink sweep and caused no problem in the uplink acquisition.

B. One-Way Acquisition at DSS 42

Acquisition of the Viking 2 one-way downlink at DSS 42 was reported at 19:27:01 GMT, 25 seconds prior to the expected spacecraft rise time of 19:27:26 GMT. This again indicates a possible error in the DSS 42 horizon mask used in the prediction software. (This problem was first noted during the Viking 1 launch. See Reference 1, Section VI-B.)

The downlink acquisition is illustrated in Figure 5. As can be seen, it appears that the receiver was being tuned through the region near the predicted one-way doppler prior to the expected spacecraft rise time. The signal was apparently detected at approximately 19:26:41 GMT with Receiver 5 (connected to the S-band Cassegrain Monopulse (SCM) Antenna) reported in lock at 19:27:01 GMT. Both monitor and tracking data indicate, however, that Receiver 6 (connected to the S-Band Acquisition Aid (SAA) Antenna) may have sustained lock from as early as 19:26:41 GMT.

C. Two-Way Acquisition at DSS 42

DSS 42 was instructed to perform the following uplink acquisition sweep designed according to the specifications described in Section II:

TRANSMITTER ON: 19:30:40 GMT

START SWEEP: 19:31:00 GMT

STARTING FREQUENCY: 22.035090 MHz (VCO)

SWEEP RATE: 180 Hz/min (VCO)

END SWEEP: 19:32:30 GMT

ENDING FREQUENCY: 22.035360 MHz (VCO)

SWEEP DURATION: 90 seconds

A comparison of the instructed sweep with the actual uplink acquisition sweep is depicted in Figure 6. As is shown, the sweep began approximately seven seconds later than planned. At 19:32:02 GMT, the switch to the two-way coherent mode occurred. The two-way downlink was very quickly acquired by DSS 42 with the receiver back in lock at 19:32:12 GMT. However, as the receiver was being locked to the downlink, tuning slowed and almost stopped for several seconds. The tuning rate for the remainder of the sweep was somewhat slower than during the initial portion of the sweep, causing the ramp to take fifteen seconds longer than originally planned.

When the doppler extractor was switched from the SAA antenna receiver to the SCM antenna receiver, it was found that that receiver was in lock on a sideband located approximately 10 kHz from the main carrier (see Table 1). Receiver lock on the sideband was broken approximately two minutes later and the carrier reacquired at 19:34:44 GMT.

D. Angle Tracking

In following the angle strategy reviewed in Section II, the antenna at DSS 42 was initially computer-driven using the preflight nominal predicts set B09D, generated at launch minus two hours. The drive mode was changed to autotrack at 19:35:51 GMT following completion of the uplink acquisition.

As was the case during the Viking 1 initial pass, it was necessary to transfer the uplink to DSS 44 in order to allow DSS 42 to switch maser No. 1 into the antenna microwave subsystem. In preparation for this reconfiguration, the drive mode at DSS 42 was changed back to computer mode at 20:17:00 GMT. Autotracking was resumed five minutes later, following the uplink transfer back to DSS 42. After the failure of maser No. 1 at 23:11:16 GMT, DSS 42 returned to computer drive for the remainder of the pass.

E. Ranging

The acquisition of range data at DSS 42 began at 22:25:02 GMT and continued with generally good results through the acquisition of seven range points. Using the Pseudo-Differenced Range Versus Integrated Doppler (DRVID) technique the range points were evaluated with the following results:

Acquisitions	Pseudo-DRVID (RU)
1/2	4
2/3	-11
3/4	376836
4/5	*
5/6	-1
6/7	352235

*Unable to compare due to erroneous reset of doppler counter.

As can be seen, two acquisitions, numbers four and seven of the seven completed, resulted in erroneous range points. Acquisition number four was started at 23:10:02 GMT and completed two minutes later, during which time maser No. 1 failed causing the acquisition to be erroneous. The seventh and final acquisition began at 00:15:02 GMT. During this acquisition the antenna drove approximately two degrees off point causing a bad acquisition.

The pseudo-DRVID computed for the remaining five points indicates that they were of good quality and usable for orbit determination.

F. Launch Pass Activities at DSS 44

Since it was designated to serve as a backup station, DSS 44 played a somewhat passive role in the Viking 2 launch phase operations. Its availability however allowed some unique (for a launch phase) configurations to be used at DSS 42.

In prelaunch planning sessions, the acquisition planning group was presented with the following constraints and requirements (among others):

(1) The downlink signal level at spacecraft rise was expected to be strong enough (~ -80 dBm for the SCM antenna) to cause saturation of the maser.

(2) A planned roll turn (at launch plus 150 minutes) of the spacecraft to execute a sky map could cause unfavorable antenna angles. This would result in the possible loss of two-way lock if the S-band Acquisition Aid antenna was transmitting.

(3) Bioshield separation needed to be observed in the attitude control system telemetry.

(4) Two-way doppler and telemetry needed to be continued without major interruption.

To resolve these difficulties, it was decided that both stations would be configured in the maser by-pass mode (i.e., the maser would be completely out of the antenna microwave system) during the period of high signal level and that the S-band Cassegrain Monopulse (SCM) antenna would be used for transmission during the roll turn. Thus, an uplink transfer would be effected between DSS 42 and DSS 44 at approximately launch plus 100 minutes in order to provide continuous telemetry and alleviate the need to reacquire the uplink while DSS 42 reconfigured the maser and transmitter. When it again had the uplink, DSS 42 would be configured for normal cruise support (i.e., maser in, SCM antenna transmitting) without loss of data to the Viking project.

Following this plan, DSS 44 acquired the one-way Viking 2 downlink at 19:29:18 GMT (as was the case with DSS 42, this time was considerably earlier than the predicted spacecraft rise time). The acquisition is shown in Figure 7. Autotracking of the spacecraft began at 19:33:38 GMT, after completion of the DSS 42 uplink acquisition sweep and confirmation of good three-way downlink.

The uplink was handed over to DSS 44 by means of a tracking synthesizer frequency (TSF) transfer (which does not require tuning of the uplink) from 20:18:02 to 20:21:02 GMT. Telemetry and tracking data continued uninterrupted during this period.

DSS 44 was reconfigured to normal cruise configuration at 20:27:40 GMT and continued tracking in the three-way mode until spacecraft set at 00:28:20 GMT.

IV. Summary

The acquisition strategy used during the Viking 1 launch was again successfully implemented during the Viking 2 launch. This strategy had been carefully planned to accommodate even the most unfavorable launch possibilities. The culmination of this careful planning and extensive training was the successful acquisition of Viking 2 and completion of the Viking launch phase.

Acknowledgement

The author wishes to acknowledge C. Linthurst and C. Darling for the fine graphical illustrations.

Reference

1. Berman, A. L. and Wackley, J. A., 'Tracking Operations During the Viking 1 Launch Phase', in *The Deep Space Network Progress Report 42-30*, Jet Propulsion Laboratory, Pasadena, Calif., Dec. 15, 1975.

Table 1. Doppler residuals

GMT	Residuals	Comments
19:30:30	−275.331	Final good one-way residual
19:31:00	−15029.743	Tuning one-way doppler flagged two-way
19:31:20	−12163.310	Tuning
19:31:40	−7095.466	Tuning
19:32:02	−1650.137	Receiver out of lock—switch to coherent mode
19:32:12	−298.039	Good two-way residual
19:32:20	−291.406	Good two-way residual
19:32:30	−286.623	Good two-way residual
19:32:34	−10026.788	Switch doppler extractor—SCM RCVR on sideband
19:33:00	−10019.764	Receiver on sideband
19:33:30	−10007.272	Receiver on sideband
19:34:00	−9993.609	Receiver on sideband
19:34:36	−11827.154	Receiver out of lock
19:34:44	−228.606	Receiver in lock on carrier
19:35:00	−203.622	Good two-way residual

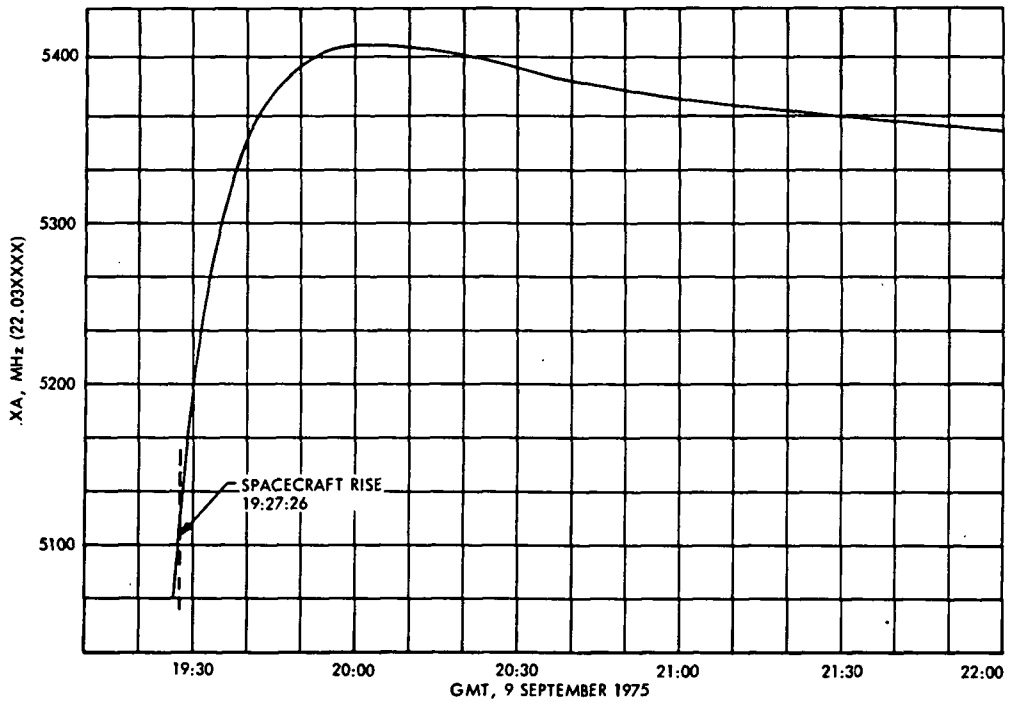

Fig. 1. Best lock frequency at DSS 42, Viking 2 launch, September 9, 1975

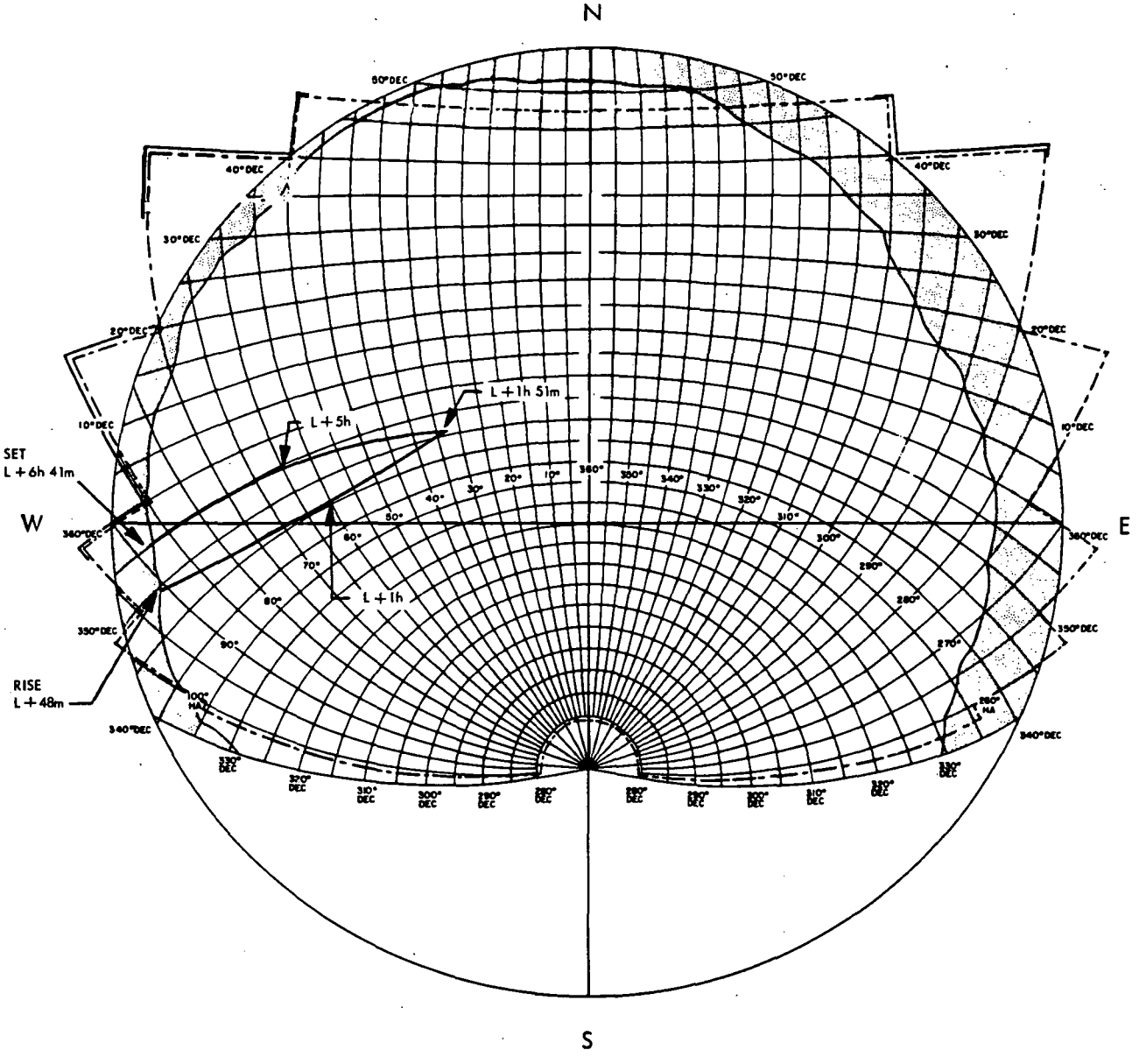

Fig. 2. DSS 42 Viking 2 launch, September 9, 1975

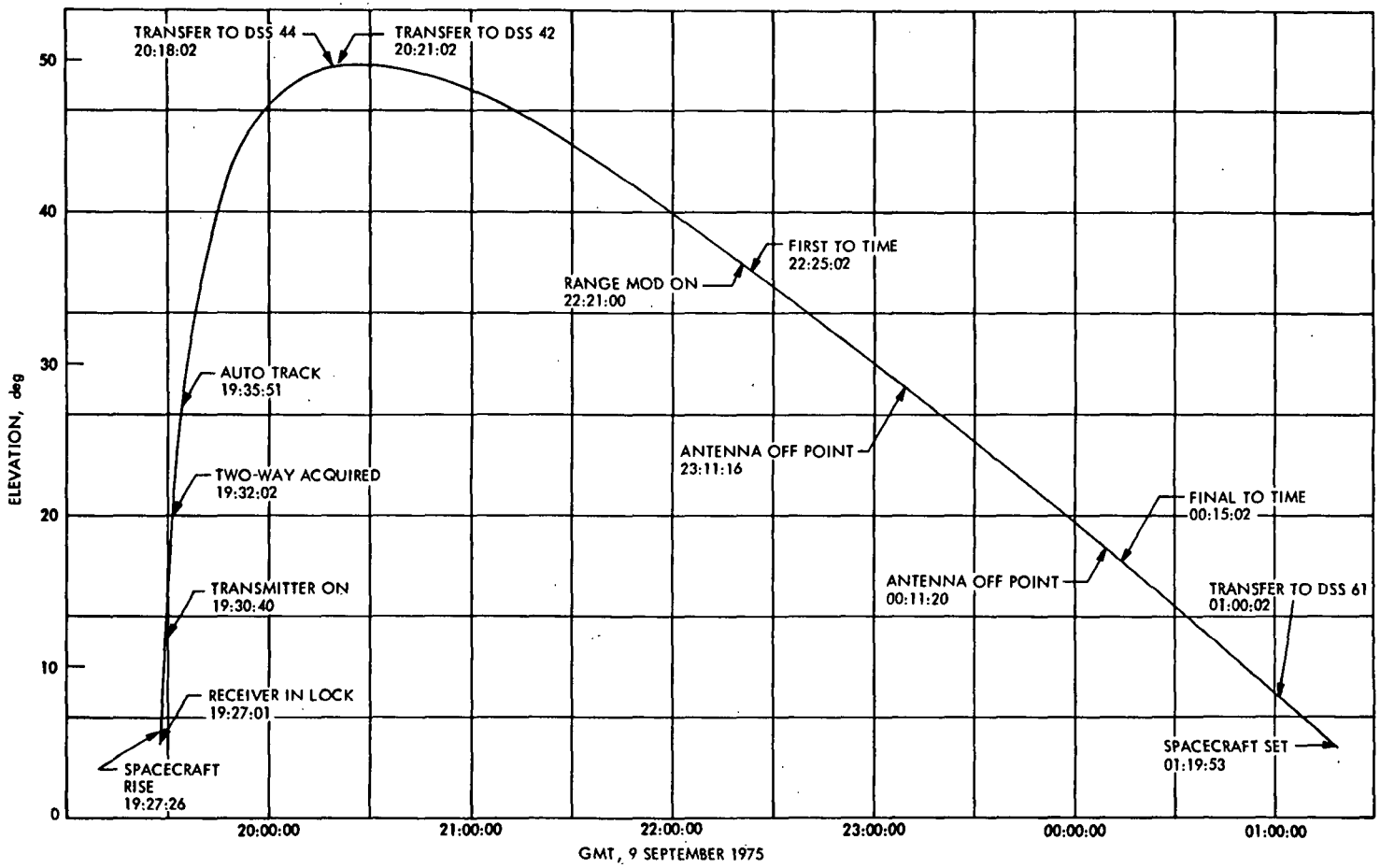

Fig. 3. Elevation at DSS 42, Viking 2 launch, September 9, 1975

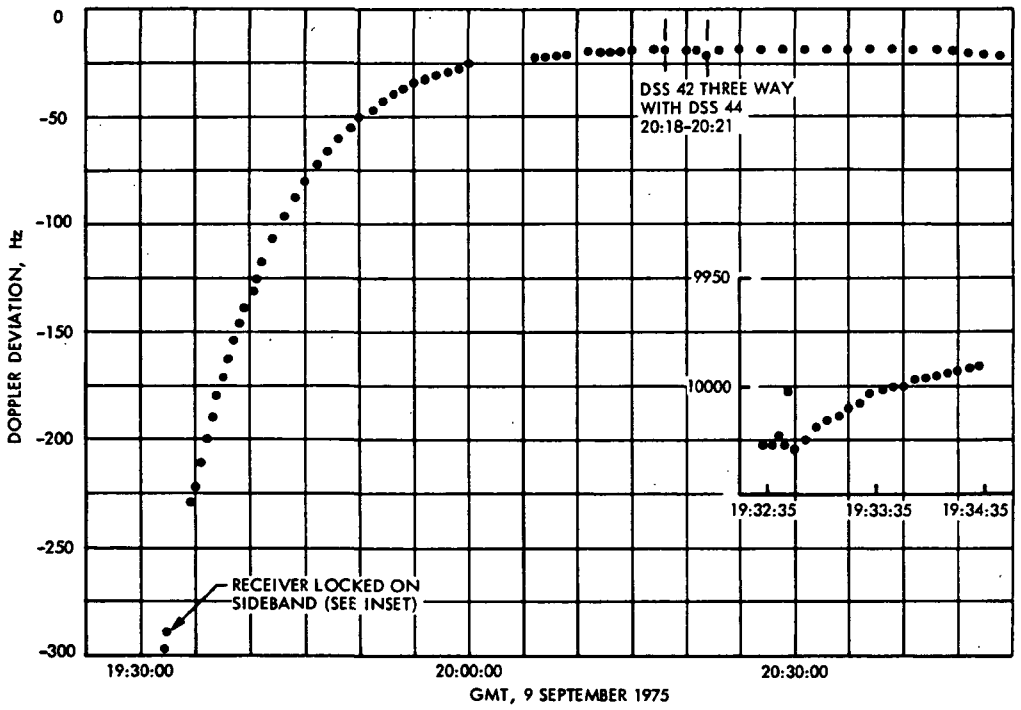

Fig. 4. Doppler deviation from preflight nominal predicts, DSS 42, predicts set B09E

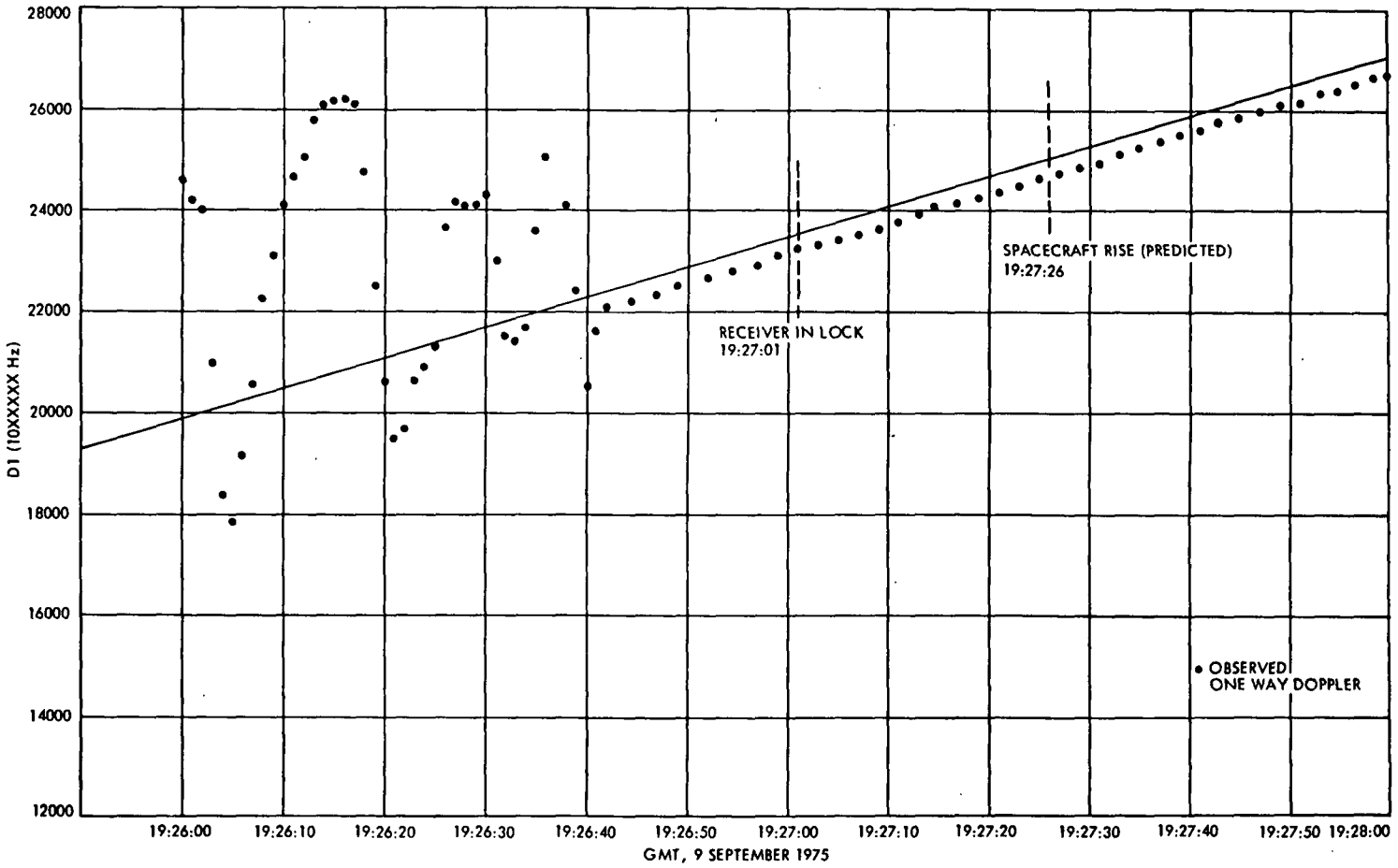

Fig. 5. Initial downlink acquisition at DSS 42, Viking 2 launch

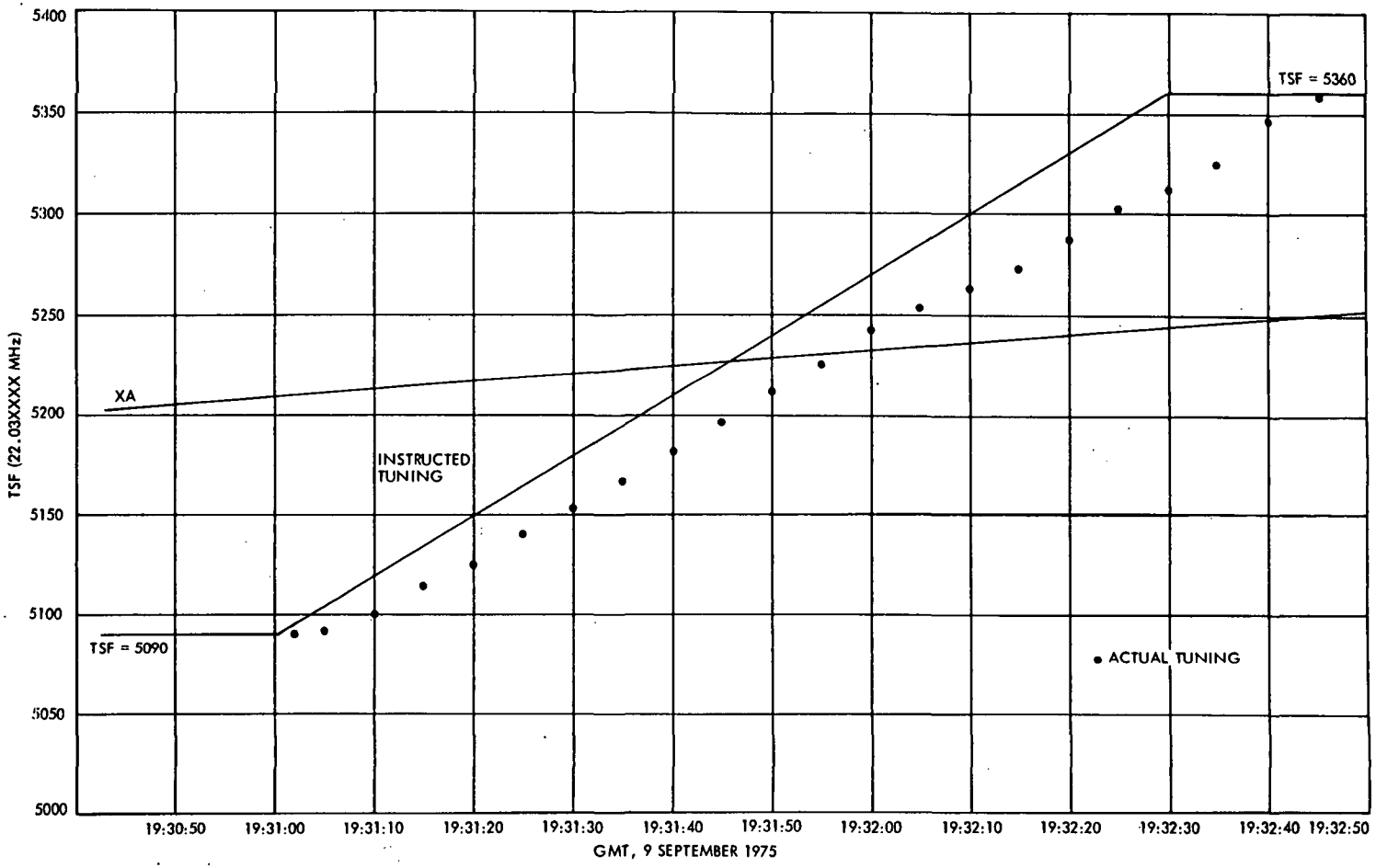

Fig. 6. Comparison of actual tuning to instructed tuning at DSS 42, Viking 2 launch

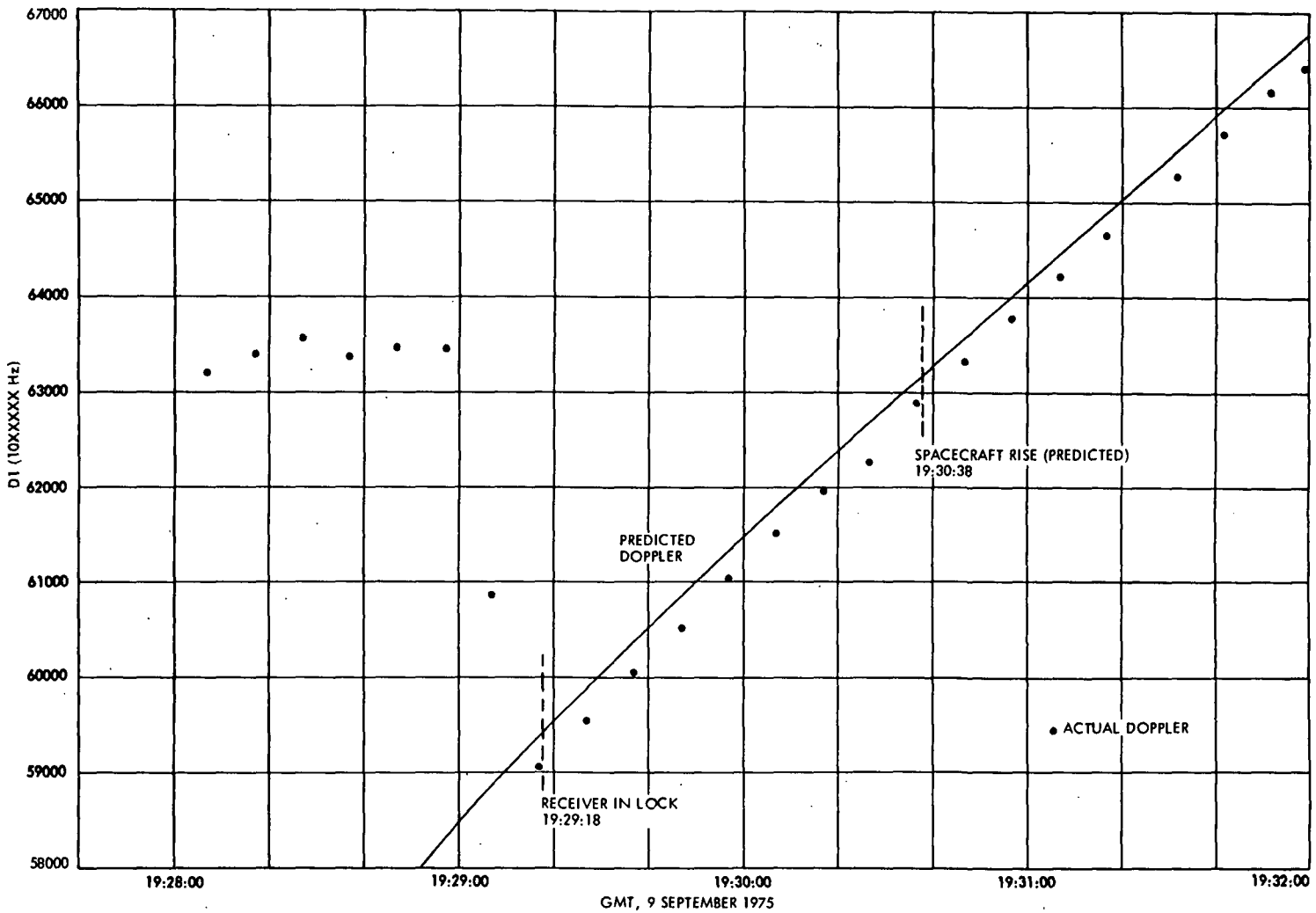

Fig. 7. Initial downlink acquisition at DSS 44, Viking 2 launch

OMIT

Network Loading Visibility for Management

D. M. Enari and C. A. Holritz
Network Operations Office

The responsibilities of the Deep Space Network (DSN) Operations Scheduling Group (NOSG) are outlined. The long-range scheduling portion of the NOSG is explained in detail. Examples of the DSN Forecast, published quarterly by the NOSG, are also included.

The Deep Space Network (DSN) Operations Scheduling Group (NOSG) has the responsibility of forecasting, allocating and scheduling the utilization of the DSN facilities in response to requirements from all of its users such as flight projects, radio science, and DSN development. In addition, requirements which are internal to the DSN such as maintenance, engineering, training and facility updates must be forecast, allocated and scheduled. The NOSG is also responsible for providing management with information which will give them visibility concerning mission support, facility utilization and Network loading.

The official NOSG publications which comply with these responsibilities are as follows:

1. *Seven-Day Schedule* — Detailed schedule for the coming week. Published weekly.

2. *Mid-Range Schedule* — Time-sensitive schedule of facility activities for each day for the next 8 weeks. Provides the basis for the Seven-Day Schedule. Published monthly.

3. *Forecast* — Gross planning of Network allocation for the next 3 years. Provides the basis for the Mid-Range Schedule. Published quarterly.

To provide management with the assessment required, a method for displaying the data is available. It consists of a set of *Network Requirements and Allocation Charts*, which display the requirements placed on the Network by users, the capability of the Network and the planned allocation of that capability to the various users in accordance with established priority guidelines. The total requirements, allocations and capability are displayed at the bottom of the chart just above the calendar. Major milestones are displayed across the top of the chart as an aid to correlating requirements (loading) with events. Figure 1 is an example of this chart. Note that it covers two fiscal years, FY 1975 and FY 1976, in 4-week increments, for the 26- and 64-meter stations at the Goldstone longitude (DSSs 11, 12 and 14). A complete set

of charts comprises 9 charts; 3 for each of the three longitudes at which the DSN has Deep Space Stations (DSSs), namely the Goldstone longitude (DSSs 11, 12 and 14), the Australian longitude (DSSs 42, 43 and 44) and the Spanish longitude (DSSs 61, 62 and 63). The three charts for each longitude cover the years of interest; one prior year, the current year and two future years.

For the purpose of long-range forecasting, the following guidelines are used in establishing the capabilities of the Network. The available station hours, as defined by the budget, are divided into two basic categories. Seventy percent are allocated for DSN user support and thirty are allocated for facility internal activities. Also, for long-range forecasting, a "pass" is considered to be an average of 12 hours in duration. To determine the capability in "passes per 4 weeks," the station hours are multiplied by 0.7, divided by 12, rounded to the nearest whole number and then multiplied by 4. Thus, a station which is staffed for 120 hours per week (3 shifts) would be allocated 84 hours per week for user support, which will provide a capability of 7 passes per week or 28 passes per 4-week period.

For "quick-look" display and for convenience in planning support of future requirements on the Network, a set of "residual" graphs is made. Figure 2 is an example of this chart. These graphs show the difference between the total requirements for each antenna size and the total capability at each longitude. The time scale shown in Fig. 1 is used. When the requirements exceed the capability, the difference is plotted as a positive (+) value and indicates an "overload" and a conflict. If the requirement is less than the capability, the difference is plotted as a negative (-) value, representing an "underload" and no conflict. The zero line represents the capability. The scale is in increments of 8 passes per 4-week period. This value was chosen for convenience because, to a first-order approximation, 8 passes represents the difference in capability resulting from changing the staffing at a station by one shift over a 4-week period.

Because of the method of display and the scales that have been chosen, these charts and graphs provide management with the visibility of Network loading and provide the basis on which decisions can be made concerning budgeting, station staffing and negotiations among Network users.

The DSN has some users whose requirements are of a nature which makes it possible to use the charts to "smooth" the loading on the Network. This can be done because their requirements, unlike those of flight projects, are not sensitive to time of day or specific days. Radio science, DSN development, Pioneer 6–9 coverage and certain types of tests fall into this category. The detailed scheduling of this support is usually accomplished during the eight-week and seven-day scheduling process in a manner which meets the broad requirements and also aids in normalizing the loading on the Network.

PREPARED BY NETWORK OPS SCHEDULING GROUP

AS OF 1 OCTOBER 1975

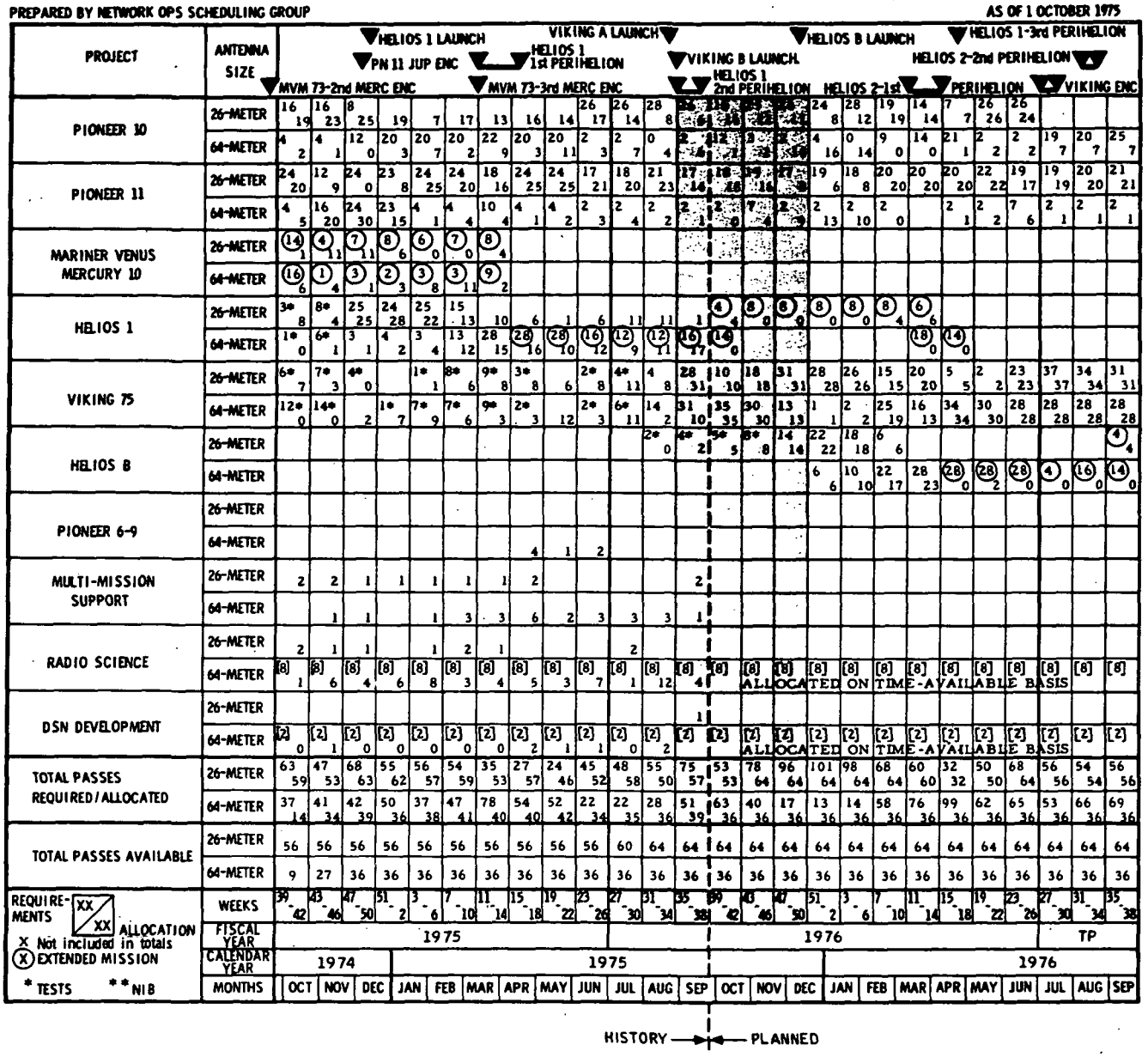

Fig. 1. DSN forecast, Goldstone

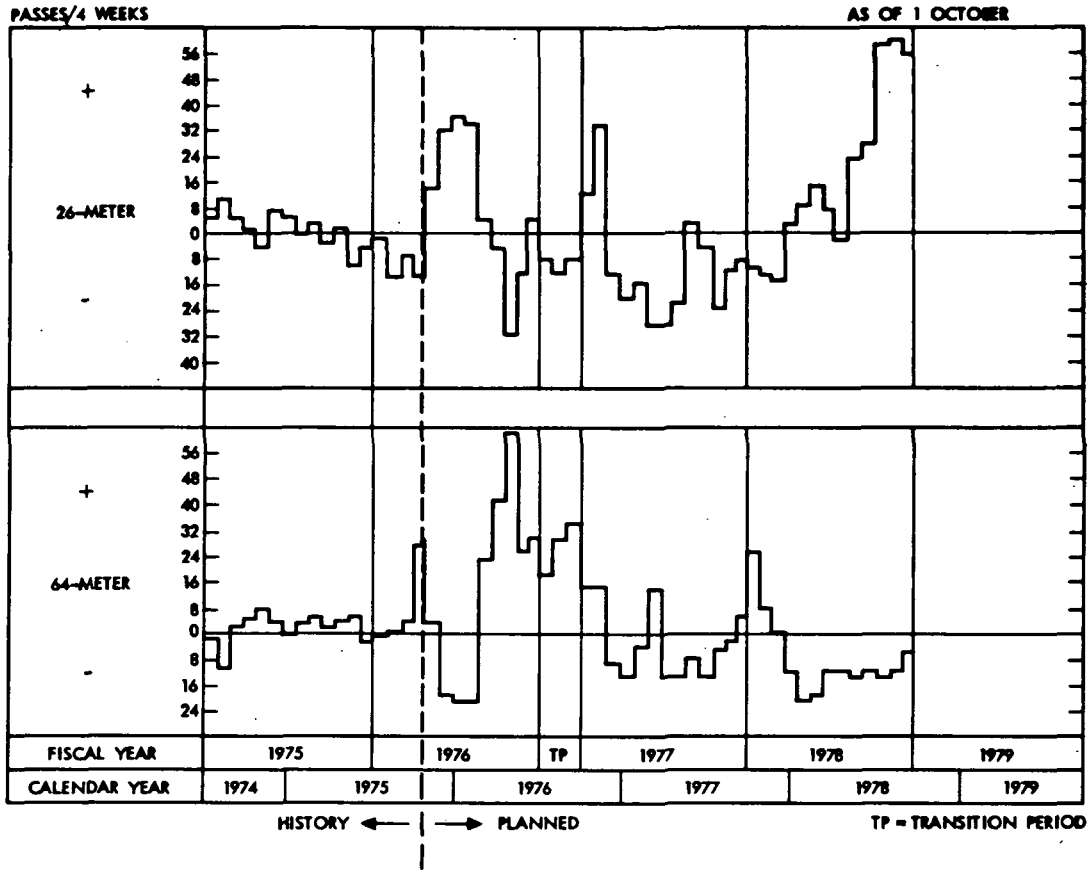

Fig. 2. Network requirements less Network capabilities, Goldstone

DSN Research and Technology Support

E. B. Jackson
R. F. Systems Development Section

The activities at the Venus Station (DSS 13) and the Microwave Test Facility (MTF), both operated by the Development Support Group, during the period Oct. 16–Dec. 7, 1975 are discussed and progress noted. Continuing testing of the remote-controlled automated station is noted as well as routine pulsar observations.. Automatic stability-reliability testing of the station maser-receiver-noise adding radiometer combination is described along with the data collected while so doing. Comparative measurements on the production version of the dichroic plate installed on the 64-m antennas are described along with mention of testing of a National Bureau of Standards (NBS) radiometer. Engineering measurements on the microwave power transmission test setup are described and a progress report of the X-Band Radar, Transmit-Receive; K-Band Receive (XKR) feedcone rehabilitation is given. Special testing of the new design feedcone for the Unified S-Band stations is mentioned, and measurements on interference received from the navigational equipment aboard military or commercial aircraft are described. Reporting of routine maintenance and support of clock synchronization transmissions and various radio science experiments is also included.

During the period Oct. 16–Dec. 7, 1975, the Development Support Group, in operating the Venus Station (DSS 13) and the Microwave Test Facility (MTF) supported various programs as discussed below.

I. Station Automation

Demonstration of a remotely operated automated station is planned using DSS 13 as the test station. Although a successful demonstration has been conducted (DSN Progress Report 42-30, pp. 214–221), refinement of software and reliability testing is continuing.

The antenna waveguide switch controller was modified, and computer monitoring of the position of the polarization selector and ambient load selector switches was provided. System testing and automated pulsar tracking continued. A total of 45 hours of station support time, including 17 hours of automated pulsar tracking, was provided during this period.

II. Pulsar Observations

In support of the Radio Science Experiment "Pulsar Rotation Constancy," DSS 13 provided 56-3/4 hours of observations during which the emissions from the pulsars tabulated in Table 1 were recorded. These data, recorded at 2388 MHz, left-circular polarization (LCP), are used to determine precise pulse-to-pulse spacing, pulse shape, and pulse power content of the signals emitted by these pulsars.

III. Maser–Receiver–Noise Adding Radiometer (NAR) Reliability–Stability Testing

Stability and reliability testing of the DSS 13 receiving system is conducted automatically during non-operational station periods. The 26-m antenna is pre-positioned in elevation and azimuth, and the NAR automatically records total system temperature as a function of time. The rotation of Earth sweeps the fixed antenna beam across the sky, resulting in generation of a radio brightness temperature sky map in addition to the data on stability and reliability of the system. During this period 391-1/4 hours of such data were automatically recorded with the antenna at 360 degrees azimuth and progressively positioned from 53.3 degrees to 52.7 degrees in elevation. Testing is done at 2295 MHz, using right-circular polarization (RCP) on the 26-m antenna.

IV. Dichroic Plate Measurements

The production versions of the dichroic plates used on the 64-m antennas contribute more system temperature than design and prototype testing indicate they should. Taking advantage of the removal of the DSS 14 Dichroic Plate for refurbishment of the XKR feedcone, DSS 13 positioned this plate atop the X-Band Low-Noise Antenna Measurement (XLA) feedcone which is operational for on-the-ground testing at DSS 13. A spot frequency measurement resulted in a system temperature of 20 K vice 16.5 K without the plate. Testing, using an angled flat sheet of aluminum and an absorber batten, indicated that a reflected signal entering from the side was contributing part of this additional system temperature.

Extensive additional measurements were conducted comparing the sensitivity of the plate to the operating frequency. The paint was then removed from the plate and "after" measurements conducted. Some frequency sensitivity was observed, but more testing of the prototype dichroic plate is necessary before final conclusions can be drawn. The plate was repainted and returned to DSS 14 for reinstallation.

V. National Bureau of Standards (NBS) Radiometer Testing

In support of Antenna Microwave Advanced Engineering and X and K-Band Propagation Calibration, an NBS design radiometer was tested at DSS 13. This testing, conducted at 2278.5 MHz, was to evaluate the stability, resolution, and overall usability of the NBS-designed radiometer. DSS 13 provided 25 hours of station support of which 22 hours were actual observing using the new radiometer. The dynamic range of the radiometer was less than desired, and further testing is planned after redesign and rebuilding.

VI. Microwave Power Transmission

Continuing with system testing (DSN Progress Report 42-30, pp. 214–221), measurements have been made of the sensitivity of the rectenna efficiency to angle of incidence of the arriving rays. Additionally, testing of system performance as a function of operating frequency and output power has been performed. By moving the 26-m subreflector, data have also been taken of the recovered power level as a function of transmitting antenna focusing. This last series of measurements indicates that additional efficiency could be gained by focusing the antenna on the rectenna instead of at infinity as was the case during preceding system testing.

System performance was demonstrated to a number of visiting groups including a contract motion picture film crew from the United States Information Agency. DSS 13 has provided 15-3/4 hours of system support, with the transmitter operating at various powers up to 250 kW during this period.

VII. X-Band Radar

In preparation for an additional series of radar observations, the XKR feedcone was removed from DSS 14 and brought to DSS 13 for extensive refurbishment of the radar system, including feedhorn, waveguide, waveguide switches, buffer amplifier, and protective circuits.

All waveguides, including the feedhorn, were removed. The voltage standing wave ratio (VSWR) of each piece of guide, as well as groups of pieces, was measured. All guides were then chemically cleaned, flanges lapped, and VSWR measurements again made. "Runs" of waveguide, as installed in the cone, were connected and VSWR measurements again made. The waveguide runs were "tuned" for minimum VSWR by careful deformation of

the waveguide walls and the system was reinstalled, along with the cleaned feedhorn.

The buffer amplifier was completely bench-tested, and the prototype crowbar circuit (DSN Progress Report 42-30, pp. 214–221) was replaced by the production version. Response time measurements were made on all of the protective circuits (arc detectors, reflected power detectors, etc.), and an inhibit circuit was added to the traveling-wave tube (TWT) power supplies to prevent the power supplies from automatically restarting when shortcircuited by the crowbar circuit.

At the request of the Viking project, arrangements were made with Varian for accelerated delivery of a repaired klystron which was installed into the XKR feedcone on the DSS 14 antenna on Dec. 4, and system testing continued with two klystrons. This testing is still in progress.

VIII. Unified S-Band Feedcone Testing

Negotiations had previously been completed with Goddard Space Flight Center (GSFC) for dual-carrier testing at the Microwave Test Facility (MTF) of the new type feedcone to be installed into Spaceflight Tracking and Data Network (STDN) stations.

Using a test plan prepared by the feedcone contractor, dual-carrier testing at total power levels up to 24 kW was performed. The MTF provided dual transmitters of variable frequency and power as well as the necessary exciters, frequency sources, and a maser-receiving system with which to detect the intermodulation products generated by dual-carrier operation.

Testing was conducted at various powers up to 24 kW and transmitter operating frequencies from 2080 to 2120 MHz. System performance was good, with intermodulation products weaker than -141 dBm. Testing at MTF has been completed with further testing to take place at Goldstone STDN.

IX. DSN Receiver Interference Susceptibility Measurements

Among the possible sources of interference to flight operations is the radiation from commercial or military aircraft navigational gear, in particular the second harmonic from the Distance Measuring Equipment (DME). Several occurrences of interference seem likely to be from this source.

Tests were performed at DSS 13 utilizing the NASA shuttle aircraft to fly patterns around DSS 13 and operate the aircraft DME on each of the possible channels. When the aircraft was in the 26-m antenna beam, at ranges of approximately 2 km, interference was observed and recorded from each channel of the DME. Signal levels of approximately -138 dBm for the interference were recorded. Having the aircraft fly toward the antenna, remaining in the beam, was particularly useful as it allowed relatively long-term observation of the interfering signal on both a spectrum analyzer and a chart recorder.

X. Antenna Maintenance

The development activities which take place at DSS 13, particularly the development of various computer-controlled automation schemes, place unusual stress on the antennas. In particular, the azimuth drive gear boxes on the 26-m antenna have failed in the past. In order to forestall, if possible, future catastrophic failure, these gear boxes are being modified and refurbished. The last of the four gear boxes was removed from the 26-m antenna, replaced with a reworked spare, and sent to the vendor for modification and refurbishment.

Scheduled periodic checking revealed that the 9-m antenna was unbalanced. Removal of 907 kg (2000 lb) of balancing weight from the elevation axis brought the system into balance for smoother tracking in the elevation axis.

XI. Planetary Radio Astronomy

In support of the Planetary Radio Astronomy experiment, DSS 13 measures radiation received at 2295 MHz from the planet Jupiter and various radio calibration sources. These measurements utilize the 26-m antenna, the maser-receiving system, and the Noise Adding Radiometer (NAR). During this period, observations were made of the calibration sources tabulated in Table 2 in addition to measurements of Jupiter itself. A total of 40 hours of observations were made.

XII. Platform Parameters, Very Long Baseline Interferometry (VLBI)

In support of this development project, DSS 13, in conjunction with DSS 43, provided 16 hours of VLBI observations. During these 16 hours, 97 sources were observed, and the received data recorded onto magnetic

tape utilizing a modified TV video recorder. These observations were made at 2290 MHz.

XIII. Clock Synchronization Transmissions

Although some troubles have been encountered with this system, three transmissions were made to DSS 42-43 and three to DSS 61-63. Difficulties encountered include failure of the programmed oscillator due to a power supply failure and a changed capacitor value in the computer interface. Additionally, the circulating water pump began leaking so badly that replacement was necessary. Repairs have been accomplished and the system is now operational.

Table 1. Pulsars observed at DSS 13

0355+54	0833−45	1642−03	1911−04	2121+51
0525+21	1133+16	1706−16	1929+10	2218+47
0736−40	1237+25	1749−28	1933+16	
0823+26	1604−00	1818−04	2045−16	

Table 2. Radio calibration sources observed at DSS 13

3C17	3C273	3C309.1	NGC 7027
3C48	3C279	3C348	Virgo A
3C123	3C286	3C353	

An Experiment in Dynamic Modeling for a Complete Solar-Powered Energy System

C. L. Hamilton
TDA Planning Office

Completion of a prototype dynamic model simulating the performance of a solar-powered energy system is described. A set of hypothetical components is specified, and the outcome of test analyses of the resulting system is outlined. On the basis of this exercise, it appears that the dynamic modeling technique will constitute a useful and convenient tool for analyzing performance of time-dependent systems.

I. Introduction

A previous report (Ref. 1) has described in general terms a technique under development to model the time-dependent performance of solar-powered energy systems. In that article, a hypothetical system intended to provide all the energy needed by the Goldstone Space Communications Complex was outlined. Two of the three computer programs needed to embody the model of that system were discussed. The third program has been finished, and some experimental runs have been made to examine the modeled performance of the entire system.

The Goldstone Energy Conservation Project is no longer directed toward development of a full energy system for the Complex. For that reason the whole-system model has not been refined past the prototype stage, and the representative programs (SUN, WIND, and SENSMOD2) are implemented without the range of user options that would be included in a fully operational version. Construction and manipulation of the prototype have constituted a useful and informative experiment that has contributed to the definition of systematic processes for creating dynamic system models. This report will summarize the completion of the prototype model and results of the exploratory performance analyses that were carried out with it.

II. Characterization of the Test System

In Ref. 1 the components of a hypothetical baseline energy system were identified, and information flow between the computational modules representing them was outlined. These are illustrated in Figs. 1 and 2. Before the model can be used to carry out a performance analysis, key characteristics of each component must be specified. A component's key characteristics are those parameters which are needed in the corresponding computational module to calculate the outgoing informa-

tion from the incoming information. In general, characterization can be carried on at several levels of detail, depending on information available and the goals of the analysis. A heat engine, for example, can be specified simply in terms of size and overall efficiency for purposes of, say, a quick-scan evaluation. If more precise system analysis is desired, the specification can be made more detailed, including variation of efficiency with working fluid and rejection temperatures. Even a complete step-by-step calculation of cycle performance, treating the engine as a subsystem in itself, may be incorporated if desired.

The following paragraphs contain a listing of key characteristics for the hypothetical system components put together for the purpose of exercising the dynamic model. Note that these are gross component characteristics derived from a first guess at some performance specifications that would be required to make a whole energy system that is economically feasible. They do not necessarily correspond to physical characteristics of actual existing or emerging components. Analysis at this level corresponds to examination of a system's operation in terms of subsystem design goals.

A. Solar Subsystem

Program SUN, described in Ref. 1, embodies the model of a subsystem consisting of solar collectors, heat storage, and a heat engine for generation of electricity.

For purposes of exploratory analysis, 200,000 m^2 of fixed flat collectors made mostly of glass were postulated. They were assumed to face south, tipped up at 35.4 degrees from horizontal. Heat loss rate was taken to be about 350 watts per square meter at a collector temperature 300°C above ambient; loss was assumed to be predominantly radiative. An organic fluid was specified for heat removal. The fluid flow rate was controlled to maintain the outlet temperature between 300°C and 340°C (flow was stopped if the fluid temperature was below 300°C). Acceptance of incident radiation was assumed to decrease drastically at angles of incidence greater than about 50 degrees from normal.

Heat storage was accomplished with a set of narrow tanks holding a total of 3.8×10^6 kg of the organic fluid. The tanks were assumed to be well enough insulated so that heat loss from them was negligible over the time span of a few days. Fluid in them was assumed stratified into two well-defined zones. Immersed in each tank was a heat transfer tube through which the heat engine working fluid was circulated. Flow to the engine was maintained at a constant rate as long as enough heat remained in the high-temperature zone to last through the next integration interval. When there was insufficient heat stored at the high temperature (roughly 300°C to 340°C), fluid flow to the engine was stopped. The total storage unit was sized to hold one day's output from the collectors under conditions of maximum insolation, estimated on the basis of annual average figures.

A Rankine cycle engine was included to generate the DC output from the solar subsystem. It was to use the same organic liquid as its working fluid. It was postulated to run at 90% of Carnot efficiency with a mechanical efficiency of 80% and generating efficiency of 90%. Total fluid flow to the engine was set at 14,200 kg/h, estimated to use up in a 24-hour period the whole output of the collectors on a day with maximum insolation.

B. Wind Subsystem

WIND is the program used to simulate the performance of a wind-driven generator. Wind turbine output was taken as proportional to the cube of wind speed whenever that fell between 8 and 32 km/h. No generation occurred when wind speed was outside that range. Maximum output rate (at 32 km/h) was 4000 kW.

C. Conversion and Storage Subsystem, SENSMOD2

Using the outputs from SUN and WIND, SENSMOD2 models the remainder of the energy system, including hydrogen generation and storage, direct DC to AC conversion, dual-fuel engine generators, load consisting of waste heat utilization and electrical demand, and the chosen dispatch strategy. Characterization of the components represented by SENSMOD2 was done in very basic terms. Efficiency of the electrolysis unit was set at 80%. A maximum capacity for hydrogen storage was not defined; the amount of hydrogen in storage was monitored, and the gas was defined to be available for use long as enough remained to satisfy the next hour's demand. The engine-generator was specified to be 33% efficient using either hydrogen or diesel fuel. DC to AC conversion was assumed to proceed at 85% efficiency using a converter with 1250-kW capacity. Diesel fuel in storage was monitored, and whenever the amount there fell below 2,000,000 kWh a "load" of 200,000 kWh was added to it. A base waste heat load of 600 kW that varied ±10% with ambient temperature was postulated. Electrical load was approximated very simply, using a cumulative density function that was linear between a base defined as half the average load and a peak defined as 1.5 times average load.

For the prototype Dispatch Module the following strategy was devised. All power from the wind turbine was

used for electrolysis. Power from the solar subsystem was routed through the DC to AC converter to the extent that it was required and available; any solar power not used directly was consumed by the electrolysis unit. The engine-generators were required to operate to meet waste heat demand, producing an equivalent base amount of electricity. Electrical demand above that base was met with direct power from the converter to the extent it was available, up to converter capacity. Demand exceeding that level was to be satisfied by additional engine-generator operation. Hydrogen would be used to fuel the generators as long as there was enough; then the engines would switch to operation on diesel fuel.

SENSMOD2 is a program analogous in design to SUN and WIND. None of the components of the conversion-storage subsystem required modeling with variable step size integration, and the simulation could be run with update at hourly intervals. While SENSMOD2 was being put together, a requirement for ordering computational modules in the program was discovered. The relationships simulating the hydrogen-oxygen subsystem, the engine-generator, and fuel storage all occur in the DOWN-STREAM subprogram, and each of those computational modules requires information from one of the other two. Thus the Hydrogen-Oxygen, Engine-Generator, and Fuel Storage Modules had to appear in the appropriate sequence in the program. This ordering requirement places some restriction on flexibility in manipulating the system model as embodied in the program, as it represents one more piece of information not related to the system under analysis that the user has to remember. It may be that more skillful design of the Dispatch Module will avoid this drawback in future efforts.

The computational module representing the dispatch function differs from those described in Ref. 1. A "normal" computational module contains relationships defining component performance. Those relationships with no need for information from other computational modules (components) are contained in the UPSTREAM subprogram, while the equations using parameters transferred from another module appear in subprogram DOWN-STREAM. Between the two, CROSS-COUPLE carries out the transfer of variables from module to module. While the Dispatch computational module is made up of a relatively complex set of logical operations, its real function remains one of transferring information. The pieces of information have been manipulated before transfer, but not used to calculate new variables. Thus the Dispatch Module belongs strictly in the CROSS-COUPLE subprogram.

III. Performance of the Test System

To test the performance of the model and programs, operation of the hypothetical system summarized above was simulated over the course of one month, January. For input to SUN, a table of hourly insolation values was generated using the ASHRAE model (Ref. 2) with clearness number 1.05; each day's values were modified by a probabilistically determined factor to include the effect of unclear days. Ambient temperature inputs were from a file containing a composite of experimental hourly values measured at Goldstone over about three years. Wind speed inputs to WIND were drawn from a cumulative distribution based on three years' measurements at Goldstone. Output from SUN and WIND was stored as hourly average values for input into SENSMOD2, which also used the ambient temperature file.

A run of SENSMOD2 was made, simulating the system as specified. Several measures of system performance were output, among them the amount of hydrogen in storage at the end of each day and daily totals for solar-generated electricity, wind-generated electricity, hydrogen consumed, and diesel fuel consumed. Production of electricity from wind turned out to be a small fraction of the output from the test system (less than 10%). Figure 3 summarizes the salient features of system operation for the month of January. The top line represents daily totals for heat gathered by the solar collectors; it was generated by program SUN. Solar subsystem daily total production of electricity varied between 58,500 and 198,000 kWh. Hydrogen in storage, starting from an initial value of 200,000 kWh, decreased rapidly while consumption of diesel fuel (graphed as a cumulative value) rose to a total of over 640,000 kWh by month's end.

Inclusion of waste heat utilization in the system required that the engine-generators run all the time to meet that demand, consuming a great deal of hydrogen in the process. Direct use of the solar-generated electricity would seem to offer a significantly more efficient strategy. As a first parameter variation, then, the provision for waste heat utilization was removed, electrical demand was increased to compensate, and the capacity of the DC to AC converter was doubled to 2500 kW. Figure 4 shows the effect of these changes on cumulative diesel demand and hydrogen storage level (heat collected and solar subsystem output remain unchanged). Contrary to expectations, lifting the requirement for compulsary base operation of the generators did not lower diesel consumption (which is the measure of overall system performance chosen here) but rather increased it substantially.

Examination of the hourly electrical output from the solar subsystem revealed that the heat engine there exhausted the heat in storage in an average of 14 hours, and there was no solar power production the rest of the day. In an effort to better match power generation with the load distribution, which was spread over all hours, the output rate of the heat engine in the solar subsystem was decreased by halving the flow rate of working fluid to the engine (from 14,200 to 7100 kg/h). SUN was re-run with that modification, and the resulting data input for a third run of SENSMOD2. Hydrogen accumulation and fuel demand observed under these conditions are plotted in Fig. 5. This last modification significantly reduced diesel fuel consumption.

IV. Summary

A dynamic model simulating the performance of a complete energy system has been formulated and embodied in a set of computer programs. Those programs are functionally complete but do not contain all the features providing user convenience that would be present in fully implemented versions. Characteristic parameters were specified for a set of hypothetical components, and the programs were used to carry out some exploratory analyses of the resulting system. Parameter variations reflecting system and component modifications were easily and quickly made. The test runs described provided considerable insight into the behavior of a fairly complex solar-powered system and allowed rapid refinement of the system leading to improved performance (by one measure at least).

Additional work in dynamic modeling involves a program that produces instantaneous and integrated performance measures for solar collectors alone, using experimentally measured solar radiation inputs at short time intervals. Collector characterization packages are undergoing continual refinement. Also in progress is a detailed analysis of a solar heating and cooling system to be designed using commercially available components.

References

1. Hamilton, C. L., "A Dynamic Model for Analysis of Solar Energy Systems," in *The Deep Space Network Progress Report 42-27*, pp. 41–51, Jet Propulsion Laboratory, Pasadena, Calif., June 15, 1975.
2. *ASHRAE Handbook of Fundamentals*, Chapter 22, pp. 386–394, American Society of Heating, Refrigerating and Air-Conditioning Engineers, New York, N. Y., 1972.

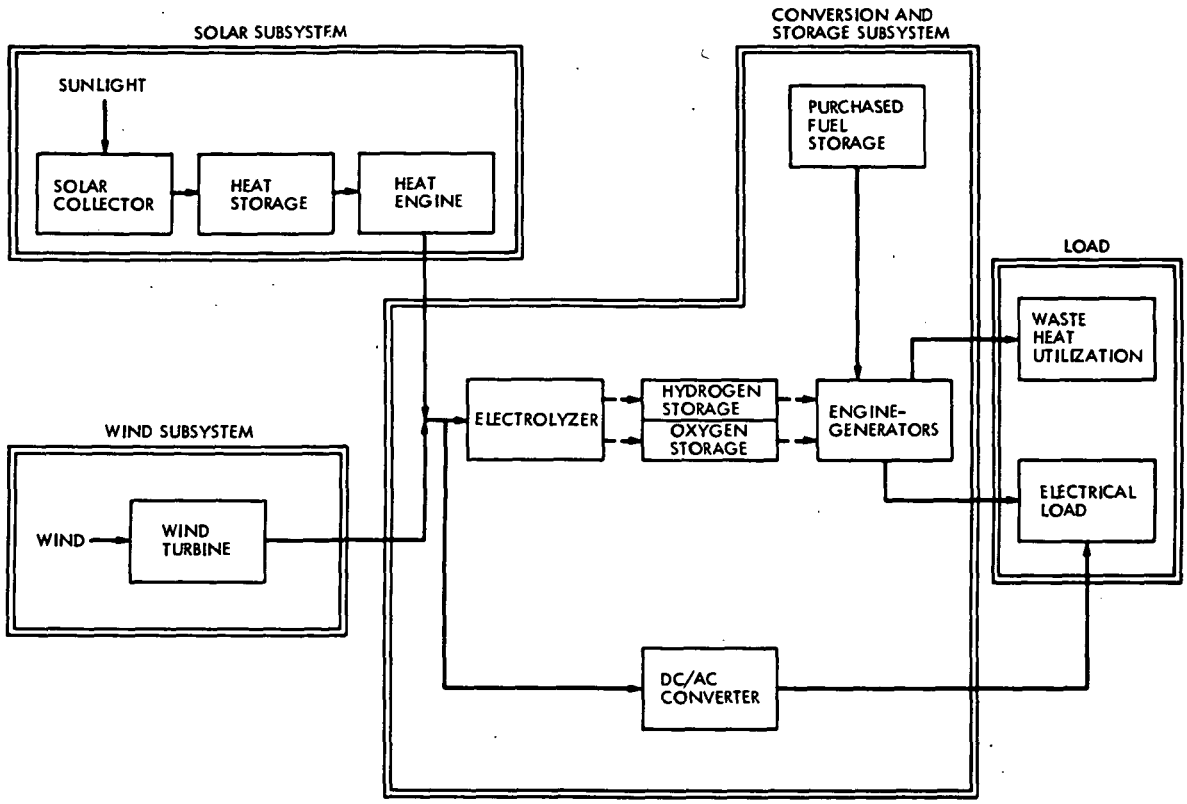

Fig. 1. Hypothetical solar energy system used in tests of model

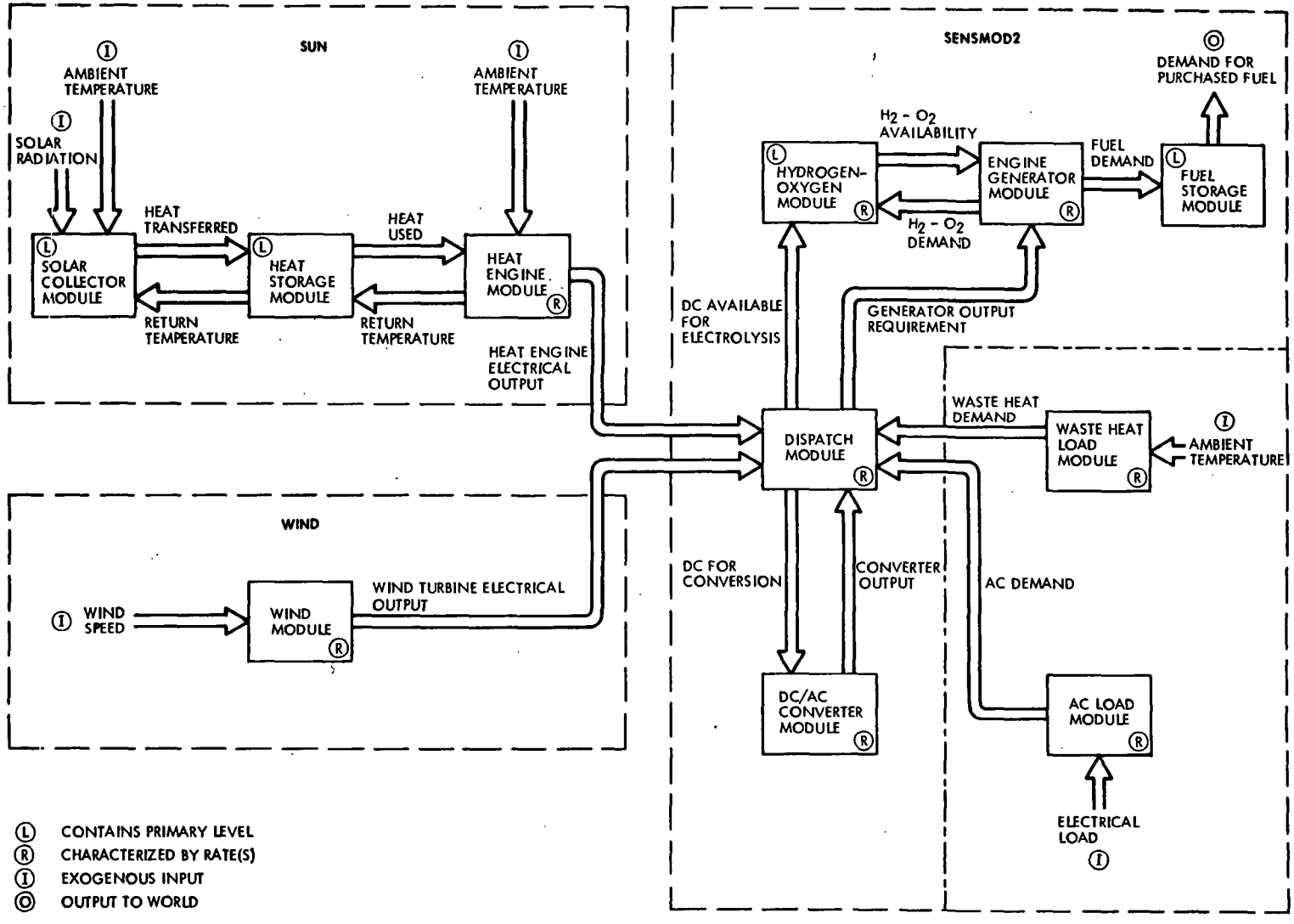

Fig. 2. Computational modules and data flow for hypothetical system

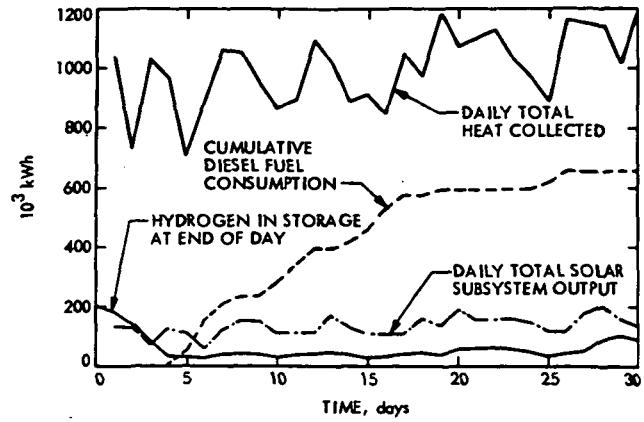

Fig. 3. Performance of hypothetical system as specified

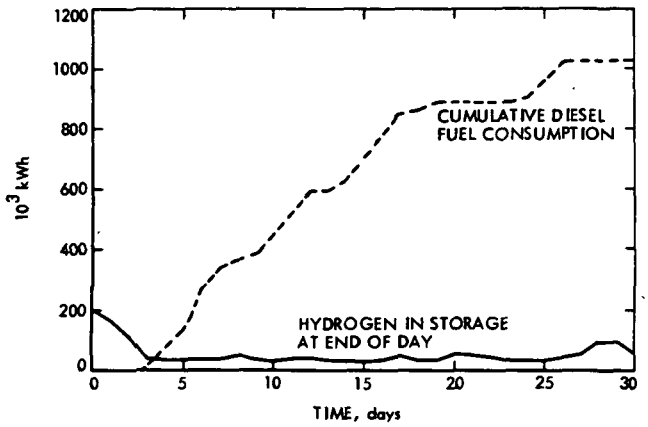

Fig. 4. Performance of hypothetical system without waste heat utilization

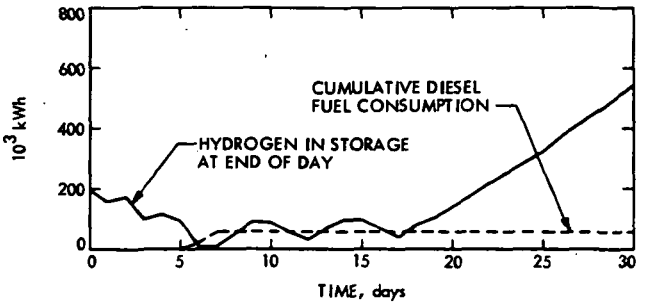

Fig. 5. Performance of hypothetical system without waste heat utilization after heat engine rating cut in half

Bibliography

Anderson, J. D., Null, G. W., and Thornton, C. T., *The Evaluation of Certain Astronomical Constants from the Radio Tracking of Mariner II*, Technical Report 32-476, Jet Propulsion Laboratory, Pasadena, Calif., reprinted from *Progr. Astronaut. Aeronaut.*, Vol. 14, 1964.

Anderson, J. D., *Determination of the Masses of the Moon and Venus and the Astronomical Unit from Radio Tracking Data of the Mariner II Spacecraft*, Technical Report 32-816, Jet Propulsion Laboratory, Pasadena, Calif., July 1, 1967.

Anderson, J. D., et al., "The Radius of Venus as Determined by Planetary Radar and Mariner V Radio Tracking Data," *J. Atmos. Sci.*, pp. 1171–1174, Sept. 25, 1968.

Anderson, J. D., and Hilt, D. E., "Improvement of Astronomical Constants and Ephemerides from Pioneer Radio Tracking Data," *AIAA J.*, Vol. 7, No. 6, pp. 1048–1054, June 1969.

Anderson, J. D., "Determination of Astrodynamic Constants and a Test of the General Relativistic Time Delay With S-Band Range and Doppler Data From Mariners 6 and 7," *Space Research*, Vol. XI, pp. 105–112, Akademie-Verlag, Berlin, 1971.

Barnum, P. W., et al., *Tracking and Data System Support for the Mariner Mars 1971 Mission: Orbit Insertion Through End of Primary Mission*, Technical Memorandum 33-523, Vol. III, Jet Propulsion Laboratory, Pasadena, Calif., May 15, 1973.

Barnum, P. W., and Renzetti, N. A., *Tracking and Data System Support for the Mariner Mars 1971 Mission: Extended Mission Operations*, Technical Memorandum 33-523, Vol. IV, Jet Propulsion Laboratory, Pasadena, Calif., Dec. 15, 1973.

Barton, W. R., and Miller, R. B., *Tracking and Data System Support for the Pioneer Project: Pioneer 11—Prelaunch Planning Through Second Trajectory Correction: to May 1, 1973*, Technical Memorandum 33-584, Vol. II, Jet Propulsion Laboratory, Pasadena, Calif., Mar. 15, 1975.

Bartos, K. P., et al., *Implementation of the 64-Meter-Diameter Antennas at the Deep Space Stations in Australia and Spain*, Technical Memorandum 33-692, Jet Propulsion Laboratory, Pasadena, Calif., Jan. 15, 1975.

Bathker, D. A., *Radio-Frequency Performance of an 85-ft Ground Antenna: X-Band*, Technical Report 32-1300, Jet Propulsion Laboratory, Pasadena, Calif., July 1, 1968.

Bathker, D. A., *Radio Frequency Performance of a 210-ft Ground Antenna: X-Band*, Technical Report 32-1417, Jet Propulsion Laboratory, Pasadena, Calif., Dec. 15, 1969.

Bathker, D. A., *Predicted and Measured Power Density Description of a Large Ground Microwave System*, Technical Memorandum 33-433, Jet Propulsion Laboratory, Pasadena, Calif., Apr. 15, 1971.

Bathker, D. A., Brown, D. W., and Petty, S. M., *Single- and Dual-Carrier Microwave Noise Abatement in the Deep Space Network*, Technical Memorandum 33-733, Jet Propulsion Laboratory, Pasadena, Calif., Aug. 1, 1975.

Baumert, L., et al., *Coding Theory and Its Applications to Communications Systems*, Technical Report 32-67, Jet Propulsion Laboratory, Pasadena, Calif., Mar. 31, 1961.

Baumgartner, W. S., *High-Power CW Radar Transmitter*, Technical Report 32-656, Jet Propulsion Laboratory, Pasadena, Calif., Sept. 1, 1964.

Berman, A. L., *Tracking System Data Analysis Report, Ranger VII Final Report*, Technical Report 32-719, Jet Propulsion Laboratory, Pasadena, Calif., June 1, 1965.

Berman, A. L., and Rockwell, S. T., *New Optical and Radio Frequency Angular Tropospheric Refraction Models for Deep Space Applications*, Technical Report 32-1601, Jet Propulsion Laboratory, Pasadena, Calif., Nov. 1, 1975.

Biber, K. W., and Whittlesey, A. C., *Description and Analysis of 890-MHz Noise-Measuring Equipment*, Technical Report 32-898, Jet Propulsion Laboratory, Pasadena, Calif., Mar. 31, 1966.

Brockman, M. H., et al., *Extraterrestrial Radio Tracking and Communication*, External Publication 808, Jet Propulsion Laboratory, Pasadena, Calif., Nov. 12, 1959. Also available in *Proc. IRE*, Vol. 48, 1960.

Brockman, M. H., and Posner, E. C., *Power Requirements for Deep-Space Telecommunication Links*, Technical Report 32-1395, Jet Propulsion Laboratory, Pasadena, Calif., reprinted from *IEEE Spectrum*, Vol. 6, No. 3, pp. 95–99, Mar. 1969.

Bunce, R. C., *Unified S-Band Receiver-Exciter Subsystem*, Technical Report 32-809, Jet Propulsion Laboratory, Pasadena, Calif., Sept. 15, 1968.

Butman, S., "A General Formulation of Linear Feedback Communication Systems with Solutions," *IEEE Trans. Inform. Theor.*, Vol. IT-15, No. 3, pp. 392–400, May 1969.

Butman, S., "Rate Distortion Over Band-Limited Feedback Channels," *IEEE Trans. Inform. Theor.*, Vol. IT-17, No. 1, pp. 110–112, Jan. 1971.

Butman, S., and Timor, U., "Interplex—An Efficient Multichannel PSK/PM Telemetry System", *IEEE Trans. Commun.*, Vol. COM-20, No. 3, pp. 415–419, June 1972.

Cain, D. L., and Hamilton, T. W., *Determination of Tracking Station Locations by Doppler and Range Measurements to an Earth Satellite*, Technical Report 32-534, Jet Propulsion Laboratory, Pasadena, Calif., Feb. 1, 1964.

Carey, C. N., and Sjogren, W. L., *Gravitational Inconsistency in the Lunar Theory: Confirmation by Radio Tracking*, Technical Report 32-1290, Pt. II, Jet Propulsion Laboratory, Pasadena, Calif., reprinted from *Science*, Vol. 160, No. 3830, pp. 875–876, May 24, 1968.

Carpenter, R. L., *Study of Venus by CW Radar—1964 Results*, Technical Report 32-963, Jet Propulsion Laboratory, Pasadena, Calif., reprinted from *Astron. J.*, Vol. 71, No. 2, pp. 142–152, Mar. 1966.

Carr, R. E., *The Jet Propulsion Laboratory Method of Tracking Lunar Probes*, External Publication 793, Jet Propulsion Laboratory, Pasadena, Calif., June 4, 1959.

Chadwick, H. D., and Springett, J. C., "The Design of a Low Data Rate MSFK Communication System," *IEEE Trans. Commun. Technol.*, Vol. COM-18, No. 6, pp. 740–750, Dec. 1970.

Chaney, W. D., *Final Mariner II Tracking System Data Analysis Report*, Technical Report 32-727, Jet Propulsion Laboratory, Pasadena, Calif., Sept. 1, 1965.

Charles, F. J., and Lindsey, W. C., *Some Analytical and Experimental Phase-Locked Loop Results for Low Signal-to-Noise Ratios*, Technical Report 32-1027, Jet Propulsion Laboratory, Pasadena, Calif., reprinted from *Proc. IEEE*, Vol. 54, No. 9, pp. 1152–1166, Sept. 1966.

Clark, B. G., et al., "High Resolution Observations of Compact Radio Sources at 13 cm," *Astrophys. J.*, Vol. 161, pp. 803–809, Sept. 1970.

Clauss, R. C., et al., *Total System Noise Temperature: 15°K*, Technical Report 32-691, Jet Propulsion Laboratory, Pasadena, Calif., Nov. 1964.

Clauss, R. C., *A 2388-Mc Two-Cavity Maser for Planetary Radar*, Technical Report 32-583, Jet Propulsion Laboratory, Pasadena, Calif., reprinted from *Microwave J.*, Vol. 8, pp. 74–77, May 1965.

Clauss, R. C., *A Traveling Wave Maser for Deep Space Communication at 2295 and 2388 MHz*, Technical Report 32-1072, Jet Propulsion Laboratory, Pasadena, Calif., Feb. 15, 1967.

Cohen, M. H., et al., "Compact Radio Source in the Nucleus of M87," *Astrophys. J.*, Vol. 158, No. 2, Pt. 2, pp. L83–L85, Nov. 1969.

Coyner, J. V., Jr., *Radial Rib Antenna Surface Deviation Analysis Program*, Technical Memorandum 33-518, Jet Propulsion Laboratory, Pasadena, Calif., Dec. 15, 1971.

Curkendall, D. W., and McReynolds, S. R., "A Simplified Approach for Determining the Information Content of Radio Tracking Data," *J. Spacecraft Rockets*, Vol. 6, No. 5, pp. 520–525, May 1969.

Curkendall, D. W., and Stephenson, R. R., "Earthbased Tracking and Orbit Determination—Backbone of the Planetary Navigation System," *Astronaut. Aeronaut.*, Vol. 7, No. 5, pp. 30–36, May 1970.

Curkendall, D. W., "Planetary Navigation: The New Challenges," *Astronaut. Aeronaut.*, Vol. 7, No. 5, pp. 26–29, May 1970.

"The Deep Space Network—An Instrument for Radio Navigation for the Mariner Mission to Mars—1969," *Proceedings of the Second International Conference of STM and AERA*, Reidel Publishing Company, Holland, May 1969.

Description of the Deep Space Network Operational Capabilities as of January 1, 1966, Technical Memorandum 33-255, Jet Propulsion Laboratory, Pasadena, Calif., July 1, 1966.

Description of World Network for Radio Tracking of Space Vehicles, Publication 135, Jet Propulsion Laboratory, Pasadena, Calif., July 1, 1958.

Didday, R. L., and Lindsey, W. C., *Subcarrier Tracking Methods and Communication System Design*, Technical Report 32-1317, Jet Propulsion Laboratory, Pasadena, Calif., reprinted from *IEEE Trans. Commun. Technol.*, Vol. COM-16, No. 4, pp. 541–550, Aug. 1968.

Downs, G. S., and Reichley, P. E., "Observations of Interstellar Scintillations of Pulsar Signals at 2388 MHz," *Astrophys. J.*, Vol. 163, No. 1, Pt. 2, pp. L11–L16, Jan. 1971.

Downs, G. S., et al., "Mars Radar Observation, A Preliminary Report," *Science*, Vol. 174, No. 4016, pp. 1324–1327, Dec. 24, 1971.

Downs, G. S., et al., "Martian Topography and Surface Properties as Seen by Radar: The 1971 Opposition," *Icarus*, Vol. 18, No. 1, pp. 8–21, Jan. 1973.

Downs, G. S., Reichley, P. E., and Morris, G. A., "Pulsar Detections at Frequencies of 8.4 and 15.1 GHz," *Astrophys. J.*, Vol. 181, No. 3, Part 2, pp. L143–L146, May 1, 1973.

Easterling, M., *A Long-Range Precision Ranging System*, Technical Report 32-80, Jet Propulsion Laboratory, Pasadena, Calif., July 10, 1961.

Easterling, M., *Methods for Obtaining Velocity and Range Information from CW Radars*, Technical Report 32-657, Jet Propulsion Laboratory, Pasadena, Calif., Sept. 1, 1964.

Easterling, M., and Goldstein, R., *The Effect of the Interplanetary Medium on S-Band Telecommunications*, Technical Report 32-825, Jet Propulsion Laboratory, Pasadena, Calif., Sept. 1, 1965.

Edelson, R. E. (ed.), *Telecommunications Systems Design Techniques Handbook*, Technical Memorandum 33-571, Jet Propulsion Laboratory, Pasadena, Calif., July 15, 1972.

Efron, L., and Solloway, C. B., *Proceedings of the Conference on Scientific Applications of Radio and Radar Tracking in the Space Program*, Technical Report 32-1475, Jet Propulsion Laboratory, Pasadena, Calif., July 1, 1970.

Eimer, M., and Stevens, R., *Tracking and Data Handling for the Pioneer III and Pioneer IV Firings*, External Publication 701, Jet Propulsion Laboratory, Pasadena, Calif., Aug. 14, 1959.

Esposito, P. B., and Wong, S. K., "Geocentric Gravitational Constant Determined from Mariner 9 Radio Tracking Data," paper presented at the International Symposium on Earth Gravity Models (American Geophysical Union, NASA), St. Louis, Aug. 1972.

Fearey, J. P., and Renzetti, N. A., "Navigation Results on the Mariner Mars Mission to Mars 1969," International Navigation Conference, Hamburg, Oct. 1969.

Fjeldbo, G., Kliore, A. J., and Seidel, B. L., "Bistatic Radar Measurements of the Surface of Mars with Mariner 1969," *Icarus*, Vol. 16, No. 3, pp. 502–508, June 1972.

Fjeldbo, G., and Eshleman, V. R., "Radio Occultation Measurements and Interpretations," in *The Atmospheres of Venus and Mars*, p. 225, Gordon and Breach, Science Publishers, Inc., New York, N.Y., 1968.

Fjeldbo, G., "Radio Occultation Experiments Planned for Pioneer and Mariner Missions to the Outer Planets," *Planet. Space Sci.*, Vol. 21, No. 9, pp. 1533–1547, Sept. 1973.

Flanagan, F. M., et al., *Deep Space Network Support of the Manned Space Flight Network for Apollo: 1962–1968*, Technical Memorandum 33-452, Vol. I, Jet Propulsion Laboratory, Pasadena, Calif., July 1970.

Flanagan, F. M., et al., *Deep Space Network Support of the Manned Space Flight Network for Apollo: 1969–1970*, Technical Memorandum 33-452, Vol. II, Jet Propulsion Laboratory, Pasadena, Calif., May 1, 1971.

Fredricksen, H., *Error Correction for Deep Space Network Teletype Circuits*, Technical Report 32-1275, Jet Propulsion Laboratory, Pasadena, Calif., June 1, 1968.

Gary, B., Olsen, E. T., and Rosenkranz, P. W., "Radio Observations of Cygnus X-3 and the Surrounding Region," *Nature Phys. Sci.*, Vol. 239, No. 95, pp. 128–130, Oct. 23, 1972.

Gates, C. R., and Johnson, M. S., *A Study of On-Site Computing and Data Processing for a World Tracking Network*, Publication 154, Jet Propulsion Laboratory. Pasadena, Calif., Feb. 9, 1959.

Georgevic, R. M., *Mathematical Model of the Solar Radiation Force and Torques Acting on the Components of a Spacecraft*, Technical Memorandum 33-494, Jet Propulsion Laboratory, Pasadena, Calif., Oct. 1, 1971.

Goldstein, R., Stevens, R., and Victor, W. K., *Radar Exploration of Venus: Goldstone Observatory Report for October-December 1962*, Technical Report 32-396, Jet Propulsion Laboratory, Pasadena, Calif., Mar. 1, 1965.

Goldstein, R. M., *The Analysis of Uncooperative Radar Targets*, Technical Report 32-658, Jet Propulsion Laboratory, Pasadena, Calif., Sept. 1, 1964.

Goldstein, R. M., et al., *The Superior Conjunction of Mariner IV*, Technical Report 32-1092, Jet Propulsion Laboratory, Pasadena, Calif., Apr. 1, 1967.

Goldstein, R. M., "Radar Time-of-Flight Measurements to Venus," *Astron. J.*, Vol. 73, No. 9, Aug. 1968.

Goldstein, R. M., et al., "Preliminary Radar Results of Mars," *Radio Sci.*, Vol. 5, No. 2, pp. 475–478, Feb. 1970.

Goldstein, R. M., and Rumsey, H., "A Radar Snapshot of Venus," *Science*, Vol. 169, Sept. 1970.

Goldstein, R. M., "Radar Observations of Mercury," *Astron. J.*, Vol. 76, No. 10, pp. 1152–1154, Dec. 1971.

Goldstein, R. M., Holdridge, D. B., and Lieske, J. H., "Minor Planets and Related Objects: XII. Radar Observations of (1685) Toro," *Astron. J.*, Vol. 78, No. 6, pp. 508–509, Aug. 1973.

Golomb, S. W., "New Problems of Space Communications: Part I. Beware of the Tigers," *Astronautics*, Vol. 7, No. 6, p. 19, June 1962.

Golomb, S. W., "New Problems in Space Communications: Part 3," *Astronautics*, Vol. 7, No. 8, p. 26, Aug. 1962.

Golomb, S. W., "Ferreting Signals Out of Noise," *Int. Sci. Technol.*, No. 22, pp. 72–82 and 120, Oct. 1963.

Gordon, H. J., et al., *The Mariner 6 and 7 Flight Paths and Their Determination From Tracking Data*, Technical Memorandum 33-469, Jet Propulsion Laboratory, Pasadena, Calif., Dec. 1, 1970.

Gottlieb, P., et al., "Lunar Gravity over Large Craters from Apollo 12 Tracking Data," *Science*, Vol. 168, No. 3930, pp. 477–479, Apr. 1970.

Gray, R. M., and Tausworthe, R. C., "Frequency-Counted Measurements, and Phase Locking to Noise Oscillators," *IEEE Trans. Commun. Technol.*, Vol. COM-19, No. 1, pp. 21–30, Feb. 1971.

Gubbay, J., et al., "Variations of Small Quasar Components at 2,300 MHz," *Nature*, Vol. 224, No. 5224, pp. 1094–1095, Dec. 1969.

Gulkis, S., and Gary, B., "Circular Polarization and Total-Flux Measurements of Jupiter at 13.1 cm Wavelength," *Astron. J.*, Vol. 76, No. 1, pp. 12–16, Feb. 1971.

Gulkis, S., et al., "Observations of Jupiter at 13-cm Wavelength During 1969 and 1971," *Icarus*, Vol. 18, No. 2, pp. 181–191, Feb. 1973.

Hachenberg, O., et al., "The 100-meter Radio Telescope at Effelsberg, "*Proc. IEEE*, Vol. 61, No. 9, pp. 1288–1295, Sept. 1973.

Hall, J. R., and Easterling, M., "The Technology of Ground Stations in the Deep Space Network from 1958 to 1968," *IEEE Conf. Rec.*, Vol. 4, pp. 576–585, 1968.

Hall, J. R., et al., "The General Problem of Data Return from Deep Space," *Space Sci. Rev.*, Vol. 8, pp. 595–664, 1968.

Hall, J. R., *Tracking and Data System Support for Lunar Orbiter*, Technical Memorandum 33-450, Jet Propulsion Laboratory, Pasadena, Calif., Apr. 1970.

Hamilton, T. W., et al., *The Ranger IV Flight Path and Its Determination From Tracking Data*, Technical Report 32-345, Jet Propulsion Laboratory, Pasadena, Calif., Sept. 15, 1962.

Hartop, R. W., *Power Loss Between Arbitrarily Polarized Antennas*, Technical Report 32-457, Jet Propulsion Laboratory, Pasadena, Calif., Sept. 1, 1964.

Havens, W. F., et al., *Scan Pointing Calibration for the Mariner Mars 1971 Spacecraft*, Technical Memorandum 33-556, Jet Propulsion Laboratory, Pasadena, Calif., Aug. 1, 1972.

Heftman, K., and Renzetti, N. A., "Data Return Capabilities of the Deep Space Network in the 1970's," AIAA Paper 67-648, *Proceedings of the AIAA Space Program Issues of the 70's Meeting*, Aug. 1967.

Higa, W. H., *Low-Level Microwave Mixing in Ruby*, Technical Report 32-1016, Jet Propulsion Laboratory, Pasadena, Calif., reprinted from *Proc. IEEE*, Vol. 54, No. 10, p. 1453, Oct. 1966.

Higa, W. H., "Time Synchronization via Lunar Radar," *Proc. IEEE*, Vol. 60, No. 5, pp. 552–557, May 1972.

Holmes, J. K., "On a Solution to the Second-Order Phase-Locked Loop," *IEEE Trans. Commun. Technol.*, Vol. COM-18, No. 2, pp. 119–126, Apr. 1970.

Holmes, J. K., "First Slip Times Versus Static Phase Error Offset for the First and Passive Second-Order Phase-Locked Loop," *IEEE Trans. Commun. Technol.*, Vol. COM-19, No. 2, pp. 234–235, Apr. 1971.

Holmes, J. K., and Tegnelia, C. R., *Digital Command System Second-Order Subcarrier Tracking Performance*, Technical Report 32-1540, Jet Propulsion Laboratory, Pasadena, Calif., Oct. 1, 1971.

Holmes, J. K., "Performance of a First Order Transition Sampling Digital Phase-Locked Loop Using Random-Walk Models," *IEEE Trans. Commun.*, Vol. COM-20, No. 2, pp. 119–131, Apr. 1972.

Hurd, W. J., and Anderson, T. O., *Digital Transition Tracking Symbol Synchronizer for Low SNR Coded Systems*, Technical Report 32-1488, Jet Propulsion Laboratory, Pasadena, Calif., reprinted from *IEEE Trans. Commun. Technol.*, Vol. COM-18, No. 2, pp. 141–147, Apr. 1970.

Jaffe, R., and Rechtin, E., *Design and Performance of Phase-Lock Loops Capable of Near-Optimum Performance over a Wide Range of Input Signal and Noise Levels*, Progress Report 20-243, Jet Propulsion Laboratory, Pasadena, Calif., Dec. 1, 1954; also available in *IRE Trans. Inform. Theory*, No. 1, pp. 66–67, Mar. 1955.

Jordan, J. F., "Orbit Determination for Powered Flight Space Vehicles on Deep Space Missions," *J. Spacecraft Rockets*, Vol. 6, No. 5, pp. 545–550, May 1969.

Kellerman, K. I., et al., "High Resolution Observations of Compact Radio Sources at 13 Centimeters," *Astrophys. J.*, Vol. 161, No. 3, pp. 803–809, Sept. 1970.

Kelly, A. J., *Microwave Probe for Plasma Plumes*, Technical Report 32-625, Jet Propulsion Laboratory, Pasadena, Calif., Feb. 1965.

Kliore, A., Cain, D. L., and Hamilton, T. W., *Determination of Some Physical Properties of the Atmosphere of Mars from Changes in the Doppler Signal of a Spacecraft on an Earth-Occultation Trajectory*, Technical Report 32-674, Jet Propulsion Laboratory, Pasadena, Calif., Oct. 15, 1964.

Kliore, A., and Tito, D. A., *Radio Occultation Investigations of the Atmosphere of Mars*, Technical Report 32-1157, Jet Propulsion Laboratory, Pasadena, Calif., reprinted from *J. Spacecraft Rockets*, Vol. 4, No. 5, pp. 578–582, May 1967.

Kliore, A., "Radio Occultation Measurements of the Atmospheres of Mars and Venus," in *The Atmospheres of Venus and Mars*, edited by J. C. Brandt and M. B. McElrow, p. 205, Gordon and Breach Science Publishers, Inc., New York, N.Y., 1968.

Kliore, A. J., et al., "Summary of Mariner 6 and 7 Radio Occultation Results on the Atmosphere of Mars," *Space Research*, Vol. XI, pp. 165–175, Akademie-Verlag, Berlin, 1971.

Kliore, A. J., et al., "Mariner 9 S-Band Martian Occultation Experiment: Initial Results on the Atmosphere and Topography of Mars," *Science*, Vol. 175, No. 4019, pp. 313–317, Jan. 1972.

Kliore, A. J., et al., "The Atmosphere of Mars From Mariner 9 Radio Occultation Measurements," *Icarus*, Vol. 17, No. 2, pp. 484–516, Oct. 1972.

Kliore, A. J., et al., "S Band Radio Occultation Measurements of the Atmosphere and Topography of Mars with Mariner 9: Extended Mission Coverage of Polar and Intermediate Latitudes," *J. Geophys. Res.*, Vol. 78, No. 20, pp. 4331–4351, July 10, 1973.

Labrum, R. G., et al., *The Surveyor V, VI, and VII Flight Paths and Their Determination from Tracking Data*, Technical Report 32-1302, Jet Propulsion Laboratory, Pasadena, Calif., Dec. 1, 1968.

Laeser, R. P., et al., *Tracking and Data System Support for the Mariner Mars 1971 Mission: Prelaunch Phase Through First Trajectory Correction Maneuver*, Technical Memorandum 33-523, Vol. I, Jet Propulsion Laboratory, Pasadena, Calif., Mar. 15, 1972.

Layland, J. W., "On Optimal Signals for Phase-Locked Loops," *IEEE Trans. Commun. Technol.*, Vol. COM-17, No. 5, pp. 526–531, Oct. 1969.

Layland, J. W., and Lushbaugh, W. A., "A Flexible High-Speed Sequential Decoder for Deep Space Channels," *IEEE Trans. Commun. Technol.*, Vol. COM-19 No. 5, pp. 813–820, Oct. 1971.

Leavitt, R. K., *The Least-Squares Process of MEDIA for Computing DRVID Calibration Polynomials*, Technical Memorandum 33-542, Jet Propulsion Laboratory, Pasadena, Calif., May 15, 1972.

Lesh, J. R., *Signal-to-Noise Ratios in Coherent Soft Limiters*, Technical Report 32-1589, Jet Propulsion Laboratory, Pasadena, Calif., Sept. 15, 1973.

Levy, G. S., Otoshi, T. Y., and Seidel, B. L., *Ground Instrumentation for Mariner IV Occultation Experiment*, Technical Report 32-984, Jet Propulsion Laboratory, Pasadena, Calif., Sept. 15, 1966.

Levy, G. S., et al., *Lunar Range Radiation Patterns of a 210-Foot Antenna at S-Band*, Technical Report 32-1079, Jet Propulsion Laboratory, Pasadena, Calif., reprinted from *IEEE Trans. Antennas Propagation*, Vol. AP-15, No. 2, pp. 311–313, Mar. 1967.

Levy, G. S., et al., *The Ultra Cone: An Ultra-Low-Noise Space Communication Ground Radio-Frequency System*, Technical Report 32-1340, Jet Propulsion Laboratory, Pasadena, Calif., reprinted from *IEEE Trans. Microwave Theor. Tech.*, Vol. MTT-16, No. 9, pp. 596–602, Sept. 1968.

Levy, G. S., et al., "Pioneer 6: Measurement of Transient Faraday Rotation Phenomena Observed During Solar Occultation," *Science*, Vol. 166, No. 3905, pp. 596–598, Oct. 1969.

Lieske, J. H., and Null, G. W., "Icarus and the Determination of Astronomical Constants," *Astron. J.*, Vol. 74, No. 2, Mar. 1969.

Lieske, J. H., et al., "Simultaneous Solution for the Masses of the Principal Planets from Analysis of Optical Radar and Radio Tracking Data," *Celest. Mech.*, Vol. 4, No. 2, pp. 233–245, Oct. 1971.

Lindsey, W. C., *Optimum and Suboptimum Frequency Demodulation*, Technical Report 32-637, Jet Propulsion Laboratory, Pasadena, Calif., June 15, 1964.

Lindsey, W. C., *Improvements to be Realized Through the Use of Block-Coded Communication Systems*, Technical Report 32-947, Jet Propulsion Laboratory, Pasadena, Calif., reprinted from *IEEE Trans. Aerosp. Electron. Syst.*, Vol. AES-2, No. 3, pp. 364–366, May 1966.

Lindsey, W. C., *Phase-Shift-Keyed Signal Detection with Noisy Reference Signals*, Technical Report 32-968, Jet Propulsion Laboratory, Pasadena, Calif., reprinted from *IEEE Trans. Aerosp. Electron. Syst.*, Vol. AES-2, No. 4, pp. 393–401, July 1966.

Lindsey, W. C., *A Theory for the Design of One-Way and Two-Way Phase-Coherent Communication Systems: Phase-Coherent Tracking Systems*, Technical Report 32-986, Jet Propulsion Laboratory, Pasadena, Calif., July 15, 1969.

Lindsey, W. C., *Optimal Design of One-Way and Two-Way Coherent Communication Links*, Technical Report 32-988, Jet Propulsion Laboratory, Pasadena, Calif., reprinted from *IEEE Trans. Commun. Technol.*, Vol. COM-14, No. 4, pp. 418–431, Aug. 1966.

Lindsey, W. C., and Charles, F. J., *A Model Distribution for the Phase Error in Second-Order Phase-Locked Loops*, Technical Report 32-1017, Jet Propulsion

Laboratory, Pasadena, Calif., reprinted from *IEEE Trans. Commun. Technol.*, Vol. COM-14, No. 10, pp. 662–664, Oct. 1966.

Lindsey, W. C., *Performance of Phase-Coherent Receivers Preceded by Bandpass Limiters*, Technical Report 32-1162, Jet Propulsion Laboratory, Pasadena, Calif., Sept. 15, 1967.

Lindsey, W. C., "Block Coding for Space Communications," *IEEE Trans. Commun. Technol.*, Vol. COM-17, No. 2, pp. 217–225, Apr. 1969.

Lindsey, W. C., *Block-Coded Communications*, Technical Report 32-1380, Jet Propulsion Laboratory, Pasadena, Calif., Aug. 15, 1969.

Lindsey, W. C., *Nonlinear Analysis of Generalized Tracking Systems*, Technical Report 32-1453, Jet Propulsion Laboratory, Pasadena, Calif., reprinted from *Proc. IEEE*, Vol. 57, No. 10, pp. 1705–1722, Oct. 1969.

Lindsey, W. C., and Simon, M. K., "The Effect of Loop Stress on the Performance of Phase-Coherent Communication Systems", *IEEE Trans. Commun. Technol.*, Vol. COM-18, No. 5, pp. 569–588, Oct. 1970.

Lindsey, W. C., and Simon, M. K., "Carrier Synchronization and Detection of Polyphase Signals," *IEEE Trans. Commun.*, Vol. COM-20, No. 3, pp. 441–454, June 1972.

Lindsey, W. C., and Simon, M. K., "L-Orthogonal Signal Transmission and Detection," *IEEE Trans. Commun.*, Vol. COM-20, No. 5, pp. 953–960, Oct. 1972.

Lindsey, W. C., and Simon, M. K., "On the Detection of Differentially Encoded Polyphase Signals, " *IEEE Trans. Commun.*, Vol. COM-20, No. 6, pp. 1121–1128, Dec. 1972.

Lindsey, W. C., *Synchronization Systems in Communication and Control*, Prentice-Hall, Inc., Englewood Cliffs, N. J., 1972.

Lindsey, W. C., and Tausworthe, R. C., *A Bibliography of the Theory and Application of the Phase-Lock Principle*, Technical Report 32-1581, Jet Propulsion Laboratory, Pasadena, Calif., Apr. 1, 1973.

Lindsey, W. C., and Simon, M. K., *Telecommunication Systems Engineering*, Prentice-Hall, Inc., Englewood Cliffs, N. J., 1973.

Lorell, J., Anderson, J. D., and Sjogren, W. L., *Characteristics and Format of the Tracking Data to Be Obtained by the NASA Deep Space Instrumentation Facility for Lunar Orbiter*, Technical Memorandum 33-230, Jet Propulsion Laboratory, Pasadena, Calif., June 15, 1965.

Lorell, J., Sjogren, W. L., and Boggs, D., *Compressed Tracking Data Used for First Iteration in Selenodesy Experiment, Lunar Orbiters I and II*, Technical Memorandum 33-343, Jet Propulsion Laboratory, Pasadena, Calif., May 1, 1967.

Lorell, J., and Sjogren, W. L., *Lunar Orbiter Data Analysis*, Technical Report 32-1220, Jet Propulsion Laboratory, Pasadena, Calif., Nov. 15, 1967.

Lorell, J., *Lunar Orbiter Gravity Analysis*, Technical Report 32-1387, Jet Propulsion Laboratory, Pasadena, Calif., June 15, 1969.

Lorell, J., et al., "Icarus: Celestial Mechanics Experiment for Mariner," *Int. J. Sol. Sys.*, Vol. 12, Jan. 1970.

Lorell, J., and Laing, P. A., *Compilation of Lunar Orbiter Tracking Data Used for Long-Term Selenodesy*, Technical Memorandum 33-419, Jet Propulsion Laboratory, Pasadena, Calif., Feb. 1, 1970.

Lorell, J., "Estimation of Gravity Field Harmonics in the Presence of Spin-Axis Direction Error Using Radio Tracking Data," *J. Astronaut. Sci.*, Vol. XX, No. 1, pp. 44–54, Aug. 1972.

Ludwig, A. C., et al., *Gain Calibration of a Horn Antenna Using Pattern Integration*, Technical Report 32-1572, Jet Propulsion Laboratory, Pasadena, Calif., Oct. 1, 1972.

Madrid, G. A., et al., *Tracking System Analytic Calibration Activities for the Mariner Mars 1971 Mission*, Technical Report 32-1587, Jet Propulsion Laboratory, Pasadena, Calif., Mar. 1, 1974.

Martin, D. P., *A Combined Radar-Radiometer With Variable Polarization*, Technical Memorandum 33-570, Jet Propulsion Laboratory, Pasadena, Calif., Oct. 15, 1972.

Mathison, R. P., *Tracking Techniques for Interplanetary Spacecraft*, Technical Report 32-284, Jet Propulsion Laboratory, Pasadena, Calif., Aug. 1, 1962.

McEliece, R. J., *Optimal Communications Nets*, Technical Report 32-697, Jet Propulsion Laboratory, Pasadena, Calif., Apr. 15, 1965.

McNeal, C. E., *Ranger V Tracking Systems Data Analysis Final Report*, Technical Report 32-702, Jet Propulsion Laboratory, Pasadena, Calif., Apr. 15, 1965.

Melbourne, W. G., et al., *Constants and Related Information for Astrodynamical Calculations*, Technical Report 32-1306, Jet Propulsion Laboratory, Pasadena, Calif., July 15, 1968.

Melbourne, W. G., "Planetary Ephemerides," *Astronaut. Aeronaut.*, Vol. 7, No. 5, pp. 38–43, May 1970.

Merrick, W. D., et al., *Deep Space Communications*, Technical Release 34-10, Jet Propulsion Laboratory, Pasadena, Calif., Jan. 29, 1960; also available in *IRE Trans. Mil. Electron.*, Vol. MIL-4, No. 2-3, pp. 158–163, April–June 1960.

Miller, L., et al., *The Atlas-Centaur VI Flight Path and Its Determination from Tracking Data*, Technical Report 32-911, Jet Propulsion Laboratory, Pasadena, Calif., Apr. 15, 1966.

Miller, R. B., *Tracking and Data System Support for the Pioneer Project: Pioneer 10—From April 1, 1972, Through the Jupiter Encounter Period, January 1974*, Technical Memorandum 33-584, Vol. III, Jet Propulsion Laboratory, Pasadena, Calif., June 15, 1975.

Miller, R. B., et al., *Tracking and Data System Support for the Pioneer Project: Pioneer 10—From January 1974 to January 1975; Pioneer 11—From May 1, 1973 Through Jupiter Encounter Period, January 1975*, Technical Memorandum 33-584, Vol. IV, Jet Propulsion Laboratory, Pasadena, Calif., Dec. 1, 1975.

Moyer, T. D., *Mathematical Formulation of the Double-Precision Orbit Determination Program (DPODP)*, Technical Report 32-1527, Jet Propulsion Laboratory, Pasadena, Calif., May 17, 1971.

Muhleman, D. O., *Relationship Between the System of Astronomical Constants and the Radar Determinations of the Astronomical Unit*, Technical Report 32-477, Jet Propulsion Laboratory, Pasadena, Calif., Jan. 15, 1964.

Muhleman, D. O., Goldstein, R., and Carpenter, R., *A Review of Radar Astronomy—Parts I, II*, Technical Report 32-824, Jet Propulsion Laboratory, Pasadena, Calif., Jan. 30, 1966, reprinted from *IEEE Spectrum*, Oct. and Nov. 1965.

Muhleman, D. O., et al., *JPL Radar Range and Doppler Observations of Venus, 1961–1966*, Technical Report 32-1123, Jet Propulsion Laboratory, Pasadena, Calif., July 1, 1968.

Muhleman, D. O., et al., "Radio Propagation Measurements of the Solar Corona and Gravitational Field: Applications to Mariner 6 and 7," in *Proceedings of the Conference on Experimental Tests of Gravitational Theories*, California Institute of Technology, Pasadena, Calif., Nov. 1970.

Mulhall, B. D., et al., *Tracking System Analytic Calibration Activities for the Mariner Mars 1969 Mission*, Technical Report 32-1499, Jet Propulsion Laboratory, Pasadena, Calif., Nov. 15, 1970.

Mulholland, J. D., and Sjogren, W. L., *Lunar Orbiter Ranging Data*, Technical Report 32-1087, Jet Propulsion Laboratory, Pasadena, Calif., reprinted from *Science*, Vol. 155, No. 3758, pp. 74–76, Jan. 6, 1967.

Mulholland, J. D., *Proceedings of the Symposium on Observation, Analysis and Space Research Applications of the Lunar Motion*, Technical Report 32-1386, Jet Propulsion Laboratory, Pasadena, Calif., Apr. 1969.

Muller, P. M., and Sjogren, W. L., *Consistency of Lunar Orbiter Residuals With Trajectory and Local Gravity Effects*, Technical Report 32-1307, Jet Propulsion Laboratory, Pasadena, Calif., Sept. 1, 1968.

Muller, P. M., and Sjogren, W. L., *Mascons: Lunar Mass Concentrations*, Technical Report 32-1339, Jet Propulsion Laboratory, Pasadena, Calif., reprinted from *Science*, Vol. 161, No. 3842, pp. 680–684, Aug. 16, 1968.

The NASA/JPL 64-Meter-Diameter Antenna at Goldstone, California: Project Report, Technical Memorandum 33-671, Jet Propulsion Laboratory, Pasadena, Calif., July 15, 1974.

Newburn, R. L., Jr., et al., *Earth-Based Research on the Outer Planets During the Period 1970–1985*, Technical Report 32-1456, Jet Propulsion Laboratory, Pasadena, Calif., Mar. 15, 1970.

Null, G. W., et al., *Mariner IV Flight Path and Its Determination From Tracking Data*, Technical Report 32-1108, Jet Propulsion Laboratory, Pasadena, Calif., Aug. 1, 1967.

O'Neil, W. J., et al., *The Surveyor III and Surveyor IV Flight Paths and Their Determination From Tracking Data*, Technical Report 32-1292, Jet Propulsion Laboratory, Pasadena, Calif., Aug. 15, 1968.

O'Neil, W. J., et al., *Mariner 9 Navigation*, Technical Report 32-1586, Jet Propulsion Laboratory, Pasadena, Calif., Nov. 13, 1973.

Otoshi, T. Y., *The Effect of Mismatched Components on Microwave Noise-Temperature Calibrations*, Technical Report 32-1345, Jet Propulsion Laboratory, Pasadena, Calif., reprinted from *IEEE Trans. Microwave Theor. Tech.*, Vol. MTT-16, No. 9, pp. 675–686, Sept. 1968.

Otoshi, T. Y., Stelzried, C. T., and Yates, B. C., "Comparisons of Waveguide Losses Calibrated by the DC Potentiometer, AC Ratio Transformer, and Reflectometer Techniques," *IEEE Trans. Microwave Theor. Tech.*, Vol. MTT-18, No. 7, pp. 406–409, July 1970.

Otoshi, T. Y., and Stelzried, C. T., "A Precision Compact Rotary Vane Attenuator," *IEEE Trans. Micro. Theor. Technique*, Vol. MTT-19, No. 11, pp. 843–854, Nov. 1971.

Otoshi, T. Y., "Precision Reflectivity Loss Measurements of Perforated-Plate Mesh Materials by a Waveguide Technique," *IEEE Trans. Instr. Meas.*, Vol. IM-21, No. 4, pp. 451–457, Nov. 1972.

Pease, G. E., et al., *The Mariner V Flight Path and Its Determination From Tracking Data*, Technical Report 32-1363, Jet Propulsion Laboratory, Pasadena, Calif., July 1, 1969.

Posner, E. C., *Properties of Error-Correcting Codes at Low Signal-to-Noise Ratios*, Technical Report 32-602, Jet Propulsion Laboratory, Pasadena, Calif., June 15, 1964.

Potter, P. D., *The Design of a Very High Power, Very Low Noise Cassegrain Feed System for a Planetary Radar*, Technical Report 32-653, Jet Propulsion Laboratory, Pasadena, Calif., Aug. 24, 1964.

Potter, P. D., Merrick, W. D., and Ludwig, A. C., *Large Antenna Apertures and Arrays for Deep Space Communications*, Technical Report 32-848, Jet Propulsion Laboratory, Pasadena, Calif., Nov. 1, 1965.

Potter, P. D., *A Computer Program for Machine Design of Cassegrain Feed Systems*, Technical Report 32-1202, Jet Propulsion Laboratory, Pasadena, Calif., Dec. 15, 1967.

Potter, P. D., et al., *A Study of Weather-Dependent Data Links for Deep Space Applications*, Technical Report 32-1392, Jet Propulsion Laboratory, Pasadena, Calif., Oct. 15, 1969.

Rechtin, E., "Communication Techniques for Space Exploration," *IRE Trans. Space Electron. Telem.*, Vol. SET-5, No. 3, pp. 95–98, Sept. 1959.

Rechtin, E., Stevens, R., and Victor, W. K., *Data Transmission and Communications*, Technical Release 34-55, Jet Propulsion Laboratory, Pasadena, Calif., Apr. 30, 1960.

Rechtin, E., *Space Communications*, Technical Release 34-68, Jet Propulsion Laboratory, Pasadena, Calif., May 1, 1960.

Rechtin, E., et al., *JPL Range and Doppler System*, Technical Memorandum 33-13, Jet Propulsion Laboratory, Pasadena, Calif., Sept. 22, 1961.

Rechtin, E., Rule, B., and Stevens, R., *Large Ground Antennas*, Technical Report 32-213, Jet Propulsion Laboratory, Pasadena, Calif., Mar. 20, 1962.

Rechtin, E., *Lunar Communications*, Technical Memorandum 33-133, Jet Propulsion Laboratory, Pasadena, Calif., June 28, 1963.

Rechtin, E., "Surprises on Venus," *Int. Sci. Technol.*, No. 20, pp. 13–14, Aug. 1963.

Rechtin, E., "Long Range Planning for the Deep Space Network," *Astronaut. Aeronaut.*, Vol. 6, No. 1, pp. 28–35, Jan. 1968.

Renzetti, N. A., et al., "Radio Tracking Techniques and Performance of the U.S. Deep Space Instrumentation Facility," *Space Research II, Proceedings of the Second International Space Science Symposium*, Florence, Italy, April 1961, North Holland Publishing Company, Amsterdam.

Renzetti, N. A., and Ostermier, B. J., *Communications with Lunar Probes*, Technical Report 32-148, Jet Propulsion Laboratory, Pasadena, Calif., Aug. 23, 1961.

Renzetti, N. A., "DSIF in the Ranger Project," *Astronautics*, Vol. 6, No. 1, pp. 34–37, 70, Sept. 1961.

Renzetti, N. A., *Tracking and Data Acquisition for Ranger Missions I–V*, Technical Memorandum 33-174, Jet Propulsion Laboratory, Pasadena, Calif., July 1, 1964.

Renzetti, N. A., *Tracking and Data Acquisition for Ranger Missions VI–IX*, Technical Memorandum 33-275, Jet Propulsion Laboratory, Pasadena, Calif., Sept. 15, 1966.

Renzetti, N. A., *Tracking and Data Acquisition Support for the Mariner Venus 1962 Mission*, Technical Memorandum 33-212, Jet Propulsion Laboratory, Pasadena, Calif., July 1, 1965.

Renzetti, N. A., *Tracking and Data Acquisition Report, Mariner Mars 1964 Mission: Near-Earth Trajectory Phase*, Technical Memorandum 33-239, Vol. I, Jet Propulsion Laboratory, Pasadena, Calif., Jan. 1, 1965.

Renzetti, N. A., *Tracking and Data Acquisition Report, Mariner Mars 1964 Mission: Cruise to Post-Encounter Phase*, Technical Memorandum 33-239, Vol. II, Jet Propulsion Laboratory, Pasadena, Calif., Oct. 1, 1967.

Renzetti, N. A., *Deep Space Network Support, Atlas/Centaur Missions 1–9*, Technical Memorandum 33-347, Jet Propulsion Laboratory, Pasadena, Calif., Sept. 15, 1967.

Renzetti, N. A., "Tracking and Data Acquisition System for Mariner Missions," *Proceedings of the Seventh International Symposium on Space Technology and Science*, Tokyo, 1967.

Renzetti, N. A., *Tracking and Data Acquisition Report, Mariner Mars 1964 Mission: Extended Mission*, Technical Memorandum 33-239, Vol. III, Jet Propulsion Laboratory, Pasadena, Calif., Dec. 1, 1968.

Renzetti, N. A., and Fearey, J. P., "The Deep Space Network: An Instrument for the Radio Navigation for the Mariner Mission to Mars 1969," IInd International Conference on Space Engineering, Venice, Italy, D. Reidel Publishing Co., Dordrecht, Holland, May 1969.

Renzetti, N. A., *Tracking and Data System Support for Surveyor: Missions I and II*, Technical Memorandum 33-301, Vol. I, Jet Propulsion Laboratory, Pasadena, Calif., July 15, 1969.

Renzetti, N. A., *Tracking and Data System Support for Surveyor: Missions III and IV*, Technical Memorandum 33-301, Vol. II, Jet Propulsion Laboratory, Pasadena, Calif., Sept. 1, 1969.

Renzetti, N. A., *Tracking and Data System Support for Surveyor: Mission V*, Technical Memorandum 33-301, Vol. III, Jet Propulsion Laboratory, Pasadena, Calif., Dec. 1, 1969.

Renzetti, N. A., *Tracking and Data System Support for Surveyor: Mission VI*, Technical Memorandum 33-301, Vol. IV, Jet Propulsion Laboratory, Pasadena, Calif., Dec. 1, 1969.

Renzetti, N. A., *Tracking and Data System Support for Surveyor: Mission VII*, Technical Memorandum 33-301, Vol. V, Jet Propulsion Laboratory, Pasadena, Calif., Dec. 1, 1969.

Renzetti, N. A., *Tracking and Data System Support for the Mariner Venus 67 Mission: Planning Phase Through Midcourse Maneuver*, Technical Memorandum 33-385, Vol. I, Jet Propulsion Laboratory, Pasadena, Calif., Sept. 1, 1969.

Renzetti, N. A., *Tracking and Data System Support for the Mariner Venus 67 Mission: Midcourse Maneuver Through End of Mission*, Technical Memorandum 33-385, Vol. II, Jet Propulsion Laboratory, Pasadena, Calif., Sept. 1, 1969.

Renzetti, N. A., *Tracking and Data System Support for the Pioneer Project: Pioneer VI. Prelaunch to End of Nominal Mission*, Technical Memorandum 33-426, Vol. I, Jet Propulsion Laboratory, Pasadena, Calif., Feb. 1, 1970.

Renzetti, N. A., *Tracking and Data System Support for the Pioneer Project: Pioneer VII. Prelaunch to End of Nominal Mission*, Technical Memorandum 33-426, Vol. II, Jet Propulsion Laboratory, Pasadena, Calif., Apr. 15, 1970.

Renzetti, N. A., *Tracking and Data System Support for the Pioneer Project: Pioneer VIII. Prelaunch Through May 1968*, Technical Memorandum 33-426, Vol. III, Jet Propulsion Laboratory, Pasadena, Calif., July 15, 1970.

Renzetti, N. A., *Tracking and Data System Support for the Pioneer Project: Pioneer IX. Prelaunch Through June 1969*, Technical Memorandum 33-426, Vol. IV, Jet Propulsion Laboratory, Pasadena, Calif., Nov. 15, 1970.

Renzetti, N. A., *Tracking and Data System Support for the Pioneer Project: Pioneer VI. Extended Mission: July 1, 1966–July 1, 1969*, Technical Memorandum 33-426, Vol. V, Jet Propulsion Laboratory, Pasadena, Calif., Feb. 1, 1971.

Renzetti, N. A., *Tracking and Data System Support for the Pioneer Project: Pioneer VII. Extended Mission: February 24, 1967–July 1, 1968*, Technical Memorandum 33-426, Vol. VI, Jet Propulsion Laboratory, Pasadena, Calif., Apr. 15, 1971.

Renzetti, N. A., *Tracking and Data System Support for the Pioneer Project: Pioneer VII. Extended Mission: July 1, 1968–July 1, 1969*, Technical Memorandum 33-426, Vol. VII, Jet Propulsion Laboratory, Pasadena, Calif., Apr. 15, 1971.

Renzetti, N. A., *Tracking and Data System Support for the Pioneer Project: Pioneer VIII. Extended Mission: June 1, 1968–July 1, 1969*, Technical Memorandum 33-426, Vol. VIII, Jet Propulsion Laboratory, Pasadena, Calif., May 1, 1971.

Renzetti, N. A., *Tracking and Data System Support for the Pioneer Project: Pioneers VI–IX. Extended Missions: July 1, 1969–July 1, 1970*, Technical Memorandum 33-426, Vol. IX, Jet Propulsion Laboratory, Pasadena, Calif., Aug. 15, 1971.

Renzetti, N. A., and Siegmeth, A. J., *Tracking and Data System Support for the Pioneer Project: Pioneers 6–9. Extended Missions: July 1, 1971–July 1, 1972*,

Technical Memorandum 33-426, Vol. XI, Jet Propulsion Laboratory, Pasadena, Calif., May 1, 1973.

Renzetti, N. A., et al., *Tracking and Data System Support for the Mariner Mars 1969 Mission: Planning Phase Through Midcourse Maneuver*, Technical Memorandum 33-474, Vol. I, Jet Propulsion Laboratory, Pasadena, Calif., May 15, 1971.

Renzetti, N. A., et al., *Tracking and Data System Support for the Mariner Mars 1969 Mission: Midcourse Maneuver Through End of Nominal Mission*, Technical Memorandum 33-474, Vol. II, Jet Propulsion Laboratory, Pasadena, Calif., Sept. 1, 1971.

Renzetti, N. A., Linnes, K. W., and Taylor, T. M., *Tracking and Data System Support for the Mariner Mars 1969 Mission: Extended Operations Mission*, Technical Memorandum 33-474, Vol. III, Jet Propulsion Laboratory, Pasadena, Calif., Sept. 15, 1971.

Renzetti, N. A., *A History of the Deep Space Network: From Inception to January 1, 1969*, Technical Report 32-1533, Vol. I, Jet Propulsion Laboratory, Pasadena, Calif., Sept. 1, 1971.

Renzetti, N. A., "Radio Communications at Planetary Distances," paper presented at the International Convention on Radio Communication, Rome and Bologna, Italy, Mar. 1974.

Richter, H. L., Rechtin, E., and Walter, W. K., *National Ground-Based Surveillance Complex (U)*, Publication 146, Jet Propulsion Laboratory, Pasadena, Calif., Feb. 16, 1959 (Confidential).

Rocci, S. A., "The 210-ft Parabolic Fully Steerable Tracking Antennas for a Deep Space Instrumentation Facility," in *Deep Space and Missile Tracking Antennas*, pp. 50–70, ASME, New York, 1966.

Rusch, W. V. T., *Phase Error and Associated Cross-Polarization Effects in Cassegrainian-Fed Microwave Antennas*, Technical Report 32-610, Jet Propulsion Laboratory, Pasadena, Calif., May 30, 1965.

Rusch, W. V. T., and Stelzried, C. T., *Observations of the Lunar Eclipse of December 19, 1964, at a Wavelength of 3.3 MM*, Technical Report 32-1097, Jet Propulsion Laboratory, Pasadena, Calif., reprinted from *Astrophys. J.*, Vol. 148, No. 1, pp. 255–259, Apr. 1967.

Rusch, W. V. T., *Applications of Two-Dimensional Integral-Equation Theory to Reflector-Antenna Analysis*, Technical Memorandum 33-478, Jet Propulsion Laboratory, Pasadena, Calif., May 1, 1971.

Sanger, D. K., *Digital Demodulation with Data Subcarrier Tracking*, Technical Report 32-1314, Jet Propulsion Laboratory, Pasadena, Calif., Aug. 1, 1968.

Siegmeth, A. J., Purdue, R. E., and Ryan, R. E., *Tracking and Data System Support for the Pioneer Project: Pioneers 6–9. Extended Missions: July 1, 1970–July 1, 1971*, Technical Memorandum 33-426, Vol. X, Jet Propulsion Laboratory, Pasadena, Calif., Aug. 15, 1972.

Siegmeth, A. J., et al., *Tracking and Data System Support for the Pioneer Project: Pioneer 10—Prelaunch Planning Through Second Trajectory Correction December 4, 1969 to April 1, 1972*, Technical Memorandum 33-584, Vol. I, Jet Propulsion Laboratory, Pasadena, Calif., Apr. 1, 1973.

Simon, M. K., "Nonlinear Analysis of an Absolute Value Type of an Early-Late Gate Bit Synchronizer," *IEEE Trans. Commun. Technol.*, Vol. COM-18, No. 5, pp. 589–596, Oct. 1970.

Simon, M. K., "Optimization of the Performance of a Digital-Data-Transition Tracking Loop," *IEEE Trans. Commun. Technol.*, Vol. COM-18, No. 5, pp. 686–689, Oct. 1970.

Simon, M. K., and Lindsey, W. C., "Data-Aided Carrier Tracking Loops," *IEEE Trans. Commun. Technol.*, Vol. COM-19, No. 2, pp. 157–168, Apr. 1971.

Simon, M. K., "On the Selection of an Optimum Design Point for Phase-Coherent Receivers Employing Bandpass Limiters," *IEEE Trans. Commun.*, Vol. COM-20, No. 2, pp. 210–214, Apr. 1972.

Simon, M. K., "On the Selection of a Sampling Filter Bandwidth for a Digital Data Detector," *IEEE Trans. Commun.*, Vol. COM-20, No. 3, pp. 438–441, June 1972.

Simon, M. K., and Springett, J. C., "The Performance of a Noncoherent FSK Receiver Preceded by a Bandpass Limiter," *IEEE Trans. Commun.*, Vol. COM-20, No. 6, pp. 1128–1136, Dec. 1972.

Simon, M. K., and Springett, J. C., *The Theory, Design, and Operation of the Suppressed Carrier Data-Aided Tracking Receiver*, Technical Report 32-1583, Jet Propulsion Laboratory, Pasadena, Calif., June 15, 1973.

Simon, M. K., and Smith, J. G., "Hexagonal Multiple Phase-and-Amplitude-Shift-Keyed Signal Sets," *IEEE Trans. Commun.*, Vol. COM-21, No. 10, pp. 1108–1115, Oct. 1973.

Sjogren, W. L., et al., *The Ranger V Flight Path and Its Determination From Tracking Data*, Technical Report 32-562, Jet Propulsion Laboratory, Pasadena, Calif., Dec. 6, 1963.

Sjogren, W. L., et al., *The Ranger VI Flight Path and Its Determination From Tracking Data*, Technical Report 32-605, Jet Propulsion Laboratory, Pasadena, Calif., Dec. 15, 1964.

Sjogren, W. L., *The Ranger III Flight Path and Its Determination From Tracking Data*, Technical Report 32-563, Jet Propulsion Laboratory, Pasadena, Calif., Sept. 15, 1965.

Sjogren, W. L., et al., *Physical Constants as Determined From Radio Tracking of the Ranger Lunar Probes*, Technical Report 32-1057, Jet Propulsion Laboratory, Pasadena, Calif., Dec. 30, 1966.

Sjogren, W. L., *Proceedings of the JPL Seminar on Uncertainties in the Lunar Ephemeris*, Technical Report 32-1247, Jet Propulsion Laboratory, Pasadena, Calif., May 1, 1968.

Sjogren, W. L., "Lunar Gravity Estimate: Independent Confirmation," *J. Geophys. Res.*, Vol. 76, No. 29, Oct. 10, 1971.

Sjogren, W. L., et al., "Lunar Gravity via Apollo 14 Doppler Radio Tracking,' *Science*, Vol. 175, No. 4018, pp. 165–168, Jan. 14, 1972.

Slobin, S. D., "Beam Switching Cassegrain Feed System and Its Applications to Microwave and Millimeterwave Radioastronomical Observations," *Rev. Sci. Instr.*, Vol. 41, No. 3, pp. 439–443, Mar. 1970.

Spier, G. W., *Design and Implementation of Models for the Double Precision Trajectory Program (DPTRAJ)*, Technical Memorandum 33-451, Jet Propulsion Laboratory, Pasadena, Calif., Apr. 15, 1971.

Springett, J. C., *Telemetry and Command Techniques for Planetary Spacecraft*, Technical Report 32-495, Jet Propulsion Laboratory, Pasadena, Calif., Jan. 15, 1965.

Springett, J. C., and Simon, M. K., "An Analysis of the Phase Coherent-Incoherent Output of the Bandpass Limiter," *IEEE Trans. Commun. Technol.*, Vol. COM-19, No. 1, pp. 42–49, Feb. 1971.

Stelzried, C. T., *Post-Amplifier Noise Temperature Contribution in a Low-Noise Receiving System*, Technical Report 32-446, Jet Propulsion Laboratory, Pasadena, Calif., Jan. 1964.

Stelzried, C. T., Reid, M. S., and Petty, S. M., *A Precision DC-Potentiometer Microwave Insertion-Loss Test Set*, Technical Report 32-887, Jet Propulsion Laboratory, Pasadena, Calif., Mar. 15, 1966.

Stelzried, C. T., Reid, M. S., and Nixon, D., *Precision Power Measurements of Spacecraft CW Signal With Microwave Noise Standards*, Technical Report 32-1066, Jet Propulsion Laboratory, Pasadena, Calif., Feb. 15, 1968.

Stelzried, C. T., and Reid, M. S., *Precision Power Measurements of Spacecraft CW Signal Level With Microwave Noise Standards*, Technical Report 32-1070, Jet Propulsion Laboratory, Pasadena, Calif., reprinted from *IEEE Trans. Instrum. Measurement*, Vol. IM-15, No. 4, pp. 318–324, Dec. 1966.

Stelzried, C. T., and Rusch, W. V. T., *Improved Determination of Atmospheric Opacity From Radio Astronomy Measurements*, Technical Report 32-1115, Jet Propulsion Laboratory, Pasadena, Calif., reprinted from *J. Geophys. Res.*, Vol. 72, No. 9, pp. 2445–2447, May 1, 1967.

Stelzried, C. T., and Otoshi, T. Y., "Radiometric Evaluation of Antenna-Feed Component Losses," *IEEE Trans. Instrumen. Measurement*, Vol. IM-18, No. 3, pp. 172–183, Sept. 1969.

Stelzried, C. T., "Precision Microwave Waveguide Loss Calibrations," *IEEE Trans. Instrum. Measurement*, Vol. IM-19, No. 1, pp. 23–25, Feb. 1970.

Stelzried, C. T., *A Faraday Rotation Measurement of a 13-cm Signal in the Solar Corona*, Technical Report 32-1401, Jet Propulsion Laboratory, Pasadena, Calif., July 15, 1970.

Stelzried, C. T., et al., "The Quasi-Stationary Coronal Magnetic Field and Electron Density as Determined From a Faraday Rotation Experiment," *Sol. Phys.*, Vol. 14, No. 2, pp. 440–456, Oct. 1970.

Stelzried, C. T., "Operating Noise-Temperature Calibrations of Low-Noise Receiving Systems," *Microwave J.*, Vol. 14, No. 6, pp. 41–46, 48, June 1971.

Stelzried, C. T., et al., "Transformation of Received Signal Polarization Angle to the Plane of the Ecliptic," *J. Space. Rock.*, Vol. 9, No. 2, pp. 69–70, Feb. 1972.

Stevens, R., and Victor, W. K., *The Goldstone Station Communications and Tracking System for Project Echo*, Technical Report 32-59, Jet Propulsion Laboratory, Pasadena, Calif., Dec. 1, 1960.

System Capabilities and Development Schedule of the Deep Space Instrumentation Facility 1963–1967, Technical Memorandum 33-83, Jet Propulsion Laboratory, Pasadena, Calif., Mar. 2, 1962.

Tardani, P. A., *Madrid Site Selection Report*, Technical Memorandum 33-149, Jet Propulsion Laboratory, Pasadena, Calif., July 17, 1963.

Tausworthe, R. C., *A Precision Planetary Range-Tracking Radar*, Technical Report 32-779, Jet Propulsion Laboratory, Pasadena, Calif., reprinted from *IEEE Trans. Space Electron. Telem.*, Vol. SET-11, No. 2, pp. 78–85, June 1965.

Tausworthe, R. C., *Theory and Practical Design of Phase-Locked Receivers*, Technical Report 32-819, Vol. I, Jet Propulsion Laboratory, Pasadena, Calif., Feb. 15, 1966.

Tausworthe, R., *Cycle Slipping in Phase-Locked Loops*, Technical Report 32-1127, Jet Propulsion Laboratory, Pasadena, Calif., reprinted from *IEEE Trans. Commun. Technol.*, Vol. COM-15, No. 3, pp. 417–421, June 1967.

Tausworthe, R. C., Easterling, M. F., and Spear, A. J., *A High-Rate Telemetry System for the Mariner Mars 1969 Mission*, Technical Report 32-1354, Jet Propulsion Laboratory, Pasadena, Calif., Apr. 1, 1969.

Tausworthe, R. C., *DSS Subsystem Implementation by Time-Shared Computer*, Technical Memorandum 33-420, Jet Propulsion Laboratory, Pasadena, Calif., Oct. 1, 1969.

Tausworthe, R. C., "Convergence of Oscillator Spectral Estimators for Counted-Frequency Measurements," *IEEE Trans. Commun.*, Vol. COM-20, No. 2, pp. 213–217, Apr. 1972.

Tausworthe, R. C., "Simplified Formula for Mean-Slip Time of Phase-Locked Loops With Steady-State Phase Error," *IEEE Trans. Commun.*, Vol. COM-20, No. 3, pp. 331–337, June 1972.

Tausworthe, R. C., and Crow, R. B., "Improvements in Deep-Space Tracking by Use of Third-Order Loops," *Proceedings of the 1972 International Telemetering Conference, Los Angeles, California, October 10–12, 1972*, pp. 577–583.

Telecommunications Systems Design Techniques Handbook, Technical Memorandum 33-571, edited by R. E. Edelson, Jet Propulsion Laboratory, Pasadena, Calif., July 15, 1972.

Textor, G. P., Kelly, L. B., and Kelly, M., *Tracking and Data System Support for the Mariner Mars 1971 Mission: First Trajectory Correction Maneuver Through Orbit Insertion*, Technical Memorandum 33-523, Vol. II, Jet Propulsion Laboratory, Pasadena, Calif., June 15, 1972.

Thornton, J. H., Jr., *The Surveyor I and Surveyor II Flight Paths and Their Determination From Tracking Data*, Technical Report 32-1285, Jet Propulsion Laboratory, Pasadena, Calif., Aug. 1, 1968.

Timor, U., "Equivalence of Time-Multiplexed and Frequency-Multiplexed Signals in Digital Communications," *IEEE Trans. Commun.*, Vol. COM-20, No. 3, pp. 435–438, June 1972.

Titsworth, R. C., and Welch, L. R., *Power Spectra of Signals Modulated by Random and Pseudorandom Sequences*, Technical Report 32-140, Jet Propulsion Laboratory, Pasadena, Calif., Oct. 10, 1961.

Titsworth, R. C., *The Algebra of Periodic Sequences*, Technical Report 32-381, Jet Propulsion Laboratory, Pasadena, Calif., Jan. 7, 1963.

Titsworth, R. C., *Correlation Properties of Cyclic Sequences*, Technical Report 32-388, Jet Propulsion Laboratory, Pasadena, Calif., July 1, 1963.

Titsworth, R. C., *Optimal Ranging Codes*, Technical Report 32-411, Jet Propulsion Laboratory, Pasadena, Calif., Apr. 15, 1963.

Titsworth, R. C., *Equivalence Classes of Periodic Sequences*, Technical Report 32-568, Jet Propulsion Laboratory, Pasadena, Calif., June 15, 1964, reprinted from *Ill. J. Math.*, Vol. 8, No. 2, June 1964.

Titsworth, R. C., *The Role of Pseudorandom Codes in Communications*, Technical Memorandum 33-185, Jet Propulsion Laboratory, Pasadena, Calif., Aug. 3, 1964.

"Tracking and Data Acquisition System for Mariner Missions," *Proceedings of the Seventh International Symposium on Space Technology and Science*, Tokyo, May 1967.

Vegos, C. J., et al., *The Ranger IX Flight Path and Its Determination From Tracking Data*, Technical Report 32-767, Jet Propulsion Laboratory, Pasadena, Calif., Nov. 1, 1968.

Victor, W. K., *Precision Frequency Control—A Communications Requirement of the Space Age*, External Publication 627, Jet Propulsion Laboratory, May 13, 1959.

Victor, W. K., and Stevens, R., "The Role of the Jet Propulsion Laboratory in Project Echo," *IRE Trans.*, Vol. SET-7, pp. 20–29, Mar. 1961.

Victor, W. K., Stevens, R., and Golomb, S. W., *Radar Exploration of Venus: Goldstone Observatory Report for March-May 1961*, Technical Report 32-132, Jet Propulsion Laboratory, Pasadena, Calif., Aug. 1, 1961.

Victor, W. K., Titsworth, R. C., and Rechtin, E., *Telecommunication Aspects of a Manned Mars Mission*, Technical Report 32-501, Jet Propulsion Laboratory, Pasadena, Calif., Aug. 20, 1963.

Viterbi, A. J., *Acquisition Range and Tracking Behavior of Phase-Locked Loops*, External Publication 673, Jet Propulsion Laboratory, Pasadena, Calif., July 14, 1959.

Viterbi, A. J., *On Coded Phase-Coherent Communications*, Technical Report 32-25, Jet Propulsion Laboratory, Pasadena, Calif., Aug. 15, 1960.

Viterbi, A. J., *Classification and Evaluation of Coherent Synchronous Sampled-Data Telemetry Systems*, Technical Report 32-123, Jet Propulsion Laboratory, Pasadena, Calif., June 15, 1961.

Viterbi, A. J., *Phase-Locked Loop Dynamics in the Presence of Noise by Fokker-Planck Techniques*, Technical Report 32-427, Jet Propulsion Laboratory, Pasadena, Calif., Mar. 29, 1963; also reprinted in *IEEE Proc.*, Vol. 51, No. 12, pp. 1737–1753, Dec. 1963.

Viterbi, A. J., *Orthogonal Tree Codes for Communication in the Presence of White Gaussian Noise*, Technical Report 32-1120, Jet Propulsion Laboratory, Pasadena, Calif., reprinted from *IEEE Trans. Commun. Technol.*, Vol. COM-15, No. 2, pp. 238–242, Apr. 1967.

Winn, F. B., "Selenographic Location of Surveyor VI," in *Surveyor VI Mission Report: Part II. Science Results*, Technical Report 32-1262, Jet Propulsion Laboratory, Pasadena, Calif., Jan. 10, 1968.

Winn, F. B., "Post Landing Tracking Data Analysis," in *Surveyor VII Mission Report: Part II. Science Results*, Technical Report 32-1264, Jet Propulsion Laboratory, Pasadena, Calif., Mar. 15, 1968.

Winn, F. B., "Surveyor Post-Touchdown Analysis of Tracking Data," in *Surveyor Project Final Report: Part II. Science Results*, Technical Report 32-1265, Jet Propulsion Laboratory, Pasadena, Calif., June 15, 1968.

Winn, F. B., *Surveyor Posttouchdown Analyses of Tracking Data*, NASA SP-184, National Aeronautics and Space Administration, Washington, D.C., p. 369.

Wollenhaupt, W. R., *Tracking System Data Analysis Report, Ranger 4 Final Report*, Technical Report 32-523, Jet Propulsion Laboratory, Pasadena, Calif., Mar. 1, 1964.

Wollenhaupt, W. R., et al., *The Ranger VII Flight Path and Its Determination From Tracking Data*, Technical Report 32-694, Jet Propulsion Laboratory, Pasadena, Calif., Dec. 15, 1964.

Wong, S. K., and Reinbold, S. J., "Earth–Moon Mass Ratio From Mariner 9 Radio Tracking Data," *Nature*, Vol. 241, No. 5385, pp. 111–112, Jan. 12, 1973.

Woo, R., and Ishimaru, A., "Remote Sensing of the Turbulence Characteristics of a Planetary Atmosphere by Radio Occultation of a Space Probe," *Radio Sci.*, Vol. 8, No. 2, pp. 103–108, Feb. 1973.

Woo, R., et al., *Effects of Turbulence in the Atmosphere of Venus on Pioneer Venus Radio—Phase I*, Technical Memorandum 33-644, Jet Propulsion Laboratory, Pasadena, Calif., June 30, 1973.

Yuen, J. H., "A Double-Loop Tracking System," *IEEE Trans. Commun.*, Vol. COM-20, No. 6, pp. 1142–1150, Dec. 1972.

Yuen, J. H., *A Practical Statistical Model for Telecommunications Performance Uncertainty*, Technical Memorandum 33-732, Jet Propulsion Laboratory, Pasadena, Calif., June 15, 1975.

NASA—JPL—Coml., L.A., Calif.